Vortex rings in axially rotating fluids

Helen Terry

School of Mathematical Sciences

Thesis submitted to The University of Nottingham for the degree of Doctor of Philosophy

January 2019

Abstract

Rotating turbulent flows are found in many geophysical, astrophysical and industrial applications. These turbulent flows can be considered to be comprised of a collection of coherent structures. An understanding of these smaller coherent structures can allow insight into the behaviour of the larger turbulent motion as a whole. This thesis focuses on the effect of rotation on one particular type of coherent structure - the vortex ring - and is motivated by the belief that greater knowledge of how individual vortex rings behave in rotating fluids will lead to a better understanding of rotating turbulent flows.

The first part of this thesis presents exact solutions of spherical vortices propagating steadily along the axis of a rotating ideal fluid. It is shown that Hill's spherical vortex and Moffatt's family of swirling vortices are able to persist in a rotating fluid with the boundary of the spherical vortex swirling in such a way as to exactly cancel out the background rotation of the system. The flow external to the spherical vortex exhibits fully nonlinear inertial wave motion and above a critical rotation rate, closed streamlines may form in this outer fluid region and hence carry fluid along with the spherical vortex. As the rotation rate is further increased, further concentric 'sibling' vortex rings are formed.

The latter part of this thesis is a numerical investigation into the effect of rotation on vortices in viscous fluids. The presence of azimuthal swirl is critical to vortex ring behaviour and similarities are drawn between the behaviour of swirling vortices in non-rotating flows and initially swirl-free vortex rings in rotating flows which subsequently induce swirl of their own. The findings corroborate past work that suggests vortex motion in rotating fluids can be highly unstable. However, the newly-discovered exact solutions of spherical vortices in rotating ideal fluids are then used to demonstrate that vortex motion in rotating viscous fluids need not be as unstable as previously thought.

Finally, as an extremal member of the Fraenkel-Norbury family of vortices this work contrasts the behaviour of Hill's spherical vortex to vortex rings in this family with narrower vortex cores.

Preface

The research reported in this thesis was carried at the School of Mathematical Sciences at the University of Nottingham between October 2015 and January 2019. No part of the thesis has been, or is being, submitted for any degree or other qualification at any other university. The contents of chapter 3 is collaborative work with Dr Matthew Scase published under the title *Spherical vortices in rotating fluids* (*J. Fluid Mech.* vol. 846 (R4) , 2018). The rest of this thesis is my own work and contains nothing which is the outcome of collaboration with others.

I would like to thank my supervisor Matt Scase, co-supervisor John Billingham, my fellow PhD students, and finally, my parents for all of their advice and support throughout.

Contents

Chapter 1

Introduction

This thesis investigates the effect of axial rotation on vortex rings. The study of vortices has been "...stimulated by the idea that turbulent fluid motion may be viewed as comprising ensembles of more or less coherent laminar structures that interact via relatively simple dynamics..." (Pullin, 1992). That is to say that an understanding of these smaller laminar structures can allow insight into the behaviour of the larger turbulent motion as a whole. This thesis is therefore motivated in the hope that a greater knowledge of how single vortices in rotating fluids behave will lead to a better understanding of rotating turbulent flows.

1.1 Vortex rings in turbulent flows

Vortex rings are one of the most fundamental phenomenon in fluid dynamics. They can be defined as toroidal volumes of rotational fluid which spin about an imaginary closed loop encircling an axis of propagation. A meridional slice through an axisymmetric vortex ring is given in figure 1.1. The grey shading highlights the vortex core. Fluid moving along with the vortex ring but not necessarily inside the vortex core is referred to as the vortex atmosphere and often resembles a flattened ellipsoid. The ring radius, R, gives the distance from the axis of propagation (dashed line) to the centre of the vortex core whilst the core radius, a, gives the thickness of the vortex core. The precise definitions of these quantities vary between works.

The compact nature of vortex rings makes them ideal as relatively simple building blocks in the modelling of more complex flows such as turbulent jets and plumes (Lim and Nickels, 1995). Richardson (1922) explained that turbulence can be thought to be composed of eddies of many different sizes. The largest

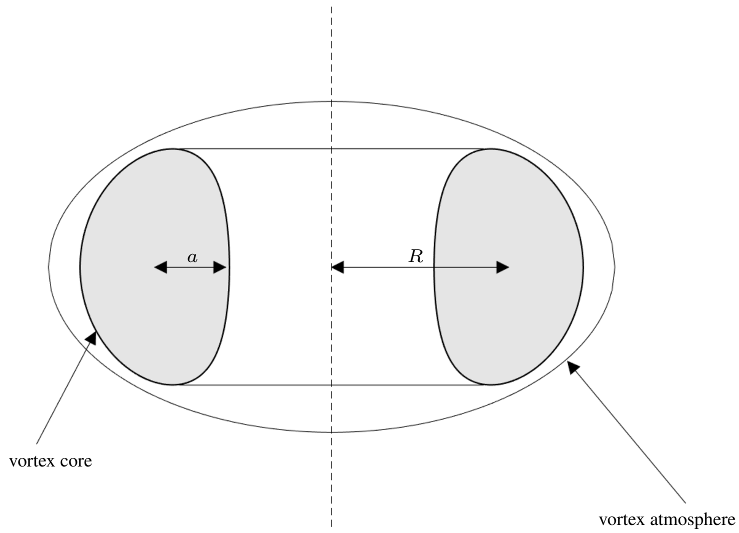

Figure 1.1: Schematic of a vortex ring introducing terminology used in this thesis: vortex core, ring radius, R, vortex core radius, a, and vortex atmosphere. The dashed line indicates the axis of propagation.

eddies in the flow receive their kinetic energy from the "basic" or averaged background flow. This could be through shear forces or buoyancy effects. An energy cascade follows where larger eddies break up and transfer energy to smaller eddies. These eddies break up into successively smaller eddies. When the Reynolds number - the dimensionless number giving the relative importance of inertial to viscous effects - associated with the eddy motion is sufficiently small the motion becomes stable and kinetic energy is then dissipated at a molecular level.

Since the work of Richardson (1922) many studies have considered turbulent flows as arrays of vortices (see Lau and Fisher, 1975; Davies and Yule, 1975; Acton, 1980). Hill's spherical vortex was used by Synge and Lin (1943) who represented isotropic turbulence as a random superposition of Hill's spherical vortices. Synge and Lin were able to derive an expression for the longitudinal velocity correlation - a function which reflects how the velocities at two points a distance r from each other affect each other. As an inviscid and steady solution to the Euler equations, Hill's spherical vortex is best viewed as a model for the larger energy containing eddies of the turbulent flow rather than the finer structure. Saffman (1997) explains: "owing to the absence of internal structure or a continuous dissipation mechanism, its use in calculating turbulence properties of the inertial and dissipation ranges is limited."

Hill's spherical vortex arises in applications such as the rise of thermals (Turner, 1964) and the motion of bubbles or droplets at high Reynolds numbers (see Moore, 1963; Harper and Moore, 1968). However, Lugt (1983) gives many further examples of naturally occurring vortex rings as well as those found in technology.

Saffman (1981) captured each aspect of the vortex ring problem in his paper *Dynamics of Vorticity*: "One particular motion exemplifies the whole range of problems of vortex motion and is also a commonly known phenomenon, namely the vortex ring or smoke ring. . . . Their formation is a problem of vortex sheet dynamics, the steady state is a problem of existence, their duration is a problem of stability, and if there are several we have the problem of vortex interactions". This work will focus on the existence and stability of vortex rings in axially rotating fluids.

1.2 Vortex rings in rotating fluids

Some of the most notable research into the effect of rotation on vortex rings is the work of Verzicco et al. (1996) who investigated numerically and in laboratory experiments the effect of rotation acting parallel to the direction of vortex propagation. The study found three main impacts of the rotation: the translation velocity of the vortex ring decreases, a region of negative azimuthal vorticity is produced ahead of the ring and a cyclonic axial vortex is generated in the wake of the ring. These structures are formed due to the presence of a self-induced swirl flow. Verzicco et al. (1996) explain this by referring to the equations of motion and considering the Coriolis term. Although in their experiments the swirl was generated by the vortex rings themselves the results agreed with that of Virk et al. (1994) for polarised vortex rings.

Polarised rings are a subclass of rings with swirl. They have vortex lines - curves whose tangent is parallel to the local vorticity vector - which are helical rather than circular (see figure 1.2). Polarised rings always have swirl, however, vortex rings with swirl are not necessarily polarised. Virk et al. (1994) found that in non-rotating fluids polarised rings develop a "head-tail structure, where the head is a vortex ring, but in contrast to unpolarised rings, the tail is an axial vortex."

Verzicco et al. (1996) also discovered that if the Reynolds number of the flow is sufficiently high and the Rossby number - the dimensionless number giving the relative importance of Coriolis to inertial effects

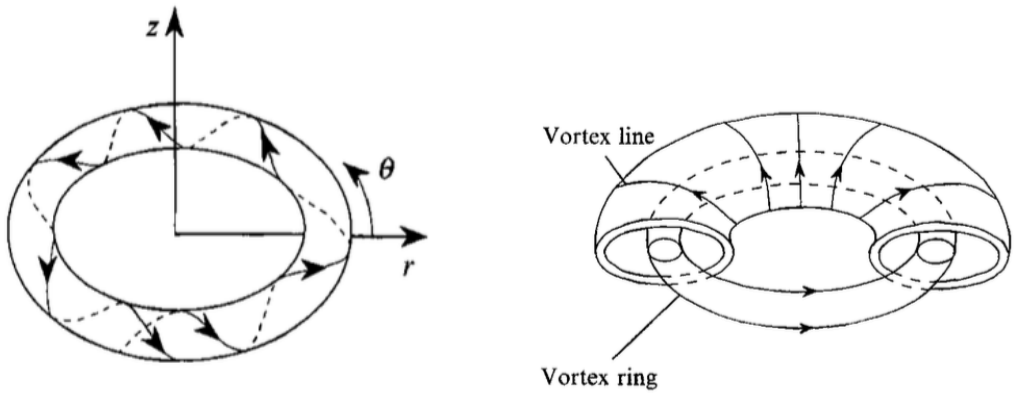

Figure 1.2: Figure 1(a) from Virk et al. (1994) (left). A vortex line on a typical polarised vortex ring. Figure 1(c) from Virk et al. (1994) (right). This vortex ring surrounded by toroidal vorticity sheath has swirl, but with circular vortex lines it is unpolarised.

- sufficiently low the phenomenon of vortex shedding is observed whereby vortex rings with oppositely signed vorticity are shed from the rear of the primary ring (see figure 1.3). Finally, they found that when the Rossby number is decreased past a critical value the Coriolis force begins to dominate the flow and we see a complete break down of the vortex ring. During this collapse inertial waves are seen propagating from the vortex ring.

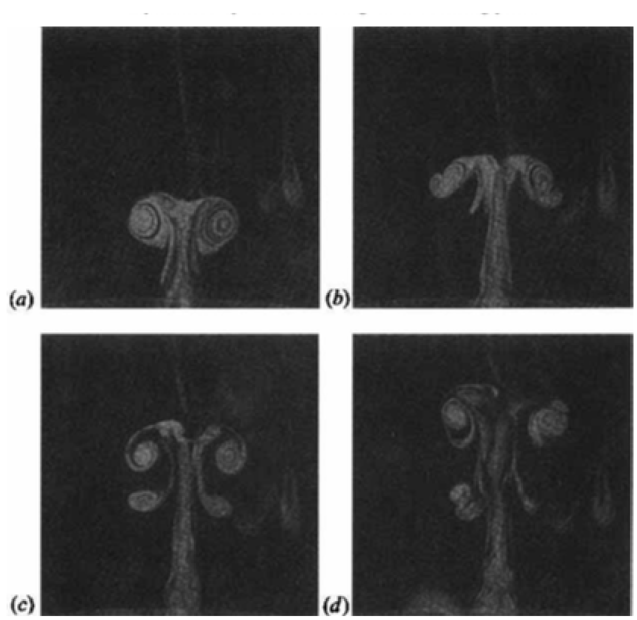

Figure 1.3: Figure 4 from Verzicco et al. (1996). Dye visualisations of a vortex ring evolution at $\mathrm{Ro} = 4.8$ *and* $\mathrm{Re} \approx 1000$. *The oppositely signed vortex ring can be seen most clearly in* (c).

Eisenga et al. (1998) conducted laboratory experiments of a vortex ring propagating orthogonally to the axis of rotation (see figure 1.4). Vortex rings were found to propagate along a curved path, following a spiral trajectory in the rotating frame but retaining their orientation in the laboratory frame. The background rotation causes one half of the vortex ring to shrink and the other to widen and the ring core is entirely deformed.

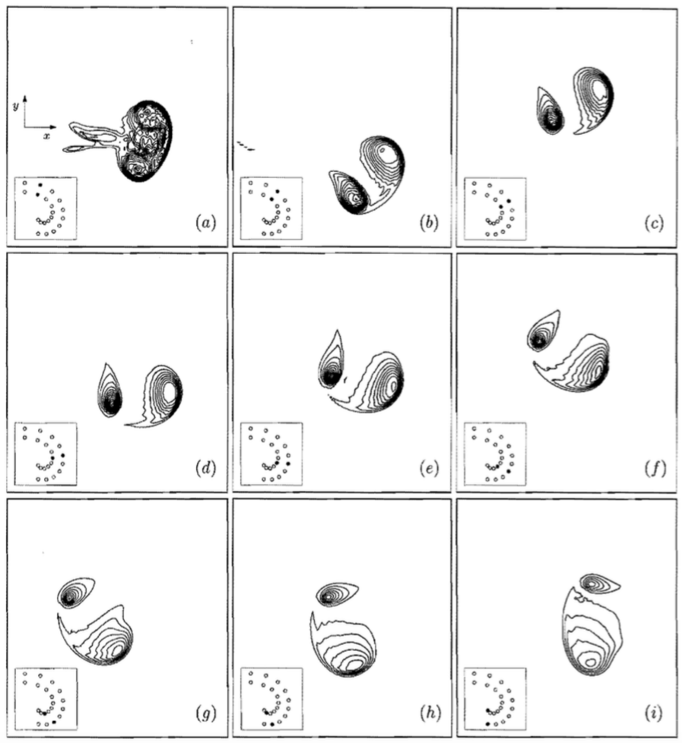

Figure 1.4: Figure 4.12 from Eisenga (1997). In a rotating frame of reference where the rotation vector is pointing out of the page. Contour plots of passive scalar concentration C in the horizontal symmetry plane $z = 0$ *of the vortex ring, obtained from a numerical simulation with* $\mathrm{Ro} = 23$ *and* $\mathrm{Re} = 900$.

Brend and Thomas (2009) have since conducted further experiments in a rotating water-filled tank. Compared to the 1m high tank available to Verzicco et al. (1996) the octagonal tank used by Brend and Thomas was 2.5m high and part of a greater 5.7m high structure. The main focus of the study was to determine a statistical expression relating the background rate of rotation and the decay length x_d of the vortex ring. The Taylor-Proudman theorem states that rotation acts to suppress variation in the velocity in the direction parallel to the axis of rotation. This suggests that the decay length x_d decreases with decreasing Rossby number and in agreement with this Brend and Thomas found that for a vortex ring generated with a nozzle of diameter D in a fluid rotating with Rossby number, Ro, the decay length and Rossby number could be related by the expression $x_d/D = 4.77\,\mathrm{Ro}^{1.06}$. Brend and Thomas also corroborated the findings of Verzicco et al. (1996) which found that a strong cyclonic tail forms in the wake of the vortex ring as well an anticyclonic swirling region ahead of the vortex ring.

Watchapon (2015) conducted a finite difference investigation into the effect of axial rotation on an axisymmetric vortex ring. His numerical method differed from Verzicco et al. (1996) as the vortex ring was not formed from the roll up of fluid against a solid boundary. Instead he prescribed a vortex ring with a slender vortical core and Gaussian distribution of azimuthal vorticity. This method of prescribing a toroidal structure with a Gaussian distribution of azimuthal vorticity was also employed by Uchiyama et al. (2015). Like Verzicco et al. (1996) both works found a swirling axial vortex generated behind the vortex ring and negative azimuthal swirl ahead of the ring. Negative azimuthal vorticity produced at the front of the vortex ring was also shed off the back of the vortex ring as its own oppositely signed structure at appropriate Reynolds and Rossby numbers. Finally, Watchapon (2015) introduced a small azimuthal perturbation to the vortex ring. This resulted in an instability in the swirling axial vortex which grows with time developing into "four secondary (spiral) vortices in front of the vortex core."

The aforementioned works all point to the importance of azimuthal swirl in vortex dynamics whether this is self-generated in a rotating fluid or initially present in a non-rotating fluid. However, there has been no dedicated work to link these findings and investigate swirling vortex rings in rotating fluids. There is scope for further research into vortex rings in rotating fluids and how azimuthal swirl plays a critical role in their behaviour and this thesis aims to address this knowledge gap.

1.3 Outline of thesis

Chapter 2 provides a derivation of the equations of motion used in this work. These are the Navier-Stokes equations in a rotating frame of reference and the derivation has been taken from Pedlosky (1987, chap.1).

Chapter 2 also includes a detailed background of the axisymmetric vortex rings considered in this thesis; the Fraenkel-Norbury vortex ring family, Moffatt vortices and Hill's spherical vortex as a special member of both of these families. Hill's spherical vortex is one of only a few exact vortex ring solutions to the Euler equations. It is known to closely resemble buoyant thermals (Turner, 1964) and the motion of bubbles and droplets at high Reynolds numbers (Harper and Moore, 1968) and will be the main focus of this work. As such a recap of the stability analyses of Moffatt and Moore (1978) and Pozrikidis (1986) are also presented.

Chapter 3 appears in modified form in the Journal of Fluid Mechanics (Scase and Terry, 2018). The chapter presents an exact, steady solution of Hill's spherical vortex in a rotating fluid. It is also shown that the infinite family of swirling vortices found by Moffatt (1969) can persist in a rotating fluid in the same way that Hill's spherical vortex does.

Chapter 4 begins by outlining the finite element formulation for the rotating Navier-Stokes equations used throughout this thesis. The numerical scheme is then used to conduct an investigation into how Hill's spherical vortex behaves in a viscous fluid. Non-rotating flows are first considered and the results are contrasted with the inviscid stability analyses of Moffatt and Moore (1978) and Pozrikidis (1986). The investigation is then repeated for a rotating fluid. Following the claim by Virk et al. (1994) that in transitional and turbulent flows most vortical structures have a swirl component the behaviour of Moffatt's swirling vortices in a rotating fluid are also simulated. Verzicco et al. (1996) suggest at the end of their work that interest in these initially swirling vortex rings "would be mostly theoretical, since it is almost impossible to generate such vortices experimentally and therefore they are not likely to be found in real applications". In contrast, Naitoh et al. (2014) argue "Turbulent shear flows frequently contain large-scale organised vortical structures including helicity. These structures dominate turbulence transport, mixing, drag, noise generation, etc. Then, the behaviour of vortex rings with swirl (i.e., the cascade and topology-changing as shown in Virk et al. (1994)) is considered as a simple and important model for understanding turbulence physics and controlling turbulence phenomena. From this viewpoint, it is important to investigate the flow field of a vortex ring with swirl".

Chapter 5 considers the difference in the developing flows when the original Hill's and Moffatt vortex solutions and the "rotating" Hill's and Moffatt solutions of chapter 3 are used as initial flow fields in the finite element solver. The results demonstrate that past analyses may be misleading in how unstable vortex motion in rotating fluids need necessarily be and this is the key finding of this thesis.

Finally, chapter 6 considers the behaviour of other Fraenkel-Norbury vortex rings in rotating fluids providing insight into whether vortex rings with narrower or fatter vortex cores are able to persist for longer in a rotating fluid. The results are compared with the behaviour of its fattest family member - Hill's spherical vortex. Conclusions are drawn in chapter 7 and suggestions for further work are given.

There are two appendices included at the end of this thesis. Appendix A gives the derivation of the finite element problem used to calculate the stream function from either the velocity or vorticity fields in chapters 2, 4, 5 and 6. Appendix B details the comptational resource used to produce the work in this thesis

Chapter 2

Background

This chapter provides the necessary background material for this thesis. It begins in section 2.1 with the derivation of the equations of motion for this work - the Navier-Stokes equations in a rotating frame of reference - before introducing the Coriolis force in section 2.2. A brief outline of axisymmetric vortex rings from Wu et al. (2006) is given in section 2.3. Section 2.4 details the Fraenkel-Norbury family of vortex rings. In section 2.5 a thorough review of Hill's spherical vortex is given. Finally, Moffatt's swirling vortices are introduced in section 2.6.

2.1 Equations of motion

The Navier-Stokes equations are an application of Newton's second law of motion, $\mathbf{F} = m\mathbf{a}$, to a fluid continuum and their derivation can be found in most introductory fluid dynamics text books (Batchelor, 1967). For an incompressible, viscous fluid with pressure field p, velocity field $\mathbf{u}$, constant density ρ and kinematic viscosity ν the equations of motion in an inertial frame of reference are

$$\frac{\mathrm{D}\mathbf{u}}{\mathrm{D}t} = -\frac{1}{\rho}\nabla p + \nu\nabla^2\mathbf{u}, \tag{2.1a}$$

$$\nabla \cdot \mathbf{u} = 0, \tag{2.1b}$$

where

$$\frac{\mathrm{D}}{\mathrm{D}t} \equiv \frac{\partial}{\partial t} + \mathbf{u} \cdot \nabla$$

is the material or total derivative of a quantity with respect to time. Equation (2.1a) states that the mass per unit volume times the acceleration is equal to the sum of the pressure gradient force and the frictional force. Equations (2.1) are only valid in an inertial frame of reference. In order to better consider rotating fluids these equations must be transformed into a rotating frame of reference.

2.1.1 Rotating coordinate frames

It can be shown (Pedlosky, 1987, chap.1) that for a vector, $\mathbf{A}$, of fixed magnitude rotating with angular velocity $\mathbf{\Omega}$, to a stationary observer the rate of change of that vector is given by

$$\frac{\mathrm{D}\mathbf{A}}{\mathrm{D}t} = \mathbf{\Omega} \times \mathbf{A} \tag{2.2}$$

whilst an observer fixed in the rotating frame of reference would see no change.

Now consider an arbitrary vector $\mathbf{B} = (B_1, B_2, B_3)$ in a rotating orthogonal coordinate system, rotating with angular velocity $\mathbf{\Omega}$. The vector $\mathbf{B}$ can be expressed as

$$\mathbf{B} = B_1\mathbf{i} + B_2\mathbf{j} + B_3\mathbf{k}, \tag{2.3}$$

so that the rate of change of $\mathbf{B}$ for the observer in the rotating frame of reference is

$$\left(\frac{\mathrm{D}\mathbf{B}}{\mathrm{D}t}\right)_R = \frac{\mathrm{D}B_1}{\mathrm{D}t}\mathbf{i} + \frac{\mathrm{D}B_2}{\mathrm{D}t}\mathbf{j} + \frac{\mathrm{D}B_3}{\mathrm{D}t}\mathbf{k}, \tag{2.4}$$

as fixed in this rotating frame of reference the magnitude and direction of the unit vectors remains constant. Subscript R is used to refer to the rotating frame of reference and subscript I is used to refer to the inertial frame of reference.

An observer in the inertial reference frame will witness not only the change to the components of $\mathbf{B}$ but also the change to the unit vectors with time. Thus

$$\left(\frac{\mathrm{D}\mathbf{B}}{\mathrm{D}t}\right)_I = \frac{\mathrm{D}B_1}{\mathrm{D}t}\mathbf{i} + \frac{\mathrm{D}B_2}{\mathrm{D}t}\mathbf{j} + \frac{\mathrm{D}B_3}{\mathrm{D}t}\mathbf{k} + B_1\frac{\mathrm{D}\mathbf{i}}{\mathrm{D}t} + B_2\frac{\mathrm{D}\mathbf{j}}{\mathrm{D}t} + B_3\frac{\mathrm{D}\mathbf{k}}{\mathrm{D}t}. \tag{2.5}$$

Application of equation (2.2) to each of the material derivatives of the unit vectors in (2.5) yields

$$\left(\frac{\mathrm{D}\mathbf{B}}{\mathrm{D}t}\right)_I = \frac{\mathrm{D}B_1}{\mathrm{D}t}\mathbf{i} + \frac{\mathrm{D}B_2}{Dt}\mathbf{j} + \frac{\mathrm{D}B_3}{\mathrm{D}t}\mathbf{k} + B_1\mathbf{\Omega} \times \mathbf{i} + B_2\mathbf{\Omega} \times \mathbf{j} + B_3\mathbf{\Omega} \times \mathbf{k} \tag{2.6}$$

which may be simplified to

$$\left(\frac{\mathrm{D}\mathbf{B}}{\mathrm{D}t}\right)_I = \left(\frac{\mathrm{D}\mathbf{B}}{\mathrm{D}t}\right)_R + \boldsymbol{\Omega} \times \mathbf{B}. \tag{2.7}$$

Thus for a vector of fixed magnitude rotating at angular velocity $\boldsymbol{\Omega}$ the rate of change of the vector with respect to time is seen differently in the rotating and inertial frames of reference.

2.1.2 The Navier-Stokes equations in a rotating coordinate frame

Let $\mathbf{x}$ represent the position vector of an arbitrary fluid parcel. Equation (2.7) gives

$$\left(\frac{\mathrm{D}\mathbf{x}}{\mathrm{D}t}\right)_I = \left(\frac{\mathrm{D}\mathbf{x}}{\mathrm{D}t}\right)_R + \boldsymbol{\Omega} \times \mathbf{x}. \tag{2.8}$$

The left hand side of this equation is the velocity of the fluid parcel observed in the inertial frame which can be denoted by $\mathbf{u}_I$. The first term on the right hand side is the velocity of the fluid parcel observed in the rotating frame and can be denoted by $\mathbf{u}_R$. Equation (2.8) can be written instead as

$$\mathbf{u}_I = \mathbf{u}_R + \boldsymbol{\Omega} \times \mathbf{x}. \tag{2.9}$$

Newton's second law relates the force per unit mass to the acceleration in an inertial frame of reference. Therefore we wish to find an expression for the acceleration - the rate of change of $\mathbf{u}_I$ - to equate with the applied forces. Equation (2.7) with $\mathbf{B} = \mathbf{u}_I$ gives

$$\left(\frac{\mathrm{D}\mathbf{u}_I}{\mathrm{D}t}\right)_I = \left(\frac{\mathrm{D}\mathbf{u}_I}{\mathrm{D}t}\right)_R + \boldsymbol{\Omega} \times \mathbf{u}_I. \tag{2.10}$$

Eliminating $\mathbf{u}_I$ from the right hand side we have

$$\begin{aligned}\left(\frac{\mathrm{D}\mathbf{u}_I}{\mathrm{D}t}\right)_I &= \left(\frac{\mathrm{D}}{\mathrm{D}t}\left(\mathbf{u}_R + \boldsymbol{\Omega} \times \mathbf{x}\right)\right)_R + \boldsymbol{\Omega} \times \left(\mathbf{u}_R + \boldsymbol{\Omega} \times \mathbf{x}\right) \\ &= \left(\frac{\mathrm{D}\mathbf{u}_R}{\mathrm{D}t}\right)_R + \frac{\mathrm{D}\boldsymbol{\Omega}}{\mathrm{D}t} \times \mathbf{x} + \boldsymbol{\Omega} \times \left(\frac{\mathrm{D}\mathbf{x}}{\mathrm{D}t}\right)_R + \boldsymbol{\Omega} \times \left(\mathbf{u}_R + \boldsymbol{\Omega} \times \mathbf{x}\right) \\ &= \left(\frac{\mathrm{D}\mathbf{u}_R}{\mathrm{D}t}\right)_R + 2\,\boldsymbol{\Omega} \times \mathbf{u}_R + \boldsymbol{\Omega} \times \left(\boldsymbol{\Omega} \times \mathbf{x}\right) + \frac{\mathrm{D}\boldsymbol{\Omega}}{\mathrm{D}t} \times \mathbf{x}. \end{aligned} \tag{2.11}$$

Equation (2.11) shows that there are three sources to the difference between the accelerations in the different frames of reference. These terms are the Coriolis acceleration, the centrifugal acceleration, and the acceleration due to variations in rotation rate with time itself. In this work the rotation rate is constant and therefore the last term on the right hand side is neglected.

Substitution of the acceleration from equation (2.11) into equation (2.1) gives the Navier-Stokes equations in a rotating coordinate frame

$$\frac{\mathrm{D}\mathbf{u}}{\mathrm{D}t} + 2\,\boldsymbol{\Omega} \times \mathbf{u} + \boldsymbol{\Omega} \times (\boldsymbol{\Omega} \times \mathbf{x}) = -\frac{1}{\rho}\nabla p + \nu\nabla^2\mathbf{u}, \tag{2.12a}$$

$$\nabla \cdot \mathbf{u} = 0. \tag{2.12b}$$

The second and third terms on the left hand side of equation (2.12a) represent the Coriolis and centrifugal forces. These forces are referred to as fictitious forces: apparent forces which are only present when non-inertial frames of reference are used. Equations (2.12) are the primary equations of motion solved throughout this thesis.

2.2 The Coriolis force

The Coriolis force acts in the direction perpendicular to both the axis of rotation and the local velocity field. Only the component of **u** in the lateral plane - the plane perpendicular to the axis of rotation - is important. The lateral component of the velocity field $\mathbf{u}_{\mathrm{lat}}$ and the Coriolis force can be seen in figure 2.1. The Coriolis force tends to change the component $\mathbf{u}_{\mathrm{lat}}$ acting in the opposite sense to the rotation of the system in the laboratory frame. As the Coriolis force is linear in the velocity **u** a material element in a flow dominated by the Coriolis force moves on a path whose projection on the lateral plane is a circle (see Batchelor, 1967). Therefore the Coriolis force will eventually restore a fluid element back to its original position on the lateral plane.

Now consider a collection of fluid elements - in the rotating reference frame - whereby a motion locally causes a positive expansion in the lateral plane with $\partial u/\partial x + \partial v/\partial y > 0$. In this region the area enclosed by the projection of a material curve onto the lateral plane will increase. With this outward motion of the material curve the Coriolis effect will generate a tangential motion to the material curve (see figure 2.1). As circulation is the line integral of the velocity field around a material curve this tangential motion produces a negative contribution to the circulation of fluid enclosed by the material curve. In fact, this negative circulation occurs to keep the circulation remaining constant in the laboratory frame of reference. This induced tangential motion itself produces a Coriolis force in a direction normal to the material curve which is directed mostly inwards. The net effect of this is a Coriolis force directed inwards which acts to reduce the area enclosed by the curve.

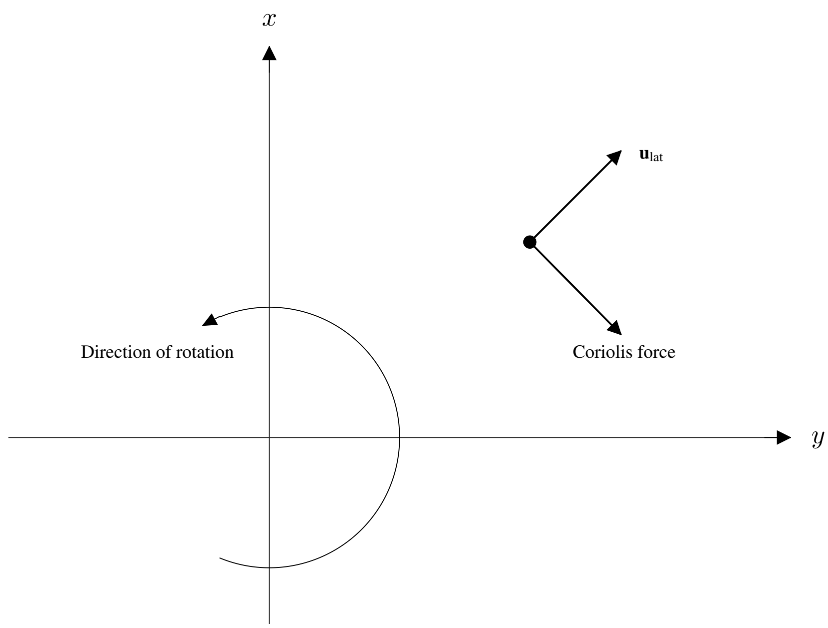

Figure 2.1: Schematic diagram showing the direction that the Coriolis force acts. The rotation vector $\mathbf{\Omega}$ *is directed into the page. The component of the velocity in the plane normal to the axis of rotation is denoted by* $\boldsymbol{u}_{lat}$.

The overall effect of the Coriolis force is to oppose the displacement of a fluid element by non-zero expansions in the lateral plane. Therefore the Coriolis force gives rise to an elasticity of the fluid, sometimes referred to as a *restoring effect* (Batchelor, 1967). It is this phenomenon that makes the propagation of waves possible and is explored further in chapter 4.

2.3 Axisymmetric vortex rings

An axisymmetric vortex ring of radius R is illustrated in figure 2.2 by the dark grey torus. The vortex core itself has radius a. Any fluid transported along with the vortex ring forms part of the vortex "atmosphere"

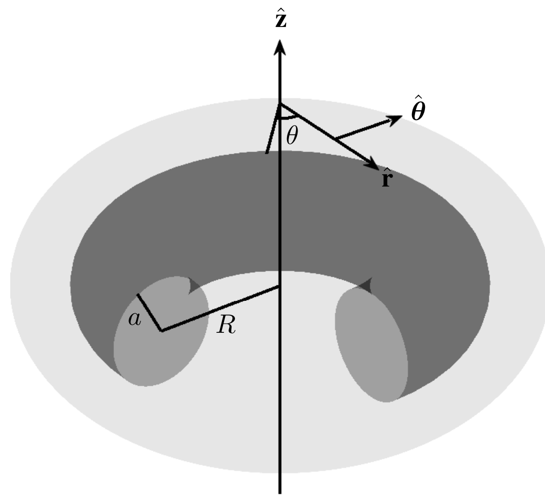

Figure 2.2: Illustration of an axisymmetric vortex ring. The direction of propagation is aligned with the z–axis in cylindrical polar coordinates (r, θ, z). The distance from the axis to the centre of the vortex core is R. The width of the vortex core is a. The light grey region is the vortex atmosphere. The dark grey region is the vortex core.

Axisymmetric vortex rings in an ideal fluid which is at rest at infinity are self-inductive, propelling themselves in the direction parallel to the axis of the vortex ring (Wu et al., 2006). In a frame of reference which moves with the vortex ring, the fluid at infinity is moving with a translational velocity opposite to the induced velocity of the vortex ring, whilst the vortex ring remains stationary in the frame of reference. A swirl-free, axisymmetric vortex ring can be described in cylindrical coordinates (r, θ, z) centred on the vortex ring by the velocity and vorticity fields

$$\mathbf{u} = (u, 0, w) \quad \text{and} \quad \boldsymbol{\omega} = (0, \omega_\theta, 0)$$

where $\omega_\theta = \dfrac{\partial u}{\partial z} - \dfrac{\partial w}{\partial r}$.

Due to the axisymmetric nature of the flow a Stokes stream function $\psi(r, z)$ may be used to represent the flow such that

$$\mathbf{u} = \left(-\frac{1}{r}\frac{\partial \psi}{\partial z}, 0, \frac{1}{r}\frac{\partial \psi}{\partial r} \right). \tag{2.13}$$

The azimuthal component of the vorticity equation is given by

$$\frac{\mathrm{D}\omega_\theta}{\mathrm{D}t} = \frac{\omega_\theta u}{r} + \nu\left(\nabla^2\omega_\theta - \frac{\omega_\theta}{r^2}\right). \tag{2.14}$$

Defining $f \equiv \dfrac{\omega_\theta}{r}$, equation (2.14) may also be expressed as

$$\frac{\mathrm{D}f}{\mathrm{D}t} = \nu\left(\nabla^2 f + \frac{2}{r}\frac{\partial f}{\partial r}\right), \tag{2.15}$$

where

$$\frac{\mathrm{D}f}{\mathrm{D}t} = \frac{\partial f}{\partial t} + u\frac{\partial f}{\partial r} + w\frac{\partial f}{\partial z}. \tag{2.16}$$

Linearising by dropping the two nonlinear terms on the right hand side of equation (2.16) gives

$$\frac{\partial f}{\partial t} = \nu\left(\frac{\partial^2 f}{\partial r^2} + \frac{3}{r}\frac{\partial f}{\partial r} + \frac{\partial^2 f}{\partial z^2}\right). \tag{2.17}$$

The simplest solution to equation (2.17) - which satisfies the equation trivially - is $f = A$, where A is a constant. This leads to the Fraenkel-Norbury family of solutions with $\omega_\theta = Ar$ where the vorticity is proportional to the radial distance, r, from the centre of the vortex ring.

2.4 The Fraenkel-Norbury family of vortex rings

Norbury (1973) outlines the Fraenkel-Norbury family of vortex rings in which the vorticity inside the vortex is proportional to the radial distance from the axis of symmetry whilst outside the vortex the fluid is irrotational. The Fraenkel-Norbury family spans from the thin-cored vortex rings of Fraenkel (see Fraenkel, 1970, 1972) to the fat-cored Hill's spherical vortex (Hill, 1894).

Taking the curl of equation (2.13) to give $\boldsymbol{\omega}$, equating the azimuthal component to Ar and rearranging gives the stream function-vorticity equation

$$\left\{\frac{\partial}{\partial r^2} - \frac{1}{r}\frac{\partial}{\partial r} + \frac{\partial^2}{\partial z^2}\right\}\psi(r,z) = \begin{cases} -Ar^2 & \text{inside } \partial\mathcal{A} \\ 0 & \text{outside } \partial\mathcal{A}. \end{cases} \tag{2.18}$$

Norbury (1973) outlines a numerical scheme for the solution of equation (2.18). The problem is cast as a nonlinear integral equation for the vortex ring boundary which is represented by a Fourier series. The coefficients of the Fourier series are found by applying Newton's method about an initial guess. Figure 2.3 has been produced following the numerical scheme outlined by Norbury. The figure gives the vortex core boundaries of some of the members of the Fraenkel-Norbury family of vortex rings. The vortex rings in this family are parameterised by α, the mean core radius, which relates the area of the meridional cross-section of the vortex ring to the ring radius with Area $= \pi L^2 \alpha^2$ where L is the ring radius (see figure 1 Norbury (1973)). For a Hill's spherical vortex of radius 2 $(L = 1)$ the area of the cross-section is 2π and therefore Hill's spherical vortex is described by the extremal parameter value $\alpha = \sqrt{2}$. The boundary of Hill's spherical vortex is given in figure 2.3 by the outermost contour.

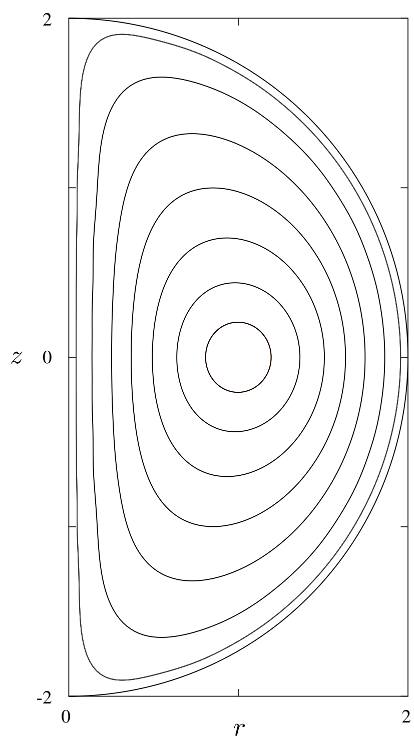

Figure 2.3: Replication of figure 3 from Norbury (1973). Boundaries of the vortex cores of the Fraenkel-Norbury vortex ring family for values of the mean core radius (from inner to outer boundary) $\alpha = 0.2,\ 0.4,\ 0.6,\ 0.8,\ 1.0,\ 1.2,\ 1.35,\ \sqrt{2}$.

The stream function for the flow can be calculated numerically everywhere in the domain using the finite element method outlined in appendix A by solving the stream function-vorticity equation

$$-\nabla^2\psi = \omega_\theta \tag{2.19}$$

together with the boundary conditions

$$\psi = k \text{ on } \partial\mathcal{A} \tag{2.20}$$

and

$$\psi \sim -\frac{1}{2}Wr^2 \text{ as } r^2 + z^2 \to \infty. \tag{2.21}$$

The value of the stream function on the vortex boundary, k, and the free-stream velocity, W, can be taken from Norbury (1973). The results of the solution of this finite element problem are given in figure 2.4 where the streamlines for each flow are plotted. The vortex ring boundaries separating the rotational and irrotational fluid are seen in blue. The thick black lines are the dividing streamline $\psi(r,z) = 0$ and these are also found in figure 4 of Norbury (1973). These dividing streamlines enclose the body of fluid which is carried along by the vortex ring.

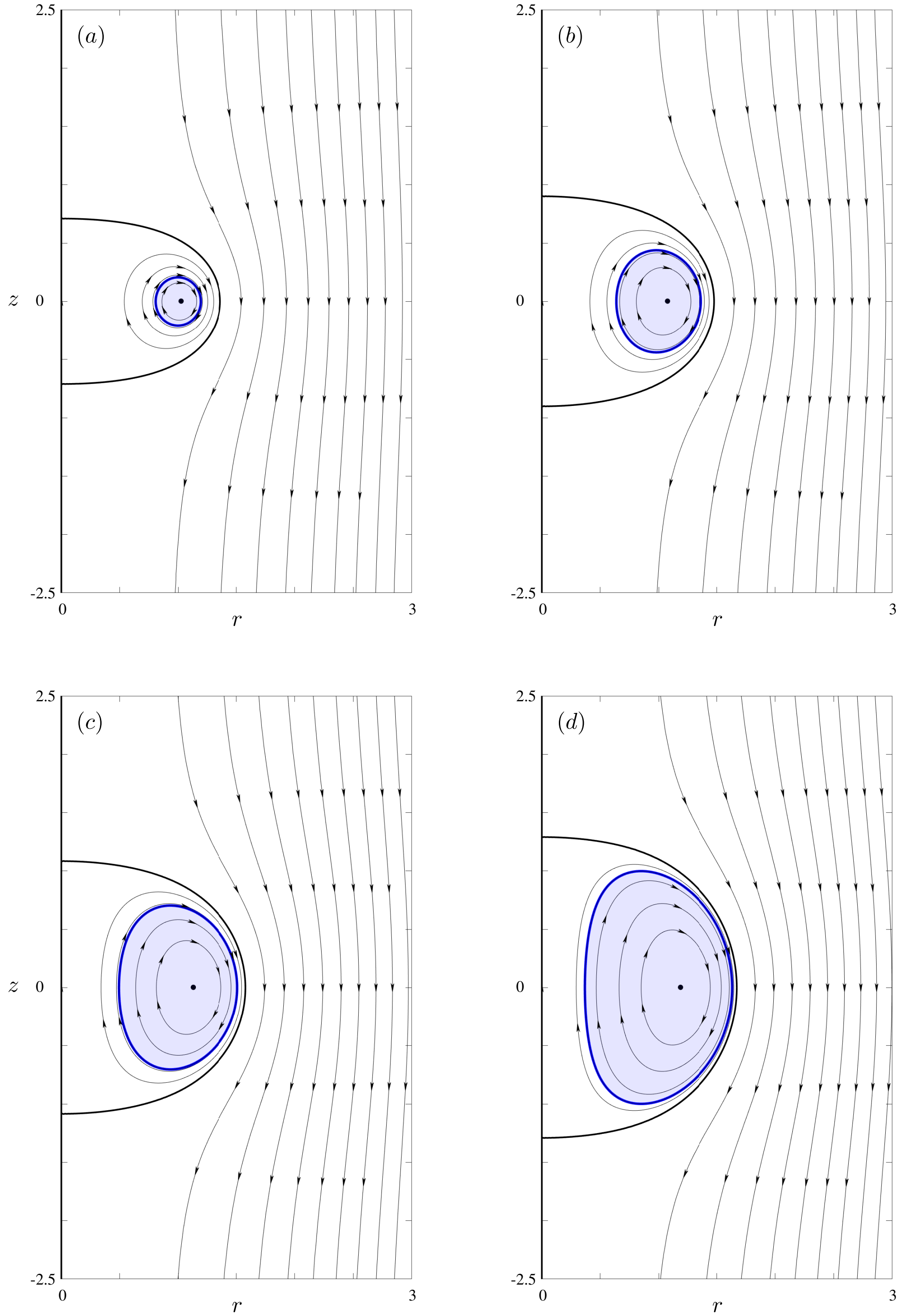

Figure 2.4: Streamlines for the Fraenkel-Norbury family of vortex rings. Mean core radius values of (a) $\alpha = 0.2$, (b) $\alpha = 0.4$, (c) $\alpha = 0.6$, (d) $\alpha = 0.8$. Blue lines give the vortex ring boundary $\partial\mathcal{A}$. The dividing streamlines $\psi(r, z) = 0$ are given by the thick black lines. The black circles show the location of the stagnation points of the flow.

2.5 Hill's spherical vortex

Hill's spherical vortex (Hill, 1894) is a special member of the Fraenkel-Norbury family of vortex rings. It has the "fattest" vortex core. In cylindrical coordinates (r, θ, z) fixed on the centre of the vortex ring the Stokes stream function for Hill's spherical vortex of radius a is given by

$$\psi = \begin{cases} -\dfrac{1}{10}Ar^2(r^2+z^2-a^2) & \text{for } r^2+z^2 \leqslant a^2, \\ -\dfrac{1}{15}Aa^2r^2\left(1-\dfrac{a^3}{(r^2+z^2)^{3/2}}\right) & \text{for } r^2+z^2 > a^2. \end{cases} \tag{2.22}$$

The parameter $A = 15W/2a^2$ is derived from the velocity, W, of a rigid sphere of radius a moving through an ideal fluid (Saffman, 1992). This velocity field is continuous across the vortex boundary. The pressure in the flow can be calculated using a Bernoulli equation

$$p + \frac{1}{2}q^2 + \int_{\mathcal{A}} \frac{\omega_\theta}{r}\,\mathrm{d}\mathcal{A} = C, \tag{2.23}$$

where C is a constant and $q = |\mathbf{u}|$ (see Wu et al. (2006), p. 273). The pressure is given by

$$p = \begin{cases} \dfrac{1}{50}\rho A^2[r^2(r^2-a^2)+2z^2a^2-z^4]+p_0 & \text{for } r^2+z^2 \leqslant a^2, \\ \dfrac{\rho\, a^4A^2}{450}\left[\dfrac{4a^3(2z^2-r^2)}{(r^2+z^2)^{5/2}} - \dfrac{a^6(r^2+4z^2)}{(r^2+z^2)^4}+5\right]+p_0 & \text{for } r^2+z^2 > a^2, \end{cases} \tag{2.24}$$

determined up to a constant p_0. The pressure field given in equation (2.24) ensures continuity of pressure across the vortex boundary.

The velocity field of Hill's vortex also satisfies the full Navier-Stokes equations if an additional pressure of $2A\mu z$ is added inside the vortex ring where μ is the dynamic viscosity (Saffman, 1992). However, although the velocity is continuous across the vortex boundary the normal and tangential stresses are not and therefore the entire flow is not an exact solution to the Navier-Stokes equations with physically meaningful boundary conditions.

Figure 2.5 gives the streamlines of Hill's spherical vortex. The frame of reference is fixed on the centre of the vortex and thus the self-propelling characteristic of the vortex is seen by the fluid flowing past the vortex in this frame. In this work the free-stream velocity is $\mathbf{u} = -W\hat{\mathbf{z}}$ with the fluid in the far-field flowing from the top to the bottom of the page.

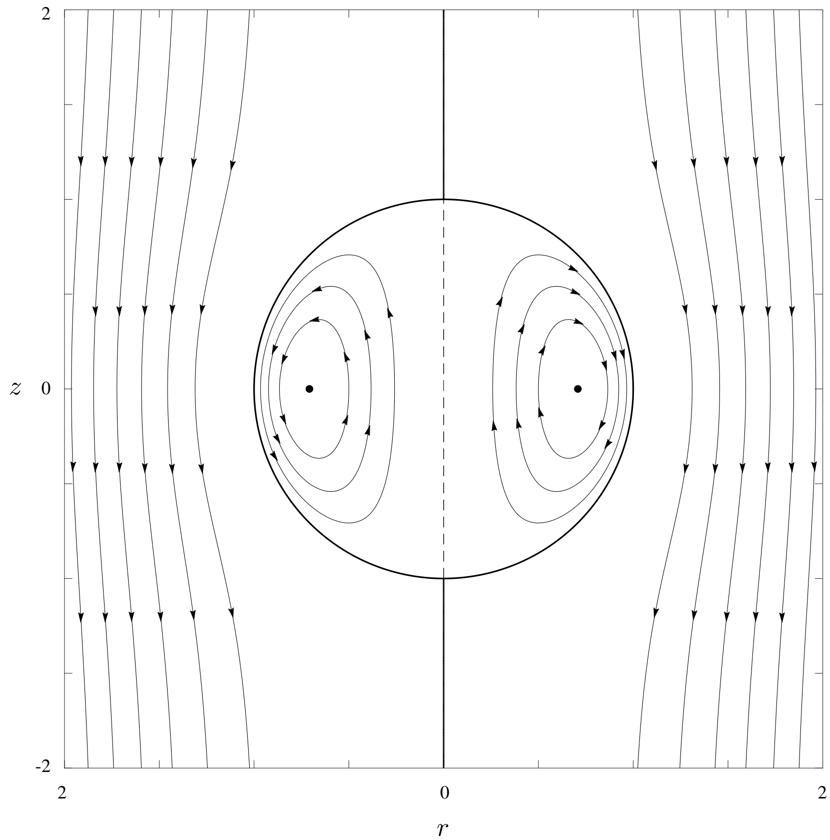

Figure 2.5: Lines of constant stream function in a meridional plane for Hill's spherical vortex with radius $r = 1$ and free-stream velocity $W = 1$. The spacing of the streamlines is $\psi = 0.2$ outside the vortex and $\psi = 0.05$ inside the vortex. The black circles represent the stagnation points of the flow.

Circulation is a macroscopic measure of the vorticity for a parcel of fluid and is defined as the line integral of the velocity field around a closed contour. Following an application of Stokes' theorem as illustrated in figure 2.6, this is equivalent to the surface integral of the vorticity field over the closed contour. For Hill's spherical vortex we have that

$$\Gamma = \oint \mathbf{u} \cdot \mathrm{d}\mathbf{x} = \int_{-a}^{a} \int_{0}^{\sqrt{a^2-z^2}} \nabla \times \mathbf{u} \ \cdot \mathrm{d}\mathbf{S} = \int_{-a}^{a} \int_{0}^{\sqrt{a^2-z^2}} Ar \, \mathrm{d}r\mathrm{d}z = \frac{2}{3}Aa^3 = 5Wa. \tag{2.25}$$

The circulation, Γ, will be used throughout this thesis to compare the strength of vortices.

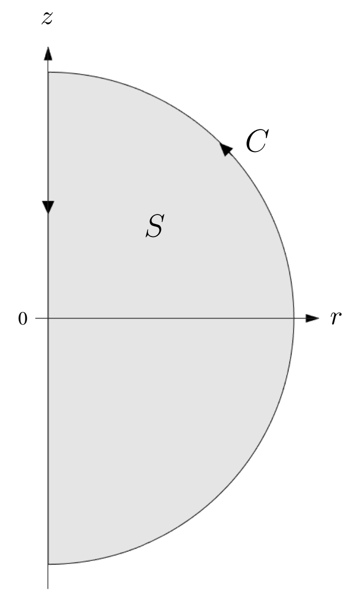

Figure 2.6: Schematic diagram showing the contour integration and application of Stokes theorem to calculate the circulation of Hill's spherical vortex. S is the shaded semi-circular region whilst C is the enclosing contour taken in the anticlockwise sense.

2.5.1 The linear stability of Hill's spherical vortex

Moffatt and Moore (1978) investigated the effect of a small axisymmetric, ellipsoidal disturbance to Hill's spherical vortex using linear perturbation theory. The problem was formulated as a system of differential equations for the evolution of the Legendre coefficients that make up the disturbance stream function. It revealed that under such a disturbance the perturbation will decay "exponentially at all points except in an exponentially decreasing region at the rear stagnation point of the vortex".

A Hill's spherical vortex of radius a was described in spherical coordinates (r, θ, ϕ) where θ is taken to be the polar angle and ϕ the azimuthal angle. The coordinates are taken such that the rear stagnation point is located at $r = a$, $\theta = 0$. An initial irrotational and volume preserving perturbation to the surface of the vortex ring of the form $r = a(1 + \varepsilon h(\theta, t))$ was considered where $h(\theta, t) = (3\cos^2\theta - 1)/2$. They showed that for small disturbances a spike of fluid emerged at the rear stagnation point given by

$$r = a + \frac{1}{10} a\varepsilon e^{3Wt/a} \left[1 + \frac{1}{4}\theta^2 e^{3Wt/a}\right]^{-\frac{3}{2}}. \tag{2.26}$$

Moffatt and Moore (1978) explain this behaviour: "The surface of the vortex behaves like a material surface. The irrotational flow outside the vortex tends to sweep the perturbation towards the rear stagnation point where it develops an increasingly spiky structure." Equation (2.26) reveals that the evolution of the spike is controlled by the convective effects of the outer flow.

The restriction to small disturbances was removed so long as the spike remained small. The evolution equations for convection of particles near the axis are, for $\varepsilon > 0$,

$$\frac{\mathrm{d}r}{\mathrm{d}t} = W\left(1 - \frac{a^3}{r^3}\right), \tag{2.27a}$$

$$r\frac{\mathrm{d}\theta}{\mathrm{d}t} = -W\left(1 + \frac{a^3}{2r^3}\right), \tag{2.27b}$$

and for $\varepsilon < 0$

$$\frac{\mathrm{d}r}{\mathrm{d}t} = -\frac{3}{2}W\left(1 - \frac{r^2}{a^2}\right), \tag{2.28a}$$

$$r\frac{\mathrm{d}\theta}{\mathrm{d}t} = \frac{3}{2}W\left(1 - \frac{2r^2}{a^2}\right). \tag{2.28b}$$

Moffatt and Moore (1978) found that if the disturbance causes the vortex to be initially prolate (stretched in the axial direction, $\varepsilon > 0$), fluid will be detrained from the rear stagnation point causing a decrease in the radius of the vortex ring by a factor of $1 - \frac{1}{5}\varepsilon$. The speed of propagation of the vortex is altered by a factor of $1 - \frac{2}{5}\varepsilon$ causing the vortex ring to slow down. The evolution for a prolate disturbance with $\varepsilon = 10^{-4}$ is found by the solution of equations (2.27) and is shown in figure 2.7. The initial conditions are given by equation (2.26) with $t = 0$. This is a reproduction of figure 1 from Moffatt and Moore (1978). Even for a small initial disturbance of $\mathcal{O}(10^{-4})$ the spike grows rapidly.

They discovered that if the disturbance causes the vortex to be initially oblate (squashed in the axial direction, $\varepsilon < 0$), irrotational fluid from outside the vortex will be entrained in the rear stagnation point. The radius of the vortex increases by a factor of $1 - \frac{1}{5}\varepsilon$ due to the entrainment of irrotational fluid. The evolution for a prolate disturbance with $\varepsilon = -10^{-4}$ is found by the solution of equations (2.28) and is shown in figure 2.8. The initial conditions are given by equation (2.26) with $t = 0$.

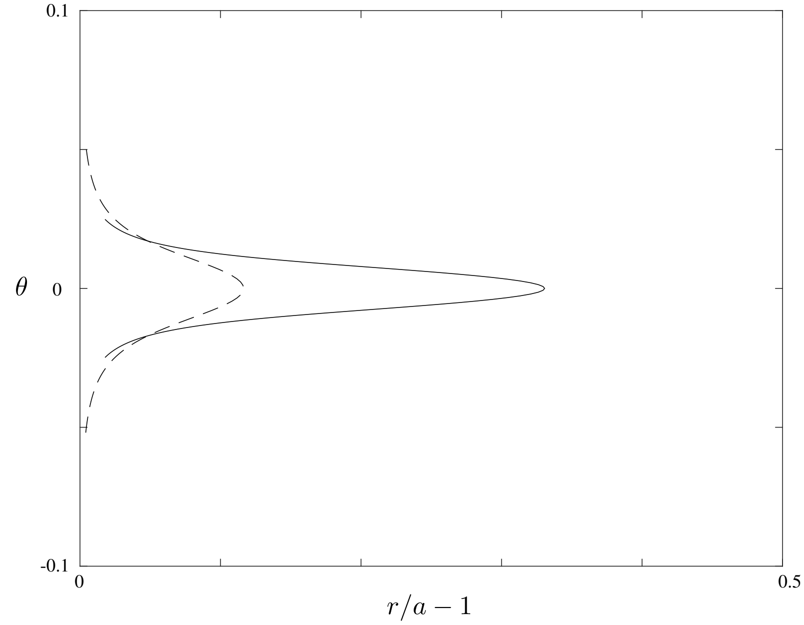

Figure 2.7: Spike of fluid detrained from Hill's vortex for a prolate perturbation as a function of θ, the polar angle describing Hill's vortex. The shape of the spike is given at $Wt/a = 3.2$ (dashed line) and $Wt/a = 3.7$ (solid line).

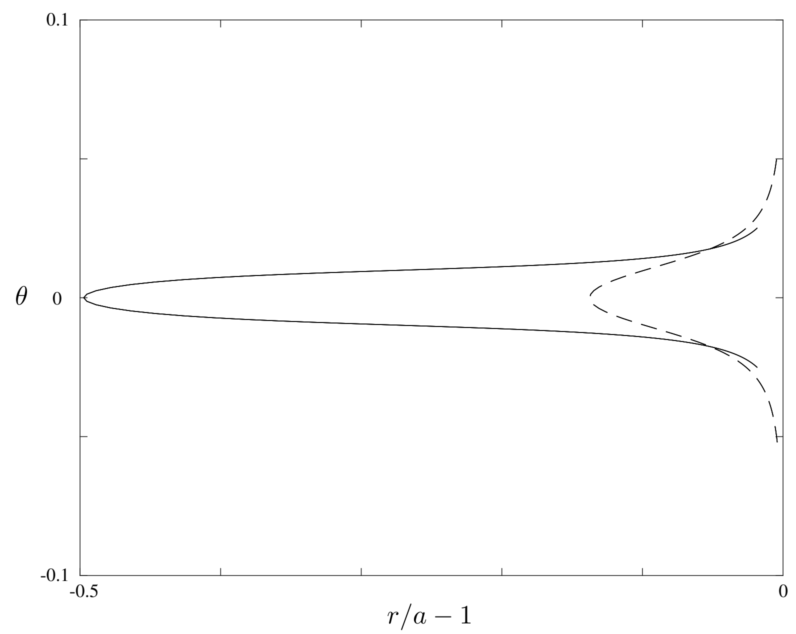

Figure 2.8: Spike of fluid entrained into Hill's vortex for an oblate perturbation as a function of θ, the polar angle describing Hill's vortex. The shape of the spike is given at $Wt/a = 3.2$ (dashed line) and $Wt/a = 3.7$ (solid line).

2.5.2 The nonlinear stability of Hill's spherical vortex

Pozrikidis (1986) corroborated the results of Moffatt and Moore (1978) by the numerical solution of a nonlinear integro-differential equation for the boundary of the vortex ring valid under an irrotational and volume preserving perturbation. Unlike Moffatt and Moore (1978) who were only able to consider small perturbations for short times, the analysis of Pozrikidis (1986) was able to demonstrate the asymptotic behaviour of the flow for finite perturbations.

Pozrikidis (1986) showed that oblate perturbations caused irrotational fluid to be entrained into the back of the vortex ring. This disturbed irrotational fluid moves towards the front of the vortex ring to restore its original shape. However, this causes the back of the vortex to flatten. Irrotational fluid is then convected into the rear of the vortex ring moving towards the front of the vortex ring. This leads Hill's spherical vortex to evolve away from a "fat-cored" spherical vortex into a toroidal vortex ring. Figure 2.9 has been reproduced using Pozrikidis' code from the FDLIB Fluid Dynamics Software Library.

Pozrikidis (1986) further showed that for prolate perturbations a tail of fluid was indeed detrained from the back of the vortex ring. In the prolate perturbation the disturbed rotational fluid is convected towards the rear of the vortex ring whilst the front regains a nearly spherical shape. This fluid at the back of the vortex ring elongates to form a vortex tail. This is seen in figure 2.10 where the results of Pozrikidis have been reproduced independently in original code in MatLab following the same numerical procedure outlined by Pozrikidis.

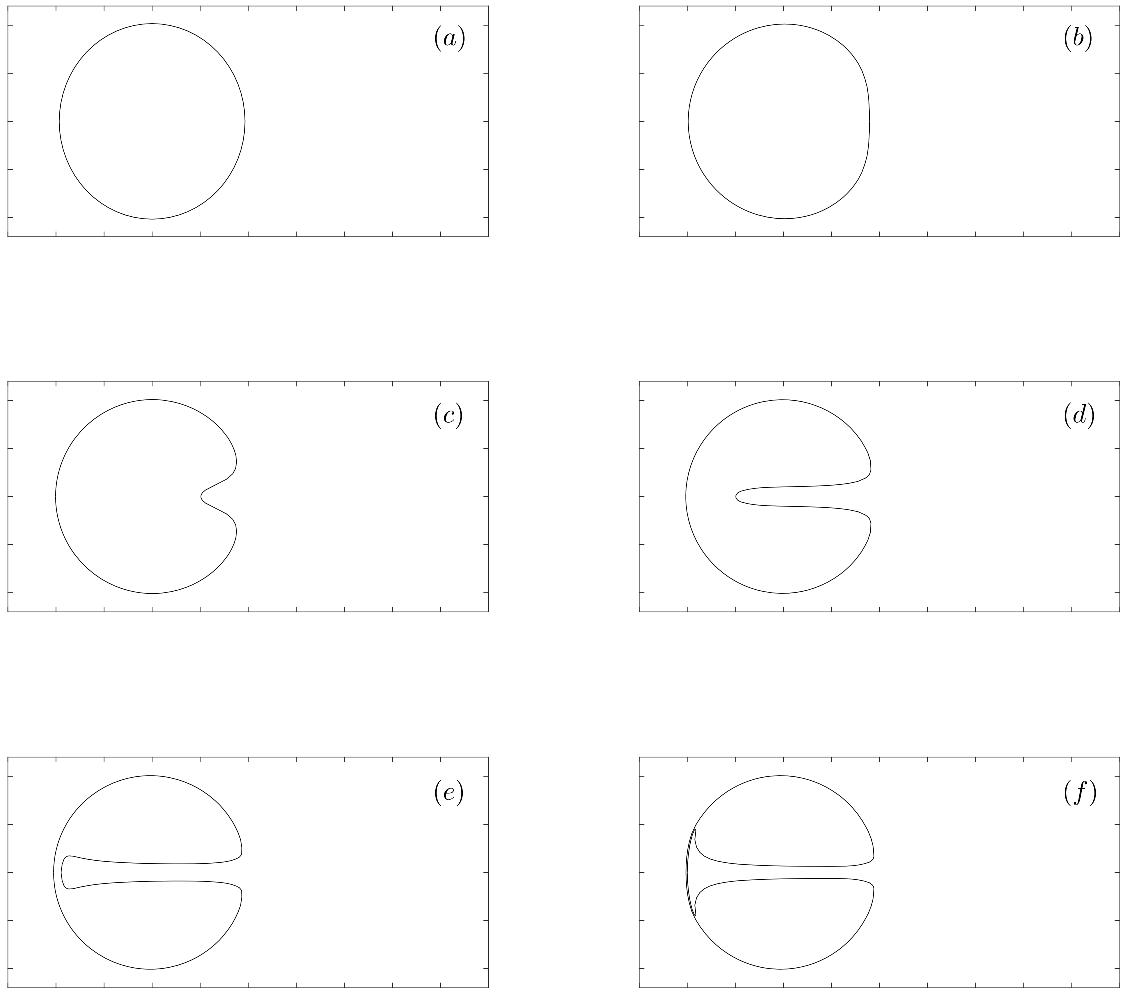

Figure 2.9: The evolution of the vortex boundary for oblate perturbation of magnitude $\varepsilon = -0.05$ *at times* (a) $t = 0.0$, (b) $t = 0.72$, (c) $t = 1.44$, (d) $t = 2.16$, (e) $t = 2.88$, (f) $t = 3.60$.

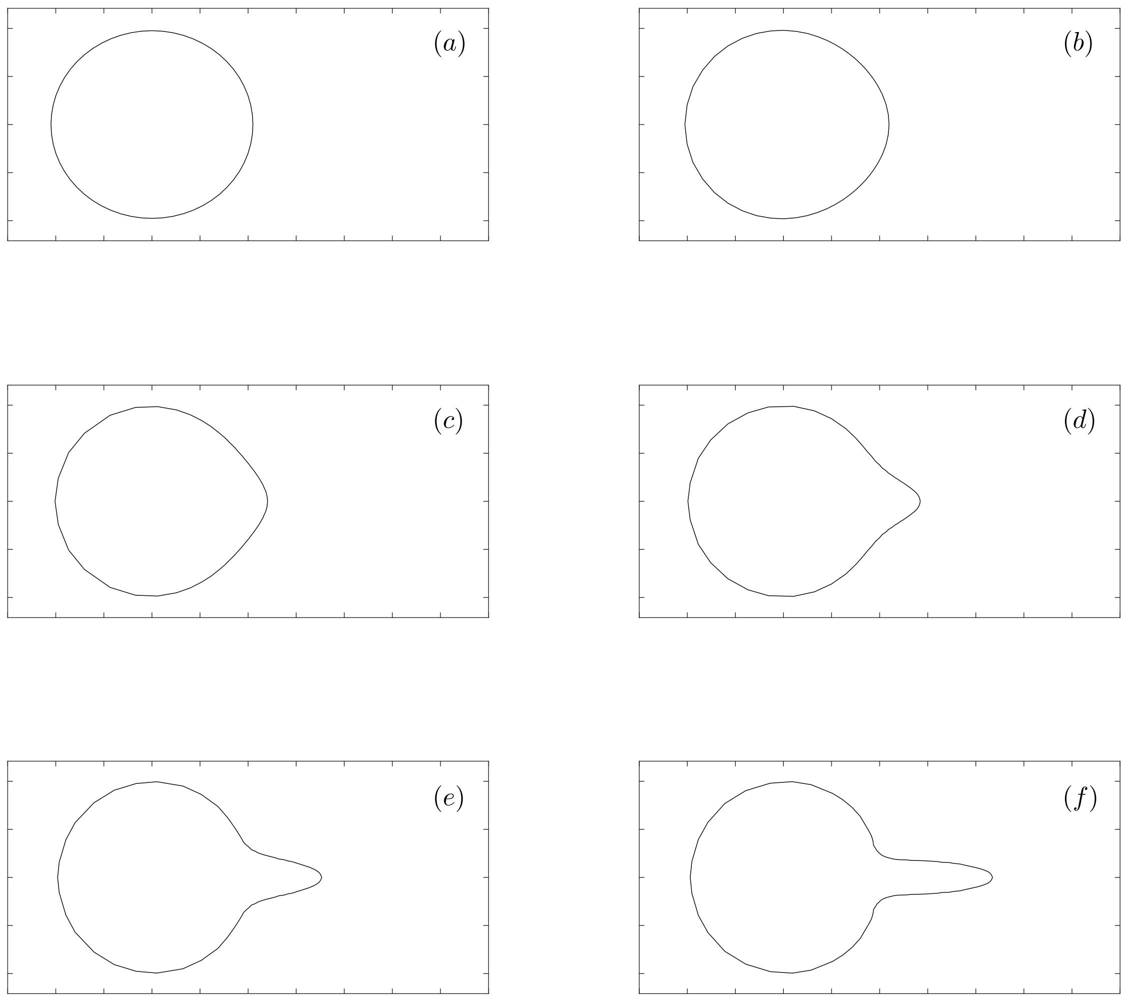

Figure 2.10: The evolution of the vortex boundary over time for a prolate perturbation of magnitude $\varepsilon = 0.05$ *at times* $(a)\ t = 0.0$, $(b)\ t = 0.36$, $(c)\ t = 0.72$, $(d)\ t = 1.08$, $(e)\ t = 1.44$, $(f)\ t = 1.80$.

2.6 Moffatt's swirling vortices

In addition to being a extreme member of the Fraenkel-Norbury vortex ring family, Hill's spherical vortex is also a special member of a family of swirling vortex rings given by Moffatt (1969). This is a doubly-infinite family of vortex rings parameterised by α and λ for $(\lambda, \alpha) \in \mathbb{R}^2$. Not to be confused with Norbury's mean core radius, here the parameter α gives the degree of swirl of the vortex ring whilst λ gives the strength of the vortex ring.

The Stokes stream function in spherical polar coordinates (σ, θ, ϕ) of Moffatt's swirling vortex, radius a is

$$\psi = \begin{cases} \dfrac{\lambda}{\alpha^2}\left[\dfrac{a^3\left(\sigma\alpha\cos(\sigma\alpha) - \sin(\sigma\alpha)\right)}{\sigma\left(\alpha a\cos\left(\alpha a\right) - \sin\left(\alpha a\right)\right)} - \sigma^2\right]\sin^2\theta & \text{for } \sigma \leqslant a, \\[2ex] -\dfrac{(\sigma^3 - a^3)}{2\sigma}\sin^2\theta & \text{for } \sigma > a, \end{cases} \tag{2.29}$$

where

$$u = \frac{1}{\sigma^2\sin\theta}\frac{\partial\psi}{\partial\theta}, \quad v = -\frac{1}{\sigma\sin\theta}\frac{\partial\psi}{\partial\sigma}, \quad w = -\frac{\alpha\,\psi}{\sigma\sin\theta}. \tag{2.30}$$

It can be shown that in the limit $\alpha \to 0$ Moffatt's swirling solution is identical to Hill's spherical vortex. Taylor expansion about $\alpha = 0$ of the trigonometric functions in the inner stream function of equation (2.29) followed by some algebraic manipulation gives, for small α

$$\psi = \frac{\lambda}{\alpha^2}\left[\frac{a^3}{\sigma}\cdot\frac{-\dfrac{\sigma^3\alpha^3}{3} + \dfrac{\sigma^5\alpha^5}{30} + \mathcal{O}(\alpha^7)}{-\dfrac{\sigma\alpha^3 a^3}{3} + \dfrac{\sigma\alpha^5 a^5}{30} + \mathcal{O}(\alpha^7)} - \sigma^2\right]\sin^2\theta \tag{2.31a}$$

$$\psi = \frac{\lambda}{\alpha^2}\left[\frac{a^3}{\sigma}\cdot\frac{-10\sigma^3\alpha^3 + \sigma^5\alpha^5 + \mathcal{O}(\alpha^7)}{-10\sigma\alpha^3 a^3 + \sigma\alpha^5 a^5 + \mathcal{O}(\alpha^7)} - \sigma^2\right]\sin^2\theta \tag{2.31b}$$

$$\psi = \lambda\left[\frac{1}{10}a^2\sigma^2 - \frac{1}{10}\sigma^4 + \mathcal{O}(\alpha^2)\right]\sin^2\theta. \tag{2.31c}$$

Taking the limit of equation (2.31c) as $\alpha \to 0$ and letting $\lambda = 15/2$ gives

$$\lim_{\alpha\to 0}\psi = \left[\frac{3}{4}a^2\sigma^2 - \frac{3}{4}\sigma^4\right]\sin^2\theta. \tag{2.32}$$

This is identical to the Stokes stream function for Hill's spherical vortex in spherical polar coordinates which is given by

$$\psi = \begin{cases} \dfrac{3\sigma^2(a^2-\sigma^2)}{4}\sin^2\theta & \text{for } \sigma \leqslant a, \\[2ex] -\dfrac{(\sigma^3-a^3)}{2\sigma}\sin^2\theta & \text{for } \sigma > a. \end{cases} \tag{2.33}$$

The streamlines and azimuthal velocity field for Moffatt's swirling vortex with $\alpha = \pi/2$ and $\lambda = 15/2$ are given in figure 2.11.

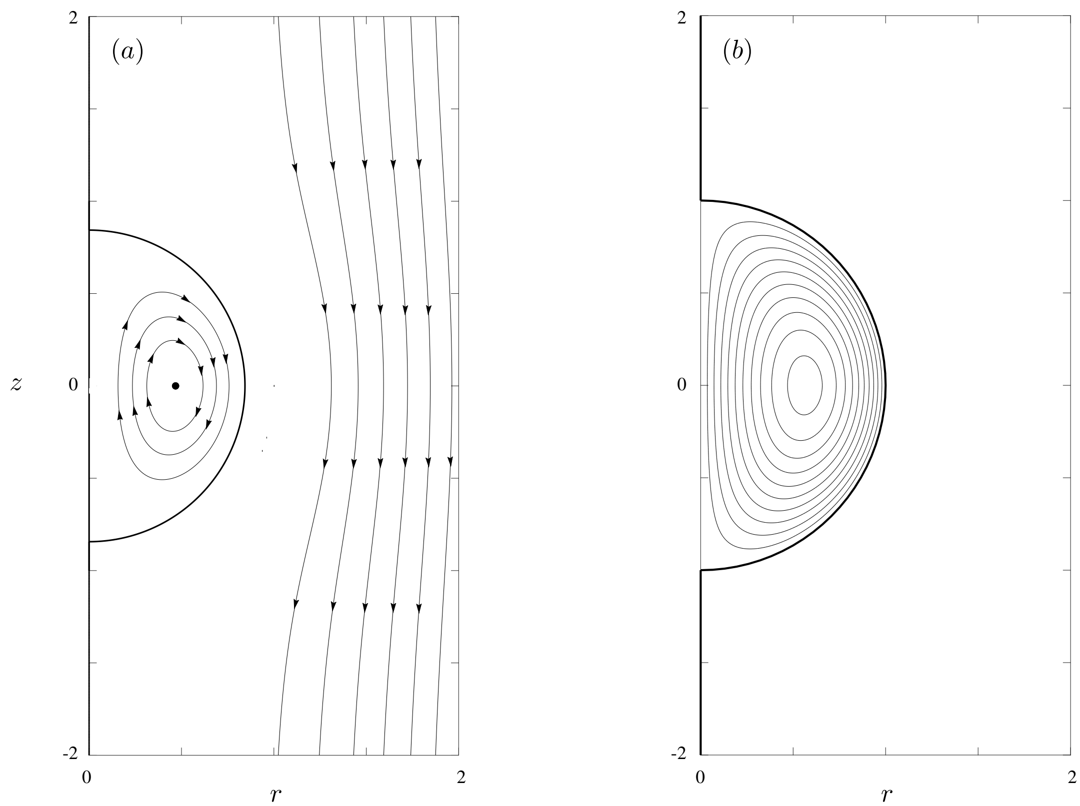

Figure 2.11: Streamlines (a) and azimuthal velocity, u_θ (b) for Moffatt's swirling vortex with $\alpha = \dfrac{\pi}{2}$ and $\lambda = \dfrac{15}{2}$. Contour increments $\Delta\psi^+ = 0.0602$ (inside vortex), $\Delta\psi^- = -0.2390$ (outside vortex) and $\Delta u_\theta = 0.0473$. The bold line indicates the contour $\psi = 0$. The black circle gives the stagnation point of the flow.

Chapter 3

Spherical vortices in rotating ideal fluids

A popular model for a generic fat-cored vortex ring or eddy is Hill's spherical vortex (Hill, 1894). This well-known solution of the Euler equations may be considered a special case of the doubly-infinite family of swirling spherical vortices identified by Moffatt (1969). Here we find exact solutions for such spherical vortices propagating steadily along the axis of a rotating ideal fluid. The boundary of the spherical vortex swirls in such a way as to exactly cancel out the background rotation of the system. The flow external to the spherical vortex exhibits fully nonlinear inertial wave motion. We show that above a critical rotation rate, closed streamlines may form in this outer fluid region and hence carry fluid along with the spherical vortex. As the rotation rate is further increased, further concentric 'sibling' vortex rings are formed.

3.1 Introduction

In 1894 Hill published his famous solution for the steady flow of a spherical vortex in an ideal fluid (Hill, 1894). The solution consists of an inner rotational spherical region of fluid that matches onto an outer irrotational region of fluid that extends to infinity. Hill's solution was later shown to be the end member of a family of steadily propagating vortex rings (Norbury, 1973) of varying core thickness that includes 'thin-cored' rings (see Fraenkel, 1970, 1972) where the rotational fluid is confined within a narrow region that does not extend to the axis. These solutions, in particular Hill's, have been the focus of a number of stability analyses (see e.g., Moffatt and Moore, 1978; Pozrikidis, 1986; Protas and Elcrat, 2016) that show that in time fluid may be detrained or entrained into the vortex according to whether it has a prolate or oblate deformation respectively. Hill's spherical vortex may also be viewed as a special non-swirling member of a doubly-infinite family of swirling spherical vortices identified by Moffatt (1969) that may be matched onto an oncoming irrotational stream. Here we show how this family of spherical vortices may be matched onto an oncoming stream in a rotating fluid.

As part of his body of work on rotating fluids in the early twentieth century, Taylor (1922) investigated the response of a rotating fluid to a sphere steadily translating along the axis of rotation. His experiments showed that while the tank of fluid rotated but the sphere was not towed, the sphere rotated with the fluid in solid body rotation. Yet, when the sphere was towed along the axis of rotation it ceased precessing and had no azimuthal velocity in the laboratory frame of reference. Taylor found an exact solution to the Euler equations that supported fully nonlinear inertial waves satisfying a no-slip boundary condition on a sphere that translated steadily along the axis of rotation of the fluid but did not precess about this axis in the laboratory frame (though he noted that it is not clear how such a flow could be realised). In the analysis of this solution Taylor found that in the limit of the radius of the sphere tending to zero, a structure that resembled Hill's spherical vortex could be observed in the flow, though he described this analogy between his flow and Hill's spherical vortex as 'only superficial'.

In the present work we combine the approach of Taylor (1922) (summarized briefly in section 3.2.1) with the solutions of Hill (1894) in section 3.2.2 and Moffatt (1969) in section 3.2.3 to find exact solutions of the rotating Euler equations for a spherical vortex propagating steadily along the axis of rotation where, like Taylor's sphere, the boundary of the spherical vortex does not precess in the laboratory frame. The flow, in a frame of reference moving with the spherical vortex, is shown schematically in figure 3.1. The inner solution, given by either Hill (1894) or Moffatt (1969), is shown in grey. This inner solution for the spherical vortex is matched onto a modified Taylor (1922) solution in the outer region by enforcing continuity of velocity and pressure across the boundary. The flow in the outer region exhibits inertial waves that above critical rotation rates may overturn. In section 3.2.4 we show that as the rotation rate of the system is increased above these critical rotation rates, closed streamlines form in the outer fluid representing a series of thin-cored 'sibling' vortex rings, propagating with the spherical vortex. In section 3.3 we draw our conclusions.

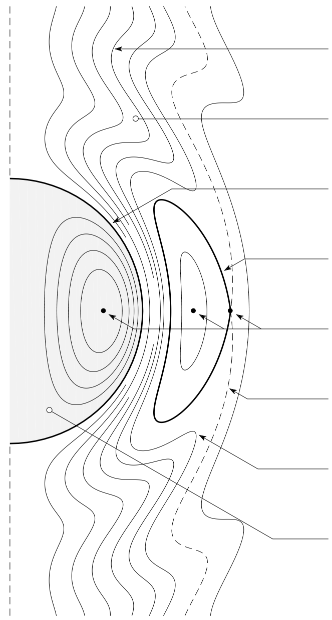

Figure 3.1: Schematic of the flow in a frame of reference moving with the spherical vortex. The grey inner region consists of either the non-precessing Hill (1894) or Moffatt (1969) solutions. This inner region matches onto a rotating outer region that is given by a modified version of the solution presented by Taylor (1922). At the boundary between the inner and outer regions continuity of velocity and pressure is enforced.

3.2 Spherical Vortices in Rotating Fluids

We consider an inviscid, incompressible fluid with pressure field p, velocity field $\boldsymbol{u}$ and constant density ρ in a frame of reference that is rotating with rotation vector $\Omega\,\hat{\boldsymbol{z}}$, where $\hat{\boldsymbol{z}}$ is a fixed unit vector. The flow is described in terms of spherical polar coordinates (σ, θ, ϕ) where $\sigma \geqslant 0$ is the radial distance from the origin, $\theta \in [0, \pi]$ is the polar angle and $\phi \in [0, 2\pi)$ is the azimuthal angle. The spherical coordinate system is aligned such that $\theta = 0$ is in the $\hat{\boldsymbol{z}}$-direction. We seek to model a spherical vortex of constant radius a and constant propagation velocity $U\hat{\boldsymbol{z}}$, hence we nondimensionalize position as $\boldsymbol{x} = a\tilde{\boldsymbol{x}}$, velocity as $\boldsymbol{u} = U\tilde{\boldsymbol{u}}$, and pressure as $p = \rho U^2\,\tilde{p}$, where tildes indicate nondimensional quantities. Dropping the tildes immediately the nondimensional steady rotating Euler equations that govern the motion are

$$\nabla \cdot \boldsymbol{u} = 0, \qquad (\boldsymbol{u} \cdot \nabla)\,\boldsymbol{u} = -\nabla p + \frac{r}{4\mathrm{Ro}^2}\hat{\boldsymbol{r}} - \frac{1}{\mathrm{Ro}}\hat{\boldsymbol{z}} \times \boldsymbol{u}, \qquad \mathrm{Ro} = \frac{U}{2a\Omega}, \tag{3.1a–c}$$

where: we have defined a Rossby number, Ro; $\hat{\boldsymbol{r}} = \sin\theta\,\hat{\boldsymbol{\sigma}} + \cos\theta\,\hat{\boldsymbol{\theta}}$ is a unit vector in the cylindrical radial direction, and $r = \sigma\sin\theta$ is the cylindrical radial position.

3.2.1 Taylor's Solution

Taylor (1922) considered the axisymmetric flow of a non-precessing sphere (in the laboratory frame) that is translating steadily with nondimensional velocity $\hat{\boldsymbol{z}}$ through a fluid rotating steadily about $\hat{\boldsymbol{z}}$. This may be described by defining an axisymmetric streamfunction, $\psi(\sigma,\theta)$, as in Batchelor (1967), and writing the velocity in the radial, polar and azimuthal directions respectively as

$$u = \frac{1}{\sigma^2\sin\theta}\frac{\partial\psi}{\partial\theta}, \quad v = -\frac{1}{\sigma\sin\theta}\frac{\partial\psi}{\partial\sigma}, \quad w = -\frac{1}{\mathrm{Ro}}\left(\frac{\psi}{\sigma\sin\theta} + \frac{\sigma\sin\theta}{2}\right). \tag{3.2a–c}$$

(The second term in brackets in the expression for w is included here as we are working in the non-inertial frame of reference of the rotating fluid.) The incompressibility condition (3.1a) is automatically satisfied. Taylor (1922) proceeded by posing that the streamfunction be of the separable form $\psi = f(\sigma)\sin^2\theta$. Substitution into the curl of (3.1b) , thus removing the pressure gradient, leads to either the trivial solution $f = 0$ or that f must satisfy

$$\sigma^3 f''' - 2\sigma^2 f'' - 2\sigma f' + 8f + \frac{\sigma^2}{\mathrm{Ro}^2}\left(\sigma f' - 2f\right) = 0, \tag{3.3}$$

where a dash denotes differentiation with respect to σ. In the frame of reference rotating with the fluid, but translating with a sphere of radius δ that is not precessing in the laboratory frame, the no-normal flow and no-precession boundary conditions on the boundary of the sphere, together with the far-field velocity boundary condition, are

$$u(\delta,\theta) = 0, \quad w(\delta,\theta) = -\frac{\delta\sin\theta}{2\mathrm{Ro}}, \quad \lim_{\sigma\to\infty}\boldsymbol{u}(\sigma,\theta) = \left(-\cos\theta, \sin\theta, 0\right). \tag{3.4a–c}$$

Equivalently, in terms of f

$$f(\delta) = 0, \quad \lim_{\sigma\to\infty}\frac{f(\sigma)}{\sigma^2} = -\frac{1}{2}. \tag{3.4d,e}$$

The pressure field is given by

$$p(\sigma,\theta) = \left(2ff'' - f'^2 + \frac{f^2}{\mathrm{Ro}^2}\right)\frac{\sin^2\theta}{2\sigma^2} - \frac{2f^2}{\sigma^4} + \frac{1}{2}, \tag{3.5}$$

where the pressure $p \sim (8\mathrm{Ro}^2)^{-1}\sigma^2\sin^2\theta$, the hydrostatic pressure field, as $\sigma \to \infty$. The vorticity field, $\boldsymbol{\omega} \equiv \nabla \times \boldsymbol{u}$, is

$$\boldsymbol{\omega} = -\frac{1}{\mathrm{Ro}}\left[\cos\theta\left(\frac{2f}{\sigma^2}+1\right)\hat{\boldsymbol{\sigma}} - \sin\theta\left(\frac{f'}{\sigma}+1\right)\hat{\boldsymbol{\theta}}\right] - \frac{\sin\theta}{\sigma}\left(f'' - \frac{2f}{\sigma^2}\right)\hat{\boldsymbol{\phi}}. \tag{3.6}$$

The solution to (3.3) that satisfies (3.4d,e) may be written as

$$f(\sigma) = -\frac{\sigma^2}{2} + \frac{1}{2\sigma}\left\{\left[\delta^3 + c\,(\sigma-\delta)\right]\cos\left(\frac{\sigma-\delta}{\mathrm{Ro}}\right) + \frac{\left[\delta^3\sigma - c\left(\delta\sigma + \mathrm{Ro}^2\right)\right]}{\mathrm{Ro}}\sin\left(\frac{\sigma-\delta}{\mathrm{Ro}}\right)\right\}, \tag{3.7}$$

for an arbitrary constant c. The remaining no-slip boundary condition in the polar direction, $v(\delta,\theta) = 0$, is satisifed when $f'(\delta) = 0$ forcing $c = \delta^2 - 3\mathrm{Ro}^2$, and this together with (3.7) can be shown to be equal to Taylor's solution. The no-precession condition and the no-slip boundary condition in the polar direction are physically motivated choices to close the system. The conditions are no-slip conditions applied to an inviscid fluid in the expectation that the inviscid solution will closely approximate the full viscous solution where no-slip conditions would be rigorously valid.

The streamlines for $\delta = 1$, $\mathrm{Ro} = (2\pi)^{-1}$ are shown in figure 3.2a. The nonlinear wavefield in the fluid can be observed (cf. figure 2 Taylor, 1922) as can the closed streamlines that show that fluid is carried with the sphere. Taylor observed that it is not clear how such a flow may be set up; indeed the radiation condition is not everywhere satisfied throughout the wavefield which prohibits the wavefield being created by the towing of the sphere alone. This observation is consistent with the later findings of Stewartson (1958) and Lighthill (1967) who both considered the wavefields built up by motion due to localized forcing along the axis of a rotating fluid *into initially quiescent fluid* and concluded that only columnar modes could exist ahead of the forcing.

Taylor (1922) observed that his analytical solution still exhibited waves even in the limit that the sphere has a vanishingly small radius, i.e., in the limit $\delta \to 0$. Figure 3.2b shows this solution, in the laboratory frame of reference. The sphere is instantaneously located at the origin, indicated by a white circle. Taylor (1922) observed that the streamlines near the origin resemble those of a Hill's spherical vortex (Hill, 1894). Here the rotation rate has been chosen such that this apparent spherical vortex has a unit radius (given by the largest Ro that satisfies $\mathrm{Ro}\sin(\mathrm{Ro}^{-1}) = \cos(\mathrm{Ro}^{-1})$, i.e., $\mathrm{Ro} \approx 0.223$). The boundary of the apparent

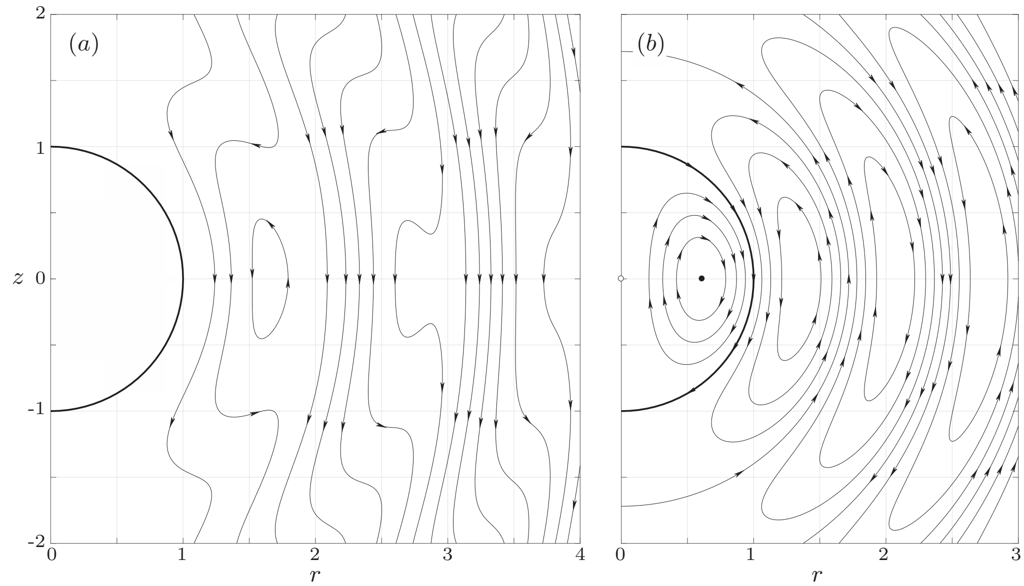

Figure 3.2: (a) Streamlines around a unit sphere translating steadily along the axis of rotation ($r = 0$) of a rotating fluid in the reference frame of the sphere. Closed streamlines show that fluid is being transported with the sphere. (b) Streamlines around a sphere of vanishing size (white circle at the origin) translating steadily along this axis of rotation of a rotating fluid in the frame of reference of the main body of fluid. Taylor (1922) observed that the streamlines near the origin resemble those of a Hill's spherical vortex (Hill, 1894) but described the analogy between the flow and a spherical vortex as 'only superficial'.

spherical vortex is shown in bold. Taylor (1922) describes this analogy with Hill's spherical vortex as superficial as the vortex can only exist when the flow is rotating and a vanishingly small sphere is translating steadily, without precession, along the axis of rotation.

3.2.2 Hill's spherical vortex in a rotating fluid

The classical Hill's spherical vortex is a spherical region of rotational fluid that propagates through an irrotational ambient fluid. The flow is found by constructing solutions inside and outside the spherical vortex and enforcing pressure and velocity continuity across the boundary of the two regions. As with the no-slip conditions enforced on the solid sphere in Taylor's solution, continuity of velocity is enforced across the boundary of the two inviscid solutions, even though this is not a strict requirement, in the expectation that the solution will closely approximate the behaviour of a real viscous fluid. In a frame of reference moving with the spherical vortex, Hill's solution is given by

$$\boldsymbol{u} = \begin{cases} \dfrac{3\cos\theta}{2}(1-\sigma^2)\hat{\boldsymbol{\sigma}} - \dfrac{3\sin\theta}{2}(1-2\sigma^2)\hat{\boldsymbol{\theta}} & \sigma \leqslant 1 \\[2ex] -\dfrac{\cos\theta}{\sigma^3}(\sigma^3-1)\hat{\boldsymbol{\sigma}} + \dfrac{\sin\theta}{2\sigma^3}(2\sigma^3+1)\hat{\boldsymbol{\theta}} & \sigma > 1. \end{cases} \tag{3.8a}$$

$$p = \begin{cases} -\dfrac{9\sigma^2(3-2\sigma^2)}{8}\sin^2\theta + \dfrac{9\sigma^2(2-\sigma^2)}{8} - \dfrac{5}{8} & \sigma \leqslant 1 \\[2ex] -\dfrac{3(4\sigma^3-1)}{8\sigma^6}\sin^2\theta + \dfrac{2\sigma^3-1}{2\sigma^6} & \sigma > 1. \end{cases} \tag{3.8b}$$

where the arbitrary pressure constant has been chosen without loss of generality such that $p \to 0$ as $\sigma \to \infty$. The solution is in the frame of reference of the spherical vortex and so the velocity in the far-field tends to $-\hat{\boldsymbol{z}}$. The solution is axisymmetric and swirl-free and the velocity can be represented by a streamfunction, ψ, of the form of (3.2a,b), where

$$\psi = \begin{cases} \dfrac{3\sigma^2(1-\sigma^2)}{4}\sin^2\theta & \sigma \leqslant 1 \\[2ex] -\dfrac{(\sigma^3-1)}{2\sigma}\sin^2\theta & \sigma > 1 \end{cases} \tag{3.9}$$

and $w = 0$. The arbitrary constant that may be added to the streamfunction is chosen such that $\psi = 0$ on the boundary of the spherical vortex. The pressure and velocity fields are continuous across the boundary of the spherical vortex, $\sigma = 1$.

We now make the following observation; if $\boldsymbol{u}(\sigma,\theta)$ together with a corresponding pressure field, $p(\sigma,\theta)$, solves the non-rotating Euler equations and $\boldsymbol{u}$ can be represented by a streamfunction $\psi(\sigma,\theta)$ in the form of (3.2a,b) with $w = 0$, then

$$\boldsymbol{u} = \left(\frac{1}{\sigma^2\sin\theta}\frac{\partial\psi}{\partial\theta}, -\frac{1}{\sigma\sin\theta}\frac{\partial\psi}{\partial\sigma}, -\frac{\sigma\sin\theta}{2\mathrm{Ro}}\right), \tag{3.10}$$

solves the rotating Euler equations with the same pressure field p. This is because the swirling component in (3.10), $w = -(2\mathrm{Ro})^{-1}\sigma\sin\theta$, exactly cancels the background rotation of the fluid. Thus, we have that (3.10) with ψ given by Hill's inner non-rotating solution ((3.9) for $\sigma \leqslant 1$), and the pressure, p ((3.8b) for $\sigma \leqslant 1$) automatically satisfies the incompressibility condition and the rotating equations of motion (3.1a,b. The solution is Hill's non-rotating spherical vortex described in a rotating frame of reference. To distinguish this solution from the classical solution we refer to it as the 'swirling' Hill's spherical vortex, even though the azimuthal component of the velocity field exactly cancels the background rotation of the fluid. The observation that Taylor's sphere in his experiments did not precess about the axis of rotation gives rise to the possibility that there may exist a form of Taylor's solution that can be matched onto the swirling Hill's spherical vortex by enforcing a different choice of polar velocity boundary condition to Taylor's no-slip condition when setting c in (3.7).

To match a solution of the form (3.2) onto the swirling Hill's spherical vortex such that the velocity field is continuous across the boundary $\sigma = 1$, we require a solution to (3.3) that satisfies, for $\delta = 1$, the conditions (3.4d,e) and yields $v(1,\theta) = \frac{3}{2}\sin\theta$. We therefore require $f'(1) = -\frac{3}{2}$ and hence the solution is given by (3.7) with $\delta = 1$, $c = 1$, so that

$$f(\sigma) = -\frac{\sigma^2}{2} + \frac{1}{2\sigma}\left\{\sigma\cos\left(\frac{\sigma-1}{\mathrm{Ro}}\right) - \mathrm{Ro}\sin\left(\frac{\sigma-1}{\mathrm{Ro}}\right)\right\}. \tag{3.11}$$

Substitution of this solution at $\sigma = 1$ into (3.5) shows that the pressure on the boundary is given by $p(1,\theta) = \frac{1}{2} - \frac{9}{8}\sin^2\theta$, exactly matching the pressure on the boundary of the swirling Hill's spherical vortex (see (3.8b) at $\sigma = 1$). The solution has the property that Hill's classical solution is recovered in the limit $\mathrm{Ro} \to \infty$. Thus, we have a complete steady solution to the nonlinear rotating Euler equations whose inner solution is Hill's spherical vortex with an additional swirling component in the azimuthal direction that cancels out the background rotation of the fluid. This inner solution matches onto an outer solution, with continuous velocity and pressure across the boundary of the vortex. In the far-field the velocity tends to the free-stream velocity $-\hat{\boldsymbol{z}}$ and pressure tends to the hydrostatic pressure field $p = (8\mathrm{Ro}^2)^{-1}\sigma^2\sin^2\theta$. We observe that ψ is even in the Rossby number and so the waves that form in a meridional plane ($\phi = $ const.) oscillate according only to the magnitude of the rotation of the system, and not the sign of the direction of rotation, as might be expected on physical grounds. Similarly, as a result of (3.2c) and (3.11), the azimuthal velocity is odd in the Rossby number and so the azimuthal flow field is reversed if the sign of the direction of rotation of the system is reversed. We see from (3.11) that the wavelength of the inertial waves in the outer fluid is $2\pi\mathrm{Ro}$ as in Taylor (1922).

Figure 3.3(a–c) shows streamlines in the (r, z) meridional plane of Hill's spherical vortex and the flow outside the spherical vortex for three different values of the Rossby number. The streamlines represent the

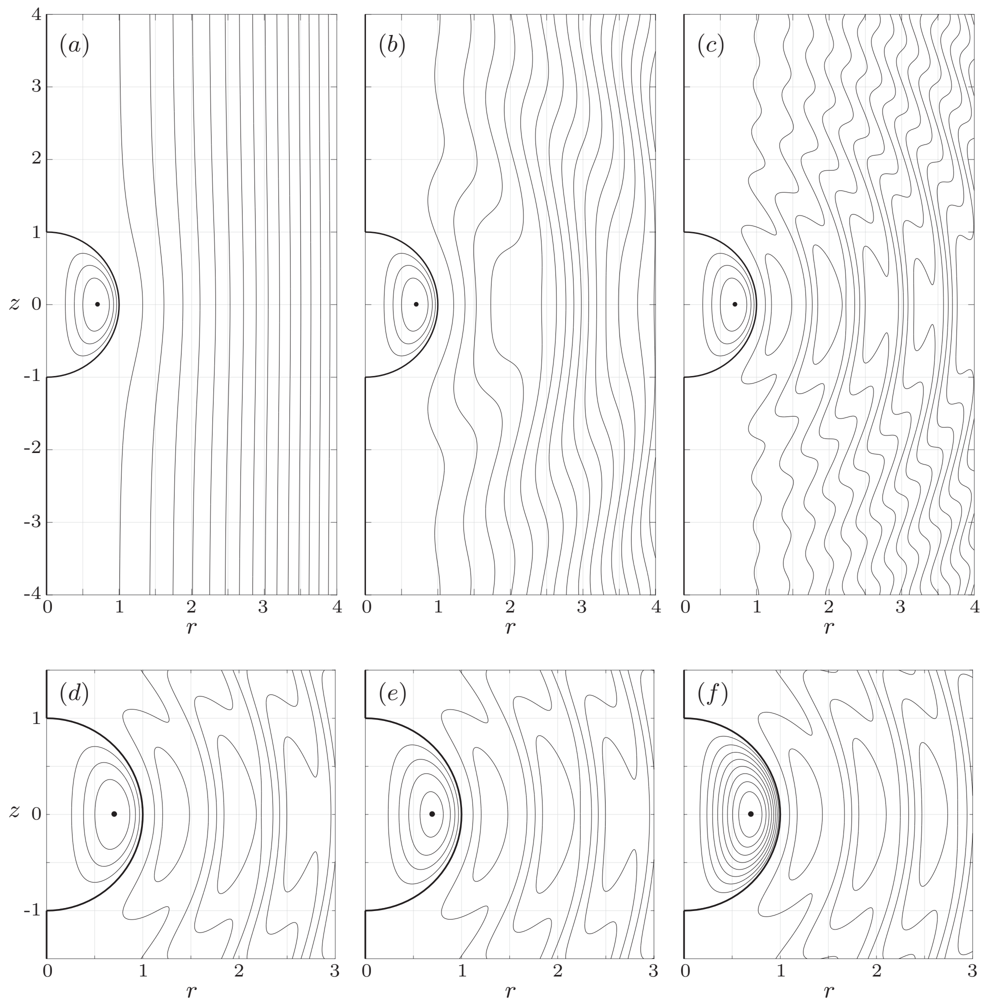

Figure 3.3: (a)–(c): Plots of the streamfunction for Hill's spherical vortex for Ro $= \infty$, $\frac{1}{4}$, $\frac{1}{10}$ *for* (a)–(c) *respectively. The meridional stagnation point in the spherical vortex is indicated by a small black circle and is located at* $r = 2^{-1/2}$, $z = 0$. *In plot* (c) *the formation of closed streamlines externally to the spherical vortex may be observed, indicating regions of fluid that are transported with the spherical vortex. (d)–(f): Plots of the streamfunction for swirling spherical vortices for Ro* $= \frac{1}{10}$. *The parameters shown are: (d)* $\alpha = 0$, $\lambda = \frac{15}{2}$ *(Hill's spherical vortex); (e)* $\alpha = \frac{\pi}{2}$, $\lambda = \frac{15}{2}$*; (f)* $\alpha = \frac{\pi}{2}$, $\lambda = 15$.

flow relative to the translating spherical vortex. The meridional velocity components are always zero at $r = 2^{-1/2}$, $z = 0$, indicated by black circles. Panel (a) is of the non-rotating Hill's spherical vortex that corresponds to the limit $\mathrm{Ro} \to \infty$. As the rate of rotation is increased, and the Rossby number reduces from $\mathrm{Ro} = \frac{1}{4}$ in panel (b) to $\mathrm{Ro} = \frac{1}{10}$ in panel (c), inertial waves can be observed in the outer fluid. Below a critical Rossby number it can be seen that these waves begin to overturn. We also observe that closed streamlines appear in the outer fluid in panel (c). These closed streamlines show that above a critical rotation rate, regions of fluid are transported with the spherical vortex, externally to the spherical vortex in the form of concentric vortex rings.

3.2.3 Swirling spherical vortices in a rotating fluid

We now generalize the method of section 3.2.2 for the family of swirling spherical vortices identified by Moffatt (1969). The spherical vortex, for $\sigma \leqslant 1$, is described in terms of a streamfunction by

$$u = \frac{1}{\sigma^2 \sin\theta}\frac{\partial\psi}{\partial\theta}, \quad v = -\frac{1}{\sigma\sin\theta}\frac{\partial\psi}{\partial\sigma}, \quad w = -\frac{\alpha\,\psi}{\sigma\sin\theta} - \frac{\sigma\sin\theta}{2\mathrm{Ro}}. \qquad (3.12a\text{–}c)$$

As with Hill's solution, the streamfunction has the same separable form as Taylor's streamfunction, specifically $\psi = F(\sigma)\sin^2\theta$, where for $(\lambda, \alpha) \in \mathbb{R}^2$ we have the doubly-infinite family of spherical vortices given by

$$F(\sigma) = \frac{\lambda}{\alpha^2}\left[\frac{\sigma\alpha\cos(\sigma\alpha) - \sin(\sigma\alpha)}{\sigma\,(\alpha\cos\alpha - \sin\alpha)} - \sigma^2\right]. \qquad (3.13)$$

The corresponding pressure field is given by (3.5) with f replaced by F and Ro replaced by α^{-1}. It follows from (3.12) that α is a measure of the degree of swirl in the spherical vortex. The special case of Hill's spherical vortex ring is recovered in the limit $\alpha \to 0$, $\lambda = \frac{15}{2}$. No-normal flow and no-precession conditions are satisfied on the boundary of the swirling spherical vortices as $F(1) = 0$, and hence $u(1,\theta) = 0$ and $w(1,\theta) = -(2\mathrm{Ro})^{-1}\sin\theta$. The conditions of continuity of pressure and polar velocity across the boundary are satisfied if a solution for f, given by (3.7) with $\delta = 1$, can be found such that $f'(1) = F'(1)$ and this condition is satisfied when

$$c = 1 + 2\mathrm{Ro}^2\left[\frac{\lambda}{\alpha^2}\left(3 + \frac{\alpha^2\sin\alpha}{\alpha\cos\alpha - \sin\alpha}\right) - \frac{3}{2}\right]. \qquad (3.14)$$

(Note that the result of section 3.2.2, $c = 1$, is recovered in the limit $\alpha \to 0$, $\lambda = \frac{15}{2}$.) Hence, any swirling spherical vortex given by (3.12) and (3.13) may be matched onto an oncoming stream in a rotating fluid whose far-field velocity tends to $-\hat{\boldsymbol{z}}$ with continuous pressure and velocity across the boundary of the spherical vortex at $\sigma = 1$. We also see that the outer flow is a singly-infinite family given by (3.14) and is equal to the outer flow of the swirling Hill's spherical vortex solution for all solutions with $c = 1$, i.e., for all $(\lambda, \alpha) \in \mathbb{R}^2$ such that the quantity in square brackets in (3.14) is zero.

Figure 3.3$(d$–$f)$ shows streamlines in the (r, z) meridional plane of the swirling spherical vortices for $\mathrm{Ro} = \frac{1}{10}$ and: (d) $\alpha = 0$, $\lambda = \frac{15}{2}$ (Hill's swirling spherical vortex); (e) $\alpha = \frac{\pi}{2}$, $\lambda = \frac{15}{2}$; (f) $\alpha = \frac{\pi}{2}$, $\lambda = 15$. It can be seen that the stronger of the two swirling Moffatt solutions (f) corresponds to a larger amplitude wavefield in the outer fluid, with three closed streamlines in the image shown.

3.2.4 Sibling vortices

The critical rotation rate at which the onset of overturning is observed may be found by considering the turning points of the streamlines. If a given streamline, $\psi = \text{const.}$ for $\sigma > 1$, is parameterized by $\theta = \theta(\sigma)$ then a necessary condition for overturning is $\mathrm{d}\theta(\sigma)/\mathrm{d}\sigma = 0$, that is, when

$$2\mathrm{Ro}^2\sigma^3 + \left\{\mathrm{Ro}^2\sigma + (c-1)\left[\sigma^2 + \mathrm{Ro}^2(\sigma - 1)\right]\right\}\cos\left(\frac{\sigma - 1}{\mathrm{Ro}}\right) + \left\{\sigma^2 - \mathrm{Ro}^2 - (c-1)\left[\mathrm{Ro}^2 - \sigma(\sigma - 1)\right]\right\}\sin\left(\frac{\sigma - 1}{\mathrm{Ro}}\right) = 0. \quad (3.15a)$$

This expression has a different number of branches of solution for a given Rossby number, Ro, as is shown in figure 3.4a for $c = 1$. There is therefore in this case a minimum rate of rotation below which no closed streamlines in the outer fluid are formed and no fluid is carried along with the spherical vortex. The first critical rotation rate occurs when $\mathrm{dRo}(\sigma)/\mathrm{d}\sigma = 0$ where $\mathrm{Ro} = \mathrm{Ro}(\sigma)$ is determined by (3.15a). This condition is given by

$$6\mathrm{Ro}^3\sigma + \mathrm{Ro}\left[\sigma + (c-1)(\sigma + 1)\right]\cos\left(\frac{\sigma - 1}{\mathrm{Ro}}\right) + \left[\mathrm{Ro}^2 + (c-1)(\mathrm{Ro}^2 - \sigma)\right]\sin\left(\frac{\sigma - 1}{\mathrm{Ro}}\right) = 0. \quad (3.15b)$$

The critical points determined by simultaneous solutions of (3.15a) and (3.15b) are shown for $c = 1$ as circles in figure 3.4a and we denote the critical Rossby numbers as $\mathrm{Ro} = \mathrm{Ro}_c^{(n)}$ and the corresponding critical radii as $\sigma = \sigma_c^{(n)}$ for $n = 1, 2, 3, \ldots$. The first critical rotation rate, $\mathrm{Ro}_c^{(1)}$, that represents the minimum rotation rate for which a closed streamline forms in the flow is found numerically, for Hill's spherical vortex, to be $\mathrm{Ro}_c^{(1)} \approx 0.239$. This rotation rate lies between those shown in figure 3.3b and 3.3c. The corresponding radius, $\sigma_c^{(1)} \approx 2.07$ and $\theta = \pi/2$ gives the location at which the overturning first occurs. For a given Rossby number, the associated number of branches of solutions of (3.15a) corresponds to the number of closed streamlines in the flow outside the spherical vortex, and hence corresponds to the number of regions of fluid that are advected with the spherical vortex.

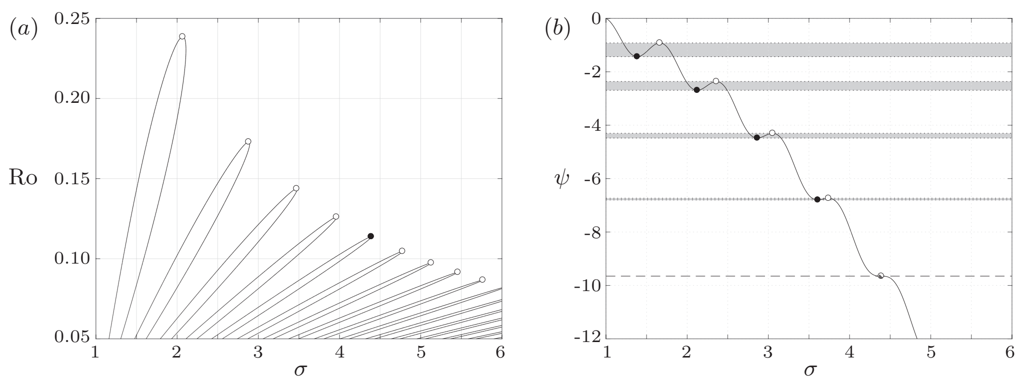

Figure 3.4: (a) Zeros of (3.15a) for $c = 1$; as the rotation rate increases the Rossby number, Ro, decreases and new branches of the solution are found. The critical rotation rates at which new branches of solution are found are given by zeros of the system (3.15), indicated by circles. The fifth critical Rossby $Ro = Ro_c^{(5)} \approx 0.114$ is indicated by the black circle. (b) The streamfunction for $\theta = \pi/2$ and $Ro = Ro_c^{(5)}$. This plot corresponds to the $z = 0$ transect of figure 3.5. The black circles that occur at local minima in ψ correspond to black stagnation points in figure 3.5. The white circles that occur at local maxima in ψ correspond to the white stagnation points in figure 3.5. For ψ lying between pairs of black and white turning points, indicated by the grey regions, the function $\sigma(\psi)$ is multi-valued and this corresponds to closed streamlines in the flow. At the chosen Rossby number the fifth set of closed streamlines is about to appear at the inflection point indicated by the dashed line, corresponding to the cusp at $r \approx 4.39$ (black-white circle) in figure 3.5.

The value of the streamfunction on the closed streamlines and the location of stagnation points in the flow can be found by considering ψ on $\theta = \pi/2$. Figure 3.4b shows $\psi(\sigma, \pi/2)$ for $\sigma > 1$ and $\mathrm{Ro} = \mathrm{Ro}_c^{(5)} \approx 0.114$, the fifth critical rotation rate (indicated by the black circle in figure 3.4a). The turning points in ψ can be seen to appear in pairs of local minima (black circles) and local maxima (white circles). For values of ψ between the local minima and maxima, indicated by the grey bands, the function $\sigma(\psi)$ is multi-valued and this corresponds to closed streamlines in the flow. As the flow considered is exactly at the fifth critical rotation rate, the fifth pair of local minima and maxima coincide at the inflection in ψ where $\sigma \approx 4.39$ and $\psi \approx -9.65$.

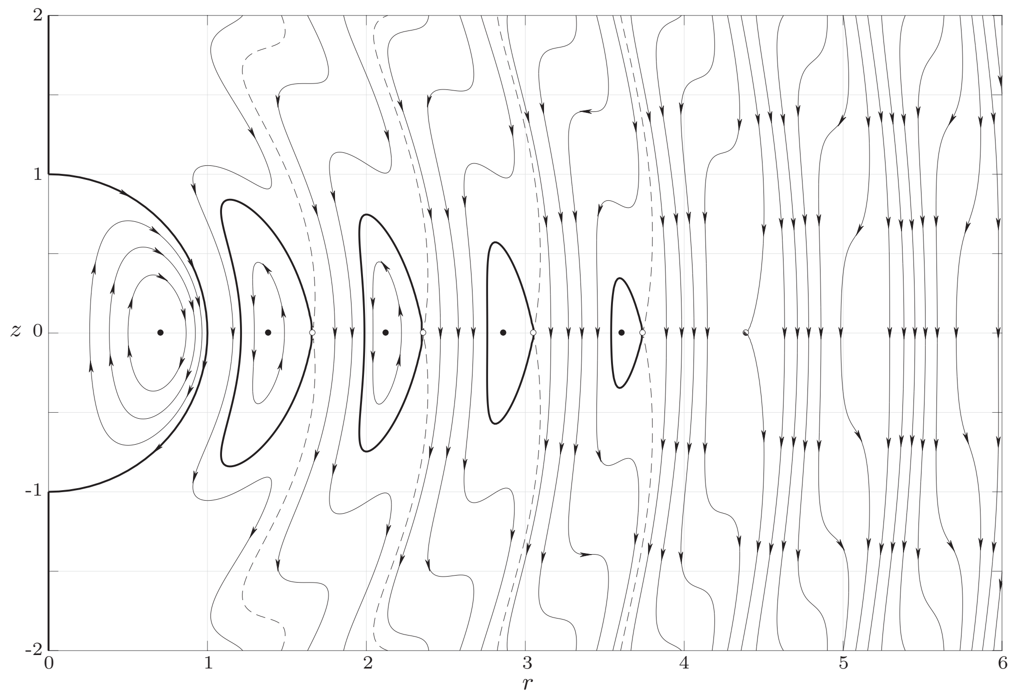

Figure 3.5: A meridional slice through the flow field in the frame of reference moving with a swirling Hill's spherical vortex ring for Ro $= Ro_c^{(5)} \approx 0.114$. This is the fifth critical Rossby number, we can see four sibling vortex rings (bold lines) have been created in the outer fluid and there is a cusp that has formed (black-white circle at $r \approx 4.39, z = 0$) on a streamline that will form the next sibling vortex ring when Ro $< Ro_c^{(5)}$.

Figure 3.5 shows streamlines of the flow for a swirling Hill's spherical vortex in a rotating fluid at $\mathrm{Ro} = \mathrm{Ro}_c^{(5)}$ corresponding to the rotation rate in figure 3.4b. The stagnation point in the spherical vortex is, as in the classical solution, at $\sigma = 2^{-1/2}$, $\theta = \pi/2$. In the outer flow there can be seen to be four closed streamlines, indicated in bold. We observe that the direction of advection around these closed streamlines (anti-clockwise) is opposite to that in the spherical vortex (clockwise), though the vorticity in the closed streamlines may change sign (see 3.6). The black stagnation points in the closed streamlines correspond to the black local minima in figure 3.4b. The white stagnation points, on the boundary of the closed streamlines, correspond to the local maxima in 3.4b. A fifth 'closed streamline' is about to form at the cusp indicated by the black-white circle at $\sigma \approx 4.39$. This corresponds to the inflection in ψ in figure 3.4b.

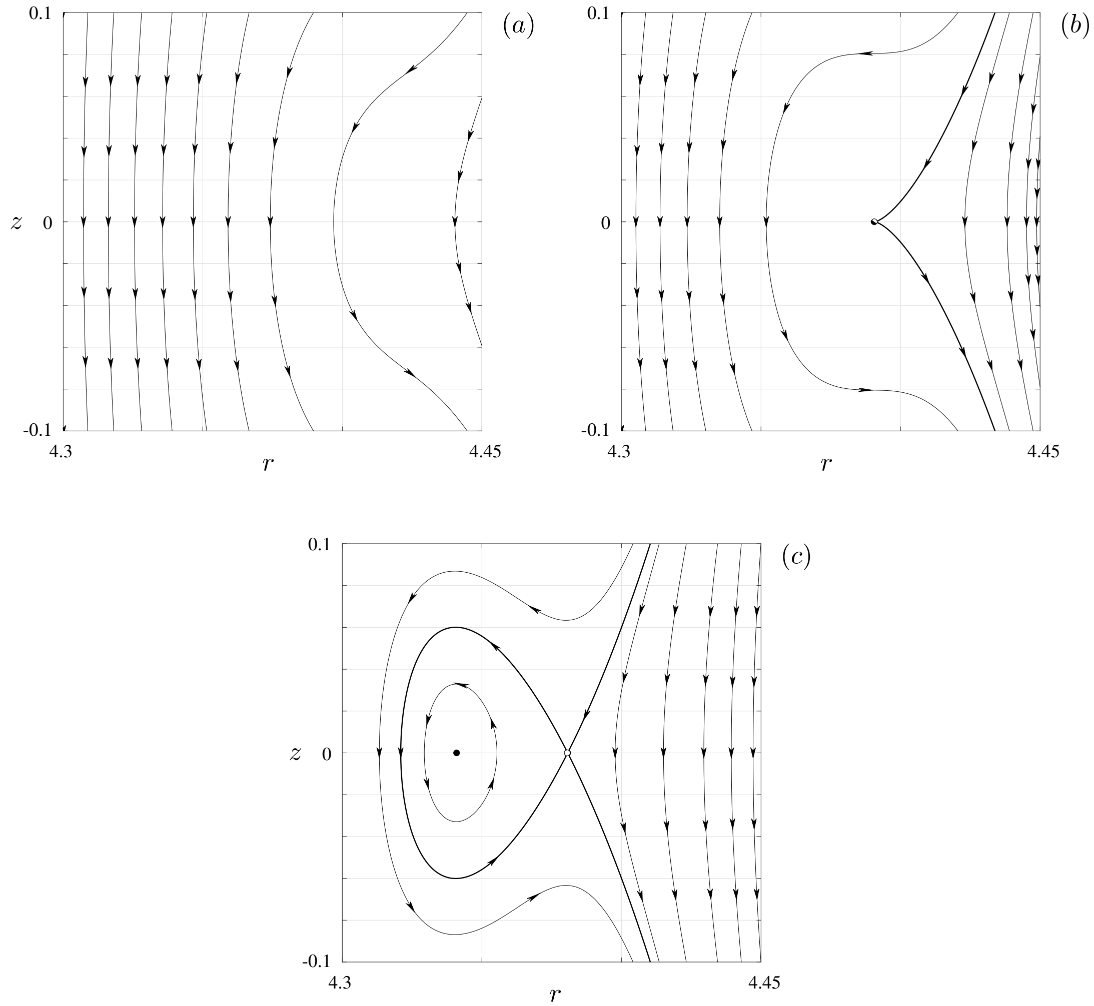

Figure 3.6: Meridional slices through the local flow field for (a) *Ro* $\approx 0.115 > Ro_c^{(5)}$, (b) *Ro* $= Ro_c^{(5)} \approx 0.114$ *and* (c) *Ro* $\approx 0.113 < Ro_c^{(5)}$. *This shows the emergence of a fifth sibling vortex ring.*

Figure 3.6 illustrates the creation of the fifth sibling vortex ring when passing through the critical Rossby number $\mathrm{Ro}_c^{(5)} \approx 0.114$. Figure 3.6a gives the local flow field for $\mathrm{Ro} \approx 0.115 > \mathrm{Ro}_c^{(5)}$. At this Rossby number there are no local maxima or minima. Figure 3.6b gives the local flow field for $\mathrm{Ro} = \mathrm{Ro}_c^{(5)} \approx 0.114$. This is an enlargement of the area around the cusp indicated by the black-white circle in 3.5. If the Rossby number is further decreased to $\mathrm{Ro} \approx 0.113 < \mathrm{Ro}_c^{(5)}$ a new closed streamline is formed producing a new sibling vortex ring and this is seen in figure 3.6c.

3.3 Conclusions

Following Taylor's (1922) observation that his analytical solution for streamlines around a steadily translating, vanishingly small, sphere on the axis of rotation of a rotating fluid resemble those of a Hill's spherical vortex (Hill, 1894), we have derived explicit solutions of the rotating Euler equations that support steadily propagating spherical vortices. The inner solution comprises spherical vortices that are members of a doubly-infinite family of solutions whose boundary swirls in such a way as to exactly cancel the background rotation of the fluid, in that way mimicking the behaviour of the sphere towed through the rotating tank in Taylor's experiments (see also experimental observations in developed vortex rings in rotating fluids (e.g., Eisenga, 1997; Verzicco et al., 1996)). This inner solution matches onto an outer free-stream solution that exhibits nonlinear inertial waves. As the rotation rate is increased the amplitude of the waves is observed to grow until, at a critical rotation rate wave overturning may be observed and closed streamlines form in the outer fluid. The closed streamlines represent vortex rings that are concentric to the spherical vortex on the axis and which propagate with the spherical vortex. As the rotation rate is increased beyond subsequent critical Rossby numbers, new 'sibling' vortex rings are added to the vortex ring family propagating along the axis of rotation.

Chapter 4

Spherical vortices in rotating and non-rotating viscous fluids

This chapter uses a two-dimensional axisymmetric finite element solver to investigate the evolution of spherical vortices in rotating and non-rotating viscous fluids. Section 4.1 begins with the nondimensionalisation of the equations of motion. Section 4.2 outlines the numerical set-up including the derivation of the two-dimensional weak formulation for the finite element problem. Moffatt and Moore (1978) and Pozrikidis (1986) found that Hill's spherical vortex is unstable to linear and nonlinear axisymmetric perturbations in an ideal fluid. However, it is unknown how closely this inviscid theory relates to real viscous fluids and so the propagation of Hill's vortex in a non-rotating fluid is simulated in section 4.3. Section 4.4 investigates the effect of rotation on this propagation by repeating the numerical experiment for different rates of rotation. This is extended to swirling Moffatt vortices in section 4.5. The results corroborate the results of Verzicco et al. (1996) and the finite element solver can be confidently used in subsequent chapters. A summary of the results is provided in section 4.6.

4.1 Nondimensionalisation of the equations of motion

This section outlines the nondimensionalisation of the equations of motion (2.12a) and (2.12b). This nondimensionalisation is identical to that of Norbury (1973). This is done so that the results of this chapter may be directly compared to those of chapter 6 in which the dimensions of the Fraenkel-Norbury vortex rings used are taken from Norbury (1973).

Rotation is about the axis of propagation of Hill's spherical vortex and will thus coincide with the z-axis in the cylindrical coordinate frame. Figure 4.1 shows the orientation of the coordinate system and the direction of rotation. The angular velocity of the rotating fluid is $\mathbf{\Omega} = \Omega\,\hat{\mathbf{z}}$.

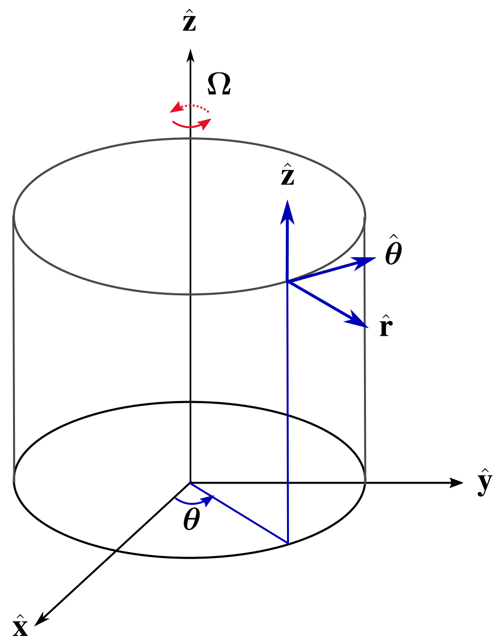

Figure 4.1: The rotation vector $\mathbf{\Omega}$ is taken parallel to the z-axis in the cylindrical coordinate frame. The direction of rotation for positive Ω is indicated by the red arrows.

The equations of motion in a rotating coordinate frame

$$\frac{\partial \mathbf{u}}{\partial t} + (\mathbf{u}\cdot\nabla)\mathbf{u} + 2\,\mathbf{\Omega}\times\mathbf{u} + \mathbf{\Omega}\times(\mathbf{\Omega}\times\mathbf{x}) = -\frac{1}{\rho}\nabla p + \nu\nabla^2\mathbf{u}, \tag{4.1a}$$

$$\nabla\cdot\mathbf{u} = 0, \tag{4.1b}$$

are repeated here from equations (2.12a) and (2.12b) in chapter 2 for convenience. The centrifugal force is conservative and since $\mathbf{\Omega}$ is parallel to $\hat{\mathbf{z}}$, may be written as

$$\mathbf{\Omega}\times(\mathbf{\Omega}\times\mathbf{x}) = -\frac{\Omega^2}{2}\nabla r^2, \tag{4.2}$$

where r is the radial distance from the axis of rotation.

Equations (4.1a) and (4.1b) can be nondimensionalised using an appropriate velocity scale U and length scale L. As in Norbury (1973) position is nondimensionalised as $\mathbf{x} = L\tilde{\mathbf{x}}$ and velocity as $\mathbf{u} = U\tilde{\mathbf{u}}$ with $U = AL^2\alpha^2$ and where: L is the ring radius, α is the nondimensional mean core radius, A is taken from the vorticity field $\boldsymbol{\omega} = Ar$ and where tildes indicate nondimensional quantities. Time is nondimensionalised as $t = L\tilde{t}/U$ and pressure as $p = \rho U^2\tilde{p}$. Equations (4.1a) and (4.1b) become

$$\frac{\partial\tilde{\mathbf{u}}}{\partial\tilde{t}} + (\tilde{\mathbf{u}}\cdot\tilde{\nabla})\tilde{\mathbf{u}} = -\tilde{\nabla}\tilde{p} + \frac{\nu}{LU}\tilde{\nabla}^2\tilde{\mathbf{u}} + \frac{1}{2}\tilde{\nabla}\frac{L^2\Omega^2\tilde{r}^2}{U^2} - \frac{2\Omega L}{U}\tilde{\mathbf{z}}\times\tilde{\mathbf{u}}, \tag{4.3a}$$

$$\tilde{\nabla}\cdot\tilde{\mathbf{u}} = 0, \tag{4.3b}$$

where

$$\tilde{\nabla} = \frac{\partial}{\partial\tilde{r}}\hat{\mathbf{r}} + \frac{1}{\tilde{r}}\frac{\partial}{\partial\theta}\hat{\boldsymbol{\theta}} + \frac{\partial}{\partial\tilde{z}}\hat{\mathbf{z}}. \tag{4.4}$$

Dropping tildes and consolidating parameters gives

$$\frac{\partial\mathbf{u}}{\partial t} + (\mathbf{u}\cdot\nabla)\mathbf{u} = -\nabla p + \frac{1}{\mathrm{Re}}\nabla^2\mathbf{u} + \frac{1}{8\mathrm{Ro}^2}\nabla r^2 - \frac{1}{\mathrm{Ro}}\hat{\mathbf{z}}\times\mathbf{u}, \tag{4.5a}$$

$$\nabla\cdot\mathbf{u} = 0, \tag{4.5b}$$

where $\mathrm{Ro} = U/2\Omega L$ is the nondimensional Rossby number, expressing the relative importance of the inertial to Coriolis forces whilst $\mathrm{Re} = LU/\nu$ is the nondimensional Reynolds number, expressing the relative importance of the inertial to viscous forces.

Combining gradient quantities leaves

$$\frac{\partial\mathbf{u}}{\partial t} + (\mathbf{u}\cdot\nabla)\mathbf{u} = -\nabla P + \frac{1}{\mathrm{Re}}\nabla^2\mathbf{u} - \frac{1}{\mathrm{Ro}}\hat{\mathbf{z}}\times\mathbf{u}, \tag{4.6a}$$

$$\nabla\cdot\mathbf{u} = 0, \tag{4.6b}$$

where the pressure $P = p - r^2/8\mathrm{Ro}^2$ is now a modified pressure which incorporates the centrifugal term and pressure term.

4.2 Formulation of the problem in FreeFem++

This three-dimensional axisymmetric problem can be reduced to a two-dimensional problem on a plane $\theta = \mathrm{const}$. This necessarily prevents the development of any azimuthal asymmetry that may occur in a real three-dimensional flow. The infinite domain is truncated at a distance of 10 times the vortex radius in the radial direction. It is truncated at 5 and 15 times the vortex radius upstream and downstream in the axial direction respectively. These dimensions have been chosen as appropriate to mimic an infinite domain as simulations using a domain with twice these dimensions made no discernible difference to the output quantities of propagation distance and circulation.

The numerical problem is formulated such that at the boundary of the domain the fluid is flowing past with free-stream velocity $-W\hat{\mathbf{z}}$. The domain is seen in figure 4.2 where the upstream arrows indicate the direction of the free-stream flow. Although the numerical problem is formulated such that at the boundary of the domain the fluid is flowing past with free-stream velocity $-W\hat{\mathbf{z}}$, the results presented have been adapted so that they give the flow in a laboratory frame of reference with fluid at the far-field at rest.

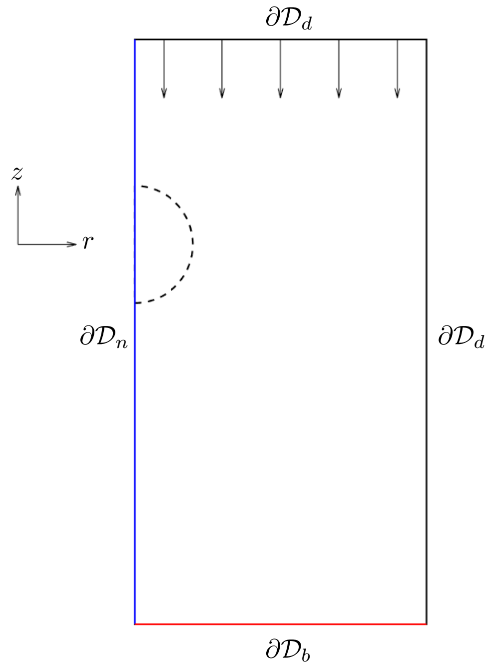

Figure 4.2: Diagram of the r–z domain on which the equations of motions are solved. Solid black edges indicate where a Dirichlet boundary condition $\partial\mathcal{D}_d$ is imposed. The blue edge indicates a Neumann boundary condition $\partial\mathcal{D}_n$ on the axis of symmetry. The red edge indicates the outflow boundary with natural boundary condition $\partial\mathcal{D}_b$. The dashed line indicates the initial location of the vortex ring.

A triangular mesh of the domain given in figure 4.2 for a Hill's vortex of radius 2 is produced in FreeFem++ and is shown in figure 4.3. The results in this chapter were produced using a mesh finer (approximately 48000 triangles) than that seen in figure 4.3. However this coarse mesh (approximately 6800 triangles) illustrates the mesh refinement. The region that Hill's vortex initially occupies - the circle outlined in blue - is more refined. This is necessary due to sharp gradients of velocity and pressure in the early stages of the flow. High refinement here will also provide higher resolution results for analysis. The edges highlighted in red are used to refine the mesh in the region near the original vortex boundary and the region that the vortex will translate through in the domain.

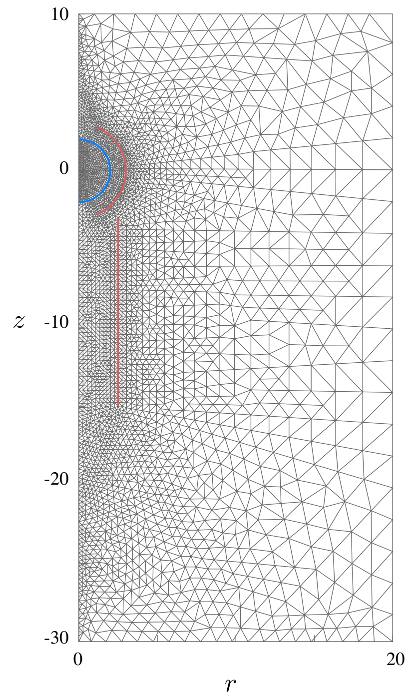

Figure 4.3: The two-dimensional mesh of the domain seen in figure 4.2 for a Hill's spherical vortex of radius 2. The blue line indicates the boundary of the area that Hill's spherical vortex initially occupies. The red line indicates a boundary used for mesh refinement close to initial position of the vortex ring.

4.2.1 The weak formulation

Taking the scalar product of equations (4.6a) and (4.6b) with the test functions **v** and q respectively before integrating over the domain gives

$$\int_{\mathcal{D}} \frac{\partial \mathbf{u}}{\partial t} \cdot \mathbf{v} \, \mathrm{d}\mathcal{D} + \int_{\mathcal{D}} (\mathbf{u} \cdot \nabla) \, \mathbf{u} \cdot \mathbf{v} \, \mathrm{d}\mathcal{D} - \frac{1}{\mathrm{Re}} \int_{\mathcal{D}} \mathbf{v} \cdot \nabla^2 \mathbf{u} \, \mathrm{d}\mathcal{D} + \int_{\mathcal{D}} \mathbf{v} \cdot \nabla P \, \mathrm{d}\mathcal{D} + \frac{1}{\mathrm{Ro}} \int_{\mathcal{D}} (\hat{\mathbf{z}} \times \mathbf{u}) \cdot \mathbf{v} \, \mathrm{d}\mathcal{D} = 0, \tag{4.7a}$$

$$\int_{\mathcal{D}} q \, (\nabla \cdot \mathbf{u}) \, \mathrm{d}\mathcal{D} = 0, \tag{4.7b}$$

for all $\mathbf{v} \in \mathbf{H}^1_{E_0}$ and all $q \in L_2(\mathcal{D})$where

$$\mathbf{u} \in \mathbf{H}^1_E := \{\mathbf{u} \in \mathcal{H}^1 (\mathcal{D})^3 \mid \mathbf{u} = \mathbf{w} \text{ on } \partial\mathcal{D}\}, \tag{4.8a}$$

$$\mathbf{v} \in \mathbf{H}^1_{E_0} := \{\mathbf{v} \in \mathcal{H}^1 (\mathcal{D})^3 \mid \mathbf{v} = \mathbf{0} \text{ on } \partial\mathcal{D}\}, \tag{4.8b}$$

and where $\mathcal{H}^1(\mathcal{D})^3$ is the *Sobolev space* given by

$$\mathcal{H}^1(\mathcal{D})^3 := \left\{ \mathbf{u} : \mathcal{D} \to \mathbb{R}^3 \;\middle|\; \mathbf{u}, \frac{\partial \mathbf{u}}{\partial r}, \frac{\partial \mathbf{u}}{\partial z} \in L_2(\mathcal{D}) \right\}, \tag{4.9}$$

which ensures that **u** and its first derivatives all have finite L_2 measure

$$L_2(\mathcal{D}) := \left\{ \mathbf{u} : \mathcal{D} \to \mathbb{R}^3 \;\middle|\; \int_{\mathcal{D}} |\mathbf{u}|^2 \, \mathrm{d}\mathcal{D} < \infty \right\} \tag{4.10}$$

(Elman et al., 2014). The appropriate pressure and test spaces are also given in Elman et al. (2014) by $P, q \in L_2(\mathcal{D})$.

Due to the axisymmetric nature of the problems considered in this thesis the three-dimensional weak formulation can be reduced to two dimensions. The θ component of our three-dimensional integrals can be integrated out, bringing out a factor of 2π in each term which is then divided through by. The problem is still three-dimensional in the sense that there are three velocity components but the order of the integration has been reduced and only a two-dimensional mesh is needed. This reduction saves on computational time.

By applying integration by parts to the term $\mathbf{v} \cdot \nabla^2 \mathbf{u}$ the order of the derivatives in the problem may be reduced and a method for implementing natural boundary conditions obtained.

Note in cylindrical coordinates

$$\mathbf{v} \cdot \nabla^2 \mathbf{u} = -\nabla \mathbf{u} : \nabla \mathbf{v} + \nabla \cdot (\nabla \mathbf{u} \cdot \mathbf{v}) - \frac{u_r v_r}{r^2} - \frac{u_\theta v_\theta}{r^2} \tag{4.11}$$

where

$$\nabla \mathbf{u} : \nabla \mathbf{v} = \nabla u_r \cdot \nabla v_r + \nabla u_\theta \cdot \nabla v_\theta + \nabla u_z \cdot \nabla v_z \tag{4.12}$$

and that

$$\mathbf{v} \cdot \nabla P = -P \left(\nabla \cdot \mathbf{v} \right) + \nabla \cdot \left(P \mathbf{v} \right). \tag{4.13}$$

The continuity requirements on the weak solution $(\mathbf{u}, P)$ are relaxed by integrating term $\mathbf{v} \cdot \nabla^2 \mathbf{u}$ by parts by applying identity (4.11) (and identity (4.13)) to equation (4.7a) to yield

$$\int_{\mathcal{D}} \frac{\partial \mathbf{u}}{\partial t} \cdot \mathbf{v} \, \mathrm{d}\mathcal{D} + \int_{\mathcal{D}} (\mathbf{u} \cdot \nabla) \, \mathbf{u} \cdot \mathbf{v} \, \mathrm{d}\mathcal{D} + \frac{1}{\mathrm{Re}} \int_{\mathcal{D}} \nabla \mathbf{u} : \nabla \mathbf{v} \, \mathrm{d}\mathcal{D} - \frac{1}{\mathrm{Re}} \int_{\mathcal{D}} \nabla \cdot (\nabla \mathbf{u} \cdot \mathbf{v}) \, \mathrm{d}\mathcal{D}$$
$$+ \frac{1}{\mathrm{Re}} \int_{\mathcal{D}} \left(\frac{u_r v_r}{r^2} + \frac{u_\theta v_\theta}{r^2} \right) \mathrm{d}\mathcal{D} - \int_{\mathcal{D}} P \, (\nabla \cdot \mathbf{v}) \, \mathrm{d}\mathcal{D} + \int_{\mathcal{D}} \nabla \cdot (P \mathbf{v}) \, \mathrm{d}\mathcal{D} + \frac{1}{\mathrm{Ro}} \int_{\mathcal{D}} (\hat{\mathbf{z}} \times \mathbf{u}) \cdot \mathbf{v} \, \mathrm{d}\mathcal{D} = 0, \tag{4.14a}$$

$$\int_{\mathcal{D}} q \, (\nabla \cdot \mathbf{u}) \, \mathrm{d}\mathcal{D} = 0. \tag{4.14b}$$

Applying the divergence theorem to the fourth and penultimate term on the left hand side of equation (4.14a) gives

$$\int_{\mathcal{D}} \frac{\partial \mathbf{u}}{\partial t} \cdot \mathbf{v} \, \mathrm{d}\mathcal{D} + \int_{\mathcal{D}} (\mathbf{u} \cdot \nabla) \, \mathbf{u} \cdot \mathbf{v} \, \mathrm{d}\mathcal{D} + \frac{1}{\mathrm{Re}} \int_{\mathcal{D}} \nabla \mathbf{u} : \nabla \mathbf{v} \, \mathrm{d}\mathcal{D} - \frac{1}{\mathrm{Re}} \int_{\partial \mathcal{D}} (\mathbf{n} \cdot \nabla \mathbf{u}) \cdot \mathbf{v} \, \mathrm{dS} +$$
$$\frac{1}{\mathrm{Re}} \int_{\mathcal{D}} \left(\frac{u_r v_r}{r^2} + \frac{u_\theta v_\theta}{r^2} \right) \mathrm{d}\mathcal{D} - \int_{\mathcal{D}} P \, (\nabla \cdot \mathbf{v}) \, \mathrm{d}\mathcal{D} + \int_{\partial \mathcal{D}} P \, (\mathbf{n} \cdot \mathbf{v}) \, \mathrm{dS} + \frac{1}{\mathrm{Ro}} \int_{\mathcal{D}} (\hat{\mathbf{z}} \times \mathbf{u}) \cdot \mathbf{v} \, \mathrm{d}\mathcal{D} = 0, \tag{4.15a}$$

$$\int_{\mathcal{D}} q \, (\nabla \cdot \mathbf{u}) \, \mathrm{d}\mathcal{D} = 0, \tag{4.15b}$$

for all $\mathbf{v} \in \mathbf{H}^1_{E_0}$ and all $q \in L_2(\mathcal{D})$.

To solve near $r \to 0$ a suitable substitution is necessary to avoid division by zero due to the terms

$$\frac{u_r v_r}{r^2} \text{ and } \frac{u_\theta v_\theta}{r^2}.$$

Making the substitutions $u_r = \tilde{u}_r r$ and $u_\theta = \tilde{u}_\theta r$ gives the final weak formulation to find $\mathbf{u} \in \mathbf{H}^1_E$ and $P \in L_2(\mathcal{D})$ such that

$$\int_{\mathcal{D}} \frac{\partial \mathbf{u}}{\partial t} \cdot \mathbf{v} \, \mathrm{d}\mathcal{D} + \int_{\mathcal{D}} (\mathbf{u} \cdot \nabla) \, \mathbf{u} \cdot \mathbf{v} \, \mathrm{d}\mathcal{D} + \frac{1}{\mathrm{Re}} \int_{\mathcal{D}} \nabla \mathbf{u} : \nabla \mathbf{v} \, \mathrm{d}\mathcal{D} - \frac{1}{\mathrm{Re}} \int_{\partial \mathcal{D}} (\mathbf{n} \cdot \nabla \mathbf{u}) \cdot \mathbf{v} \, \mathrm{dS} +$$
$$\frac{1}{\mathrm{Re}} \int_{\mathcal{D}} \left(\frac{\tilde{u}_r v_r}{r} + \frac{\tilde{u}_\theta v_\theta}{r} \right) \mathrm{d}\mathcal{D} - \int_{\mathcal{D}} P \, (\nabla \cdot \mathbf{v}) \, \mathrm{d}\mathcal{D} + \int_{\partial \mathcal{D}} P \, (\mathbf{n} \cdot \mathbf{v}) \, \mathrm{dS} + \frac{1}{\mathrm{Ro}} \int_{\mathcal{D}} (\hat{\mathbf{z}} \times \mathbf{u}) \cdot \mathbf{v} \, \mathrm{d}\mathcal{D} = 0, \tag{4.16a}$$

$$\int_{\mathcal{D}} q \, (\nabla \cdot \mathbf{u}) \, \mathrm{d}\mathcal{D} = 0, \tag{4.16b}$$

for all $\mathbf{v} \in \mathbf{H}^1_{E_0}$ and all $q \in L_2(\mathcal{D})$. Division by zero is now avoided noting that in cylindrical coordinates $\mathrm{d}\mathcal{D} = r\,\mathrm{d}r\mathrm{d}z$. The numerical scheme solves for $\tilde{\mathbf{u}} = (\tilde{u}_r, \tilde{u}_\theta, u_z)$ and the actual velocity field $\mathbf{u}$ is retrieved with $\mathbf{u} = (r\tilde{u}_r, r\tilde{u}_\theta, u_z)$.

The Dirichlet boundary conditions

$$\mathbf{u} = \mathbf{w} \quad \text{and} \quad P = \Pi \text{ on } \partial\mathcal{D}_d \tag{4.17}$$

will be applied on upper and right hand edges of the domain as indicated by the solid black lines in figure 4.2. This Dirichlet condition will be used to impose that the free-stream flow remains unchanged far from the vortex ring.

On the axis $r = 0$ the Neumann boundary conditions

$$\frac{\partial \mathbf{u}}{\partial r} = \mathbf{0} \quad \text{and} \quad \frac{\partial P}{\partial r} = 0 \text{ on } \partial\mathcal{D}_n \tag{4.18}$$

enforce smooth velocity and pressure profiles on the axis of symmetry. This is indicated by the blue line in figure 4.2.

The bottom of the domain - indicated by the red line in figure 4.2 - will be an outflow boundary and the natural boundary condition

$$\mathbf{n} \cdot \nabla\mathbf{u} - P\,\mathbf{n} = \mathbf{0} \text{ on } \partial\mathcal{D}_b \tag{4.19}$$

is imposed. Elman et al. (2014) explain that for problems that are of inflow/outflow type - not enclosed problems which have $\mathbf{u} \cdot \mathbf{n} = 0$ everywhere on the boundary - care must be taken to ensure the volume of fluid entering the domain is the same amount of fluid exiting the domain. This can be achieved if the natural outflow condition is imposed as $\mathbf{u} \cdot \mathbf{n}$ adjusts itself on the outflow boundary to ensure that mass is conserved. The pressure solution will also always be unique in this case (pp.120, Elman et al., 2014).

The choice of basis functions for the velocity and pressure fields is influenced by stability and computational speed. The simplest combination of triangular basis functions known to be uniformly stable is the $\mathbf{P}_2 - \mathbf{P}_1$ combination (Elman et al., 2014). The velocity field is approximated by quadratic basis functions ($\mathbf{P}_2$) and the pressure field is approximated by linear basis functions ($\mathbf{P}_1$).

The time derivative is implemented using the implicit backward Euler approximation as it is unconditionally stable. As a first-order method the local truncation error is proportional to the square of the step size whilst the global error is proportional to the step size. In this chapter the step size used is $\Delta t = 0.01$. This was chosen as a reduction in the step size to $\Delta t = 0.005$ made no discernible difference to the results. For the partial differential equation

$$\frac{\partial \mathbf{u}}{\partial t} = f\left(\mathbf{u}, \mathbf{x}, t, \frac{\partial \mathbf{u}}{\partial \mathbf{x}}, \frac{\partial^2 \mathbf{u}}{\partial \mathbf{x}^2}\right)$$

the backward Euler approximation states

$$\frac{\mathbf{u}^t - \mathbf{u}^{t-1}}{\Delta t} = f^t(\mathbf{u}), \tag{4.20}$$

or equivalently

$$\frac{\mathbf{u}^t - \mathbf{u}^{t-1}}{\Delta t} - f^t(\mathbf{u}) = \mathbf{0}. \tag{4.21}$$

Taking the scalar product with **v** leaves

$$F(\mathbf{u}) = \frac{\mathbf{u}^t - \mathbf{u}^{t-1}}{\Delta t} \cdot \mathbf{v} - f^t(\mathbf{u}) \cdot \mathbf{v} = 0. \tag{4.22}$$

which is of the same form as (4.16). The Newton method may now be used to solve the nonlinear problem $F(\mathbf{u}) = 0$ at each time step.

The Newton algorithm to solve the nonlinear problem $F(\mathbf{u}) = 0$ at each time step is as follows:

- Choose $\mathbf{u}_0$, an initial guess in the vicinity of the root.
- For $i = 1...n$
  - Solve $DF(\mathbf{u}_i)\delta\mathbf{u}_i = F(\mathbf{u}_i)$
  - Let $\mathbf{u}_{i+1} = \mathbf{u}_i - \delta\mathbf{u}_i$
  - Substitute $\mathbf{u}_{i+1}$ back into the equations of motion and calculate the error ε_i.
- Stop when the error drops below some tolerance i.e. $|\varepsilon_i| < tol$ where $tol \ll 1$ or if $n > N$ and the error is not converging.

For the unsteady rotating Navier-Stokes equations F and DF are

$$\begin{aligned} F(\mathbf{u},p) = \int_{\mathcal{D}} \Big\{ & \frac{\mathbf{u}_t - \mathbf{u}_{t-1}}{\Delta t} \cdot \mathbf{v} + (\mathbf{u}_t \cdot \nabla)\mathbf{u}_t \cdot \mathbf{v} + \frac{1}{\mathrm{Re}} \nabla \mathbf{u}_t : \nabla \mathbf{v} + \frac{\tilde{u}_{r,t} v_r}{r} + \frac{\tilde{u}_{\theta,t} v_\theta}{r} \\ & - P\left(\nabla \cdot \mathbf{v}\right) - q\left(\nabla \cdot \mathbf{u}_t\right) + \frac{1}{\mathrm{Ro}} \left(\hat{\mathbf{z}} \times \mathbf{u}_t\right) \cdot \mathbf{v} \Big\} \, \mathrm{d}\mathcal{D}, \end{aligned} \tag{4.23}$$

$$\begin{aligned} DF(\mathbf{u},p)(\delta\mathbf{u},\delta p) = \int_{\mathcal{D}} \Big\{ & \frac{\delta \mathbf{u}_t}{\Delta t} \cdot \mathbf{v} + (\delta\mathbf{u}_t \cdot \nabla)\mathbf{u}_t \cdot \mathbf{v} + (\mathbf{u}_t \cdot \nabla)\delta\mathbf{u}_t \cdot \mathbf{v} + \frac{1}{\mathrm{Re}} \nabla \delta\mathbf{u}_t : \nabla \mathbf{v} + \frac{\delta\tilde{u}_{r,t} v_r}{r} + \frac{\delta\tilde{u}_{\theta,t} v_\theta}{r} \\ & - \delta P\left(\nabla \cdot \mathbf{v}\right) - q\left(\nabla \cdot \delta\mathbf{u}_t\right) + \frac{1}{\mathrm{Ro}} \left(\hat{\mathbf{z}} \times \delta\mathbf{u}_t\right) \cdot \mathbf{v} \Big\} \mathrm{d}\mathcal{D}. \end{aligned} \tag{4.24}$$

Note that $DF(\mathbf{u})$ is the differential of the function F at point $\mathbf{u}$ having made use of the Taylor expansion $F(\mathbf{u} + \delta\mathbf{u}) \approx F(\mathbf{u}) + DF(\mathbf{u})\delta\mathbf{u}$.

The Courant-Friedrichs-Lewy (CFL) is a necessary but not sufficient condition for numerical stability and should be satisfied everywhere in the flow. Interpreted for fluids problems, the CFL condition states that the distance a fluid parcel travels during one time step must be less than the distance between mesh elements. A fluid parcel situated in one mesh element may only travel to a directly neighbouring element in each time step. The CFL condition applied throughout this thesis is

$$C = U_M \frac{\Delta t}{\Delta x} \leq 1 \tag{4.25}$$

where U_M is the maximum local velocity, Δt is the time step and Δx is the local mesh size. C is referred to as the Courant number.

FreeFem++ produces its mesh using Delaunay-Voronoi triangulation (see appendix A) once the number of mesh elements running along each boundary is specified. The smallest triangle edge running along a boundary was given by $\Delta x = 0.0314$. The Delaunay-Voronoi triangulation maximises the minimum angle of all the angles of the triangles in the triangulation to avoid long thin triangles so it is therefore reasonable to suggest that $\Delta x = 0.0314$ is an appropriate value to use as the minimum the local mesh size. With a maximum velocity in the flow of $U_M = 0.679$ at most we have $C = 0.216 < 1$.

4.2.2 The stream function

To plot the streamlines and visualise the evolution of the flow the stream function $\boldsymbol{\psi}(r,z)$ may be calculated from the velocity field. This is possible because the problem is axisymmetric. A Stokes stream function can be used to describe the streamlines of an incompressible, three-dimensional, axisymmetric flow (Batchelor, 1967). This stream function will fully describe the flow in the radial and axial directions. Any azimuthal swirl must be described separately.

The derivation of the weak formulation for this problem can be found in appendix A following similar principles used to derive the weak formulation for the equations of motion in the previous section. Equation (1.8) gives that the weak formulation is to find $\boldsymbol{\psi} \in \mathbf{H}^1_E$ such that

$$\int_{\mathcal{D}} \nabla\boldsymbol{\psi} : \nabla\mathbf{v}\, r\, \mathrm{d}r\mathrm{d}z - \int_{\partial\mathcal{D}} (\mathbf{n}\cdot\nabla\boldsymbol{\psi})\cdot\mathbf{v}\, r\, \mathrm{dS} + \int_{\mathcal{D}} \left(\tilde{\psi}_r v_r + \tilde{\psi}_\theta v_\theta\right) \mathrm{d}r\mathrm{d}z = \int_{\mathcal{D}} (\nabla\times\mathbf{u})\cdot\mathbf{v}\, r\, \mathrm{d}r\mathrm{d}z \quad (4.26)$$

for all $\mathbf{v} \in \mathbf{H}^1_{E_0}$.

The boundary condition on the upper and right hand boundary will be applied as the far-field Dirichlet condition

$$\boldsymbol{\psi} = (0, \psi_\theta, 0) = \psi_F \hat{\boldsymbol{\theta}} \text{ on } \partial D_d \quad (4.27)$$

which assumes that far from the vortex the flow will remain unchanged with the free-stream velocity $\mathbf{u} = -W\hat{\mathbf{z}}$. On the axis of symmetry $r = 0$ the Neumann boundary condition

$$\frac{\partial\boldsymbol{\psi}}{\partial r} = \mathbf{0} \text{ on } \partial\mathcal{D}_n \quad (4.28)$$

is imposed whilst the natural boundary condition

$$\frac{\partial\boldsymbol{\psi}}{\partial\mathbf{n}} = \mathbf{0} \text{ on } \partial\mathcal{D}_b \quad (4.29)$$

is applied on the outflow boundary.

Using a Hill's spherical vortex of radius 2 it was verified that the calculated stream function converges to the exact stream function as the resolution was increased. The error in the calculated stream function

$$E = \int_{\mathcal{D}} (\psi - \psi_E)\, \mathrm{d}\mathcal{D} \quad (4.30)$$

decreases as the mesh is refined which shows that the solution ψ tends to the exact solution ψ_E as the mesh elements become infinitesimally small. This is seen in figure 4.4 in the linear relationship between the logarithm of the error against the logarithm of the inverse of the square of the number of triangles in the mesh. This is to be expected with a second order accurate spatial discretisation (pp. 42 Elman et al., 2014).

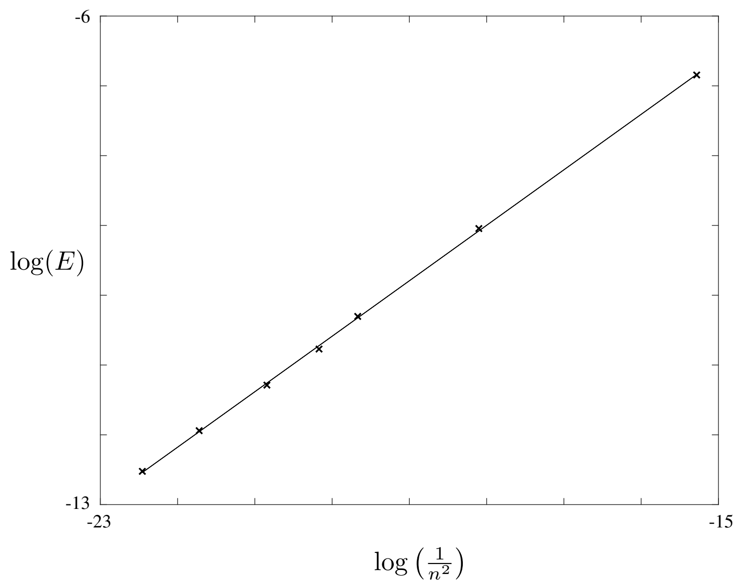

Figure 4.4: Graph of the logarithm of the total error E, in the calculation of the stream function for Hill's vortex against the logarithm of $\frac{1}{n^2}$, where n is the number of triangles in the mesh.

The stream function calculated from the solution of equation (4.26) is shown in figure 4.5 alongside the pressure field. The vortex is stationary in this reference frame with fluid at the free-stream flowing from top to bottom. The region at $r = 0, z = 2$ will be referred to as the front of the vortex ring as it is facing the incoming fluid. The region at $r = 0, z = -2$ will be referred to as the back of the vortex ring.

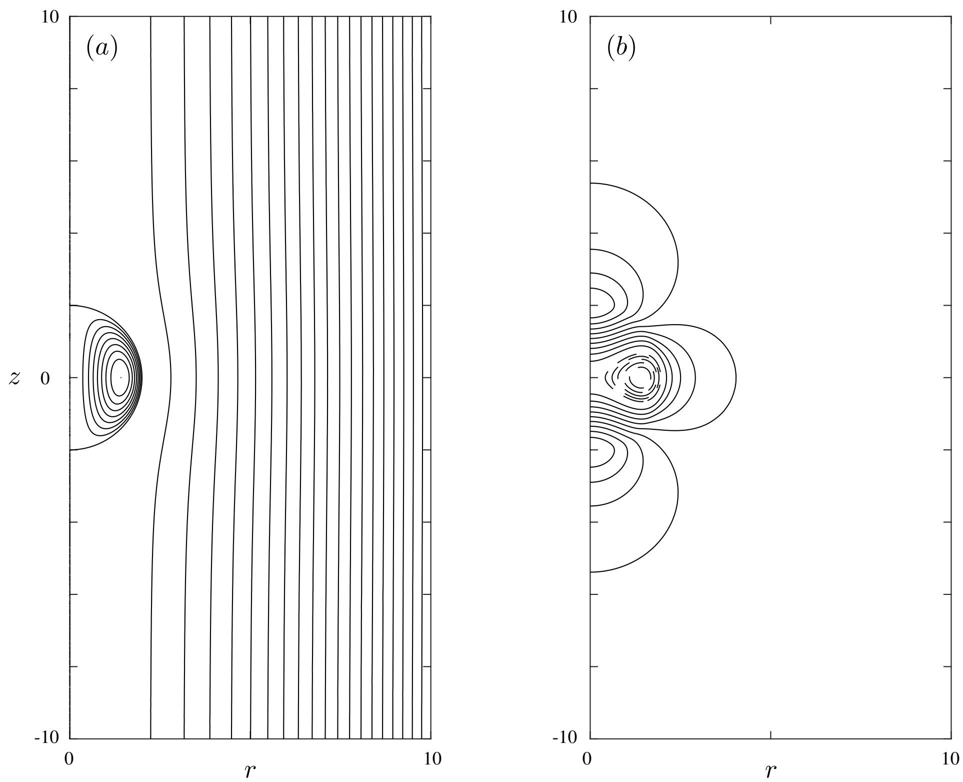

Figure 4.5: Streamlines (a) *and pressure field* (b) *for Hill's spherical vortex. Inside the vortex* $\Delta\psi = 0.025$ *and outside the vortex* $\Delta\psi = -0.62$*. Positive contours of pressure are given by solid lines with* $\Delta p = 0.11$*. Negative contours of pressure are given by dashed lines with* $\Delta p = -0.05$*.*

4.2.3 Circulation

Circulation is a measure of the strength of a vortex ring. In chapter 2 the circulation of Hill's spherical vortex was shown in equation (2.25) to be $\Gamma = 5Wa$. Therefore the nondimensionalisation of Norbury (1973) with a Hill's vortex radius $a = 2$ and free-stream velocity $W = 4/15$ gives a circulation of $\Gamma = 8/3$. Numerically calculating the circulation of the vortex ring is achieved by integrating over the region of positive azimuthal vorticity using the two-dimensional integration function *int2d* in *FreeFem++*. The implementation of this method was verified against the initial velocity field of Hill's vortex. The numerical solution differed from the exact answer of $8/3$ by less than 0.7% and as the mesh is refined the value of the circulation converges to the exact value of $8/3$ like $1/n^2$. In figure 4.6 the linear relationship between the logarithm of the error against the logarithm of the inverse of the number of triangles in the mesh shows that the solution tends to the exact answer as the mesh elements become infinitesimally small.

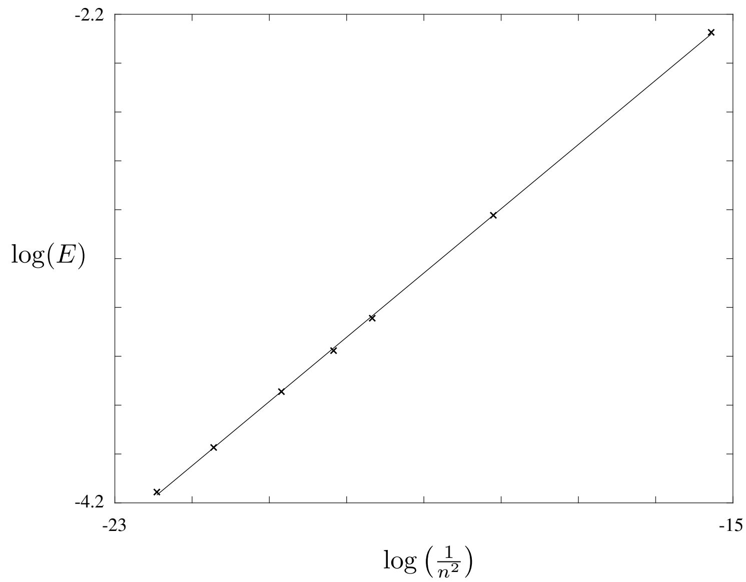

Figure 4.6: Graph of the logarithm of the total error E, in the caluclation of the circulation for Hill's vortex against the logarithm of $\frac{1}{n^2}$*, where* n *is the number of triangles in the mesh and* E *is the difference between the calculated circulation and the exact answer of* $8/3$.

Hill's spherical vortex has a compact region of azimuthal vorticity and calculating the circulation using the above procedure is straightforward. However, in a viscous fluid this is not the case as the boundary of the vortex ring is not well-defined. Furthermore, in some of the following simulations the vortex rings develop a trailing wake of azimuthal vorticity which could affect the calculation of the circulation. Balakrishnan (2013) acknowledged this in his study of swirling vortex rings. In Balakrishnan (2013) the integration to calculate the circulation for a vortex centred at $z = 0$ is performed over the range $-2R_0 \leqslant z \leqslant 2R_0$, where R_0 is the vortex ring radius. This minimises the contribution of the vortex tail to the circulation. In this work a similar principle is employed and the region of integration seen in figure 4.7 is taken to be $-R_0 \leqslant z - Z \leqslant R_0$, where Z is the axial position of the vortex core centre. Having observed Hill's spherical vortex in viscous flows at many different Rossby numbers this range was found appropriate to capture the strength of the vortex ring whilst avoiding too great a contribution to the circulation by any vortex tail generated.

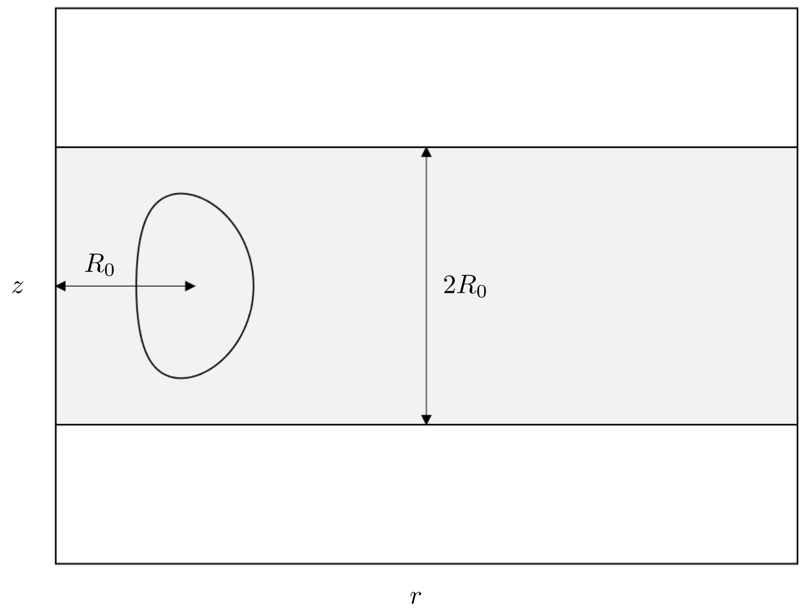

Figure 4.7: Schematic diagram of the "logging" area used when calculating the circulation of the vortex ring. The parameter R_0 is the vortex ring radius - the distance from the vortex core centre to the axis of propagation.

4.3 The evolution of Hill's vortex in a non-rotating fluid

Moffatt and Moore (1978) and Pozrikidis (1986) found that Hill's spherical vortex is unstable to linear and nonlinear axisymmetric perturbations in an ideal fluid. In their stability analyses they found that under oblate perturbations irrotational fluid would be entrained into the rear of Hill's spherical vortex whilst under prolate perturbations rotational fluid is detrained from the back of the vortex ring. How closely this inviscid theory relates to viscous fluids is investigated in this section by observing the evolution of a flow where Hill's spherical vortex is used as the initial flow field in a viscous fluid.

Figures 4.8 – 4.10 give the streamlines, azimuthal vorticity field and pressure field for the subsequent flow with Reynolds number $\mathrm{Re} = 1000$. The stream function field in the resulting flow remains qualitatively similar to the initial stream function. The dividing streamline $\psi = 0$ remains approximately semi-circular in the meridional plane shown. However, in the inviscid case this dividing streamline coincided with the boundary of rotational fluid - the vortex boundary - whilst in this flow the dividing streamline $\psi = 0$ no longer coincides with the boundary of rotational fluid. This can be seen in figure 4.9 where the red dashed contours at $\omega_\theta = 10^{-2}$ indicate the approximate boundary of rotational and irrotational fluid.

Initially the azimuthal vorticity field of Hill's vortex is linear in r inside the vortex boundary. This is observed to evolve into a smooth, continuous vorticity field as the viscosity smooths the discontinuity in vorticity at the boundary. The red contours show that in a viscous fluid Hill's spherical vortex detrains a tail of rotational fluid from its rear. This is similar to the behaviour of a prolate perturbation in the results of Pozrikidis (1986) where a tail of rotational fluid is detrained from the back of the vortex ring. However, the tail in the present case is much wider than in Pozrikidis (1986) and is composed of weakly rotational fluid.

It was noted in chapter 2 that the velocity field of Hill's spherical vortex does satisfy the full, viscous Navier-Stokes equations provided that an additional pressure $15z/\mathrm{Re}$ is added to the inner pressure field since $\nabla^2\mathbf{u} = 15\hat{\mathbf{z}}$ (Saffman, 1992). However, this 'viscous solution' does not give continuous stress across the vortex boundary so is not an exact solution to the steady Navier-Stokes equations and has not been used as the initial flow field in this thesis. However, this does explain why the pressure field of the vortex becomes asymmetric in the developing viscous flow. The viscous term $\nabla^2\mathbf{u}$ is balanced by pressure gradient which results in a slightly higher pressure found at the front of the vortex ring to the back of the vortex ring. This pressure gradient will act to slow down the vortex ring. Over the range of Reynolds numbers investigated herein the behaviour outlined for $\mathrm{Re} = 1000$ is enhanced at lower Reynolds numbers and occurs more slowly at higher Reynolds numbers.

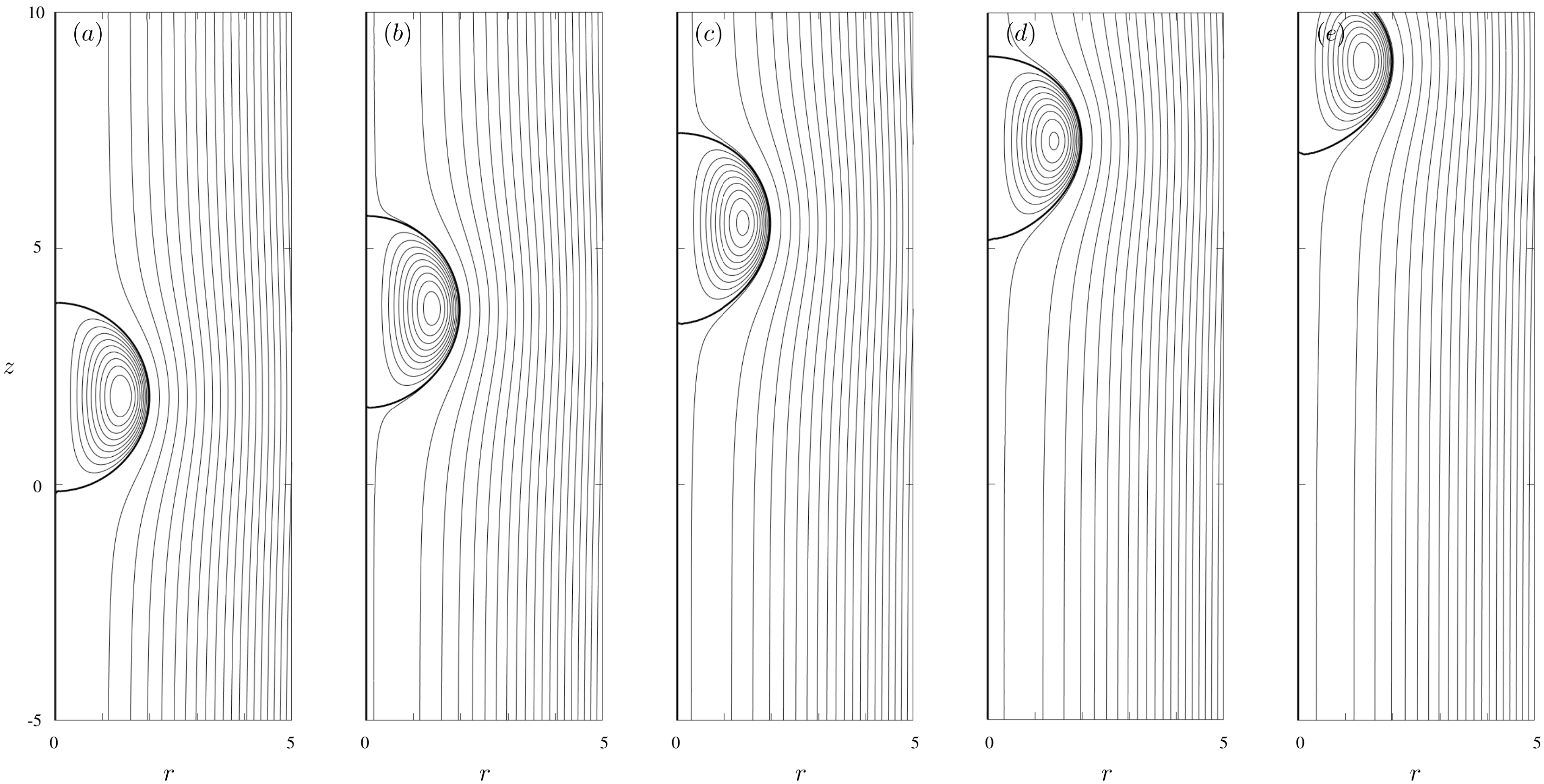

Figure 4.8: Contours of constant stream function at times $t = 7\ (a),\ t = 14\ (b),\ t = 21\ (c),\ t = 28\ (d)$ *and* $t = 35\ (e)$ *for a flow with Reynolds number* $\mathrm{Re} = 1000$ *and Rossby number* $\mathrm{Ro} = \infty$*. Contour increments* $\Delta\psi = 0.0194$ *(inside bold boundary) and* $\Delta\psi = -0.1653$ *(outside bold boundary).*

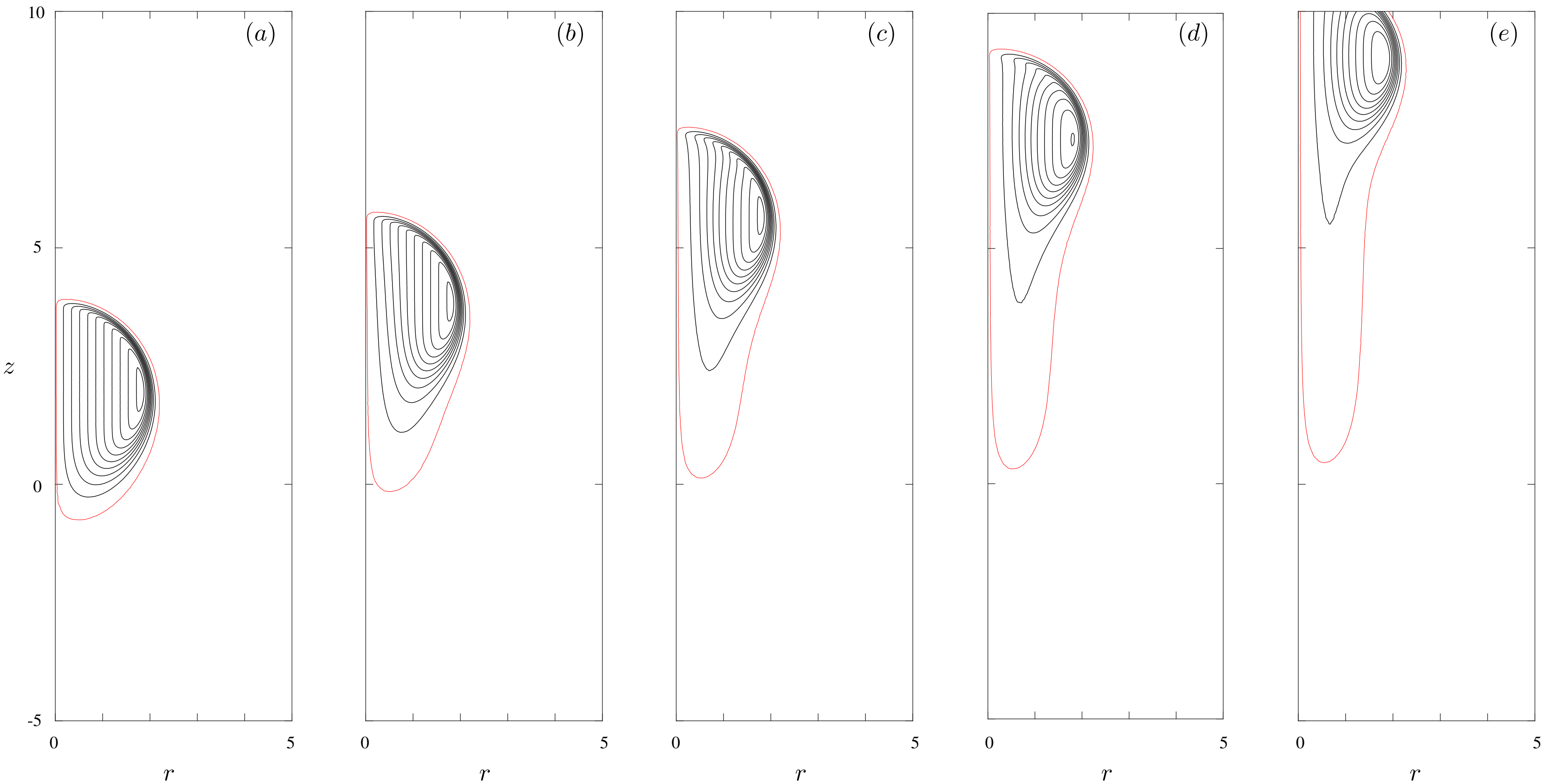

Figure 4.9: Contours of constant azimuthal vorticity at times $t = 7\,(a),\ t = 14\,(b),\ t = 21\,(c),\ t = 28\,(d)$ *and* $t = 35\,(e)$ *for a flow with Reynolds number* $\mathrm{Re} = 1000$ *and Rossby number* $\mathrm{Ro} = \infty$*. Contour increments* $\Delta\omega_\theta = 0.0856$*. the red dashed line indicated the contour* $\omega_\theta = 10^{-2}$.

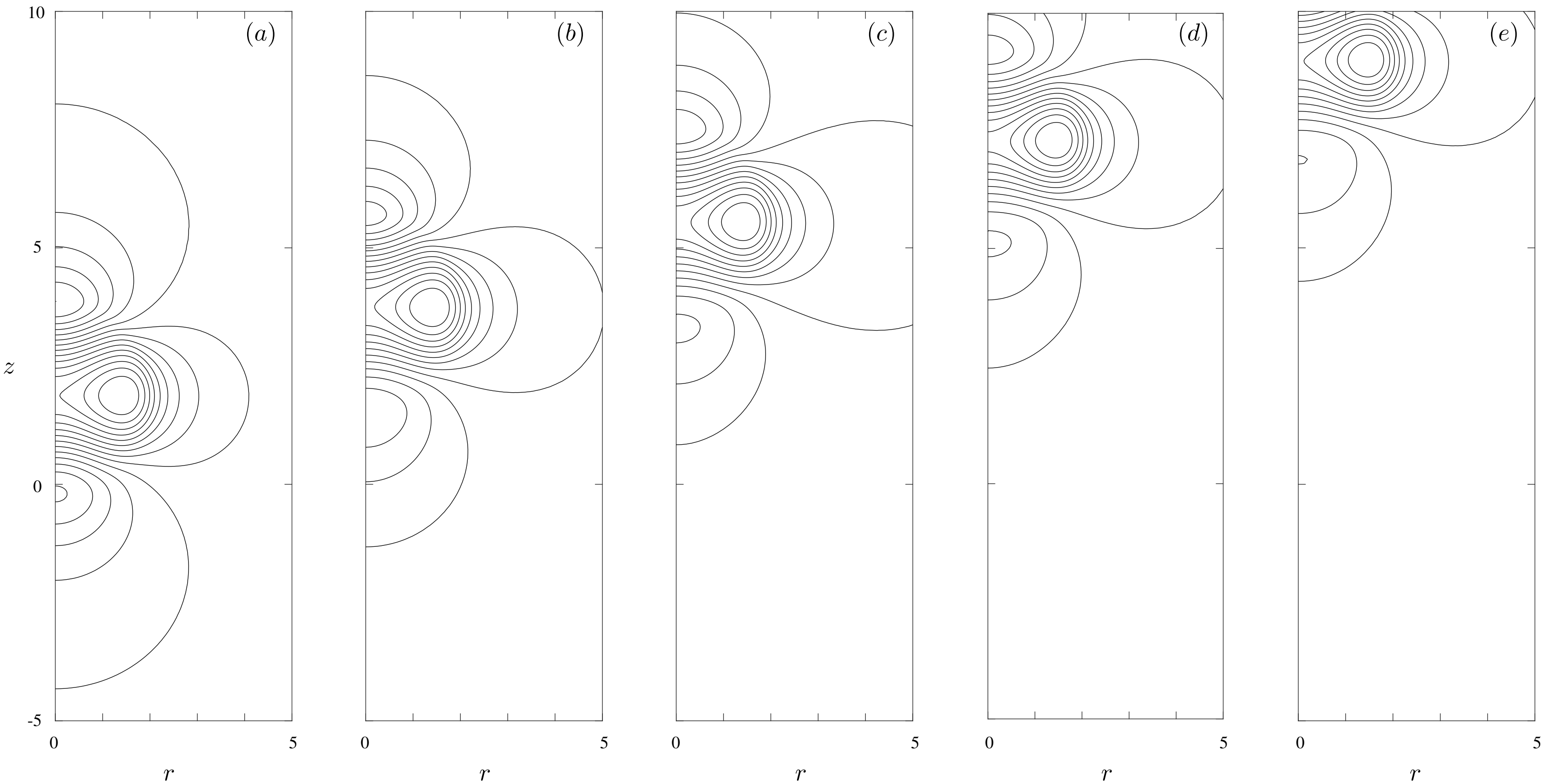

Figure 4.10: Contours of constant pressure at times $t = 7\ (a),\ t = 14\ (b),\ t = 21\ (c),\ t = 28\ (d)$ *and* $t = 35\ (e)$ *for a flow with Reynolds number* $\mathrm{Re} = 1000$ *and Rossby number* $\mathrm{Ro} = \infty$ *with* $\Delta p = 0.0065$.

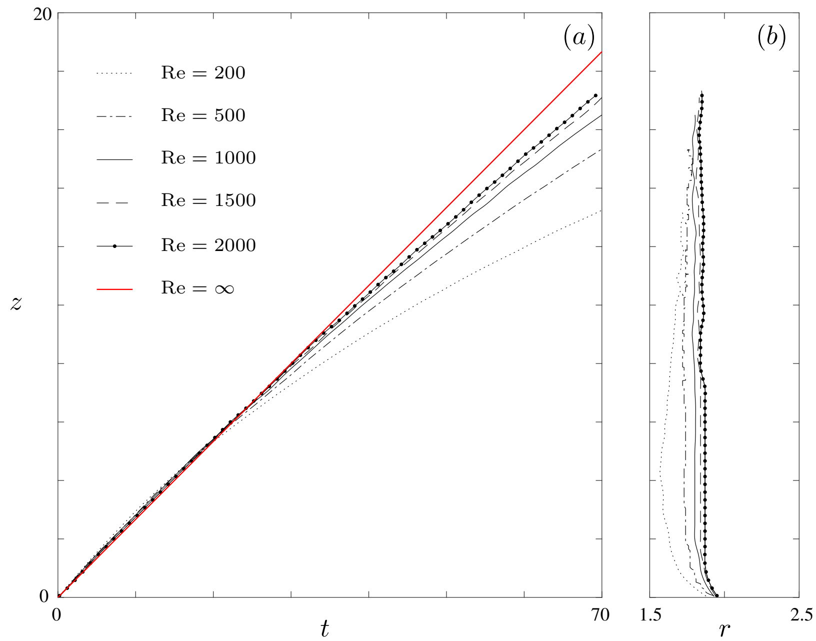

Figure 4.11: (a): The distance travelled in the axial direction by the vortex cores against time for flows of different Reynolds number (b): The trajectory of the vortex cores in the $r-z$ plane.

The vortex core centre is defined as the location of maximum azimuthal vorticity and this is used to track the trajectory of the vortex ring. In Hill's spherical vortex this maximum is initially located on the vortex boundary at $r = 2, z = 0$. Figure 4.11(a) shows the axial distance travelled by the vortex core centres for flows of different Reynolds numbers. As anticipated the vortex ring travels a greater distance in a flow with a greater Reynolds number. Figure 4.11(b) gives the trajectories of the vortex rings in the $r-z$ plane. As previously mentioned viscosity smooths the discontinuity in the azimuthal vorticity field which means the location of maximum azimuthal vorticity initially moves inwards towards the axis of propagation before settling at a constant distance from the axis. This is more pronounced at lower Reynolds numbers - at $\mathrm{Re} = 200$ the vortex core centre moves radially inward considerably before slowly migrating outwards again.

The velocity of the vortex cores, v_c, is calculated using a central fourth-order finite difference method. The normalised velocities $v_n = v_c/W$ are calculated and shown in figure 4.12. The non-monotonicity is due to the non-smooth propagation distance data limited by the coarseness of the mesh. As expected the propagation velocity of the vortex rings decrease from the initial value with vortex rings in more viscous fluids decelerating more quickly. This deceleration is the result of loss of energy due to viscous diffusion and through entrainment of fluid from the surroundings following the need to ensure conservation of momentum. Krutzsch (1939) was the first to document this entrainment process followed by a closer study by Maxworthy (1972).

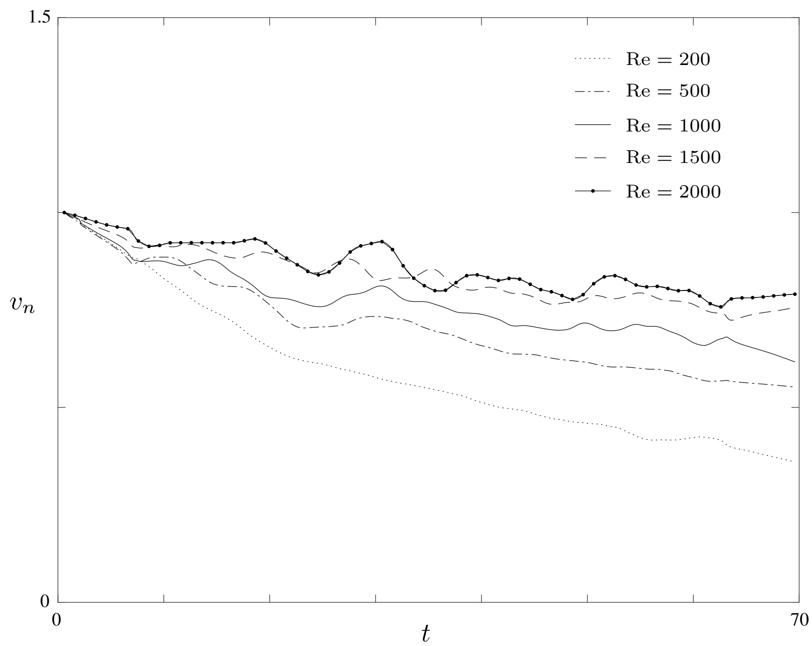

Figure 4.12: The normalised propagation velocity v_n in the axial direction by the vortex cores against time for flows of different Reynolds number.

Following dimensional arguments, Manton (1976) presented relations for the propagation distance and velocity of spherical vortices of radius a. He considered the two limiting cases of zero and infinite Reynolds number and the results were in agreement with the independent measurements of Banerji and Barave (1931), Keedy (1967) and Maxworthy (1972).

In the high Reynolds number limit $(\mathrm{Re} \gtrsim 500)$ Manton found the propagation distance to be given by

$$\frac{z}{a} = \frac{3}{\beta}\left(\left(1+\frac{t}{t_1}\right)^{1/4} - 1\right) \tag{4.31}$$

where $t_1 = (3/4\beta)(a/U)$, U is the free-stream velocity and β is a constant.

MatLab's *fitnlm* function was used to fit a nonlinear regression model to the results of the form

$$z = \frac{3a}{A}\left(\left(1+\frac{4AU}{3a}t\right)^{B} - 1\right) \tag{4.32}$$

where A will give the value of the constant β and we anticipate B to be close to $1/4$. The results are presented in table 4.1 and are in good agreement with the relationship predicted by Manton. We see that $B = 0.2815$ at $\mathrm{Re} = 500$ and as the Reynolds number increases the value of B tends towards the value predicated by Manton of $1/4$ in the infinite Reynolds number limit.

Re	200	500	1000	1500	2000
A	0.2319	0.1003	0.0549	0.0373	0.0316
B	0.3184	0.2815	0.2701	0.2641	0.2632

Table 4.1: Coefficients obtained when fitting time-distance data to equation (4.32)

Figure 4.13 gives the evolution of the circulation of Hill's vortex at each Reynolds number. As anticipated vortex rings in more viscous flows see their circulation decrease more rapidly due to greater viscous diffusion of vorticity and an increase in vortex size (pp.897 Tinaikar et al., 2018). The circulation can be used to test the relationship between circulation and time proposed by Manton (1976)

$$\frac{\Gamma}{\Gamma_0} = \left(1+\frac{\beta}{3}\left(\frac{z}{a}\right)\right)^{-2} = \left(1+\frac{t}{t_1}\right)^{-1/2} \tag{4.33}$$

where Γ_0 is the initial circulation and again $t_1 = (3/4\beta)(a/U)$ and β is a constant.

MatLab's *fitnlm* function was used to fit a nonlinear regression model of the form

$$\Gamma = \Gamma_0\left(1+\frac{t}{t_1(A)}\right)^{-B} \tag{4.34}$$

to the results and the coefficients are given in table 4.2. Again, A is an estimate of the constant β and Manton's model predicts that B should take the value of $1/2$. As seen from the table some of the results are not too dissimilar from this value but for $\mathrm{Re} = 200$ and $\mathrm{Re} = 1500$ the value for B is higher than anticipated. This is understandable for $\mathrm{Re} = 200$ as equation (4.33) is for the high Reynolds number limit. However, the disagreement at $\mathrm{Re} = 1500$ is not understood. Further simulations in this region of Reynolds number could be repeated to determine why.

Re	200	500	1000	1500	2000
A	0.2319	0.1306	0.0821	0.0467	0.0453
B	0.6840	0.5620	0.5435	0.6925	0.6128

Table 4.2: Coefficients obtained when fitting time-circulation data to equation (4.34)

Overall, the relationships between propagation distance, circulation and time fit the theory proposed by Manton (1976) sufficiently well to be confident that the numerical scheme is reliable for use in subsequent sections.

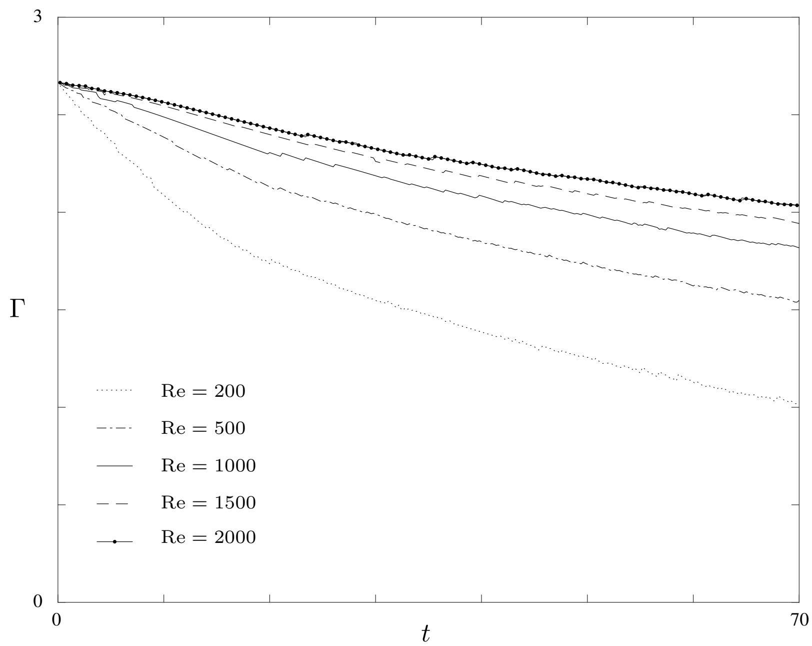

Figure 4.13: The circulation of the vortex cores against time for flows of different Reynolds number.

4.4 The evolution of Hill's vortex in a rotating fluid

Rotating flows exhibit behaviour not found in non-rotating flows. Before presenting numerical results some underlying theory on rotating flows is presented. The Taylor-Proudman theorem considers the dominant balance of the equations of motion where the inertial and viscous terms are assumed negligible.

The Taylor-Proudman theorem

At high rates of rotation the Coriolis force dominates the flow. Proudman and Lamb (1916) showed that for steady flow at small Rossby number the Coriolis effect acts to supress variation in the velocity in the direction parallel to the axis of rotation. This can be seen by taking $\partial \mathbf{u}/\partial t = \mathbf{0}$ and assuming for $\mathrm{Ro} \ll 1$ the terms $(\mathbf{u} \cdot \nabla)\mathbf{u}$ and $\dfrac{1}{\mathrm{Re}}\nabla^2\mathbf{u}$ in equation (4.6) are negligible to give

$$\nabla P = -\frac{1}{\mathrm{Ro}}\hat{\mathbf{z}} \times \mathbf{u}, \tag{4.35a}$$

$$\nabla \cdot \mathbf{u} = 0. \tag{4.35b}$$

Taking the curl of equation (4.35a) gives

$$\nabla \times \nabla P = \mathbf{0} = -\frac{1}{\mathrm{Ro}}\nabla \times (\hat{\mathbf{z}} \times \mathbf{u}). \tag{4.36}$$

Use of a vector calculus identity and the incompressibility of the flow leaves

$$\mathbf{0} = \nabla \times (\hat{\mathbf{z}} \times \mathbf{u}) = \hat{\mathbf{z}}(\nabla \cdot \mathbf{u}) - \mathbf{u}(\nabla \cdot \hat{\mathbf{z}}) + (\mathbf{u} \cdot \nabla)\hat{\mathbf{z}} - (\hat{\mathbf{z}} \cdot \nabla)\mathbf{u} \tag{4.37a}$$

$$= (\hat{\mathbf{z}} \cdot \nabla)\mathbf{u} \tag{4.37b}$$

which gives that all velocity components are independent of z. Flows with small Rossby number can be seen as two-dimensional motion in the plane perpendicular to the axis of rotation whilst motion in the axial direction must also be independent of z. If rotation acts to inhibit variation in the axial direction then for a vortex with a flow field dependent upon z it can be expected rotation will act to destroy the vortex ring.

4.4.1 Low Reynolds number results

The finite element problem (4.16) is now solved with finite Rossby number. The streamlines for the flow are again achieved by the solution of the stream function - velocity problem (4.26). Figures 4.14 and 4.15 show the streamlines and azimuthal vorticity field evolving from Hill's spherical vortex in a flow with Reynolds number $\mathrm{Re} = 200$ and Rossby number $\mathrm{Ro} = 10$. In contrast to the non-rotating case an azimuthal swirl is induced. In figure $4.17(a)$ we see this comprises an anticyclonic part ahead and to the outside of the vortex ring - as indicated by the dashed lines - and a cyclonic "tail" to the back of the vortex ring. This behaviour was also observed in Verzicco et al. (1996) and Brend and Thomas (2009) and can be explained through the angular momentum of the system.

Verzicco et al. (1996) considered the angular momentum of a particle with unit mass at a distance r from the axis of symmetry. In a non-rotating flow this particle would have angular momentum $L = ru_\theta$. However, in a rotating frame of reference this particle has the additional angular momentum provided by the background rotation of Ωr^2. Therefore from conservation of angular momentum a particle in a rotating system undergoing a displacement of r_c in the radial direction must preserve the quantity $(r_c u_\theta + {r_c}^2\Omega)$. Conservation of this quantity means that an azimuthal swirl can be induced even if the flow began swirl-free.

Ahead of the vortex ring fluid parcels have an outward radial motion whilst behind the vortex ring fluid parcels have an inward radial motion. Therefore when seeking to preserve the quantity $(r_c u_\theta + {r_c}^2\Omega)$, an inward radial motion r_c must be accompanied by an increase in azimuthal swirl that is greater than the decrease required of the same magnitude radially outward due to the r_c^2 term. This means that greater intensity swirl is induced where fluid particles are moving inwards - at the rear of the vortex ring - than ahead of it where fluid parcels are moving outwards. This can be seen in figure 4.17(a) noting that the contour increments for negative velocity are much smaller.

Rotation also induces a region of negative azimuthal vorticity ahead of the vortex ring which is seen in figure 4.15 . This agrees with the findings of Verzicco et al. (1996) whose explanation for this behaviour by examining the azimuthal component of the vorticity equation is recast here.

The azimuthal component of the vorticity equation is achieved by taking the curl of equation (4.6) to give

$$\frac{\partial \omega_\theta}{\partial t} + (\mathbf{u}\cdot\nabla\boldsymbol{\omega})_\theta = \underbrace{(\boldsymbol{\omega}\cdot\nabla\mathbf{u})_\theta}_{\omega_r\frac{\partial u_\theta}{\partial r} + \omega_z\frac{\partial u_\theta}{\partial z} + \frac{\omega_\theta u_r}{r}} + \frac{1}{\mathrm{Re}}\left(\nabla^2\boldsymbol{\omega}\right)_\theta + \frac{1}{\mathrm{Ro}}\frac{\partial u_\theta}{\partial z}. \tag{4.38}$$

From the third term on the right hand side of equation (4.38) we see that the Coriolis term can act as a source of azimuthal vorticity if there are axial gradients of azimuthal swirl in the flow. Figure 4.17 gives the azimuthal swirl and axial vorticity fields at $t = 21$. The red lines show the boundary of positive azimuthal vorticity. Following a vertical line through figure $4.17(a)$ at $r \approx 0.5$ from bottom to top one firstly finds a positive axial gradient of azimuthal swirl with $\partial u_\theta/\partial z > 0$. In this region positive azimuthal vorticity is generated. However, travelling further up the vertical line one finds a negative axial gradient of azimuthal swirl with $\partial u_\theta/\partial z < 0$ explaining the generation of negative azimuthal vorticity at the head of the vortex ring. Azimuthal vorticity is also generated from azimuthal swirl by the vortex tilting term

$$(\boldsymbol{\omega} \cdot \nabla \mathbf{u})_\theta = \omega_r \frac{\partial u_\theta}{\partial r} + \omega_z \frac{\partial u_\theta}{\partial z} + \frac{\omega_\theta u_r}{r} \tag{4.39}$$

which gives the change in vorticity due to local expansion of the velocity field in the direction parallel to $\boldsymbol{\omega}$. The term which is the product of the axial gradient of azimuthal swirl (figure $4.17(a)$) and axial vorticity (figure $4.17(b)$) is particularly important. This will be explained further in section 4.5 when considering Moffatt's swirling vortex rings.

Figure 4.16 shows a clear region of low pressure at the back of the vortex ring as a result of the strongly swirling cyclonic tail. This pressure gradient from the front to the rear of the vortex ring inhibits axial flow through the centre of the vortex ring and causes the vortex ring to slow down. The same behaviour is seen in figures $11(a)$ and $11(b)$ of Verzicco et al. (1996).

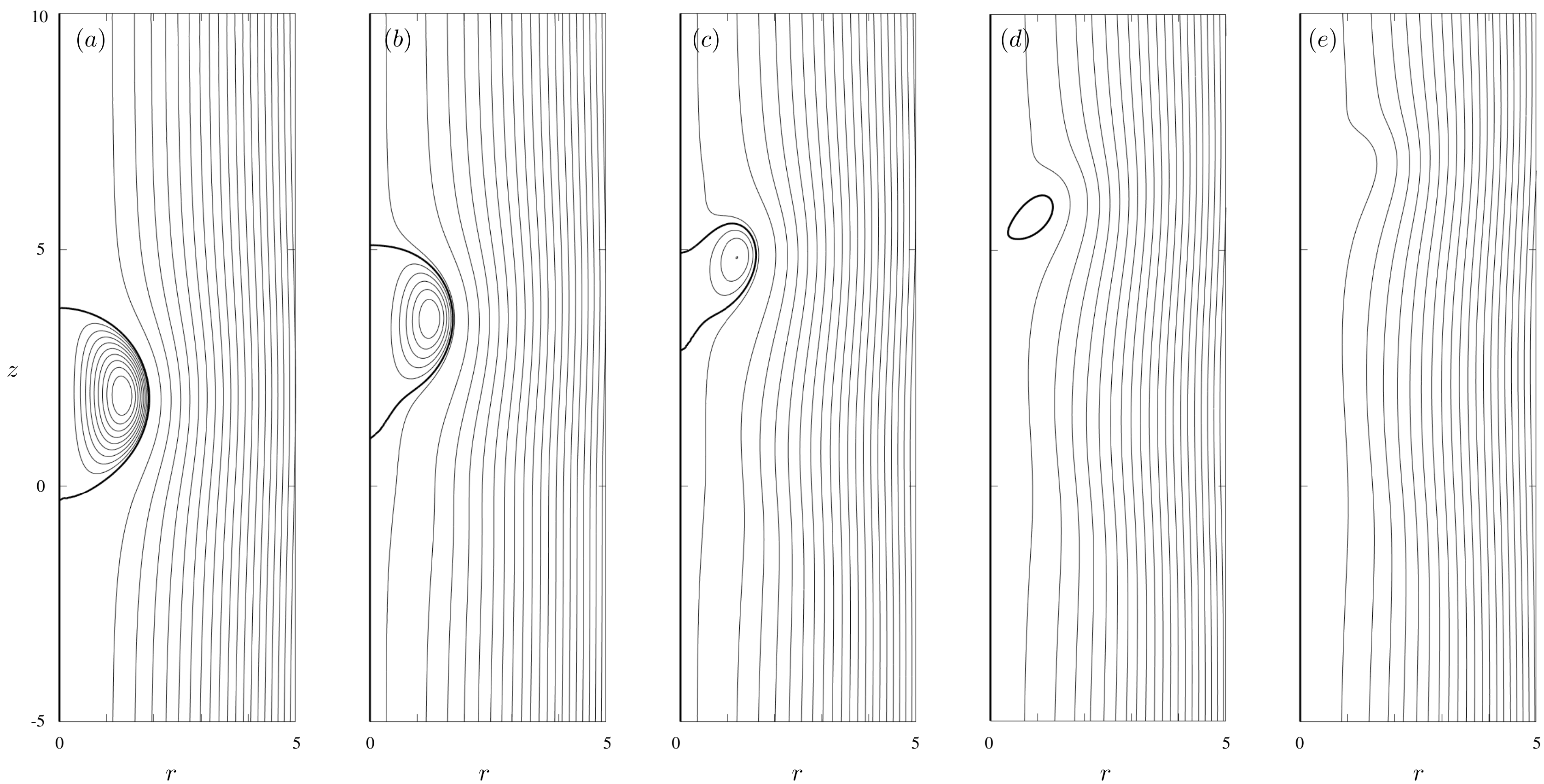

Figure 4.14: Contours of constant stream function at times $t = 7\ (a),\ t = 14\ (b),\ t = 21\ (c),\ t = 28\ (d)$ *and* $t = 35\ (e)$ *for a flow with Reynolds number* $\mathrm{Re} = 200$ *and Rossby number* $\mathrm{Ro} = 10$*. The bold line gives the streamline* $\psi = 0$*. Contour increments* $\Delta\psi = 0.0148$ *(inside bold boundary) and* $\Delta\psi = -0.1651$ *(outside bold boundary).*

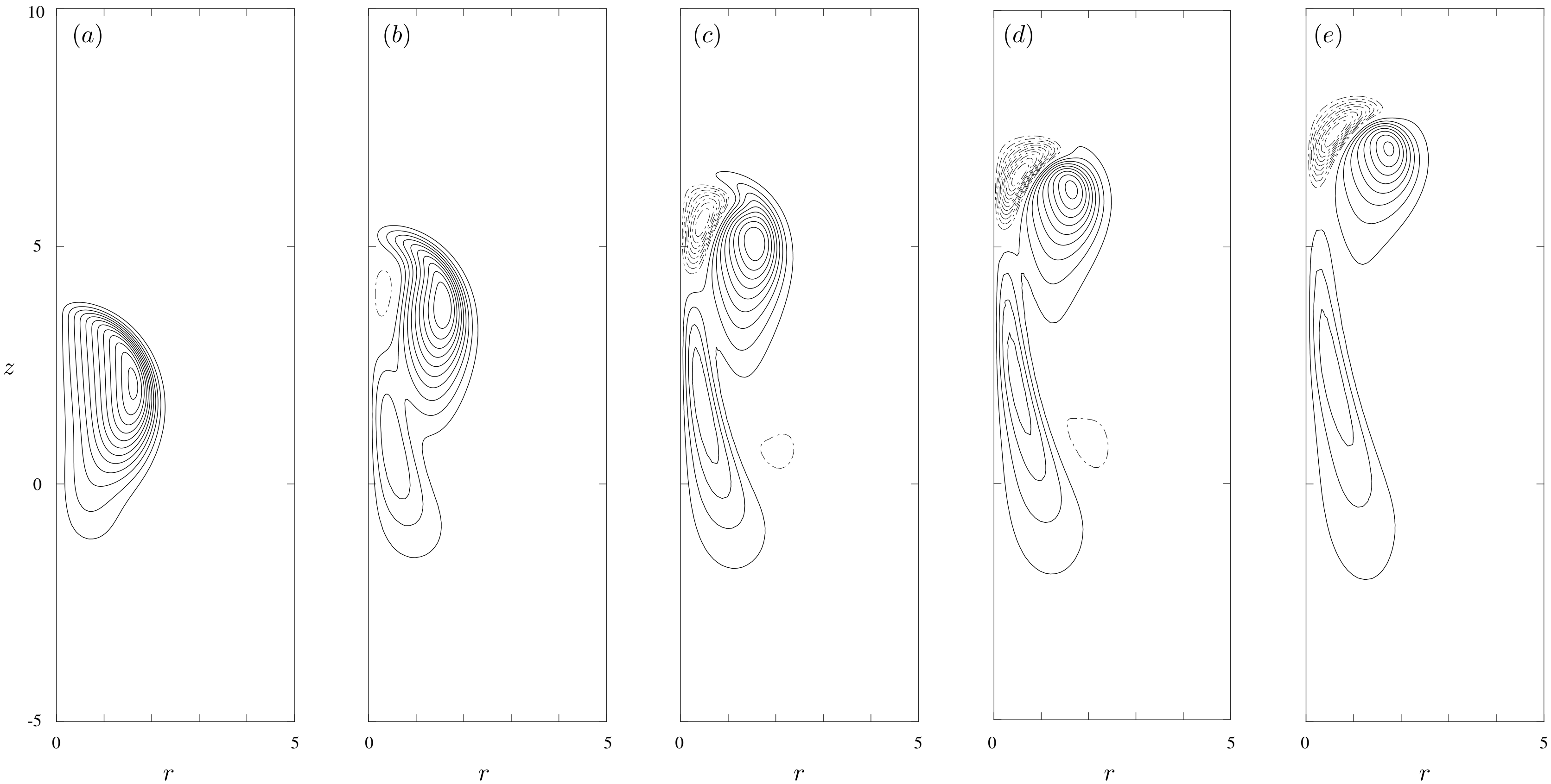

Figure 4.15: Contours of constant azimuthal vorticity at times $t = 7\ (a),\ t = 14\ (b),\ t = 21\ (c),\ t = 28\ (d)$*and* $t = 35\ (e)$ *for a flow with Reynolds number* $\mathrm{Re} = 200$ *and Rossby number* $\mathrm{Ro} = 10$*. Contour increments* $\Delta\omega_\theta^+ = 0.03$ *(solid lines) and* $\Delta\omega_\theta^- = -0.06$ *(dashed lines).*

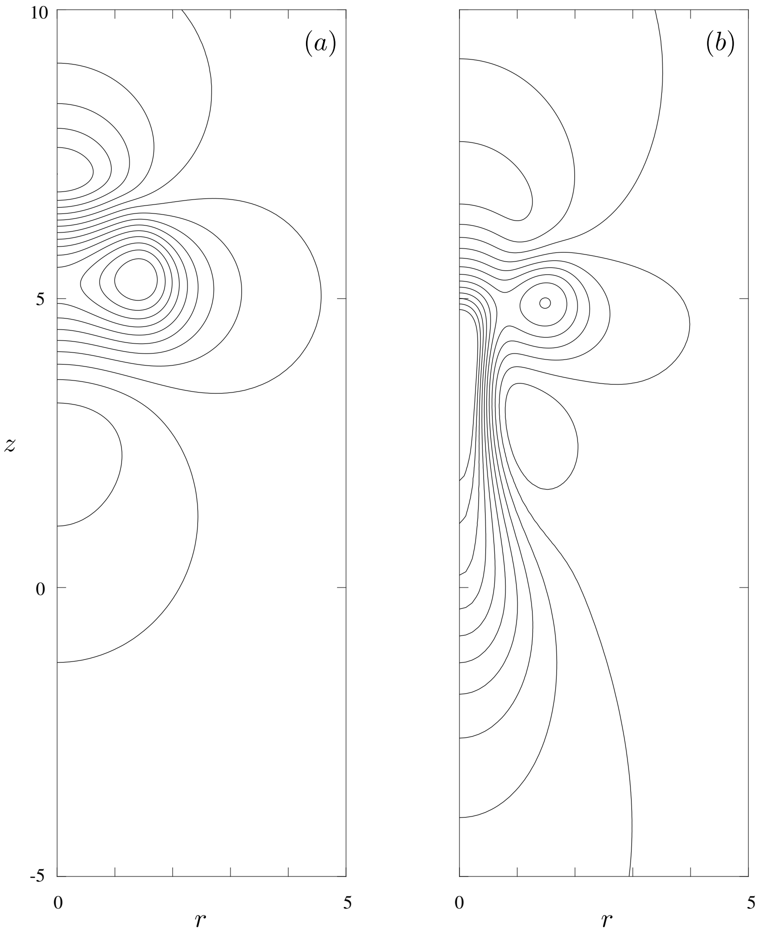

Figure 4.16: Contours of constant pressure at $t = 21$ *for flows with* $\mathrm{Re} = 200$ *and* $\mathrm{Ro} = \infty$ (a) *and* $\mathrm{Ro} = 10$ (b) *with* $\Delta p = 0.0056$.

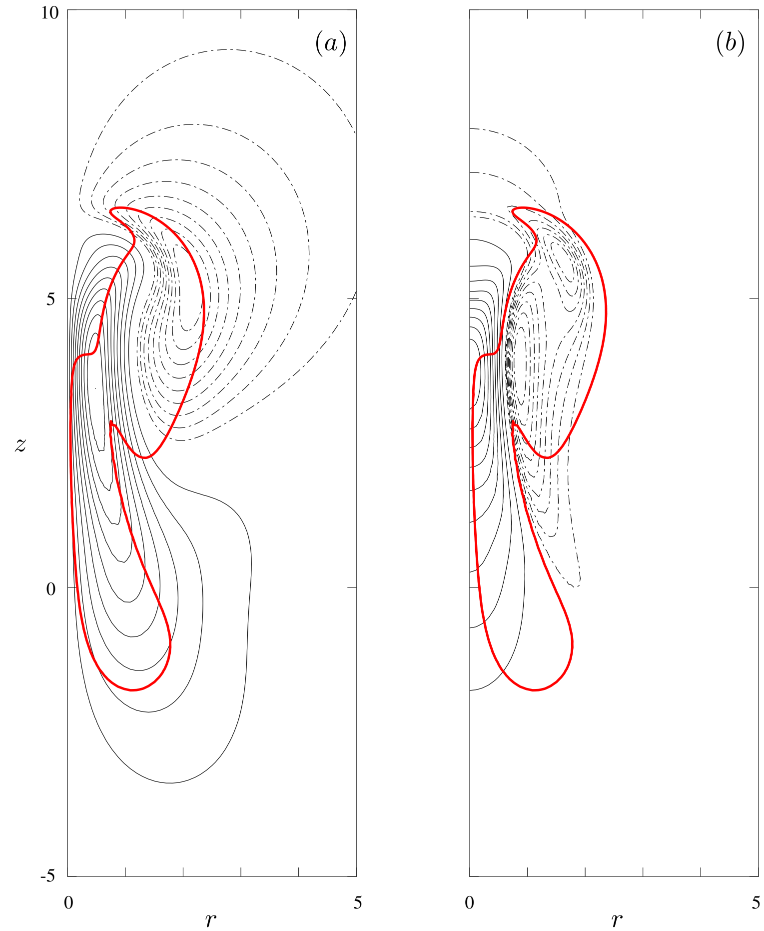

Figure 4.17: (a)*: Contours of constant azimuthal swirl at* $t = 21$ *for* $\mathrm{Ro} = 10$ *and* $\mathrm{Re} = 200$ *with* $\Delta u_\theta^- = -0.0076$ *and* $\Delta u_\theta^+ = 0.0188$. (b)*: Contours of constant axial vorticity at* $t = 21$ *for* $\mathrm{Ro} = 10$ *with* $\Delta \omega_z^- = -0.0257$ *and* $\Delta \omega_z^+ = 0.1196$.

4.4.2 Higher Reynolds number results

In the low Reynolds number regime viscous forces dominate the flow and the region of negative azimuthal vorticity seen in figure 4.15 remains ahead of the vortex ring until the vortex is destroyed by viscosity. However, Verzicco et al. (1996) found that when the Reynolds number is increased the phenomenon of vortex shedding may be observed (see figure 13 Verzicco et al. (1996)). Figures 4.18 and 4.19 show the azimuthal vorticity field in a flow with a Reynolds number of $\mathrm{Re} = 1000$ where viscous effects are less dominant and the region of negative azimuthal vorticity that forms ahead of the vortex ring is advected around the outside of the vortex ring and "elongated by the strain field of the primary ring" (Verzicco et al., 1996). This thin unstable layer of negative vorticity then rolls up to become an oppositely signed vortex ring and is shed behind the primary ring at $t \approx 56$. Verzicco et al. (1996) go on to explain that this secondary ring is subsequently subject to "flow dynamics similar to that described above with the role of positive and negative vorticity reversed; however, this structure is smaller and weaker than the primary ring and is thus rapidly diffused". In agreement with this figure 4.19 shows the shedded vortex ring is already almost completely diffused by $t = 70$.

Figure 4.20 provides a comparison of the pressure fields in the rotating and non-rotating cases. Figure 4.21 gives the azimuthal swirl and axial vorticity fields showing again the anticyclonic swirling head and strongly swirling axial vortex tail generated by the effects of rotation. Note how the contours of azimuthal velocity in figure 4.21(a) with contour spacing $\Delta u_\theta^+ = 0.0356$ are more tightly packed than in figure 4.17(a) with contour spacing $\Delta u_\theta^+ = 0.0188$. In this higher Reynolds number regime the swirling tail generated is much more intense. As a consequence of this intense swirling tail a region of low pressure to the rear of the ring on the axis is observed in tightly packed contours in figure 4.20(b).

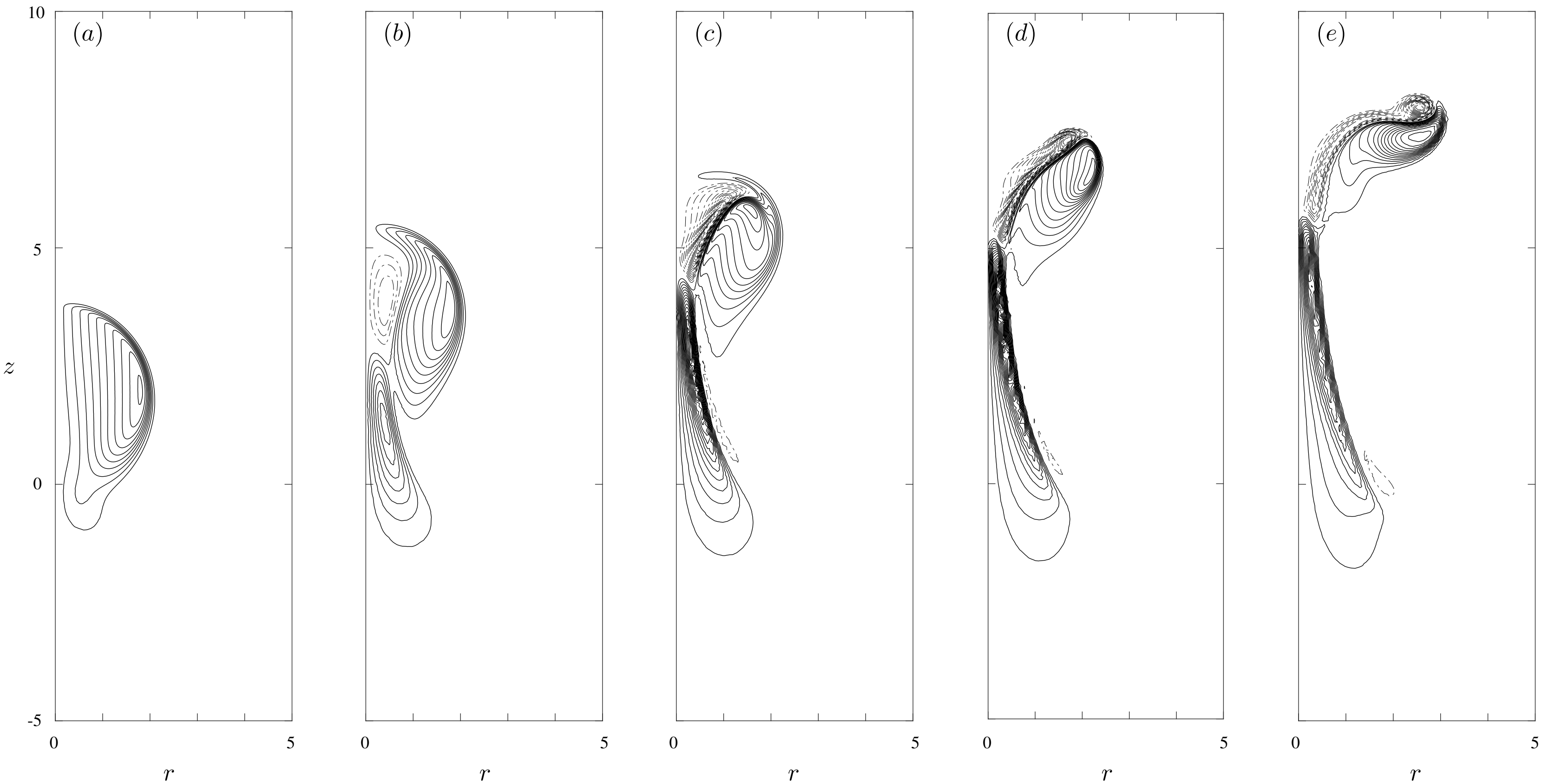

Figure 4.18: Contours of constant azimuthal vorticity at times $t = 7\,(a),\ t = 14\,(b),\ t = 21\,(c),\ t = 28\,(d)$ *and* $t = 35\,(e)$ *for a flow with Reynolds number* $\mathrm{Re} = 1000$ *and Rossby number* $\mathrm{Ro} = 10$*. Contour increments* $\Delta\omega_\theta^+ = 0.0856$ *(solid lines) and* $\Delta\omega_\theta^- = -0.104$ *(dashed lines).*

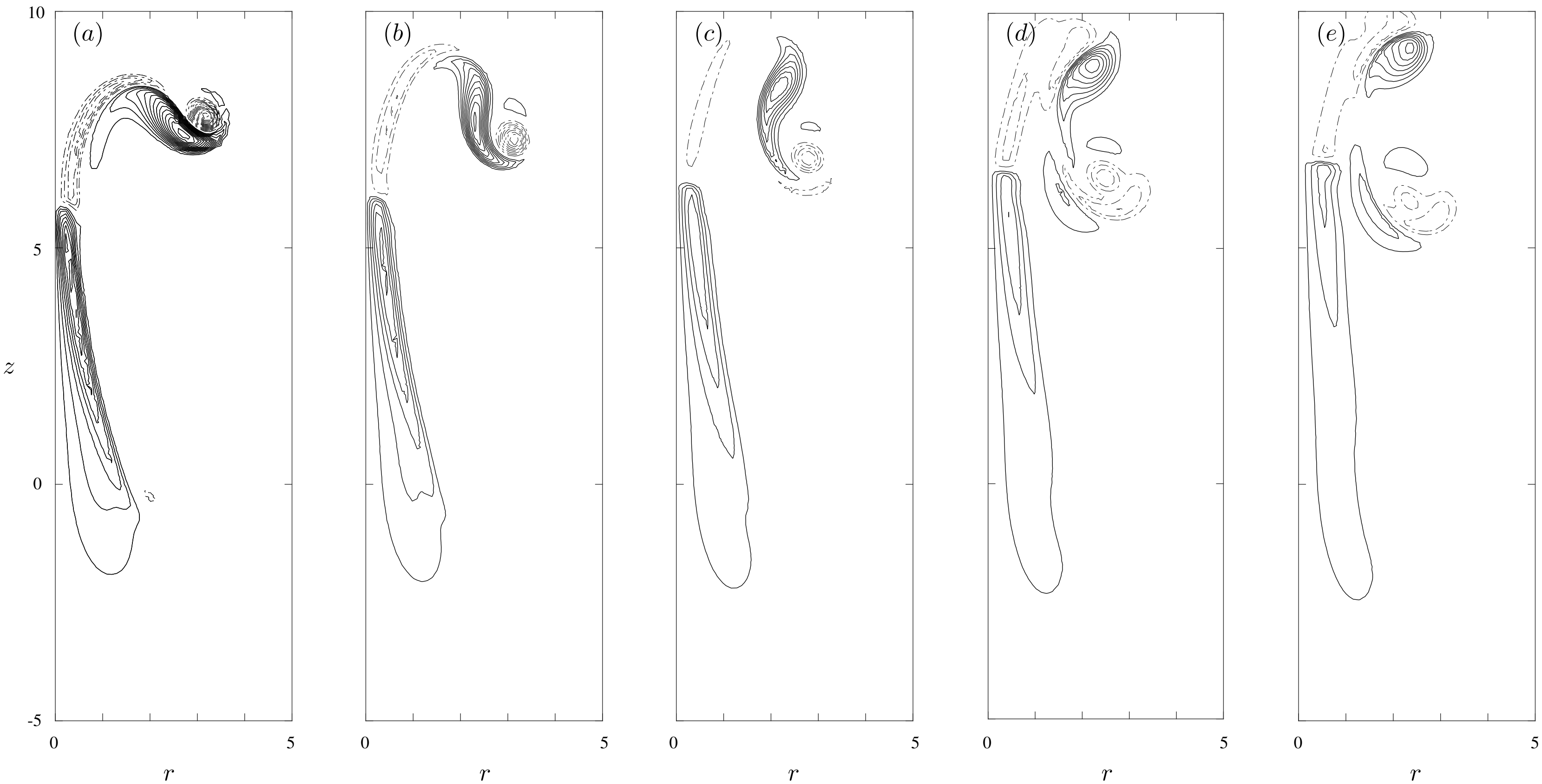

Figure 4.19: Contours of constant azimuthal vorticity at times $t = 42$ (a), $t = 49$ (b), $t = 56$ (c), $t = 63$ (d) *and* $t = 70$ (e) *for a flow with Reynolds number* $\mathrm{Re} = 1000$ *and Rossby number* $\mathrm{Ro} = 10$*. Contour increments* $\Delta\omega_\theta^+ = 0.0856$ *(solid lines) and* $\Delta\omega_\theta^- = -0.104$ *(dashed lines).*

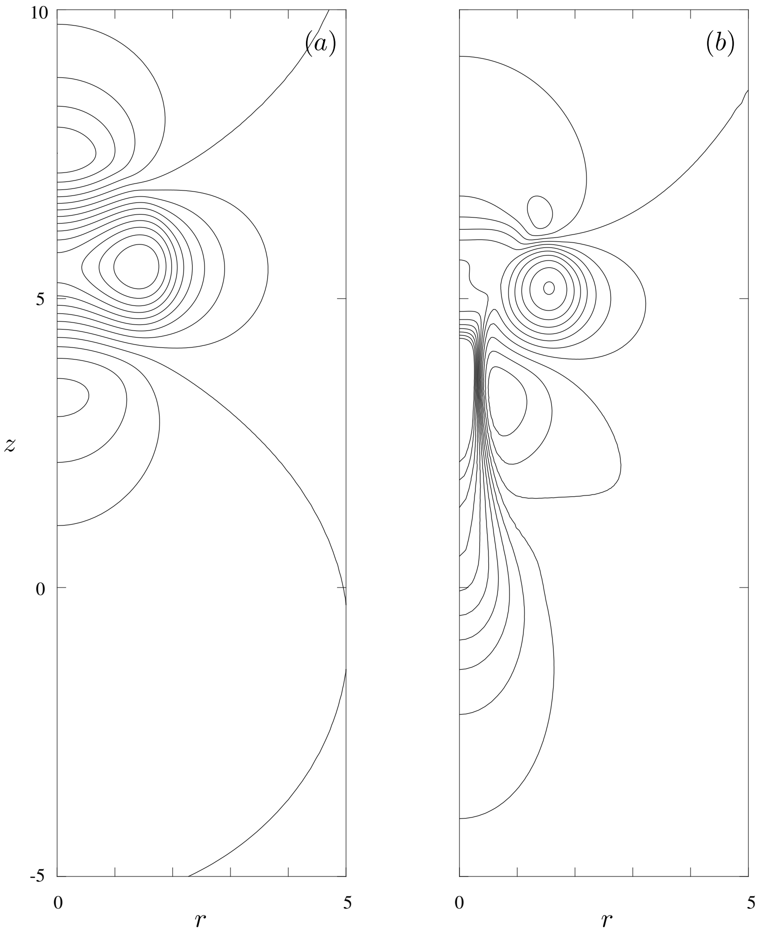

Figure 4.20: Contours of constant pressure at $t = 21$ *for flows with* $\mathrm{Re} = 1000$ *and* $\mathrm{Ro} = \infty$ (a) *and* $\mathrm{Ro} = 10$ (b) *with* $\Delta p = 0.0059$.

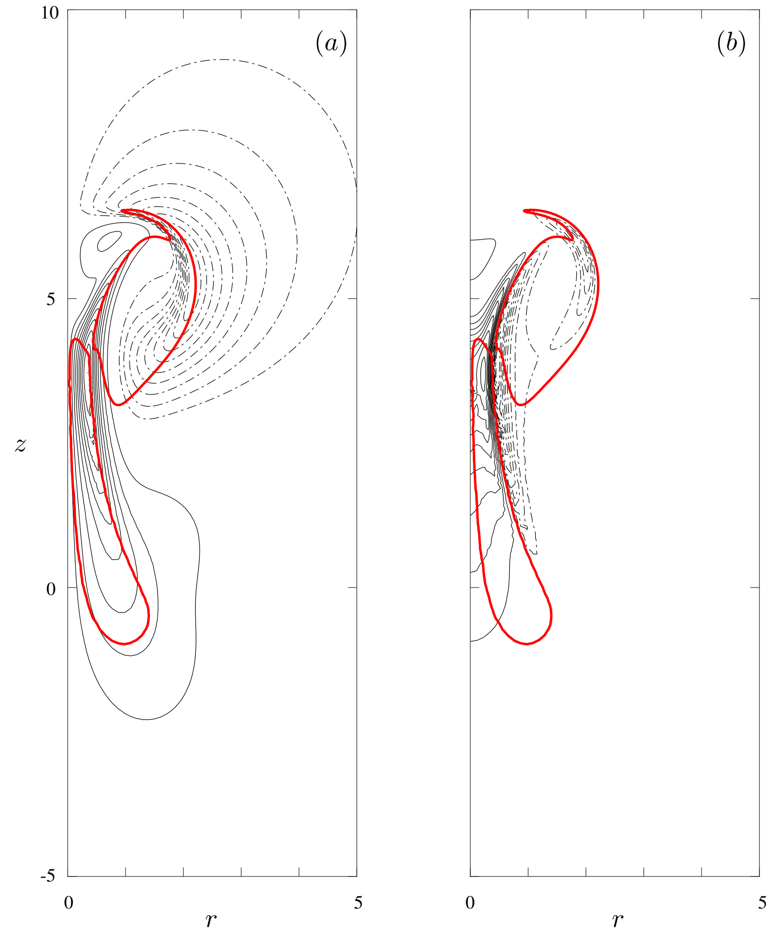

Figure 4.21: (a)*: Contours of constant azimuthal swirl at* $t = 21$ *for* $\mathrm{Ro} = 10$ *and* $\mathrm{Re} = 1000$ *with* $\Delta u_\theta^- = -0.0092$ *and* $\Delta u_\theta^+ = 0.0356$. (b)*: Contours of constant axial vorticity at* $t = 21$ *for* $\mathrm{Ro} = 10$ *with* $\Delta \omega_z^- = -0.1016$ *and* $\Delta \omega_z^+ = 0.2613$.

Figure 4.22 gives the trajectories and distance travelled in the axial direction by the vortex cores for flows at different rates of rotation. The solid black line represents non-rotating flow where the vortex core sees little deceleration in propagation velocity and follows a path approximately parallel to the axis of rotation. At a low rate of rotation $\mathrm{Ro} = 50$ the vortex ring sees a greater reduction in velocity indicated by a reduction in the gradient in figure 4.22(a) (dashed line). The vortex core centre also propagates with a slightly greater radius.

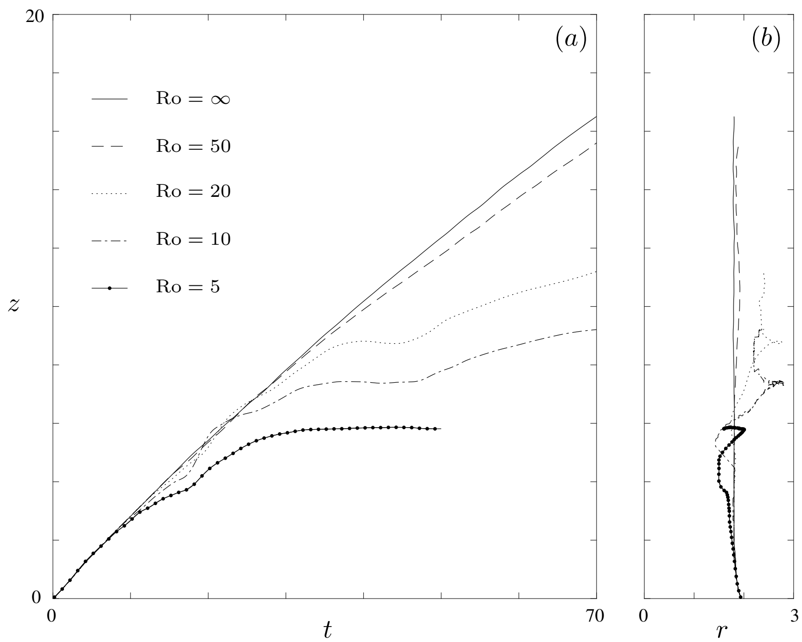

Figure 4.22: (a): The distance travelled in the axial direction by the vortex cores against time for flows with $\mathrm{Re} = 1000$ *and* $\mathrm{Ro} = 5, 10, 20, 50$ *and* ∞. (b)*: The trajectory of the vortex cores in the* r–z *plane.*

At rotation rates where vortex shedding is observed the trajectory of the vortex cores follows an irregular path in the r–z plane as the path of the vortex core is distorted by the shedding process. This is also reflected in the distance travelled in the axial direction. When a shedding event occurs the primary vortex core also stops propagating in the axial direction for a short time. At sufficiently high rotation rates the vortex ring eventually stops propagating altogether and this is seen in the trajectory of the vortex core at $\mathrm{Ro} = 5$ (line with circles).

This behaviour is also reflected in the propagation velocities in figure 4.23. At $\mathrm{Ro} = \infty$ and $\mathrm{Ro} = 50$ the propagation velocities decrease quite steadily. However, when Ro $\leq$ 20 the process of vortex shedding is seen in the irregular oscillations of the velocity field.

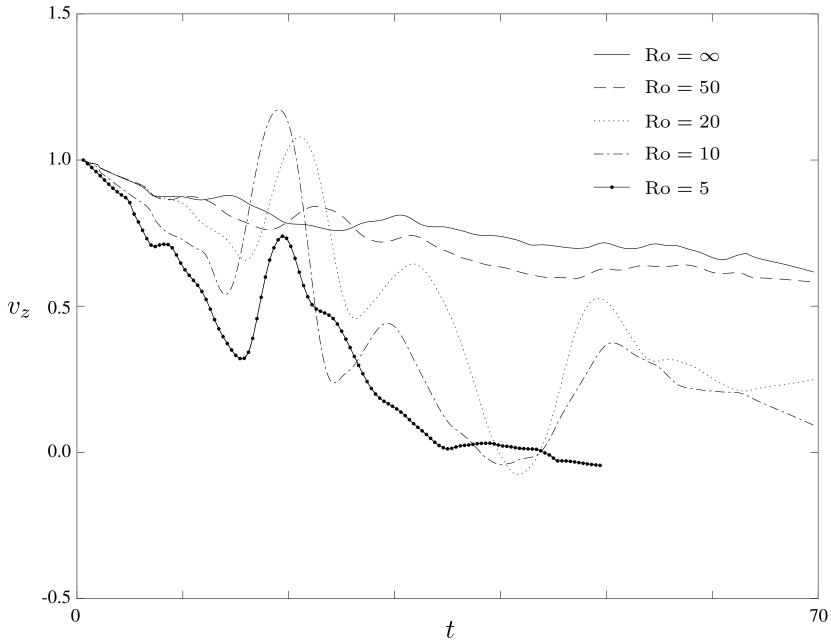

Figure 4.23: The normalised propagation velocity in the axial direction by the vortex cores against time for flows of different Rossby number.

Figure 4.24 gives the circulation of the vortex ring in fluids at different rates of rotation. Rotation causes a reduction in the circulation of a vortex ring with vortices in more rapidly rotating fluids seeing the greatest reduction in circulation. Rotation ultimately acts to accelerate the decay of a vortex ring (Brend and Thomas, 2009) and therefore as measure of the strength of a vortex ring we would anticipate the circulation to decrease until it reaches zero and the vortex ring is completely destroyed. For $\mathrm{Ro} = 10$ there is a sudden drop in circulation at $t \approx 20$. The drop coincides with a jump in the location of maximum vorticity in the vortex core towards the front of the vortex ring. Therefore the logging region (demonstrated in figure 4.7) experiences a jump in the positive z–direction and a portion of azimuthal vorticity towards the rear of the vortex ring which once fell in the logging region is now discounted. This highlights a disadvantage of the logging method. However, later on in the vortex motion the location of maximum vorticity migrates back to a more central location in the vortex core and provides a more accurate approximation of the circulation and so at later times this logging method can still be considered reliable.

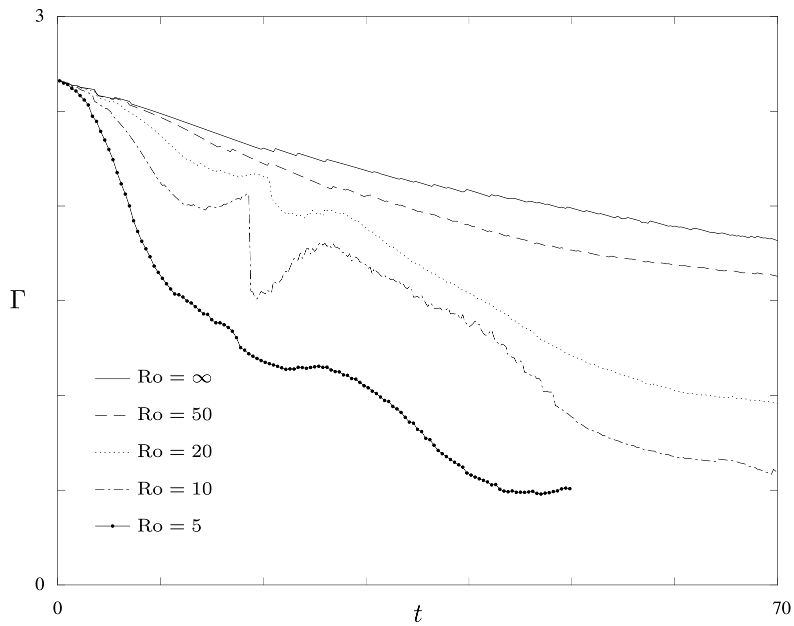

Figure 4.24: The value of the circulation, Γ, of the vortex ring against time, t, for flows with Reynolds number $\mathrm{Re} = 1000$ and Rossby numbers $\mathrm{Ro} = 5, 10, 20, 50, \infty$.

4.4.3 High rotation rate results

When the numerical experiments are repeated at high rotation rates $(\mathrm{Ro} \approx 1)$ inertial waves are observed in the fluid and considering the dominant balance of the terms in the equations of motion can provide insight into why the fluid behaves in this way. Before the results are presented inertial waves are introduced by considering the unsteady equations of motion where inertial and viscous terms are neglected.

Inertial waves

Section 2.2 of chapter 2 explained that the displacement of a fluid element in a rotating fluid causes expansion in the plane perpendicular to the rotation and is accompanied by Coriolis forces which work against this expansion. The restoring effect of the Coriolis force results in oscillations. These oscillations are known as inertial waves and take their name from the rotational inertia and the resistance of a fluid element to changes in its rotational velocity. The following theory from Greenspan (1968) demonstrates how rapidly rotating fluid can admit wave solutions.

In a rapidly rotating inviscid system with $\mathrm{Ro} \ll 1$ the terms $(\mathbf{u} \cdot \nabla)\mathbf{u}$ and $\frac{1}{\mathrm{Re}}\nabla^2\mathbf{u}$ in equation (4.6) are neglected and the governing equations become

$$\frac{\partial \mathbf{u}}{\partial t} + \frac{1}{\mathrm{Ro}}\hat{\mathbf{\Omega}} \times \mathbf{u} = -\nabla P, \tag{4.40a}$$

$$\nabla \cdot \mathbf{u} = 0. \tag{4.40b}$$

These equations have wave solutions of the form

$$\mathbf{u} = \Re(\mathbf{u}_1 e^{i(\boldsymbol{\kappa}\cdot\mathbf{x} - \lambda t)}), \tag{4.41a}$$

$$P = \Re(P_1 e^{i(\boldsymbol{\kappa}\cdot\mathbf{x} - \lambda t)}), \tag{4.41b}$$

where $\boldsymbol{\kappa}$ is the wave vector with wave number $|\boldsymbol{\kappa}|$, λ is the wave frequency, $\mathbf{x}$ is the position vector and $\mathbf{u}_1$ and P_1 are constant.

The incompressibility condition (4.40b) together with (4.41a) implies that

$$\mathbf{u}_1 \cdot \boldsymbol{\kappa} = 0 \tag{4.42}$$

so that the velocity vector and propagation directions are perpendicular and the waves must be transverse.

Substitution of (4.41) into the momentum equation leads to the condition

$$\lambda = \pm\frac{1}{\mathrm{Ro}}\hat{\mathbf{\Omega}} \cdot \hat{\boldsymbol{\kappa}} = \pm\frac{1}{\mathrm{Ro}}\cos\Theta, \tag{4.43}$$

where

$$\hat{\boldsymbol{\kappa}} = \frac{\boldsymbol{\kappa}}{|\boldsymbol{\kappa}|}, \tag{4.44}$$

and Θ is the polar angle measured from the rotation axis. The frequency of the wave motion is dependent on the direction but not magnitude of the wave vector. It may take any value less than $1/\mathrm{Ro}$. The phase velocity $\mathbf{c}_p$ of waves moving in the direction $\boldsymbol{\kappa}$ is

$$\mathbf{c}_p = \frac{1}{\mathrm{Ro}}\frac{\hat{\mathbf{\Omega}} \cdot \hat{\boldsymbol{\kappa}}}{|\boldsymbol{\kappa}|}\hat{\boldsymbol{\kappa}}. \tag{4.45}$$

Note that the phase velocity is inversely proportional to the magnitude of $\boldsymbol{\kappa}$ meaning that waves are dispersive with longer waves travelling faster than shorter waves.

The group velocity $\mathbf{c}_g$ is the velocity of energy propagation and is given by

$$\mathbf{c}_g = \frac{\hat{\boldsymbol{\Omega}}}{\mathrm{Ro}|\boldsymbol{\kappa}|} - \mathbf{c}_p. \tag{4.46}$$

The group velocity and phase velocity are perpendicular with

$$\mathbf{c}_g \cdot \mathbf{c}_p = 0 \tag{4.47}$$

so that energy transport is at right angles to the phase velocity. A wave appearing to move in one direction is actually propagating energy in a direction perpendicular.

Figure 4.25 illustrates the orientation of the wave vector $\boldsymbol{\kappa}$, group velocity $\mathbf{c}_g$ and phase velocity $\mathbf{c}_p$ of inertial waves in a rotating fluid. Figure 4.25(a) shows these inertial waves on a plane θ = const. whilst figure 4.25(b) shows how in three-dimensions these inertial waves lie on a double cone.

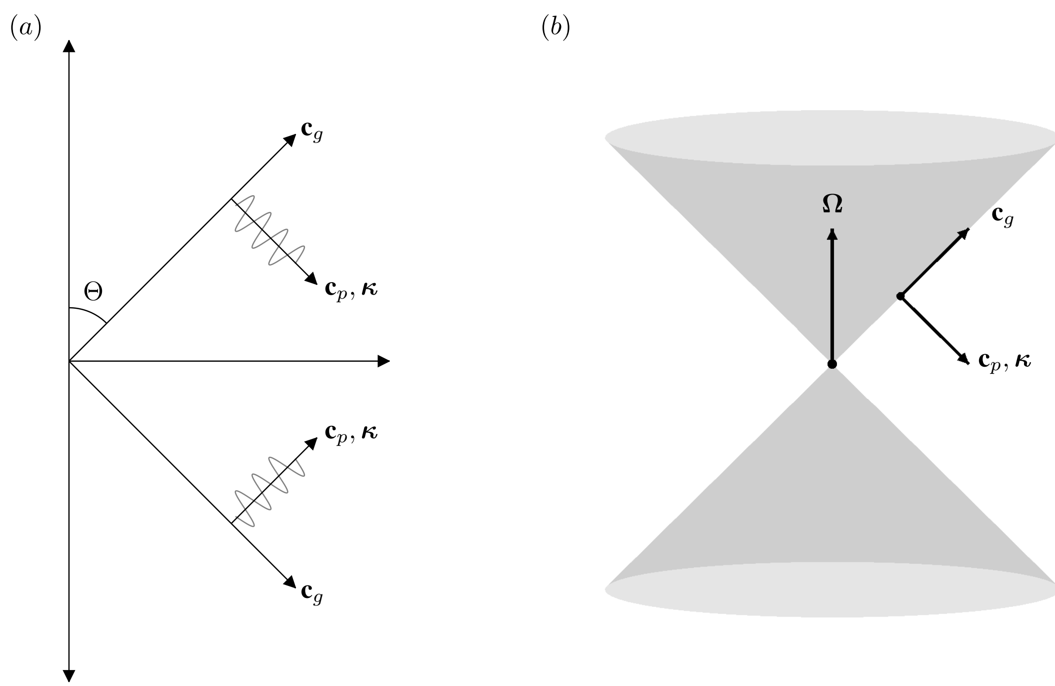

Figure 4.25: Schematic of inertial waves on a plane propagating from a source (a). In three dimensions these inertial waves form a double cone shape (b). The group and phase velocities are given by $\mathbf{c}_g$ and $\mathbf{c}_p$. The wave vector is given by $\boldsymbol{\kappa}$ and the rotation of the fluid is given by $\boldsymbol{\Omega}$. The polar angle measured from the axis of rotation is denoted by Θ.

Figures 4.26 and 4.27 give the resulting streamlines and azimuthal vorticity field of Hill's spherical vortex in a flow with $\mathrm{Re} = 1000$ and $\mathrm{Ro} = 1$. Very quickly the vortex ring collapses emitting inertial waves which are observed in the azimuthal swirl in figure 4.28. These are labelled A, B and C on figure 4.28(e). The flow fields look similar to the results of Verzicco et al. (1996) who observed "oblique shear layers of large axial extent".

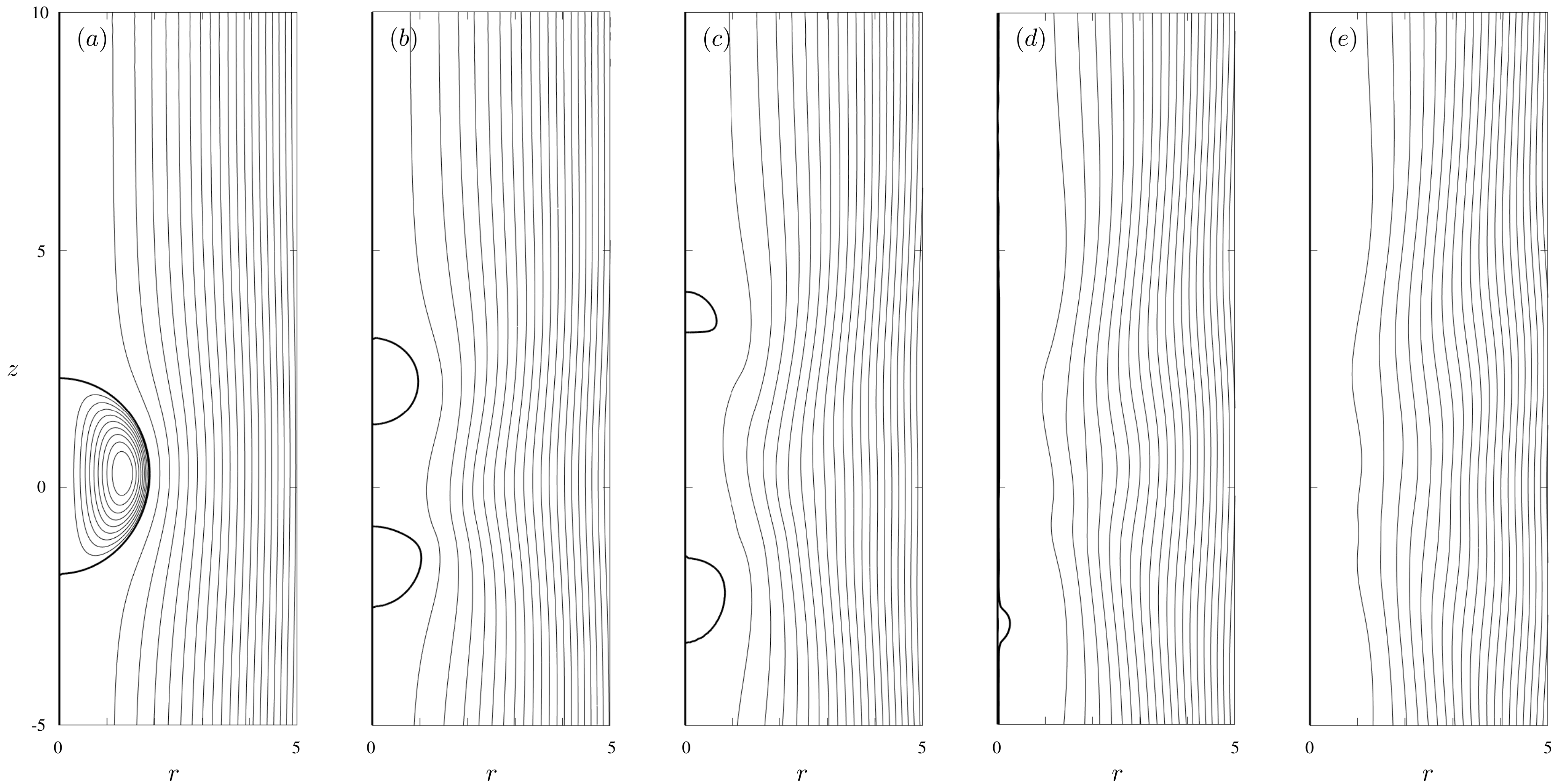

Figure 4.26: Contours of constant stream function at times $t = 1\ (a),\ t = 3\ (b),\ t = 5\ (c),\ t = 7\ (d),\ t = 9\ (e)$ *for a flow with Reynolds number* $\mathrm{Re} = 1000$ *and Rossby number* $\mathrm{Ro} = 1$.

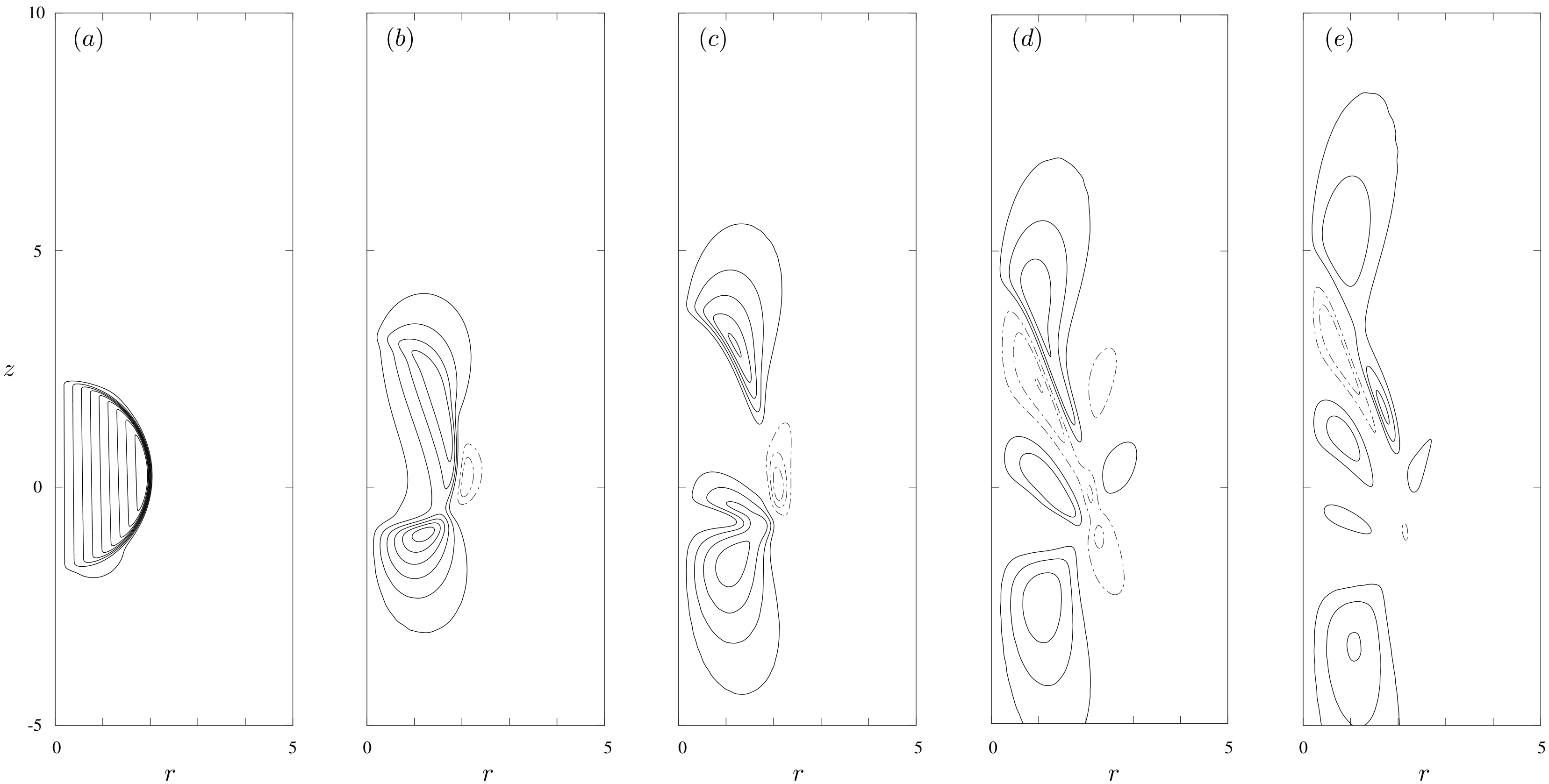

Figure 4.27: Contours of constant azimuthal vorticity at times $t = 1\,(a),\ t = 3\,(b),\ t = 5\,(c),\ t = 7\,(d),\ t = 9\,(e)$ *for a flow with Reynolds number* $\mathrm{Re} = 1000$ *and Rossby number* $\mathrm{Ro} = 1$. *Contour spacing* $\omega_\theta^+ = 0.0856$ *and* $\omega_\theta^- = -0.104$.

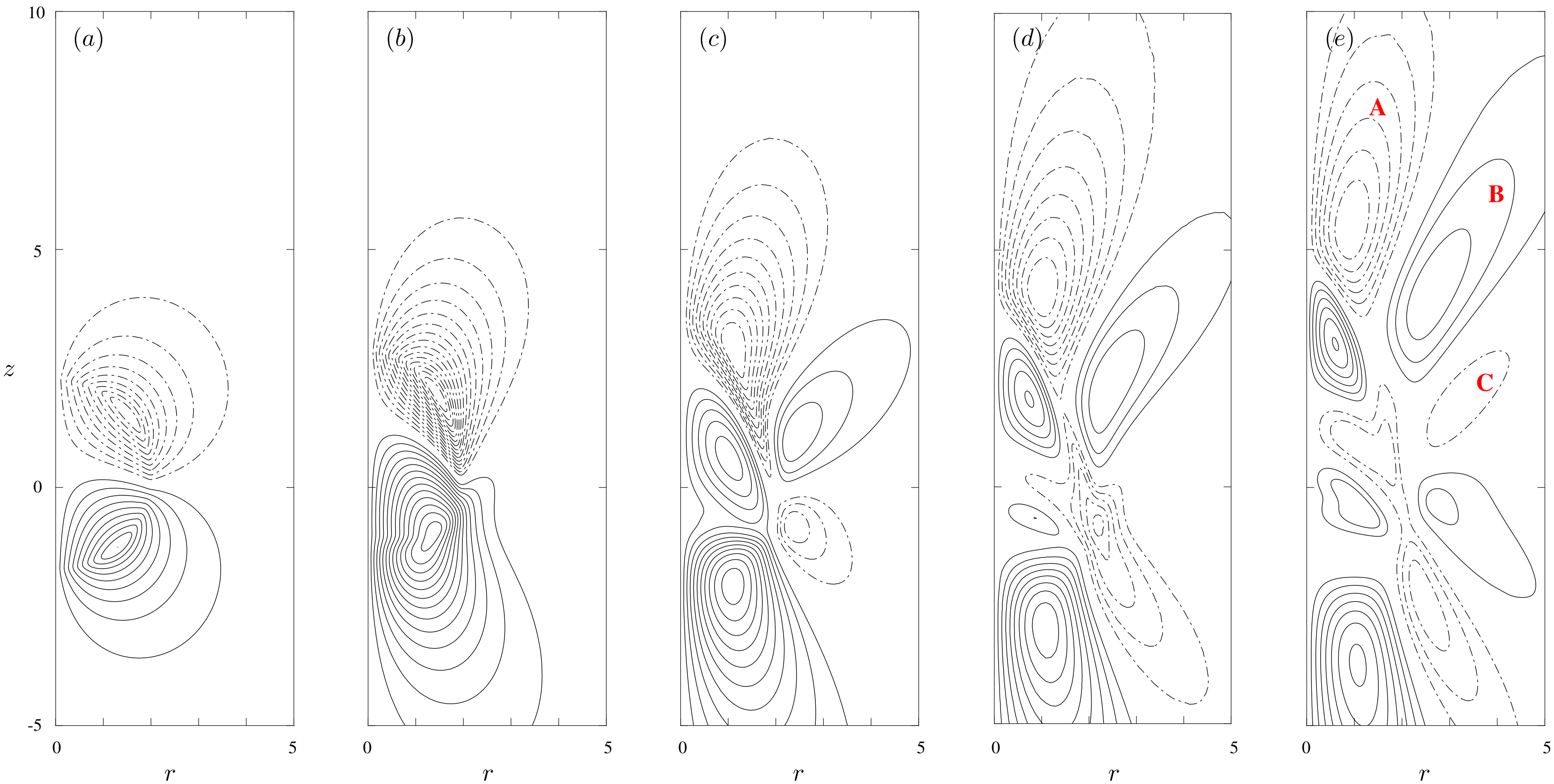

Figure 4.28: Contours of constant azimuthal swirl at times $t = 1\ (a),\ t = 3\ (b),\ t = 5\ (c),\ t = 7\ (d),\ t = 9\ (e)$ *for a flow with Reynolds number* $\mathrm{Re} = 1000$ *and Rossby number* $\mathrm{Ro} = 1$. *Contour spacing* $u_\theta^+ = 0.0188$ *(solid lines) and* $u_\theta^- = -0.0167$ *(dashed lines).*

4.5 Moffatt vortices

It the preceding section conservation of angular momentum arguments showed that an azimuthal swirl may be generated in a rotating fluid even if the flow began swirl-free (see figure 4.27). This is the case in section 4.4.1 where Hill's spherical vortex - which is initially swirl-free - is able to generate an azimuthal swirl. As seen by inspection of equation (4.38) axial gradients of azimuthal swirl act as a source of azimuthal vorticity in a rotating fluid due to the Coriolis effect. However, the azimuthal swirl also acts as a source of azimuthal vorticity through the vortex tilting term $(\boldsymbol{\omega} \cdot \nabla \mathbf{u})_\theta$.

Through force-balance arguments Moore et al. (1972) and Widnall et al. (1971) found that adding azimuthal swirl to thin-cored vortex rings will cause them to slow down. Virk et al. (1994) conducted a numerical study into the behaviour of polarised vortex rings of circular cross-section. Polarised vortex rings - which are defined by helical rather than circular vortex lines - are a subclass of vortex rings with swirl. The polarised vortex rings develop a head-tail structure where the head is a vortex ring with a region of negative azimuthal vorticity ahead of it whilst the tail is an axial vortex. They show that the coupling between the meridional flow ω_θ/r and swirl leads to the generation and destruction of the meridional flow due to the twisting of vortex lines. They also show that the propagation velocity of vortex rings decreases monotonically with increasing swirl. Furthermore, using vortex-dynamics-based explanations they also found this - contrary to Shariff and Leonard (1992) - to be true even of thick vortex rings with weak swirl (specifically Moffatt's swirling vortex). The authors note this is also found in Hicks (1899).

Ooi et al. (2001) carried out a numerical investigation into swirling vortex rings which simulated vortex generation through an orifice using a piston. They too found that azimuthal vorticity of opposite sign is generated ahead of the vortex ring near the axis of symmetry due to the tilting of the filaments of the axial vortex. This was then "convected away from the axis of symmetry by the primary vortex ring". They found the presence of this azimuthal vorticity reduces the propagation velocity of the vortex and that greater intensity swirl reduces the propagation velocity more dramatically. The results of Virk et al. (1994) and Ooi et al. (2001) are echoed by Balakrishnan (2013) who simulated two types of swirling vortex rings. Swirling vortex rings initialised with Gaussian distribution of vorticity and those initialised with a steady-state Euler solution (swirling toroidal vortex rings given in Eydeland and Turkington (1988) and Lifschitz et al. (1996)) are both shown to develop an intense axial vortex as well as a region of negative azimuthal vorticity ahead of the vortex ring.

Cheng et al. (2010) also investigated swirling vortex rings with Gaussian distributions of vorticity. Like Ooi et al. (2001) they were able to observe the oppositely signed vorticity generated upstream of the vortex ring "peeling off" along the leading edge shear layer into a secondary vortex ring. This is the same phenomenon of vortex shedding observed in section 4.4.2. Gargan-Shingles et al. (2015) investigated the development of this instability on the leading edge shear layer. They found the shear layer to be unstable to the Kelvin-Helmholtz instability which results in the roll up of the oppositely signed secondary vortex rings for shear layers of sufficient strength.

Figure 4.29 shows the evolution of the azimuthal vorticity field of a swirling Moffatt vortex with $\alpha = \pi/2, \lambda = 0.7277$ in a non-rotating fluid. The transfer of azimuthal velocity from the core to the axis generates a strong axial vortex behind the vortex ring. Balakrishnan (2013) explains that viscous diffusion causes azimuthal swirl to be diffused across the entrainment bubble (vortex atmosphere) and transported to the rear stagnation point. Some of this fluid with azimuthal swirl re-enters the entrainment bubble whilst some is lost to the wake. Balakrishnan (2013) continues: " The angular momentum of a fluid particle (ru_θ) is approximately conserved in a high Re axisymmetric flow. Therefore as the fluid particles move nearer to the axis of the vortex ring, their azimuthal swirl increases as $1/r$. But at $r = 0$ the azimuthal swirl must become zero. This is enforced by viscous diffusion generating an axial vortex. The axial velocity gradient $\partial u_z/\partial z$ is positive in the vicinity of the rear stagnation point and hence stretches the axial vortex in this region."

Negative azimuthal vorticty is generated ahead of the vortex ring and elongates into a thin shear layer wrapped around the primary vortex core. In section 4.4.1 it was briefly mentioned that azimuthal vorticity is generated from the vortex tilting term $(\boldsymbol{\omega} \cdot \nabla \mathbf{u})_\theta$. This can be seen by taking the azimuthal component of

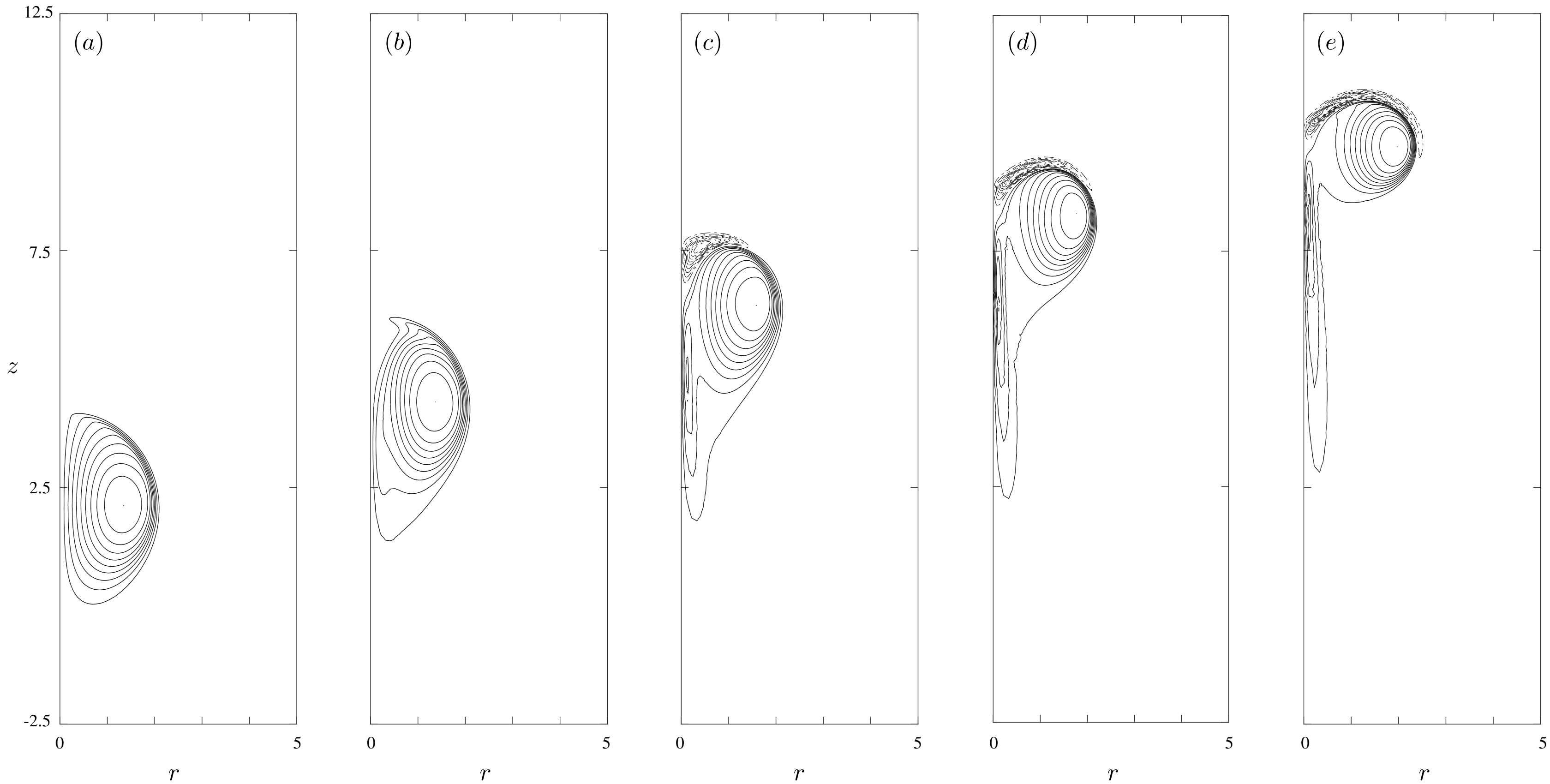

Figure 4.29: Contours of constant azimuthal vorticity at times $t = 8$ (a), $t = 16$ (b), $t = 24$ (c), $t = 32$ (d) *and* $t = 40$ (e) *for a flow with Reynolds number* $\mathrm{Re} = 1000$ *and Rossby number* $\mathrm{Ro} = \infty$*. Contour increments* $\Delta\omega_\theta^+ = 0.0935$ *(solid lines) and* $\Delta\omega_\theta^- = -0.0757$ *(dashed lines).*

the vorticity equation

$$\frac{\partial \omega_\theta}{\partial t} + u_r \frac{\partial \omega_\theta}{\partial r} + u_z \frac{\partial \omega_\theta}{\partial z} + \frac{u_\theta \omega_r}{r} = \omega_r \frac{\partial u_\theta}{\partial r} + \omega_z \frac{\partial u_\theta}{\partial z} + \frac{\omega_\theta u_r}{r} + \frac{1}{\mathrm{Re}} \left(\nabla^2 \boldsymbol{\omega}\right)_\theta + \frac{1}{\mathrm{Ro}} \frac{\partial u_\theta}{\partial z} \qquad (4.48)$$

where the first two terms on the right hand side of the equation that represent the vortex tilting terms which generate this negative and positive azimuthal vorticity at the front and rear of the vortex ring. Along the axis of propagation we have $\omega_z > 0$ (seen in figure 4.30(a)) whilst ahead of the vortex ring $\partial u_\theta / \partial z < 0$ (figure 4.30(b)). Due to the vortex tilting term $\omega_z \dfrac{\partial u_\theta}{\partial z}$ this induces negative azimuthal vorticity at the front vortex ring. A similar argument can be made for the positive tail of azimuthal vorticity to the rear.

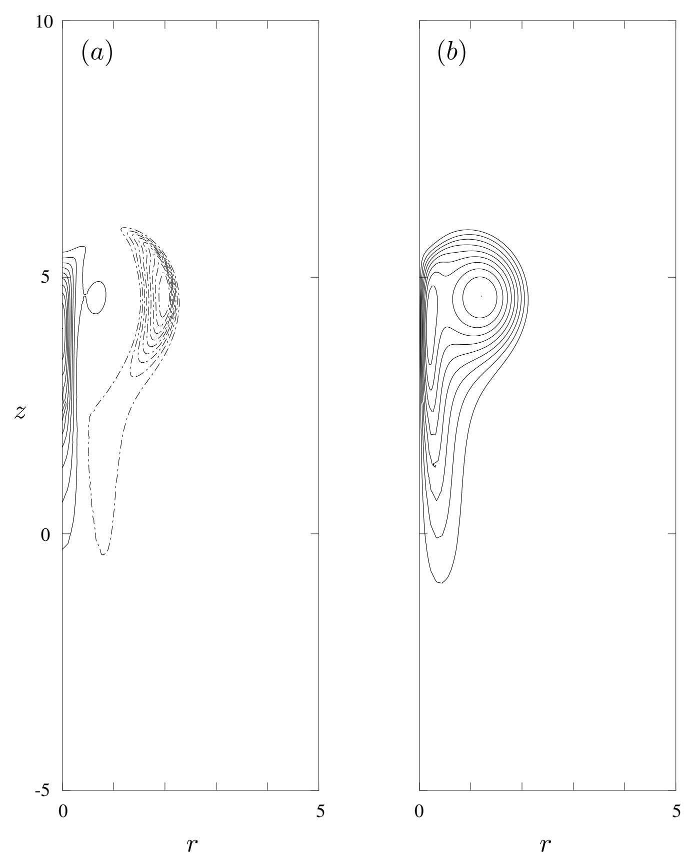

Figure 4.30: (a): Contours of constant axial vorticity at time $t = 24$ for $\alpha = \pi/2$ and $\mathrm{Re} = 1000$. Contour increments $\Delta\omega_z^+ = 0.2464$ (solid lines) and $\Delta\omega_z^- = -0.3204$ (dashed lines). (b): Contours of azimuthal swirl with increments $\Delta u_\theta = 0.0239$.

Virk et al. (1994) showed that for Moffatt vortices of the same circulation if the degree of swirl α is increased the propagation velocity W must decrease. Therefore when comparing vortices with different degrees of swirl one may only keep circulation or free-stream velocity constant in each case. In the following work the initial circulation of each Moffatt vortex is kept constant at $\Gamma = 8/3$.

Figure 4.31 compares the azimuthal vorticity field at $t = 32$ in a non-rotating fluid for Moffatt vortices with different degrees of swirl from $\alpha = 0$ (left - Hill's spherical vortex) to $\alpha = \pi/2$ (right). At $\alpha = \pi/16$ the swirl has little impact on the propagation of the vortex ring. However for $\alpha = \pi/2$ a relatively intense region of azimuthal vorticity is found ahead of the vortex ring.

It has been demonstrated that swirling vortex rings in non-rotating fluids decelerate due to oppositely signed vorticity generated ahead of the vortex ring by their azimuthal swirl. We have also seen vortex rings in rotating fluids that are initially swirl-free generate an azimuthal swirl which in causes them to decelerate through the same phenomenon. Therefore it can be reasonably expected that an initially swirling vortex ring in a rotating fluid would see generation of azimuthal vorticity at a quicker rate than a non-swirling vortex ring. This would lead to faster vortex shedding and ultimately quicker destruction of the vortex ring. Furthermore, we would expect these effects to be exacerbated for a more strongly swirling vortex with greater parameter value α.

Figure 4.32(b)–(c) shows the azimuthal vorticity fields at $t = 24$ for Hill's spherical vortex and Moffatt's swirling vortex with $\alpha = \pi/2$ in flows with $\mathrm{Ro} = 10$. Whilst Hill's spherical vortex has seen a region of negative azimuthal vorticity generated ahead of itself Moffatt's swirling vortex is already undergoing vortex shedding with a clear negatively signed vortical structure rolled up on its outer edge. Following the arguments presented in section 4.4.1 considering axial gradients of azimuthal swirl a Moffatt vortex with $\alpha = \pi/2$ (positive cyclonic swirl) will undergo vortex shedding faster than an initially non-swirling vortex ring. However, the direction of the swirl is important and figure 4.32(a) has been included to demonstrate the behaviour if α is chosen to be negative. The axial gradients of azimuthal swirl in the initial flow field are reversed and at early times this inhibits the generation of the patch of negatively signed azimuthal vorticity at the head of the vortex ring. Figure 4.32 shows Moffatt's vortex with $\alpha = -\pi/2$ as the least distorted in a rotating fluid.

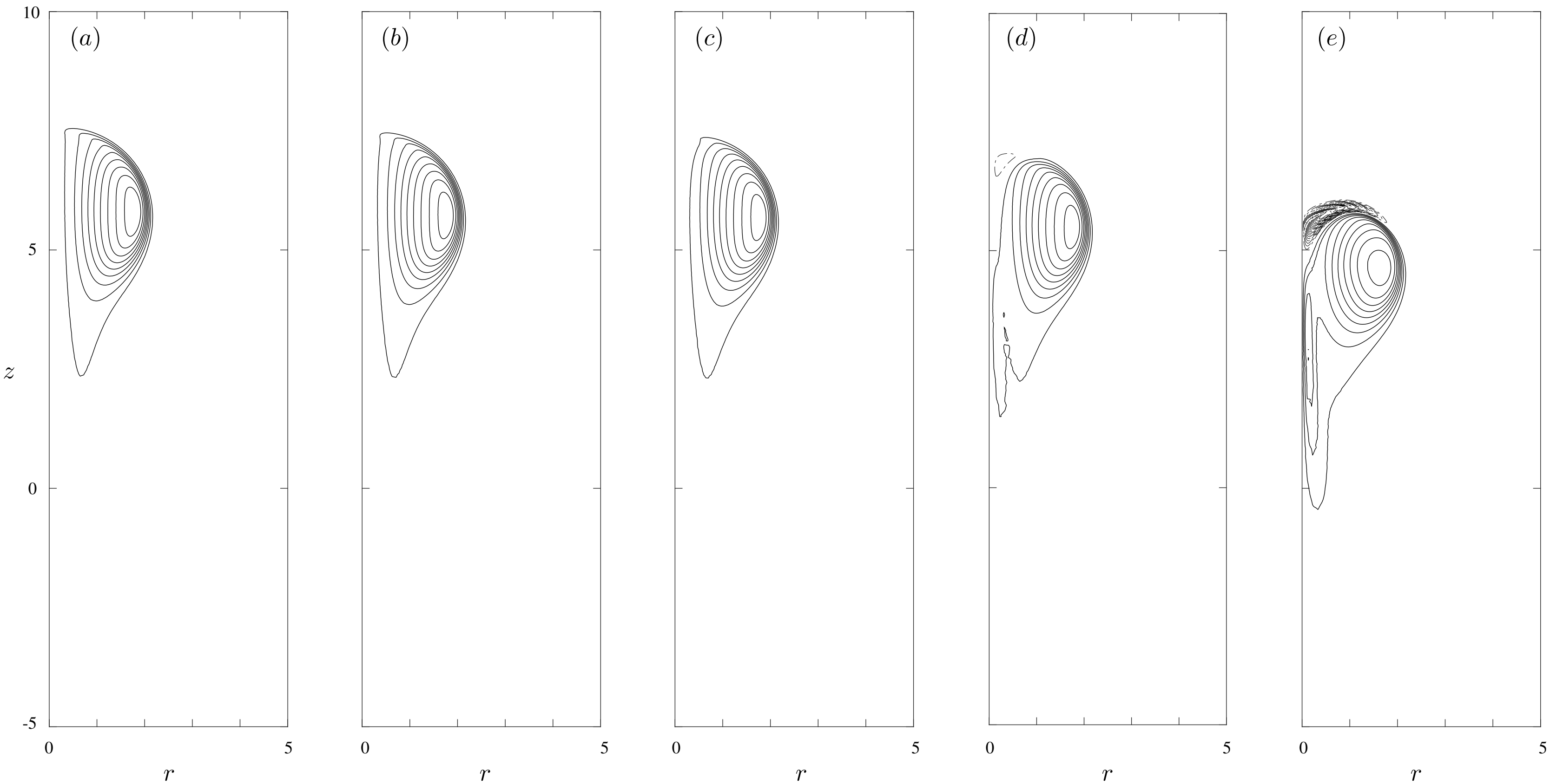

Figure 4.31: Contours of constant azimuthal vorticity at time $t = 32$ *for* $\alpha = 0\,(a)$, $\alpha = \pi/16\,(b)$, $\alpha = \pi/8\,(c)$, $\alpha = \pi/4\,(d)$ *and* $\alpha = \pi/2\,(e)$ *for a flow with Reynolds number* $\mathrm{Re} = 1000$ *and Rossby number* $\mathrm{Ro} = \infty$. *Contour increments* $\Delta\omega_\theta^+ = 0.1310$ *(solid lines) and* $\Delta\omega_\theta^- = -0.0606$ *(dashed lines).*

This section has highlighted the similarities between the behaviour exhibited by by swirling vortex rings in non-rotating fluids and initially swirl-free vortex rings in rotating fluid. In both cases the behaviour is driven by axial gradients of azimuthal swirl.

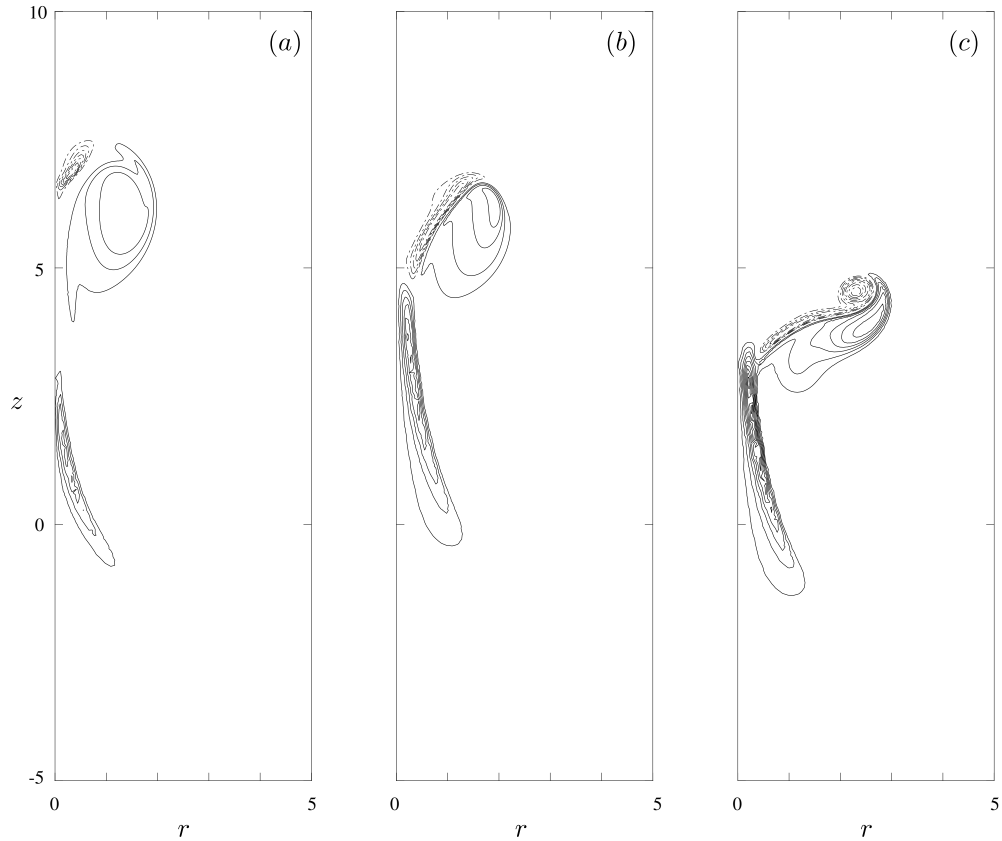

Figure 4.32: Contours of constant azimuthal vorticity at time $t = 24$ for $\alpha = -\pi/2$ (a), $\alpha = 0$ (b) and $\alpha = \pi/2$ (c) for a flow with Reynolds number $\mathrm{Re} = 1000$ and Rossby number $\mathrm{Ro} = 10$. Contour increments $\Delta\omega_\theta^+ = 0.2464$ (solid lines) and $\Delta\omega_\theta^- = -0.3204$ (dashed lines).

4.6 Summary

This chapter has investigated how axial rotation affects vortices by using spherical vortices as initial flow fields in a finite element solver for the rotating Navier-Stokes equations. The numerical procedure used throughout this thesis has been described and then validated against the results of Verzicco et al. (1996) for use in following chapters.

The inviscid stability analyses of Moffatt and Moore (1978) and Pozrikidis (1986) of spherical vortex rings were tested to see how closely their results apply for the decay of Hill's vortex in a viscous fluid. It is now understood that in a viscous fluid Hill's vortex detrains a wide tail of weakly rotational fluid from its rear in a similar way to the prolate stability analysis of Pozrikidis (1986).

Section 4.4 verified some known results about vortex rings in rotating fluids. Firstly, rotation causes vortices to develop anticyclonic swirling heads and cyclonic swirling tails. This in turn induces a region of negative azimuthal vorticity ahead of the ring and a region of low pressure behind the vortex ring. Together this results in a reduction in the propagation velocity of the vortex ring. At low Reynolds numbers the vortex ring and the negatively signed structure ahead of it diffuse into one another until both have completely decayed. However, at higher Reynolds numbers and sufficiently low Rossby numbers the oppositely signed structure is elongated into a thin layer which then rolls up into an oppositely signed vortex ring and is shed off the back of the primary ring. At very high rotation rates the vortex ring collapses and inertial waves are produced.

Section 4.5 highlighted the link between the behaviour exhibited by swirling vortex rings in non-rotating fluids and initially swirl-free vortex rings in rotating fluids. The negative region of secondary azimuthal vorticity found ahead of the vortex ring in both cases is the result of an azimuthal swirl. In a swirling vortex this is already present. However, in a initially swirl-free vortex ring in a rotating fluid an azimuthal swirl is generated due to Coriolis effects.

This chapter has observed the stabilising effect of anticyclonic swirl in Moffatt's vortex with $\alpha = -\pi/2$. This provides motivation for the following chapter which will explore the how the vortex rings discovered in chapter 3 - which also possess anticyclonic swirl - behave in a viscous fluid and whether they too are more robust than their non-swirling counterparts.

Chapter 5

Rotating spherical vortices in viscous fluids

Past research (Verzicco et al., 1996; Brend and Thomas, 2009; Watchapon, 2015; Uchiyama et al., 2015) suggests that vortex rings in rotating fluids can be highly unstable. All agree that in a rotating fluid an oppositely signed region of azimuthal vorticity is generated ahead of the vortex ring which causes the deceleration of the vortex ring. At low Rossby number cancellation of vorticity occurs between this region of negative azimuthal vorticity and the vortex ring itself causing the premature destruction of the vortex ring. At lower Rossby numbers vortex rings can be considered to be highly unstable undergoing vortex shedding. At sufficiently low Rossby number vortex rings collapse emitting inertial waves.

The aforementioned works considered vortex rings which were either generated by the roll up of fluid at the edge of an orifice (Verzicco et al., 1996; Brend and Thomas, 2009) or were prescribed as a torus with Gaussian distribution of vorticity in the meridional plane of the vortex core (Watchapon, 2015; Uchiyama et al., 2015). In Verzicco et al. (1996) and Brend and Thomas (2009) the vortex rings were generated in the rotating flow. However, Watchapon (2015) and Uchiyama et al. (2015) were not concerned with how the vortex is produced only how it evolves after it is generated. This is the method employed in chapter 4 where we assume that somehow Hill's spherical vortex or a swirling Moffatt vortex is generated and we observe the subsequent flow. It is not unreasonable to make this assumption as Turner (1964) analyses an expanding Hill's spherical vortex noting that it very closely resembles a buoyant thermal. In addition, we recall that Naitoh et al. (2014) claim that often vortical structures in transitional and turbulent flows have a swirl component so consideration of swirling Moffatt vortices in this way is also reasonable. The questions then arise: given a rotating spherical vortex solution from chapter 3 has been generated, what will the developing flow look like and will it be more stable than its non-rotating counterpart?

In chapter 4 the original Hill's and Moffatt vortex solutions - referred to in this chapter by $(\tilde{\mathbf{u}}_O, P_O)$ - were used as the initial flow fields in rotating fluids. Relative to the ambient fluid these solutions had no initial swirling component. In this section the rotating solutions found in chapter 3 - referred to in this chapter by $(\tilde{\mathbf{u}}_R, P_R)$ - will also be used as the initial flow field. Relative to the ambient rotating fluid these solutions have non-zero swirling component with the vortex ring swirling in such a way to cancel out the background rotation of the flow. If viewed in a laboratory frame the vortex rings in these solutions are not themselves rotating. If these vortices persist as coherent structures for longer it may suggest that vortex motion in rotating fluid need not be as unstable as suggested by previous work.

Like in chapter 4, Dirichlet boundary conditions will be applied on the the upper (upstream) and right hand side of the domain (see figure 4.2). These Dirichlet conditions will enforce that the free stream of either solution ($(\tilde{\mathbf{u}}_O, P_O)$ or $(\tilde{\mathbf{u}}_R, P_R)$) remains unchanged. A natural outflow condition is again applied on the bottom (downstream) boundary.

The work in this chapter follows the same nondimensionalisation as chapter 3. In the equations of motion (2.12) position is nondimensionalised with ring radius a as $\mathbf{x} = a\tilde{\mathbf{x}}$, velocity with free-stream velocity U as $\mathbf{u} = U\tilde{\mathbf{u}}$ and pressure as $p = \rho U^2 \tilde{p}$. This nondimensionalisation defines a Reynolds number $\mathrm{Re} = aU/\nu$ and Rossby number $\mathrm{Ro} = U/2a\Omega$. All simulations in this chapter are conducted at Reynolds number $\mathrm{Re} = 1000$.

5.1 Hill's spherical vortex

For reference figure 5.1(a)–(c) gives the streamlines, azimuthal vorticity and azimuthal swirl at time $t = 10$ for a Hill's spherical vortex in a flow with $\mathrm{Ro} = \infty$. Figure 5.1(d)–(f) gives the streamlines, azimuthal vorticity and azimuthal swirl at time $t = 10$ for a Hill's spherical vortex $(\tilde{\mathbf{u}}_O, P_O)$ in a flow with $\mathrm{Ro} = 5$. Like the results seen in chapter 4 rotation has resulted in vortex shedding and will lead to the premature destruction of the vortex ring.

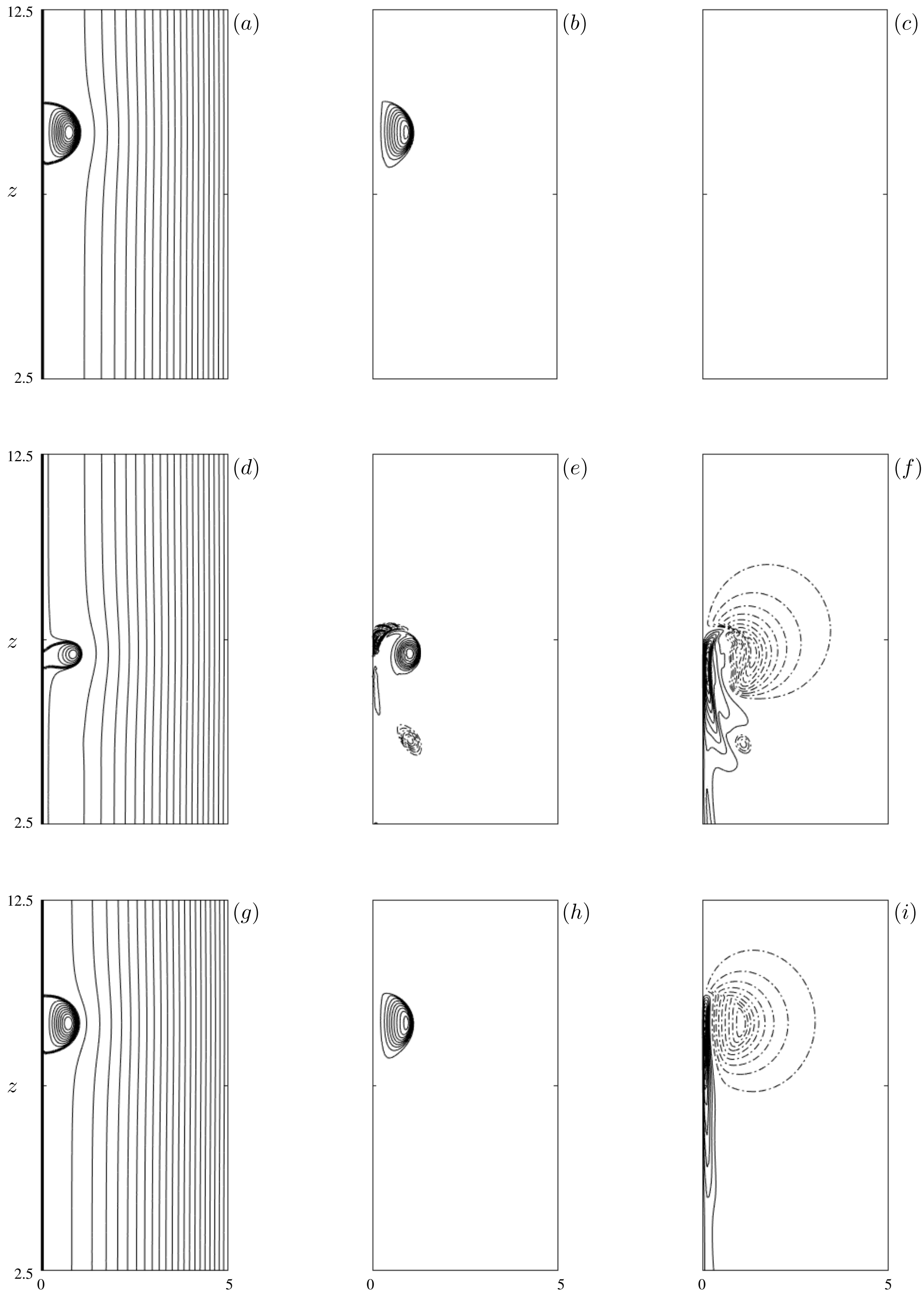

Figure 5.1: Streamlines (left), azimuthal vorticity (centre) and azimuthal swirl (right) at $t = 10$ *for Hill's vortex,* $\mathrm{Ro} = \infty$ (a)–(c), *Hill's vortex,* $\mathrm{Ro} = 5$ (d)–(f) *and the rotating Hill's vortex solution,* $\mathrm{Ro} = 5$ (g)–(i). *Contour spacing* $\Delta\psi^+ = 0.0159$, $\Delta\psi^- = -0.6263$, $\Delta\omega_\theta^+ = 0.6945$, $\Delta\omega_\theta^- = -0.2423$, $\Delta u_\theta^+ = 0.0252$, $\Delta u_\theta^- = -0.0100$.

Figure 5.2(a) gives the distance travelled by the non-rotating Hill's vortex in flows at different rates of rotation. As demonstrated in section 4.4 rotation causes a vortex ring to decelerate and travel a shorter distance - with higher rates of rotation seeing a greater deceleration and reduction in propagation distance. At sufficiently high rotation rates ($\mathrm{Ro} \lesssim 5$) vortex shedding occurs, affecting the trajectory of the vortex ring in the $r - z$ plane (figure 5.2(b)) and eventually may cause the vortex ring to cease propagating (seen at $t = 15$ for $\mathrm{Ro} = 2$, line with circles) .

Figure 5.1(g)–(i) gives the resulting flow at time $t = 10$ for the rotating Hill's vortex solution $(\tilde{\mathbf{u}}_R, P_R)$. The stream function field and azimuthal vorticity field are qualitatively similar to the Hill's solution in a non-rotating fluid. The vortex remains as a single ring with no vortex shedding even at a moderate Rossby number of $\mathrm{Ro} = 5$. There has been no production of a region of negative azimuthal vorticity ahead of the vortex ring which has prevented vortex shedding from occurring.

Figure 5.3(a) shows the distance travelled by the rotating Hill's vortex $(\tilde{\mathbf{u}}_R, P_R)$. Comparison with figure 5.2(a) highlights how the rotating vortex ring maintains a much higher propagation velocity - it shows much less deceleration at the same rate of rotation. Vortex shedding is no longer observed and the trajectory the vortex core centres now follow in the $r - z$ plane remain very similar to the non-rotating case even at a Rossby numbers as low as $\mathrm{Ro} = 2$. Furthermore, an examination of the circulation of the vortex rings in each case also demonstrates how the rotating solutions are more stable. Figure 5.4 shows the evolution of the circulation of the non-rotating Hill's vortex which see a large loss of circulation at lower Rossby numbers. However, in figure 5.5 it can be seen that even at a Rossby number of $\mathrm{Ro} = 2$ the rotating Hill's vortex has lost only a small proportion of the circulation compared to the $\mathrm{Ro} = \infty$ case.

Figure 5.6 provides a similar comparison at $t = 7$ for $\mathrm{Ro} = 1$. In figure 5.6(d)–(f) the Hill's vortex has began to collapse and emit inertial waves. However, in figure 5.6(g)–(i) the rotating Hill's vortex remains a coherent vortical structure with some azimuthal vorticity just beginning to form along its axis.

If the rotating Hill's solution $(\tilde{\mathbf{u}}_R, P_R)$ is used as the initial flow field but the original Hill's free-stream velocity $(\tilde{\mathbf{u}}_O, P_O)$ is imposed on the boundaries the results are indistinguishable. This implies that the greater robustness of the rotating solution is not dependent on the free-stream flow. This is a key finding.

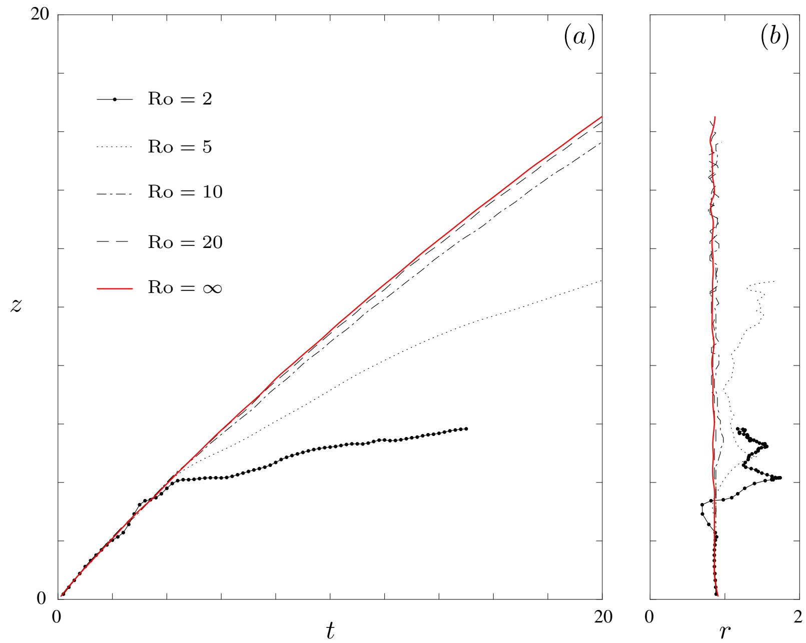

Figure 5.2: (a) The distance travelled in the axial direction by the vortex cores against time for flows of different Rossby number with initial velocity field $\tilde{\boldsymbol{u}} = \tilde{\boldsymbol{u}}_O$. (b) The trajectory of the vortex cores in the r–z plane.

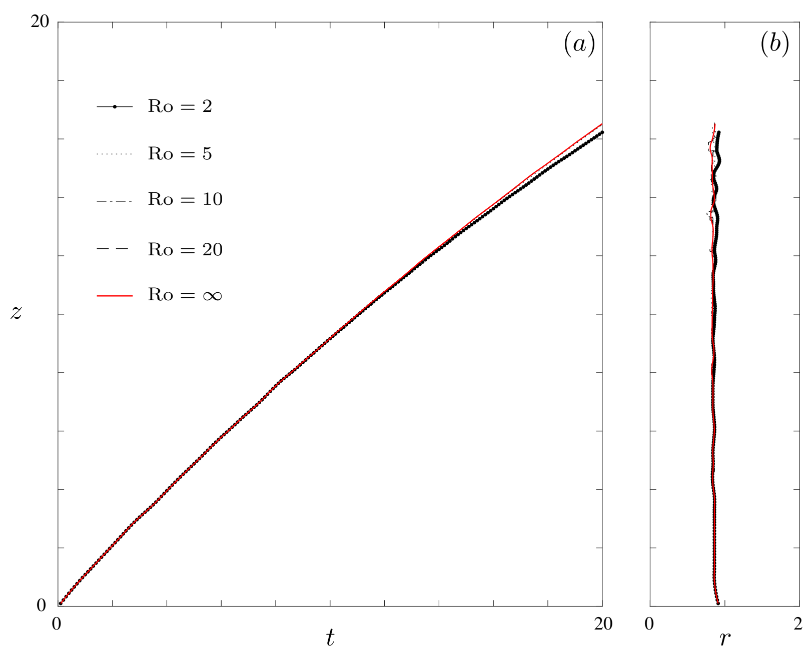

Figure 5.3: (a) The distance travelled in the axial direction by the vortex cores for flows of different Rossby number with inital velocity field $\tilde{\boldsymbol{u}} = \tilde{\boldsymbol{u}}_R$. (b) The trajectory of the vortex cores in the r–z plane.

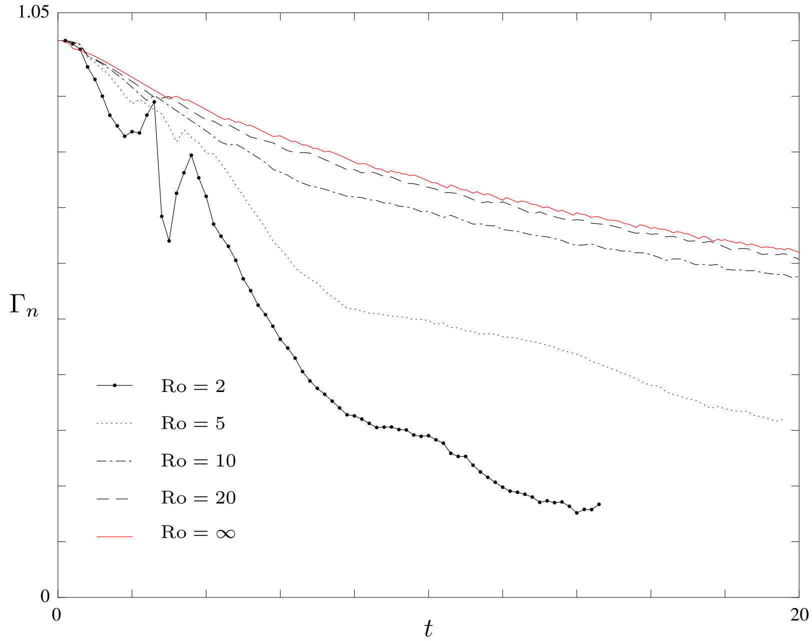

Figure 5.4: The normalised circulation, Γ_n of the vortex cores in flows of different Rossby number with initial velocity field $\tilde{\boldsymbol{u}} = \tilde{\boldsymbol{u}}_O$. The sharp drop in circulation for $\mathrm{Ro} = 2$ is due to the logging process employed.

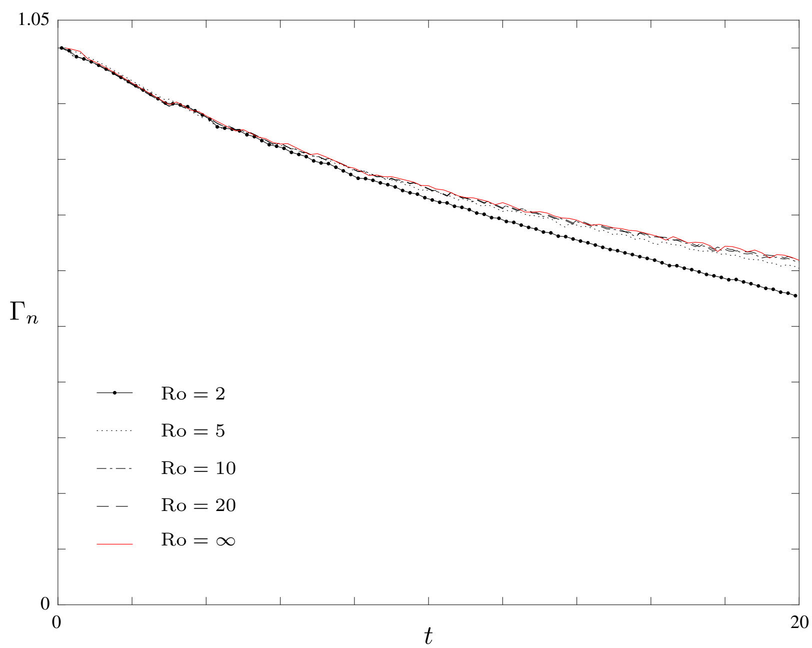

Figure 5.5: The normalised circulation, Γ_n, of the vortex cores for flows of different Rossby number with initial velocity field $\tilde{\boldsymbol{u}} = \tilde{\boldsymbol{u}}_R$.

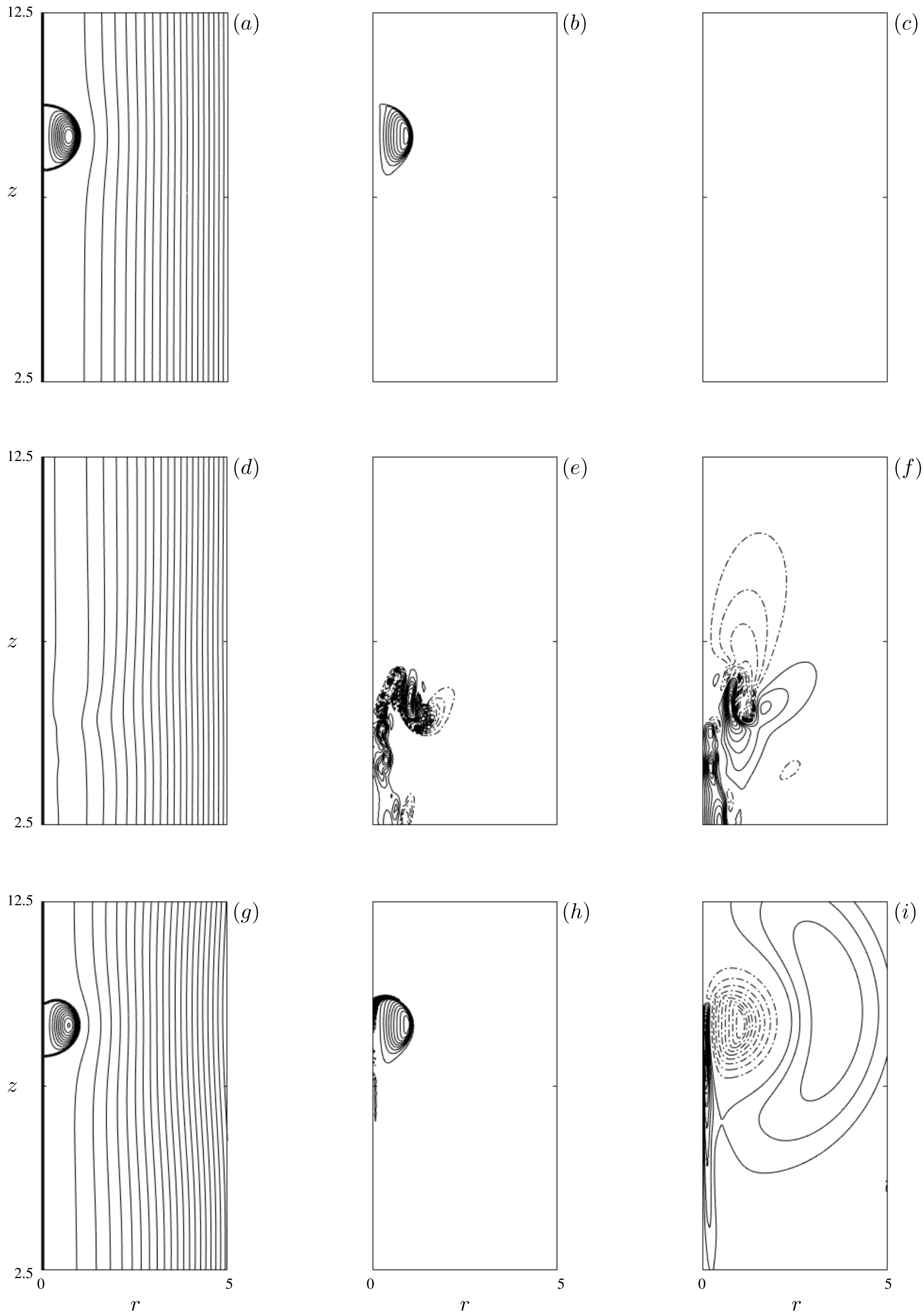

Figure 5.6: Streamlines (left), azimuthal vorticity (centre) and azimuthal swirl (right) at $t = 7$ *for Hill's vortex,* $\mathrm{Ro} = \infty$ (a)–(c), *Hill's vortex,* $\mathrm{Ro} = 1$ (d)–(f) *and the rotating Hill's vortex,* $\mathrm{Ro} = 1$ (g)–(i). *Contour increments* $\Delta\psi^+ = 0.0159$, $\Delta\psi^- = -0.6263$, $\Delta\omega_\theta^+ = 0.6945$, $\Delta\omega_\theta^- = -0.2423$, $\Delta u_\theta^+ = 0.0252$, $\Delta u_\theta^- = -0.0100$.

5.2 Moffatt vortices

The above comparison made for Hill's spherical vortex is repeated for a swirling Moffatt vortex of circulation $\Gamma = 5$ for completeness. To ensure vortices of equal circulation are compared the degree of swirl α is fixed at $\alpha = \pi/4$ and λ is adjusted to produce vortices of circulation $\Gamma = 5$.

Figure 5.7(a)–(c) gives the streamlines, azimuthal vorticity and azimuthal swirl field for a Moffatt vortex $(\tilde{\mathbf{u}}_O, P_O)$ with $(\alpha, \lambda) = (\pi/4, 7.4828)$ at $t = 10$ in a flow with Rossby number $\mathrm{Ro} = \infty$. The stream function remains largely unchanged. A small region of negative azimuthal vorticity has been generated ahead of the vortex ring due to axial gradients of azimuthal swirl in the Moffatt vortex. A cyclonic swirling tail has elongated along the axis.

Figure 5.7(d)–(f) gives the streamlines, azimuthal vorticity and azimuthal swirl field for a Moffatt vortex $(\tilde{\mathbf{u}}_O, P_O)$ with $(\alpha, \lambda) = (\pi/4, 7.4828)$ at $t = 10$ in a flow with Rossby number $\mathrm{Ro} = 5$. Like in section 4.5 the vortex has undergone vortex shedding and has decelerated significantly. This is reflected in the dotted line in figure 5.8(a). The vortex shedding is observed in the sinuous trajectory in the r–z plane in 5.8(b) whilst the considerable loss of circulation can be observed in figure 5.10.

Figure 5.7(g)–(i) gives the resulting flow at $t = 10$ from a rotating Moffatt vortex $(\tilde{\mathbf{u}}_R, P_R)$ with $(\alpha, \lambda) = (\pi/4, 7.2060)$. The azimuthal vorticity field is akin to the $\mathrm{Ro} = \infty$ case but with a slightly stronger region of azimuthal vorticity ahead of the vortex ring. Like in the $\mathrm{Ro} = \infty$ case a cyclonic swirling tail has elongated to the back of the vortex ring. Vortex shedding has not occurred like in figure 5.7(d)–(f) and the vortex ring has not seen a great reduction in propagation velocity (figure 5.9) . A Rossby number as low as $\mathrm{Ro} = 2$ is required to see a discernible difference in propagation distance. Finally, the circulation is shown in figure 5.11. At $\mathrm{Ro} = 2$ the non-rotating Hill's vortex saw its circulation drop to approximatelly 12% of its initial value by $t = 15$ whilst the rotating Hill's vortex maintained over 50% of its initial circulation.

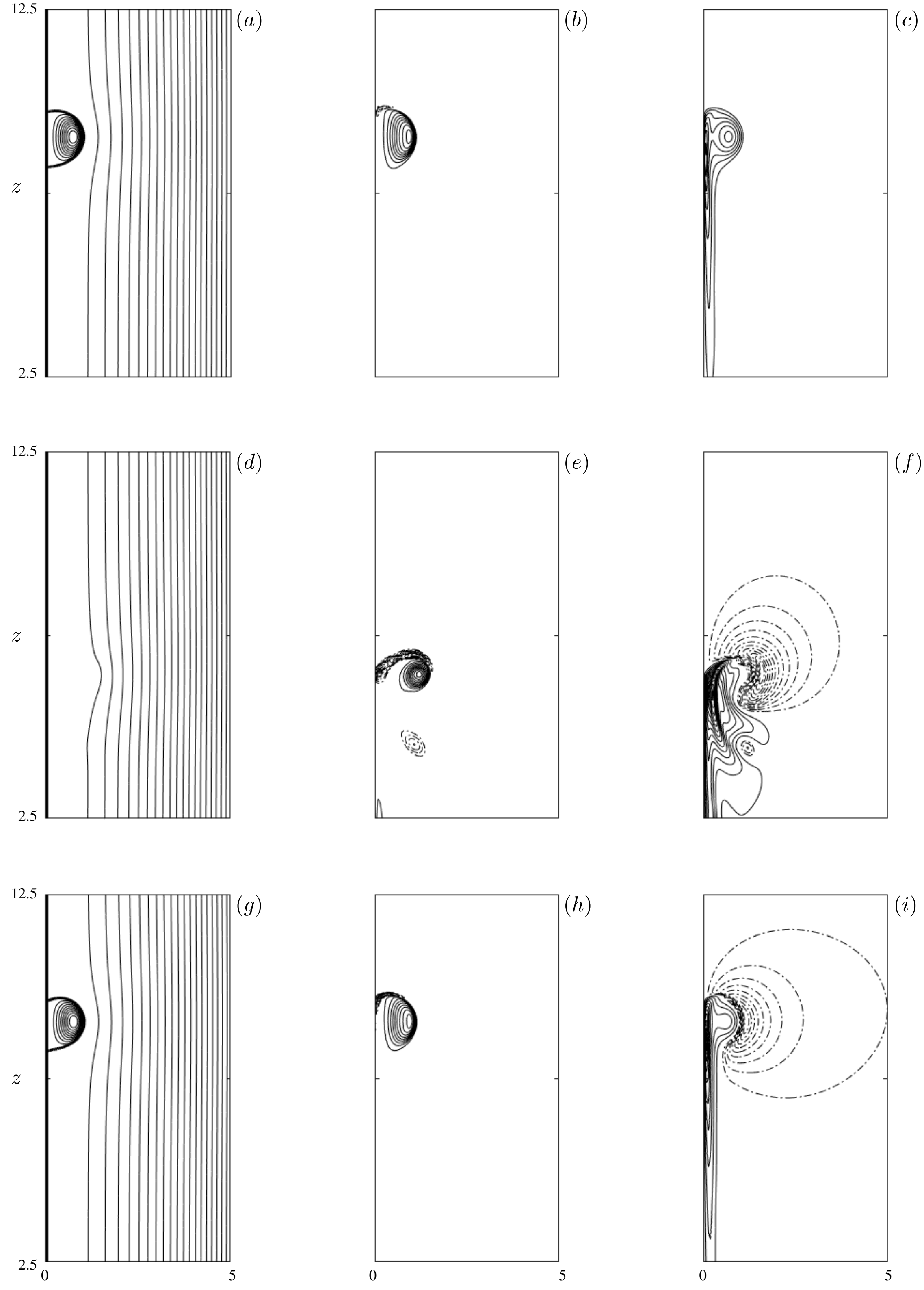

Figure 5.7: Streamlines (left), azimuthal vorticity (centre) and azimuthal swirl (right) at $t = 10$ *for Moffatt's vortex,* $\mathrm{Ro} = \infty$ (a)–(c), *Moffatt's vortex,* $\mathrm{Ro} = 5$ (d)–(f) *and the rotating Moffatt vortex,* $\mathrm{Ro} = 5$ (g)–(i). *Contour spacing* $\Delta\psi^+ = 0.0159$, $\Delta\psi^- = -0.6263$, $\Delta\omega_\theta^+ = 0.6945$, $\Delta\omega_\theta^- = -0.2423$, $\Delta u_\theta^+ = 0.0252$, $\Delta u_\theta^- = -0.0100$.

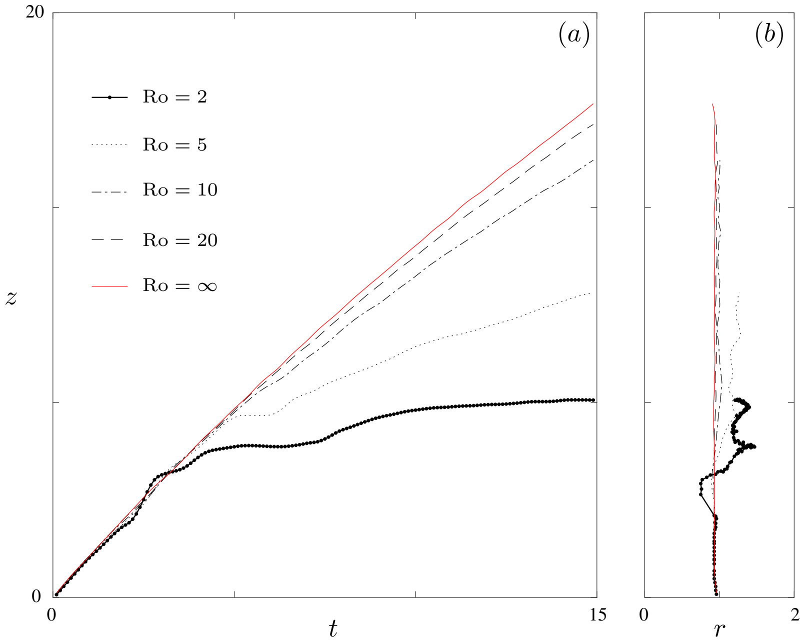

Figure 5.8: (a) The distance travelled in the axial direction by the vortex cores against time for flows of different Rossby number with initial velocity field $\tilde{\boldsymbol{u}} = \tilde{\boldsymbol{u}}_O$. (b) The trajectory of the vortex cores in the r–z plane.

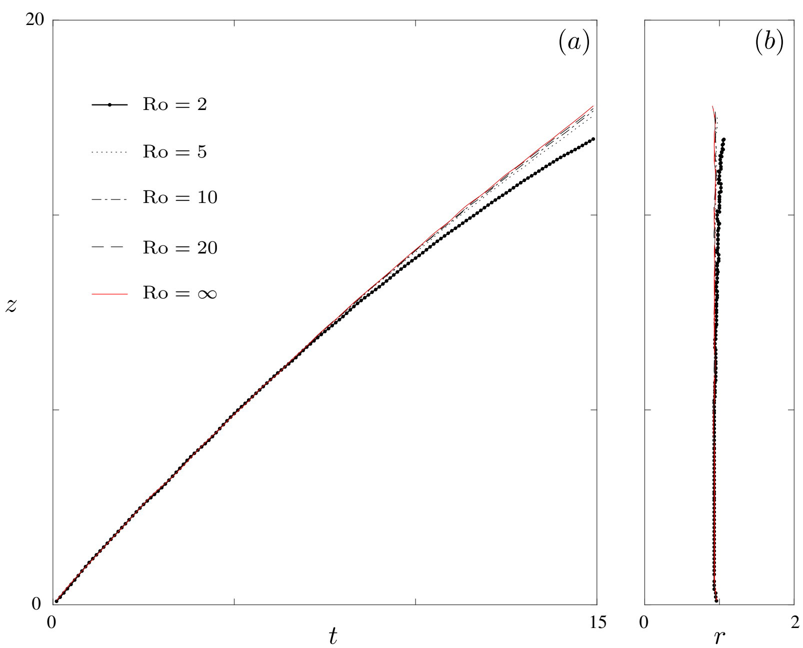

Figure 5.9: (a) The distance travelled in the axial direction by the vortex cores for flows of different Rossby number with initial velocity field $\tilde{\boldsymbol{u}} = \tilde{\boldsymbol{u}}_R$. (b) The trajectory of the vortex cores in the r–z plane.

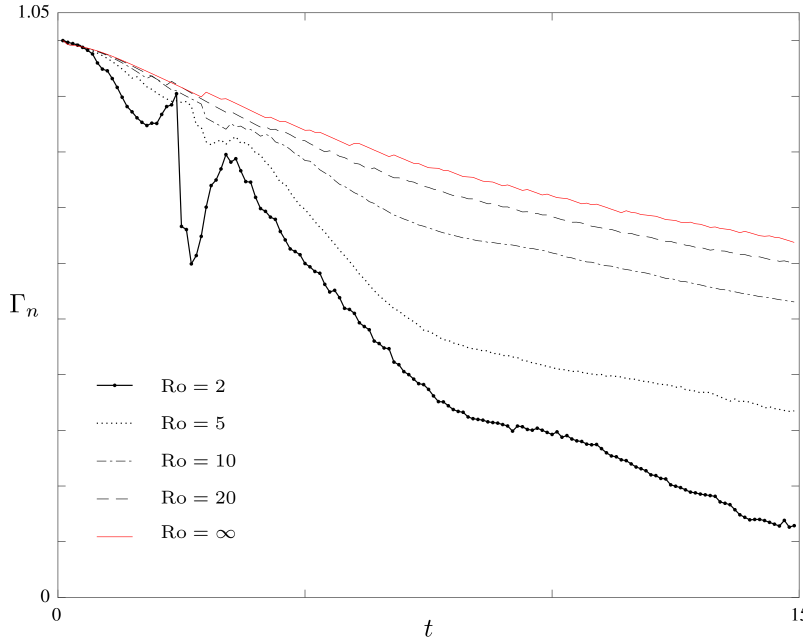

Figure 5.10: The normalised circulation, Γ_n of the vortex cores in flows of different Rossby number with initial velocity field $\tilde{\boldsymbol{u}} = \tilde{\boldsymbol{u}}_O$. The sharp drop in circulation for $\mathrm{Ro} = 2$ is due to the logging process employed.

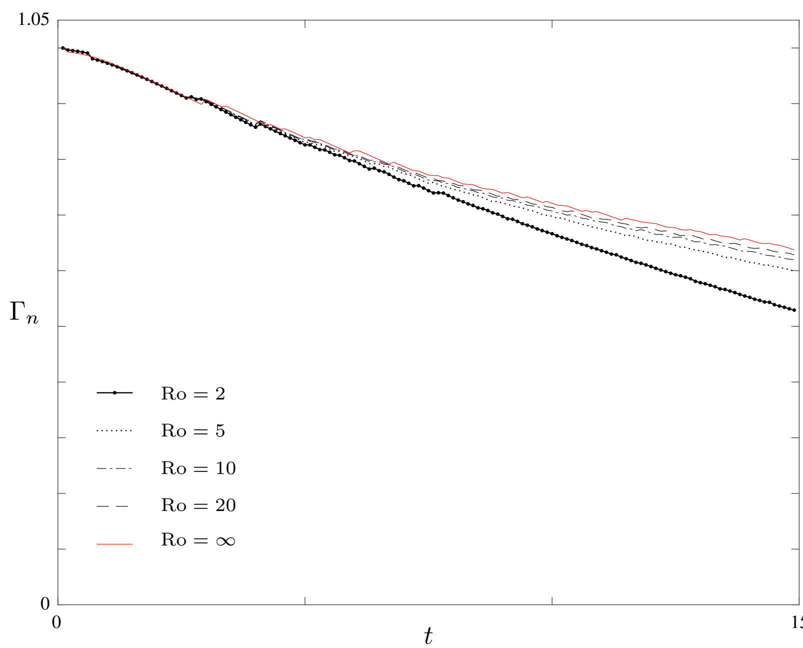

Figure 5.11: The normalised circulation, Γ_n, of the vortex cores for flows of different Rossby number with initial velocity field $\tilde{\boldsymbol{u}} = \tilde{\boldsymbol{u}}_R$.

5.3 Summary

This chapter began by highlighting the difference in the approach by Verzicco et al. (1996) and Brend and Thomas (2009) to Watchapon (2015) and Uchiyama et al. (2015) to the problem of vortex rings in rotating fluids. It was discussed how the approach of Watchapon (2015) and Uchiyama et al. (2015) - initially prescribing vortex cores with Gaussian distributions of vorticity - was unconcerned with how the vortex rings were generated. Following the same approach the rotating spherical vortex solutions found in chapter 3 were used as initial flow fields in the rotating finite element solver.

Section 5.1 compared the evolution of the non-rotating and rotating Hill's spherical vortex as the initial flow field. Whilst at $\mathrm{Ro} = 5$ the non-rotating Hill's vortex was found to be highly unstable undergoing vortex shedding the rotating Hill's vortex did not. This was also reflected in propagation distance and circulation. The rotating Hill's solution - even at a low Rossby number of $\mathrm{Ro} = 2$ - maintained its propagation velocity almost as well as Hill's vortex in a non-rotating flow and saw a much smaller reduction in circulation compared to the non-rotating Hill's vortex at $\mathrm{Ro} = 2$.

Similarly, in section 5.2 the non-rotating and rotating Moffatt vortex solutions were used as the initial flow fields. Again whilst vortex shedding was observed by the non-rotating Moffatt vortex it was not for the rotating Moffatt vortex solution.

This chapter has demonstrated that it is possible for certain vortex rings to persist in rotating viscous flows without becoming highly unstable and undergoing vortex shedding - even at low Rossby number. Use of the rotating solutions from chapter 3 as initial flow fields has shown that if similar such vortices were produced in real fluids - as Turner (1964) claimed was possible with Hill's spherical vortex - then the subsequent flow need not be as unstable as previously anticipated. Furthermore, the robustness of these vortex rings in rotating fluids is not dependent on the free-stream flow and arises from the possession of anticyclonic swirl.

Chapter 6

Fraenkel-Norbury vortices in viscous fluids

This chapter uses the two-dimensional axisymmetric finite element solver to investigate the evolution of other vortex rings in the Fraenkel-Norbury family with narrower vortex cores than Hill's spherical vortex. It aims to discover whether vortex rings with thinner or fatter cores are able to persist for longer in a rotating fluid. Previous work (see Watchapon, 2015) has investigated how a thin cored vortex ring with Gaussian vorticity distribution behaves in a rotating fluid. However, an investigation over a whole range of Fraenkel-Norbury vortex rings will provide new insight into whether vortices with thinner or fatter cores are able to persist for longer in a rotating fluid and show how Hill's spherical vortex compares. Section 6.1 outlines the numerical set-up of the problem. In section 6.2 the propagation of a variety of Fraenkel-Norbury vortices in a non-rotating fluid are simulated. Section 6.3 investigates the effect of rotation on this propagation by repeating the numerical experiment for different rates of rotation. Conclusions are drawn in section 6.4.

6.1 Formulation of the problem in FreeFem++

A Fraenkel-Norbury vortex ring is taken such that its axis of propagation $(r = 0)$ coincides with the axis of rotation of the fluid. The vortex ring will initially be located at the origin. Following Norbury (1973), the frame of reference is such that the fluid at infinity is moving past the vortex ring with free-stream velocity $-W\hat{\mathbf{z}}$. This three-dimensional axisymmetric problem cast in the cylindrical coordinate system (r, θ, z) is reduced to a two-dimensional problem on a plane $\theta = \text{const}$. The reduction of this problem to two dimensions again removes the possibility of axisymmetric instabilities which may be present in a three-dimensional flow (see Watchapon, 2015). The infinite half-plane will be truncated at a distance of $r = 20$ in the radial direction and at $z = 10$ and $z = -30$ in the axial direction which has been chosen to match the size of the domain in chapter 4 for consistency. This domain is seen in figure 6.1. The free-stream flow is from the top to the bottom of the domain indicated by the arrows. The dashed line indicates the initial location of the vortex boundary. The blue line is the axis of symmetry $r = 0$. Black edges indicate where a Dirichlet boundary condition is imposed whilst the red line indicates a natural outflow edge.

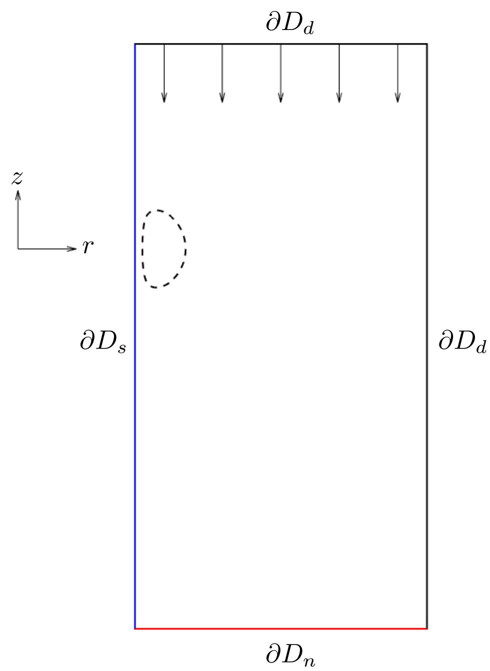

Figure 6.1: Diagram of the r–z domain on which the equations of motions are solved. Solid black edges indicate a Dirichlet boundary condition ∂D_d. The blue edge indicates a Neumann boundary condition ∂D_s. The red edge indicates a natural outflow boundary condition ∂D_n. The dashed line gives the initial location of the vortex ring.

A triangular mesh of the domain given in figure 6.1 produced by FreeFem++ is shown in figure 6.2. The results in this chapter were produced using a mesh finer (approximately 44000 triangles) than that seen in figure 6.2. However, this coarse mesh (approximately 8100 triangles) presents the mesh refinement clearly. The region that the vortex ring initially occupies - outlined in blue - is more refined. This is necessary due to sharp gradients of velocity and pressure in the early stages of the flow. High refinement here will also provide higher resolution results for analysis. The edge highlighted in red is used to refine the mesh in the region of the domain that the vortex will move through.

The work in this chapter - like chapter 4 - uses the same nondimensionalisation as Norbury (1973). The Fourier expansions describing the vortex ring boundaries - which were replicated in chapter 2 - can therefore be taken directly from Norbury (1973). The initial velocity and pressure fields are obtained from the stream function fields calculated in chapter 2.

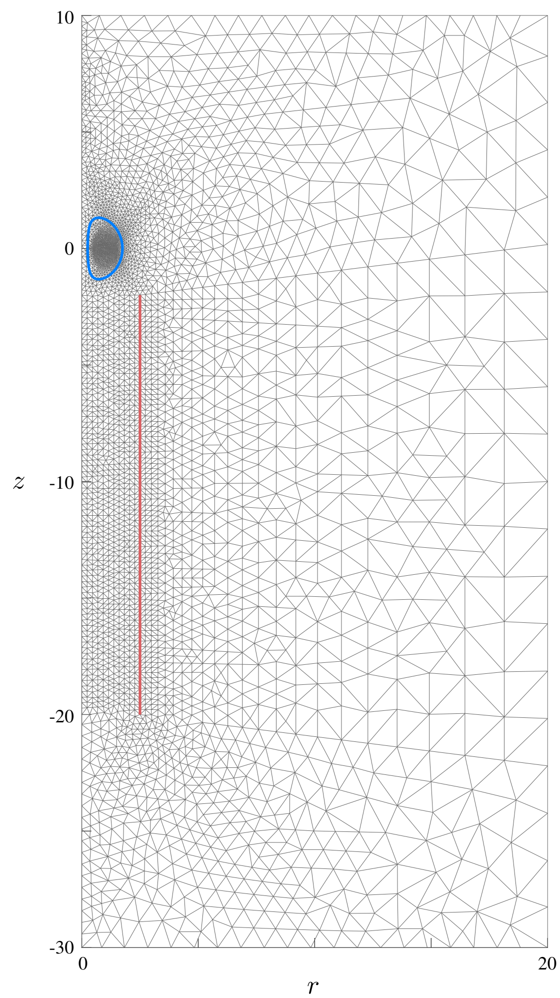

Figure 6.2: The two-dimensional mesh representing the truncated r–z half-plane. The blue line indicates the boundary of the vortex ring. The red line indicates a boundary used for mesh refinement in the part of the domain that the vortex moves through.

From equation (4.16) of chapter 4 we have that the weak formulation for the rotating Navier-Stokes equations is to find $\mathbf{u} \in \mathbf{H}^1_E$ and $P \in L_2(\mathcal{D})$ such that

$$\int_{\mathcal{D}} \frac{\partial \mathbf{u}}{\partial t} \cdot \mathbf{v} \, \mathrm{d}\mathcal{D} + \int_{\mathcal{D}} (\mathbf{u} \cdot \nabla) \, \mathbf{u} \cdot \mathbf{v} \, \mathrm{d}\mathcal{D} + \frac{1}{\mathrm{Re}} \int_{\mathcal{D}} \nabla \mathbf{u} : \nabla \mathbf{v} \, \mathrm{d}\mathcal{D} - \frac{1}{\mathrm{Re}} \int_{\partial \mathcal{D}} (\mathbf{n} \cdot \nabla \mathbf{u}) \cdot \mathbf{v} \, \mathrm{dS} +$$
$$\frac{1}{\mathrm{Re}} \int_{\mathcal{D}} \left(\frac{\tilde{u}_r v_r}{r} + \frac{\tilde{u}_\theta v_\theta}{r} \right) \mathrm{d}\mathcal{D} - \int_{\mathcal{D}} P \, (\nabla \cdot \mathbf{v}) \, \mathrm{d}\mathcal{D} + \int_{\partial \mathcal{D}} P \; (\mathbf{n} \cdot \mathbf{v}) \, \mathrm{dS} + \frac{1}{\mathrm{Ro}} \int_{\mathcal{D}} (\hat{\mathbf{z}} \times \mathbf{u}) \cdot \mathbf{v} \, \mathrm{d}\mathcal{D} = 0, \tag{6.1a}$$

$$\int_{\mathcal{D}} q \, (\nabla \cdot \mathbf{u}) \, \mathrm{d}\mathcal{D} = 0, \tag{6.1b}$$

for all $\mathbf{v} \in \mathbf{H}^1_{E_0}$ and all $q \in L_2(\mathcal{D})$where

$$\mathbf{u} \in \mathbf{H}^1_E := \{\mathbf{u} \, \in \, \mathcal{H}^1 \, (\mathcal{D})^3 \mid \mathbf{u} = \mathbf{w} \text{ on } \partial \mathcal{D}\}, \tag{6.2a}$$

$$\mathbf{v} \in \mathbf{H}^1_{E_0} := \{\mathbf{v} \, \in \, \mathcal{H}^1 \, (\mathcal{D})^3 \mid \mathbf{v} = \mathbf{0} \text{ on } \partial \mathcal{D}\}, \tag{6.2b}$$

and where $\mathcal{H}^1(\mathcal{D})^3$ is the *Sobolev space* given by

$$\mathcal{H}^1(\mathcal{D})^3 := \left\{ \mathbf{u} : \mathcal{D} \to \mathbb{R}^3 \; \middle| \; \mathbf{u}, \frac{\partial \mathbf{u}}{\partial r}, \frac{\partial \mathbf{u}}{\partial z} \in L_2(\mathcal{D}) \right\}, \tag{6.3}$$

which ensures that $\mathbf{u}$ and its first derivatives all have finite L_2 measure

$$L_2(\mathcal{D}) := \left\{ \mathbf{u} : \mathcal{D} \to \mathbb{R}^3 \; \middle| \; \int_{\mathcal{D}} |\mathbf{u}|^2 \; \mathrm{d}\mathcal{D} < \infty \right\}. \tag{6.4}$$

The appropriate pressure and test spaces are also given in Elman et al. (2014) by $P, q \in L_2(\mathcal{D})$.

The Dirichlet boundary conditions

$$\mathbf{u} = \mathbf{w} \quad \text{and} \quad P = \Pi \text{ on } \partial D_d \tag{6.5}$$

will be applied on upper and right hand edges of the domain as indicated by the solid black lines in figure 6.1. This Dirichlet condition will be used to impose that the free-stream flow remains unchanged “far” from the vortex ring.

On the axis $r = 0$ the Neumann boundary conditions

$$\frac{\partial \mathbf{u}}{\partial r} = \mathbf{0} \quad \text{and} \quad \frac{\partial P}{\partial r} = 0 \text{ on } \partial D_s \tag{6.6}$$

enforce smooth velocity and pressure profiles on the axis of symmetry. This is indicated by the blue line in figure 6.1. The bottom boundary of the domain given by the red line in figure 6.1 will be an outflow boundary and the natural boundary condition

$$\frac{\partial \mathbf{u}}{\partial n} - P\,\mathbf{n} = \mathbf{0} \text{ on } \partial D_n \tag{6.7}$$

imposed will ensure that mass is conserved and that the pressure solution is unique (see Elman et al., 2014, chap. 3). Like in chapter 4, the stream function is calculated by solving the velocity - stream function finite element problem outlined in appendix A.

Circulation

To compare the behaviour of Hill's spherical vortex and thinner-cored Fraenkel-Norbury vortex rings the azimuthal vorticity ω_θ in each vortex ring is chosen such that every vortex ring begins at $t = 0$ with the same circulation. This is to ensure we are considering vortex rings of the same strength and removing

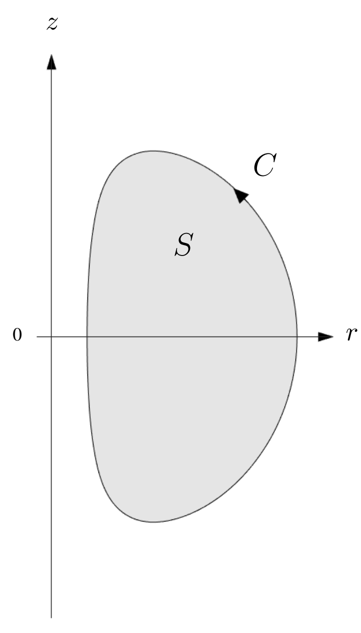

Figure 6.3: Schematic of the contour integral used when calculating the circulation of a Fraenkel-Norbury vortex ring. C is the enclosing contour taken in the anticlockwise sense whilst S is the shaded region that the integration is performed over.

another possible variable in the experiment. Each vortex ring still has vorticity proportional to the radial distance from the axis of symmetry, $\omega_\theta = Ar$, however, the constant of proportionality A is chosen such that the circulation of the vortex ring is $\Gamma = 8/3$ - matching that of Hill's spherical vortex of radius $a = 2$. Figure 6.3 shows an example of the contour enclosing the initial vortex ring core used when calculating the circulation.

As there is no explicit stream function for the Fraenkel-Norbury vortex ring family the vorticity-stream function problem is solved to provide the stream function and initial velocity field. As a reminder from chapter 4, the "logging" procedure calculates the circulation for a vortex centred at $z = Z$ by integrating over the range $-R_0 \leqslant z - Z \leqslant R_0$, where R_0 is the vortex ring radius. This minimises the contribution of the vortex tail to the circulation. Checking the circulation using the "logging" procedure on the initial velocity field, a higher value for the circulation is obtained. This is partly due to a contribution of azimuthal vorticity just outside the vortex ring boundary. Fraenkel-Norbury vortex rings have a discontinuous vorticity field and use of a continuous Galerkin finite element method leads to mesh elements outside the initial vortex ring boundary having non-zero azimuthal vorticity. The combined process of solving the vorticity-stream function problem, calculating the velocities from the stream function and then integrating over the logging region is a source of non-zero numerical error. Therefore when comparing vortex rings of different mean core radii, their circulation will be normalised with their initial calculated value. The same "logging" procedure is used throughout the chapter to minimise the contribution of any axial vortex tail to the value of the circulation.

6.2 Fraenkel-Norbury vortex rings in a non-rotating fluid

This section shows the evolution of Fraenkel-Norbury vortex rings in a viscous but non-rotating fluid. This will be contrasted with the behaviour of Hill's spherical vortex in a non-rotating fluid and will provide a benchmark to compare how the vortices behave differently in a rotating fluid to a non-rotating fluid. Although the numerical problem was formulated such that at the boundary of the domain the fluid is flowing past with free-stream velocity $-W\hat{\mathbf{z}}$, the results presented here have been adapted so that they give the flow in a laboratory frame of reference with fluid at the far-field at rest.

Figure 6.4(a)–(e) gives the streamlines of the resulting flow of a Fraenkel-Norbury vortex ring with mean-core radius $\alpha = 0.6$ at Reynolds number $\mathrm{Re} = 1000$. Figure 6.4(f)–(j) gives the contours of constant azimuthal vorticity. The vortex atmosphere - the fluid transported along with the vortex ring - enclosed by the bold dividing streamline $\psi = 0$ propagates without much qualitative change. However, whereas in the inviscid case this dividing streamline separated rotational and irrotational fluid, this is no longer the case. Viscosity has smoothed the discontinuity in vorticity at the boundary and the maximum value of azimuthal vorticity is now located closer to the centre of the vortex core.

Saffman (1970) considered the viscous motion of a thin vortex core with Gaussian distribution of vorticity where initially the vorticity is a δ-function concentrated on the vortex ring radius, R. Using a new approach Saffman first derived Fraenkel's (1970) formula for the propagation velocity of a steady inviscid vortex ring of narrow cross-section a as

$$U = \frac{\Gamma_0}{4\pi R}\left(\ln 8 - \frac{1}{2} + Z + \mathcal{O}\left[\frac{\Gamma a}{R^2}\ln\left(\frac{a}{R}\right)\right]\right) \tag{6.8}$$

where

$$Z = \int_0^a \Gamma^2 \frac{\mathrm{d}s}{s} - \ln\frac{a}{R}. \tag{6.9}$$

Saffman (1970) then further showed that for a viscous vortex ring the circulation Γ is given by

$$\Gamma(s,t) = 1 - e^{-s^2/4\nu t}. \tag{6.10}$$

Substitution of equation (6.10) into equations (6.8) and (6.9) and taking the limit $a \to \infty$ Saffman showed the propagation velocity of a viscous vortex ring to be

$$U = \frac{\Gamma_0}{4\pi R}\left(\ln\left(\frac{8R}{\sqrt{4\nu t}}\right) - 0.558 + \mathcal{O}\left[\left(\frac{\nu t}{R^2}\right)^{1/2}\ln\left(\frac{\nu t}{R^2}\right)\right]\right) \tag{6.11}$$

where ν is the kinematic viscosity, Γ_0 is the initial circulation and t is the time from the moment the core is infinitely thin. Tinaikar et al. (2018) conducted experiments using high-speed particle image velocimetry (PIV) and laser induced fluorescence (LIF) techniques. They created a wide variety of vortex rings over a large range of Reynolds numbers $(\mathrm{Re} = 100 - 1500)$ with their experimental results showing good agreement with theoretical predictions. However, they observed that neither Saffman's thin-core theory nor thick-core model (see pp. 378 Saffman, 1970) could correctly explain vortex ring evolution for all initial conditions. Their transitional theory which considered the viscous torque on a vortex ring derived the velocity as

$$U = \frac{\Gamma_0}{4\pi a_0 \left(1 + \frac{2\phi\nu t}{\sigma_0^2}\right)^{3/2}} \left(\ln\left(\frac{8a_0}{\sigma_0}\right) - 0.558\right) \tag{6.12}$$

where

$$\phi = \left| \frac{5(1-2k_1^2)e^{-k_1^2}}{k_1^2(5-4(1-e^{-k_1^2}))} \right| \tag{6.13}$$

and the parameter k_1 defines the size of the initial vortex core with initial core radius $\varepsilon = k_1\sigma$. Note σ is the standard deviation of the vorticity distribution and σ_0 is its value at time $t = 0$. In general vortex rings with a greater value of σ_0 will have fatter vortex cores. From (6.12) we find that vortex rings with fatter vortex cores retain their propagation velocity for longer in comparison to a thinner vortex core of equal initial circulation.

Again, considering the effect of viscous torque on the vortex core Tinaikar et al. (2018) also provided an expression for the circulation of a viscous vortex core. They found that

$$\Gamma \propto \frac{\Gamma_0}{\left(1 + \frac{2\phi\nu t}{\sigma_0^2}\right)} \tag{6.14}$$

which states that vortex cores with greater standard deviations of vorticity will retain their circulation for longer. Note that Fraenkel-Norbury vortex rings have linear vorticity distribution in contrast to the Gaussian profiles of Tinaikar et al. (2018).

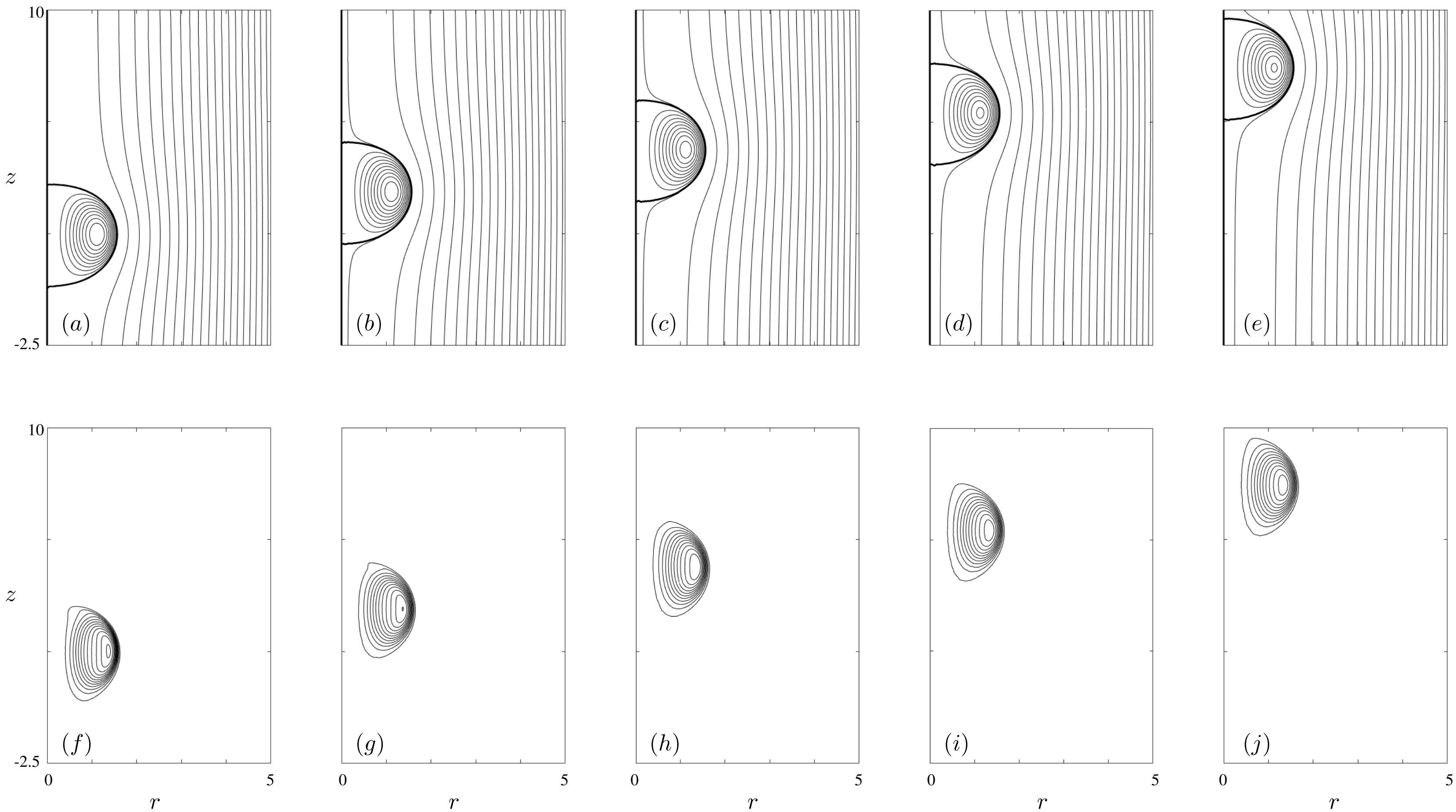

Figure 6.4: Streamlines at times $t = 10$ (a), $t = 12$ (b), $t = 14$ (c), $t = 16$ (d) *and* $t = 18$ (e). *Thick black lines gives the streamline* $\psi = 0$. *Contour spacing* $\Delta\psi^+ = 0.03$ *(inside* $\psi = 0$*) and* $\Delta\psi^- = -0.33$ *(outside* $\psi = 0$*). Contours of constant azimuthal vorticity at times* $t = 10$ (f), $t = 12$ (g), $t = 14$ (h), $t = 16$ (i) *and* $t = 18$ (j) *Contour spacing* $\Delta\omega_\theta = 0.32$. *Reynolds number* $\mathrm{Re} = 1000$, *Rossby number* $\mathrm{Ro} = \infty$.

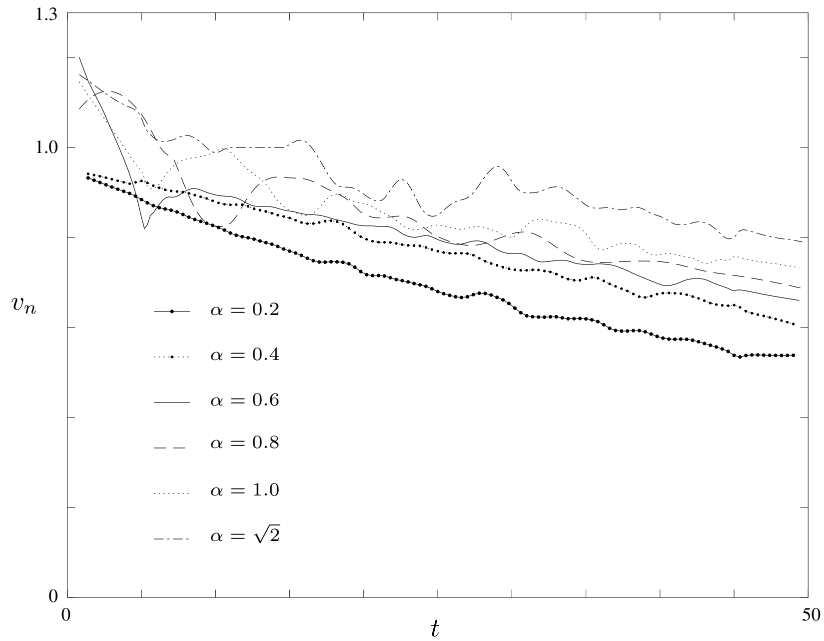

Figure 6.5: The normalised velocity, v_n, of vortex rings with mean core radius $\alpha = 0.2, 0.4, 0.6, 0.8, 1.0$ and $\sqrt{2}$ in flows with Reynolds number $\mathrm{Re} = 1000$.

Norbury (1973) provides the boundaries of many of the Fraenkel-Norbury vortex ring family. However, for each vortex ring - defined by its mean-core radius α - the free-stream velocity differs. The change in propagation speed for each vortex cannot be directly compared. Instead the velocity of the vortex core v_c is normalised with the initial propagation velocity W and the quantity $v_n = v_c/W$ is compared for each vortex ring. Figure 6.5 gives the normalised velocity v_n versus time for vortex rings of different mean-core radii. Due to deformation of the vortex cores at the beginning of the motion - and movement of the point of maximum vorticity towards the front of the vortex core - the speed of the vortex core v_c is distorted temporarily. This gives rise to initial normalised velocities greater than unity. Figure 6.5 shows that vortex rings with narrower vortex cores see a greater reduction in propagation velocity in agreement with the theory of Tinaikar et al. (2018).

The circulation of the vortices versus time is seen in figure 6.6. No clear relationship between mean-core radius and circulation can be deduced. These results are calculated with a logging area spanning twice the distance in the axial direction than in previous chapters i.e. $-2R_0 \leqslant z - Z \leqslant 2R_0$, where Z is the axial position of the vortex core centre and R_0 is the ring radius. The logging procedure on the smaller range $-R_0 \leqslant z - Z \leqslant R_0$ resulted in loss of circulation in vortex rings with larger mean-core radius. This is seen in figure 6.7. The region highlighted in red gives a region of azimuthal vorticity which does not contribute to the circulation as it is removed by the logging procedure. Hill's spherical vortex loses a portion of positive azimuthal vorticity whereas the Fraenkel-Norbury vortex ring with mean core radius $\alpha = 0.6$ does not. However, we recall that the logging region is used to eliminate the contribution of azimuthal vorticity in any axial tail generated in rotating flows to the circulation. Therefore when making comparisons between the non-rotating and rotating results the smaller logging region and corresponding circulations will be used for consistency. The size of the truncation was chosen following qualitative observation of the azimuthal vorticity field. However, further investigation could be conducted to investigate how sensitive the results are to the size of the logging region.

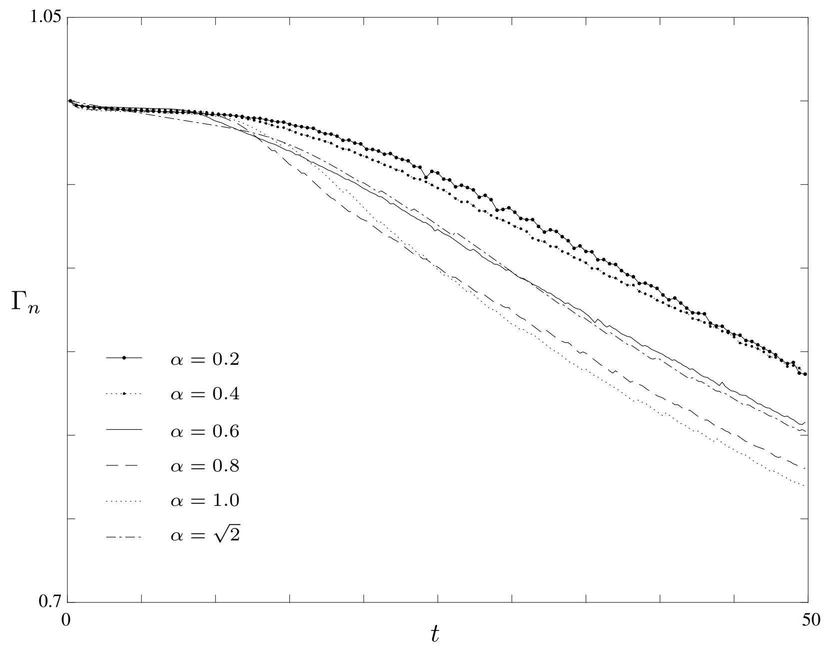

Figure 6.6: The normalised circulation, Γ_n, of vortex rings with mean core radius $\alpha = 0.2, 0.4, 0.6, 0.8, 1.0$ and $\sqrt{2}$ against time t in flows with Reynolds number $\mathrm{Re} = 1000$.

To summarise, Fraenkel-Norbury vortex rings of narrower cross section see a greater reduction in propagation velocity than their fatter cored counterparts of equal circulation. As an extremal member of this family Hill's spherical vortex is found to maintain its propagation velocity best. However, the results in this section have demonstrated that the circulation is insensitive to mean-core radius variations in a non-rotating viscous fluid.

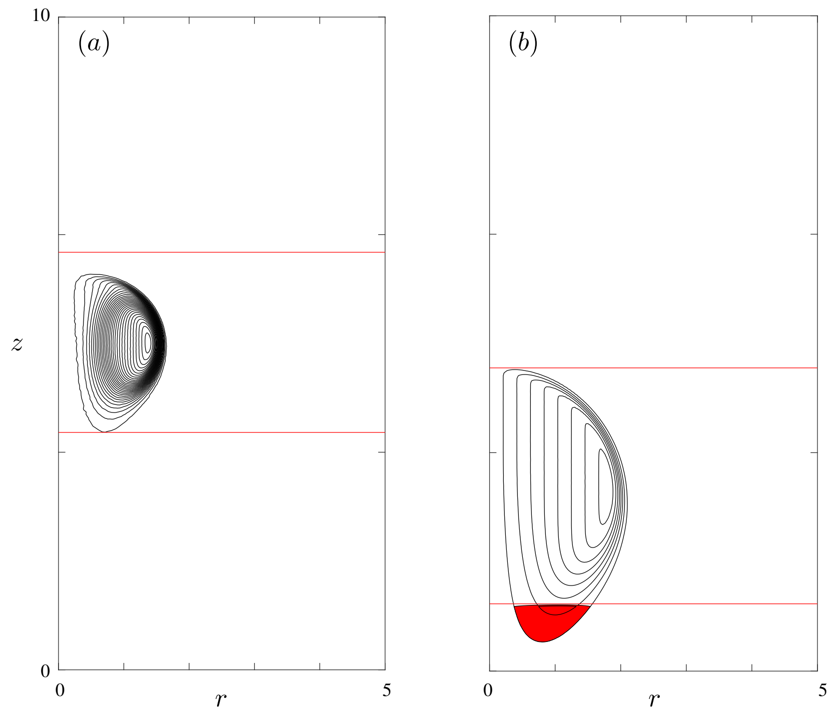

Figure 6.7: Contours of constant azimuthal vorticity at time $t = 50$ for $(a) : \alpha = 1.0$ $(b) : \alpha = \sqrt{2}$, for a flow with Reynolds number $\mathrm{Re} = 1000$ and Rossby number $\mathrm{Ro} = \infty$. Contour spacing $\Delta\omega_\theta = 0.104$. The red lines indicate the boundary of the logging region. The red shaded area indicates a region of azimuthal vorticity omitted from the calculation of the circulation.

6.3 Fraenkel-Norbury vortex rings in a rotating fluid

Section 6.3.1 begins by investigating how a Fraenkel-Norbury vortex ring with mean core radius $\alpha = 0.6$ behaves in a fluid at different rates of rotation. In section 6.3.2 some higher Reynolds number results are presented. Finally, section 6.3.3 compares how Fraenkel-Norbury vortex rings of different mean-core radii behave in a rotating fluid.

6.3.1 Varying the rate of rotation

Figure 6.8 shows the azimuthal vorticity field evolving from a Fraenkel-Norbury vortex ring with mean-core radius $\alpha = 0.6$ in a flow with Reynolds number $\mathrm{Re} = 1000$ and Rossby number $\mathrm{Ro} = 10$. At $t = 10$ a region of negative azimuthal vorticity lies at the front of the vortex ring. As explained in chapter 4 this is generated by the vortex tilting term $(\boldsymbol{\omega} \cdot \nabla)\mathbf{u}_\theta$ - in particular the contribution from the term $\omega_z \partial u_\theta / \partial z$. The azimuthal swirl and axial vorticity field at $t = 10$ are seen in figure 6.9. The red line gives the boundaries of positive and negative azimuthal vorticity. In figure 6.9(a) a strongly swirling cyclonic tail is observed by the tightly packed solid contours whilst a weaker anticyclonic head is observed by the dashed contours.

The region of negative azimuthal vorticity is then swept around the outside of the vortex ring and by time $t = 14$ can be seen rolling up as an oppositely signed patch of azimuthal vorticity. At $t = 16$ it is seen shed off the back of the vortex ring and by $t = 18$ becomes its own weak negatively-signed secondary vortex ring which is subsequently dissipated by viscous diffusion.

In figure 6.10 the pressure field at $t = 10$ is presented for flows with Rossby numbers $\mathrm{Ro} = \infty$ and $\mathrm{Ro} = 10$. In the rotating case a clear region of low pressure on the axis of rotation can be seen behind the vortex ring. This is the same behaviour exhibited by Hill's vortex in figure 4.20 of chapter 4.

Verzicco et al. (1996) also observed multiple shedding events. In their simulations at $\mathrm{Re} = 480$ and $\mathrm{Ro} = 2$ the primary vortex core shed only one oppositely signed vortex. They explain that this is due to cross-cancellation of vorticity ahead of the vortex ring. The remaining patch of negative azimuthal vorticity ahead of the vortex ring is not intense enough to roll up to form a tertiary vortex ring. However, in a flow where viscosity is less dominant ($\mathrm{Re} = 1500$ and $\mathrm{Ro} = 6$) the vortex ring is able to undergo two shedding events.

Multiple shedding events can also be brought about by reducing the Rossby number. At lower Rossby number the region of negative azimuthal vorticity generated ahead of the vortex ring is more intense enabling more shedding events. Figures 6.11 and 6.12 show the azimuthal vorticity field evolving from a Fraenkel-Norbury vortex ring with mean-core radius $\alpha = 0.6$ in a flow with Rossby number $\mathrm{Ro} = 5$. At this higher rotation rate an oppositely signed vortex ring is first shed at $t \approx 16$ followed by a further shedding at $t \approx 22$.

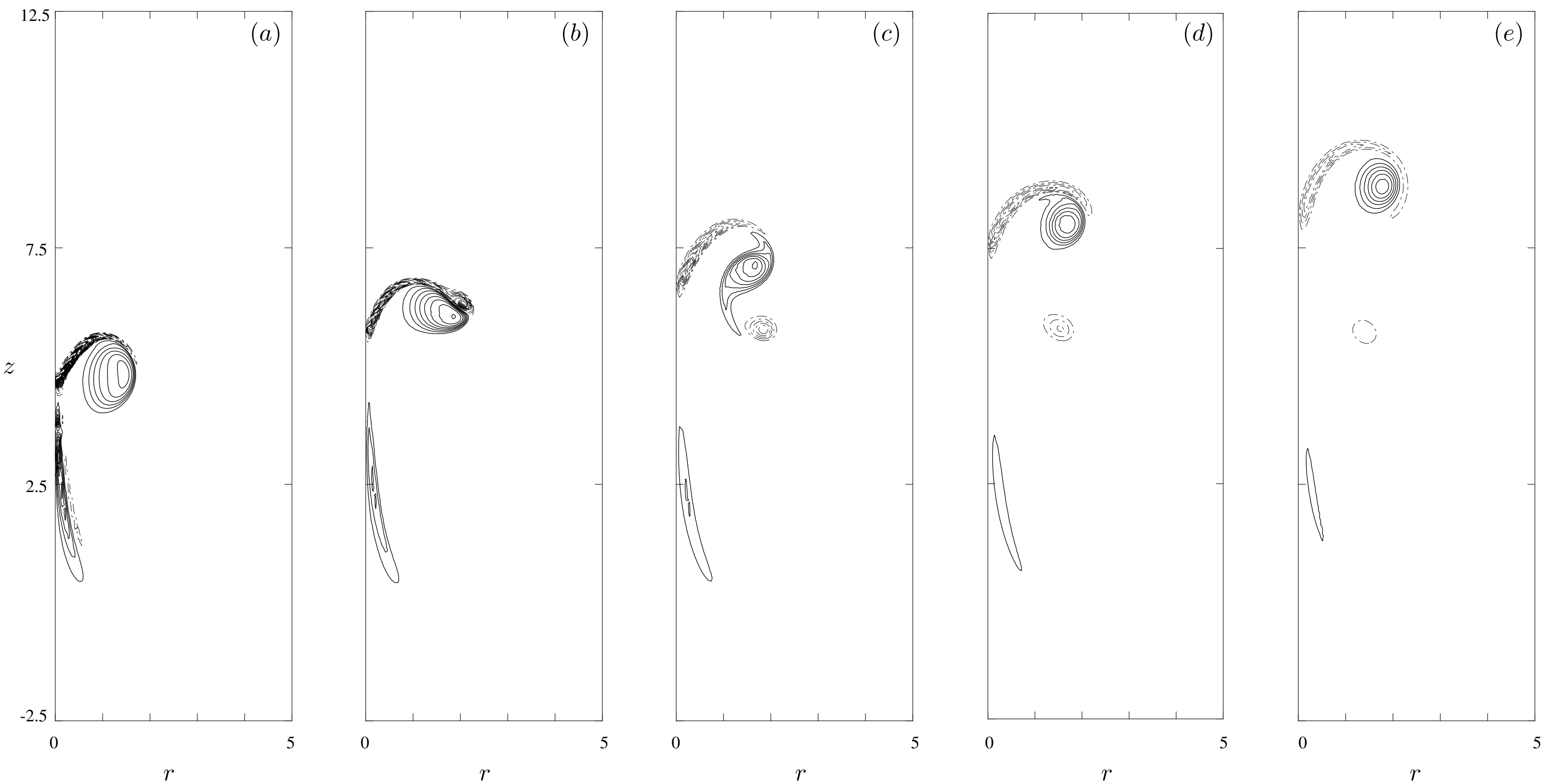

Figure 6.8: Contours of constant azimuthal vorticity at times $t = 10$ (a), $t = 14$ (b), $t = 18$ (c), $t = 22$ (d) *and* $t = 26$ (e), *for a flow with Reynolds number* $\mathrm{Re} = 1000$ *and Rossby number* $\mathrm{Ro} = 10$. *Solid lines give positive contours and dashed lines give negative contours with spacing* $\Delta\omega_\theta^+ = 0.52$ *and* $\Delta\omega_\theta^- = -0.28$.

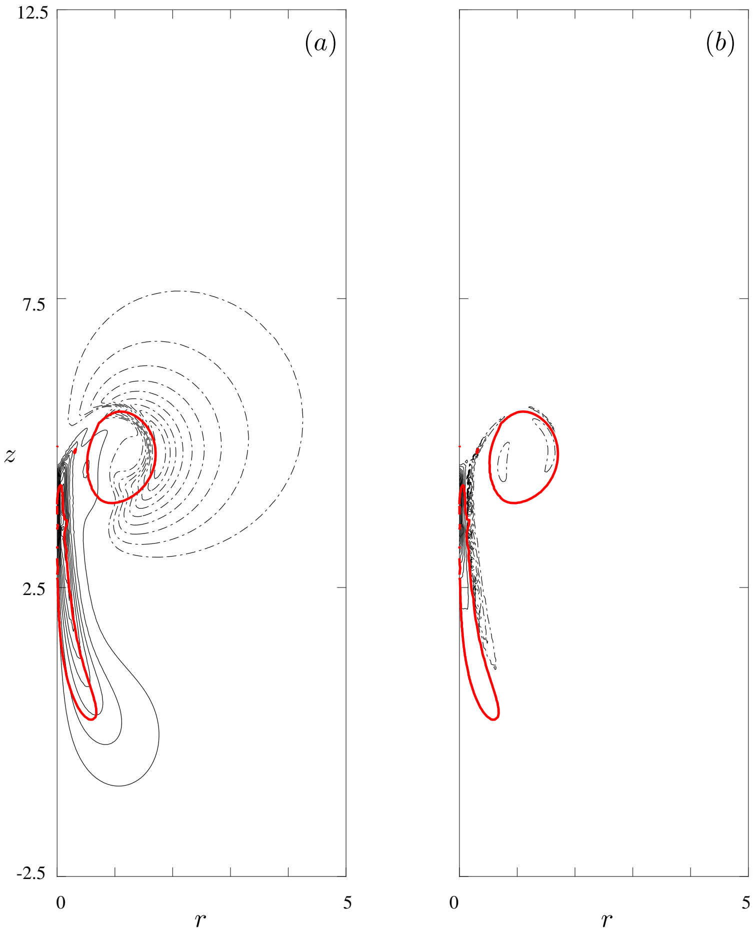

Figure 6.9: (a) *Contours of constant azimuthal velocity at* $t = 10$ *for* $\mathrm{Ro} = 10$ *with* $\Delta u_\theta^- = -0.0074$ *and* $\Delta u_\theta^+ = 0.0409$. (b) *Contours of constant axial vorticity at* $t = 10$ *for* $\mathrm{Ro} = 10$ *with* $\Delta\omega_z^- = -0.2244$ *and* $\Delta\omega_z^+ = 2.9$.

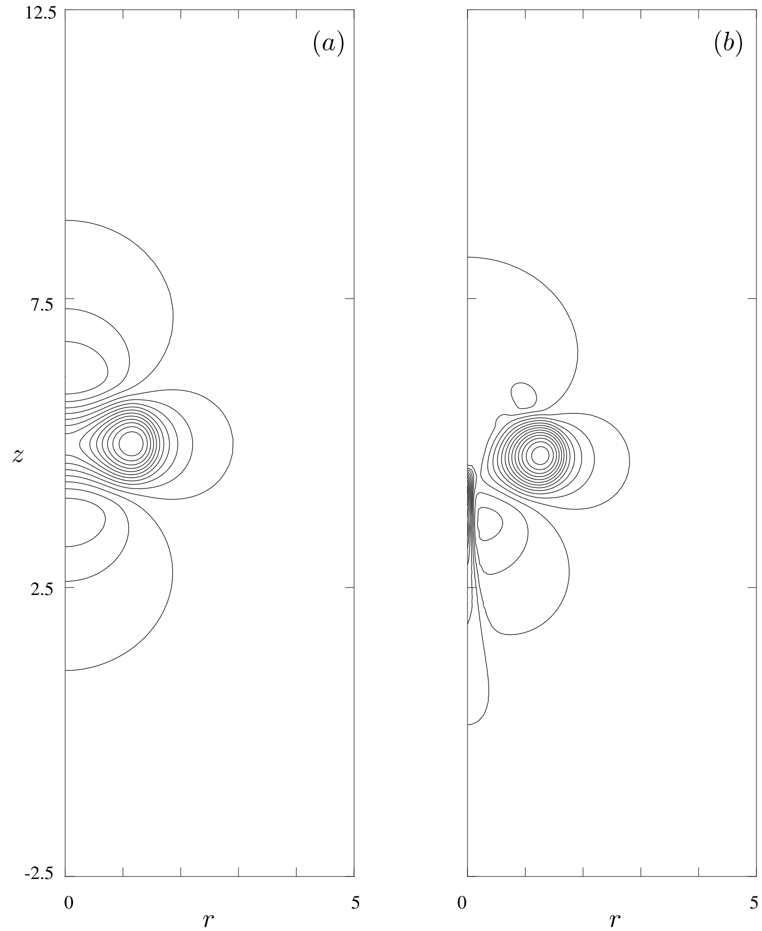

Figure 6.10: *Contours of constant pressure at* $t = 10$ *for flows with* $\mathrm{Ro} = \infty$ (a) *and* $\mathrm{Ro} = 10$ (b) *with* $\Delta p = 0.034$.

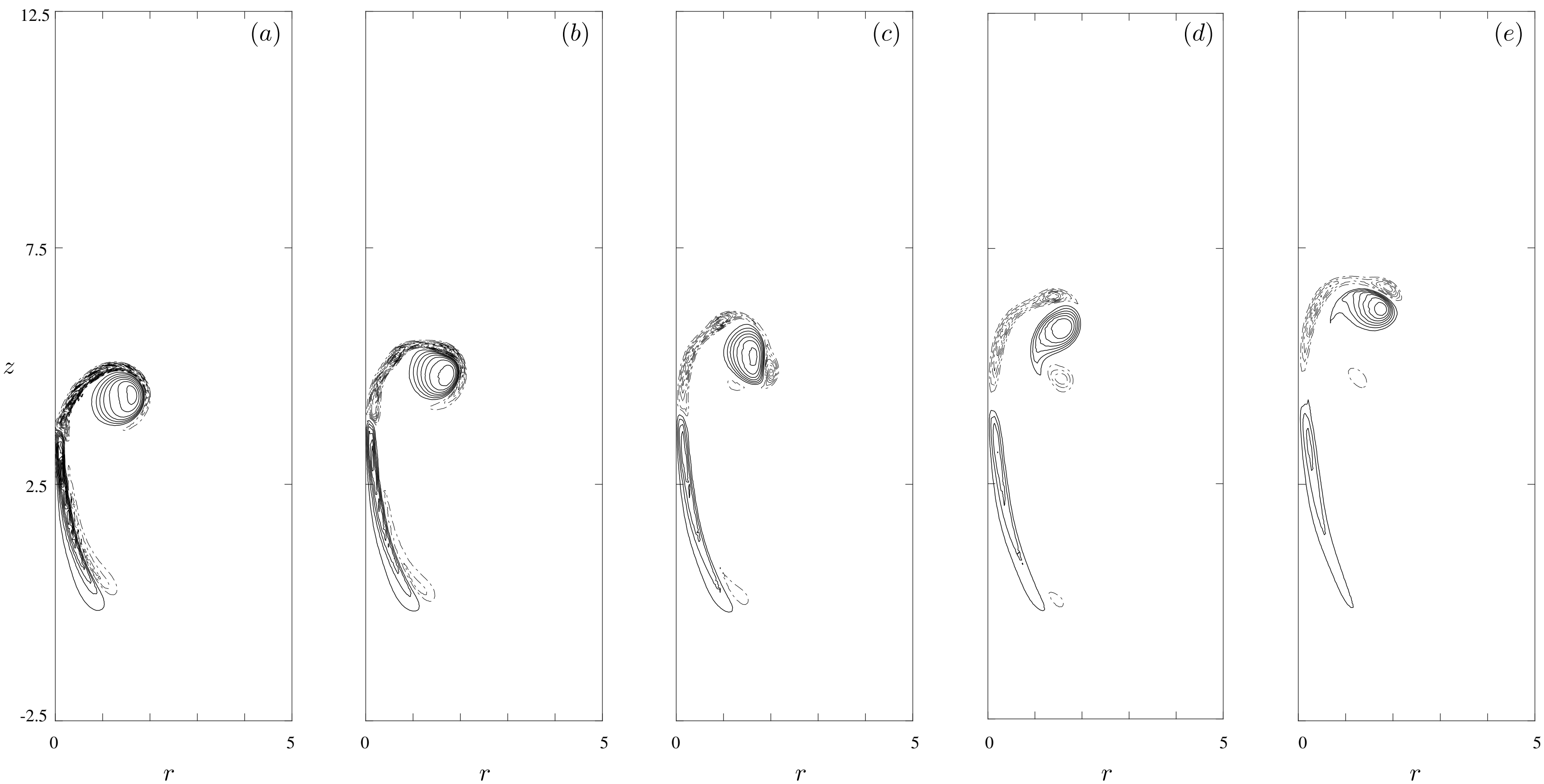

Figure 6.11: Contours of constant azimuthal vorticity at times $t = 10$ (a), $t = 12$ (b), $t = 14$ (c), $t = 16$ (d) *and* $t = 18$ (e), *for a flow with Reynolds number* $\mathrm{Re} = 1000$ *and Rossby number* $\mathrm{Ro} = 5$. *Solid lines give positive contours and dashed lines give negative contours with spacing* $\Delta\omega_\theta^+ = 0.52$ *and* $\Delta\omega_\theta^- = -0.28$.

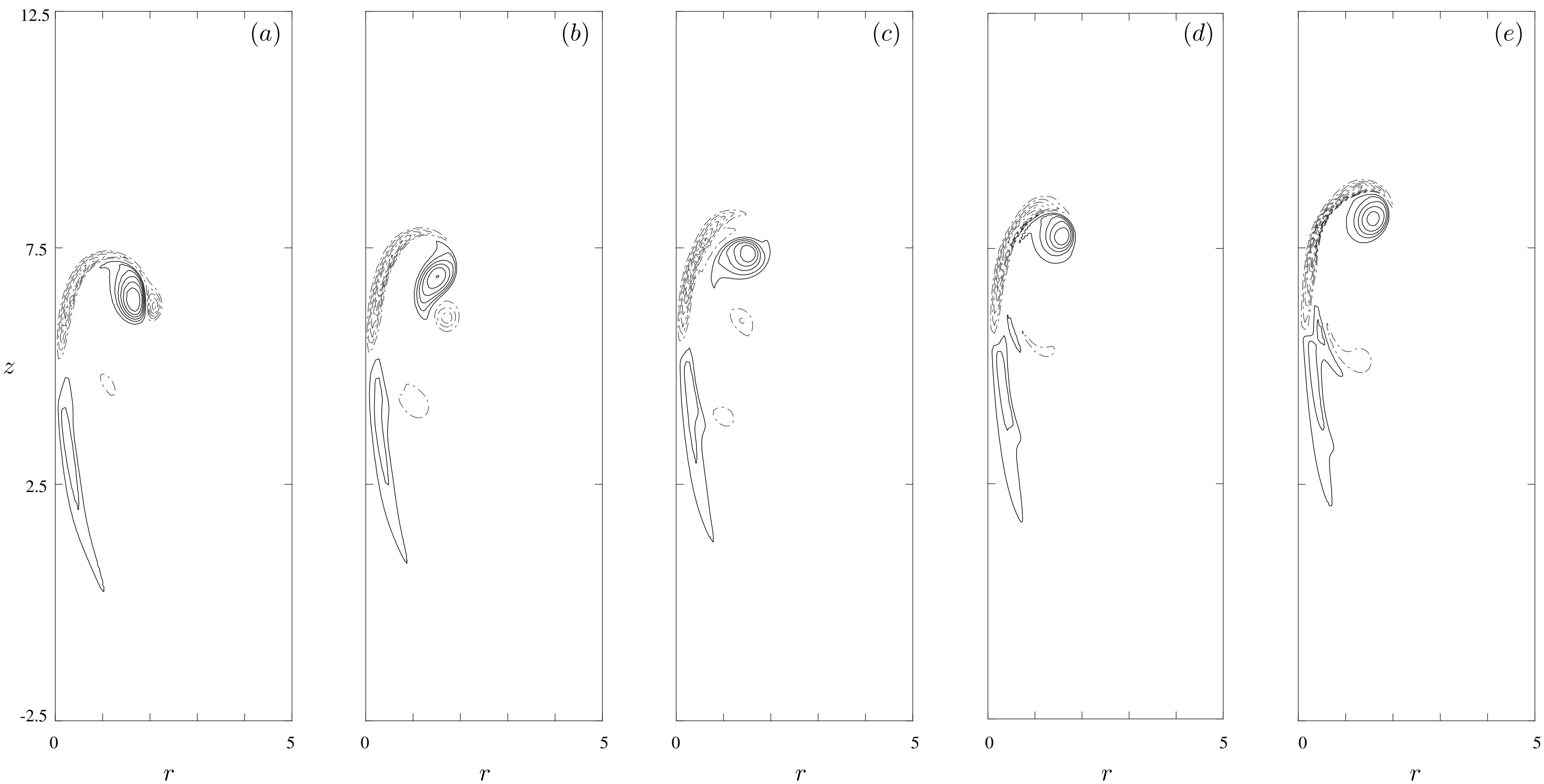

Figure 6.12: Contours of constant azimuthal vorticity at times $t = 20$ (a), $t = 22$ (b), $t = 24$ (c), $t = 26$ (d) *and* $t = 28$ (e), *for a flow with Reynolds number* $\mathrm{Re} = 1000$ *and Rossby number* $\mathrm{Ro} = 5$. *Solid lines give positive contours and dashed lines give negative contours with spacing* $\Delta\omega_\theta^+ = 0.52$ *and* $\Delta\omega_\theta^- = -0.28$.

Figure 6.13(a) gives the distance travelled in the axial direction by the vortex cores in flows at different rates of rotation. As with Hill's spherical vortex in chapter 4 a rotation rate corresponding to a Rossby number of $\mathrm{Ro} = 50$ is seen to make little impact on the distance travelled by the vortex ring whilst at $\mathrm{Ro} = 5$ the vortex ring travels less than half the distance it did in the non-rotating case and by $t = 50$ cease propagating altogether. Figure 6.13(b) gives the trajectories of the vortex cores in the r–z plane. In a non-rotating fluid the vortex core travels in a path parallel to the axis of propagation. Small rotation rates $(\mathrm{Ro} = 20)$ cause the vortex cores to move outwards radially due to the centrifugal force. Recall that the centrifugal force is a "fictitious force" which accounts for the rotating frame of reference. However, for sufficiently high rotation rates ($\mathrm{Ro} = 5$–10) vortex shedding causes the primary vortex core to follow a sinuous trajectory. Figure 6.14 gives the propagation speed of the vortex ring. The vortex shedding process is reflected in the oscillations in the propagation velocity for $\mathrm{Ro} = 5$–10.

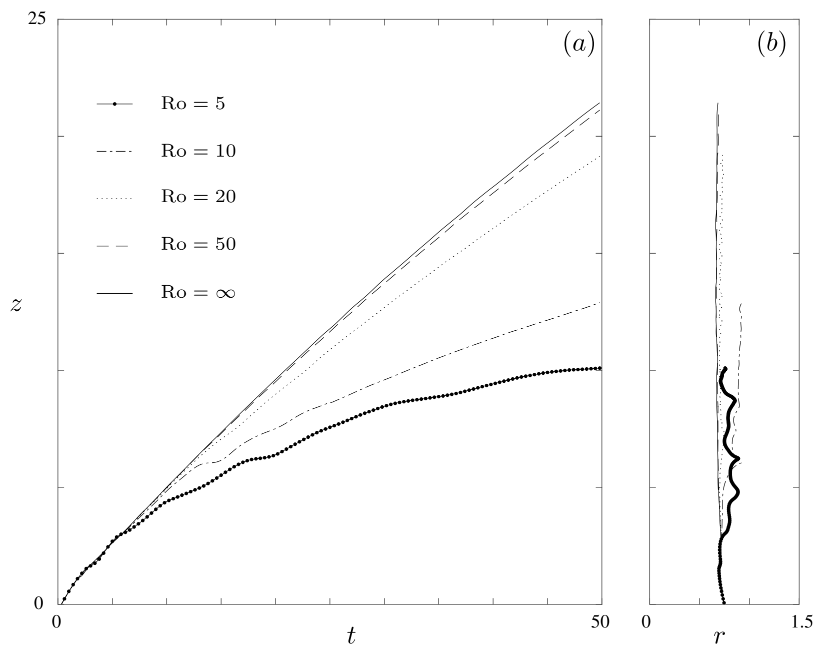

Figure 6.13: (a): The distance travelled by the vortex core against time of a vortex ring with initial mean-core radius $\alpha = 0.6$ in flows with Reynolds number $\mathrm{Re} = 1000$ and Rossby number $\mathrm{Ro} = 5, 10, 20, 50, \infty$. (b): The trajectory in the r–z plane.

Figure 6.15 shows the circulation of the vortex ring in fluids of different rates of rotation. The solid black line gives the circulation of the vortex ring in a non-rotating flow. A rotation rate corresponding to a Rossby number of $\mathrm{Ro} = 50$ makes little difference to the reduction seen in circulation. As the Rossby number is reduced below $\mathrm{Ro} = 20$ a significant reduction in the circulation is observed.

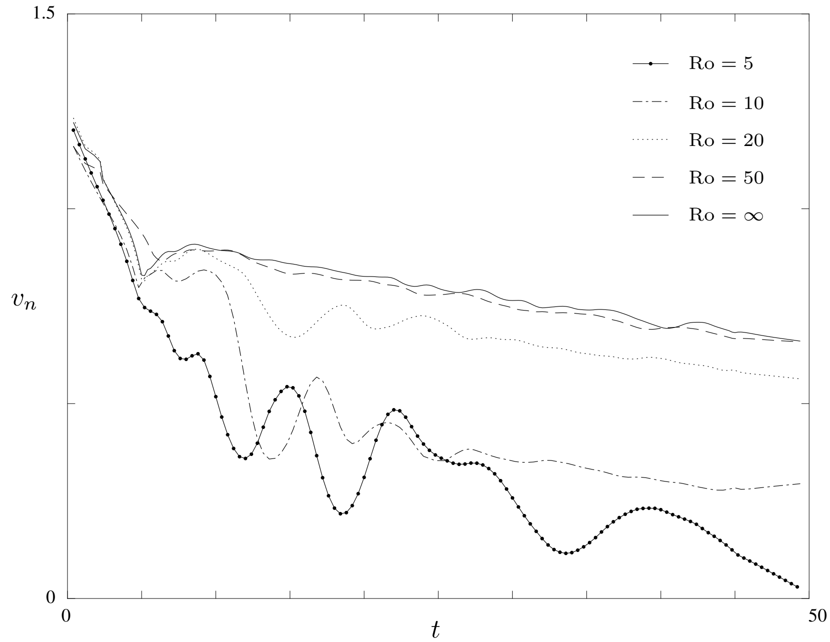

Figure 6.14: The normalised velocity, v_n, of vortex rings against time, t, for flows with Reynolds number $\mathrm{Re} = 1000$ *and Rossby number* $\mathrm{Ro} = 5, 10, 20, 50, \infty$.

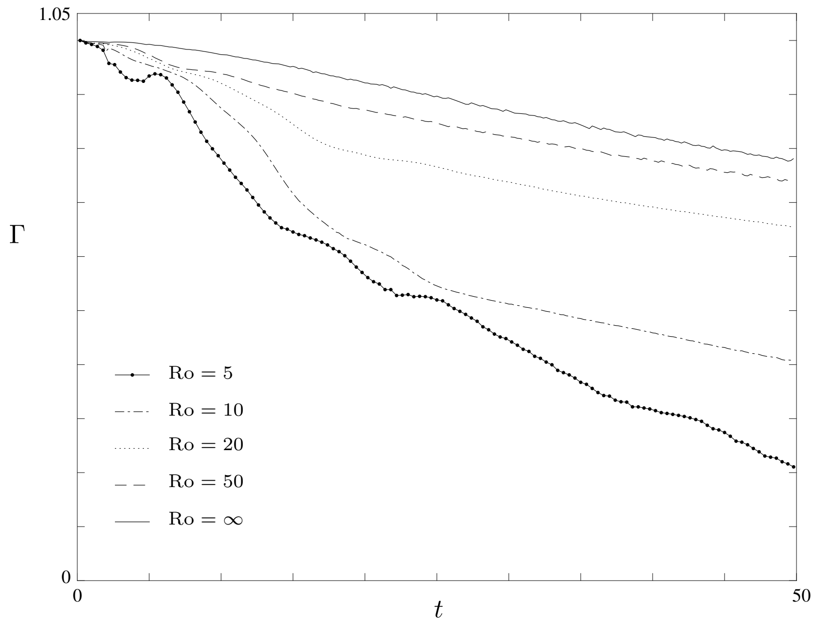

Figure 6.15: The circulation, Γ_n, of the vortex rings against time, t, of a vortex ring with initial mean-core radius $\alpha = 0.6$ in a flow with Reynolds number $\mathrm{Re} = 1000$ and Rossby numbers $\mathrm{Ro} = 5, 10, 20, 50, \infty$.

6.3.2 Higher Reynolds number results

Verzicco et al. (1996) found that more shedding events occurred when the Reynolds number was increased. Figures 6.16 and 6.17 show the azimuthal vorticity field for a Fraenkel-Norbury vortex ring with mean-core radius $\alpha = 0.6$ in a flow with Reynolds number $\mathrm{Re} = 2000$ and $\mathrm{Ro} = 10$. At time $t = 13$ two oppositely signed vortical structures can be seen rolling up on the outside of the vortex ring simultaneously strongly distorting the shape of the vortex ring. The first of these is shed at $t = 16$ and the second at $t = 19$. A third oppositely signed vortex is also shed at $t = 31$.

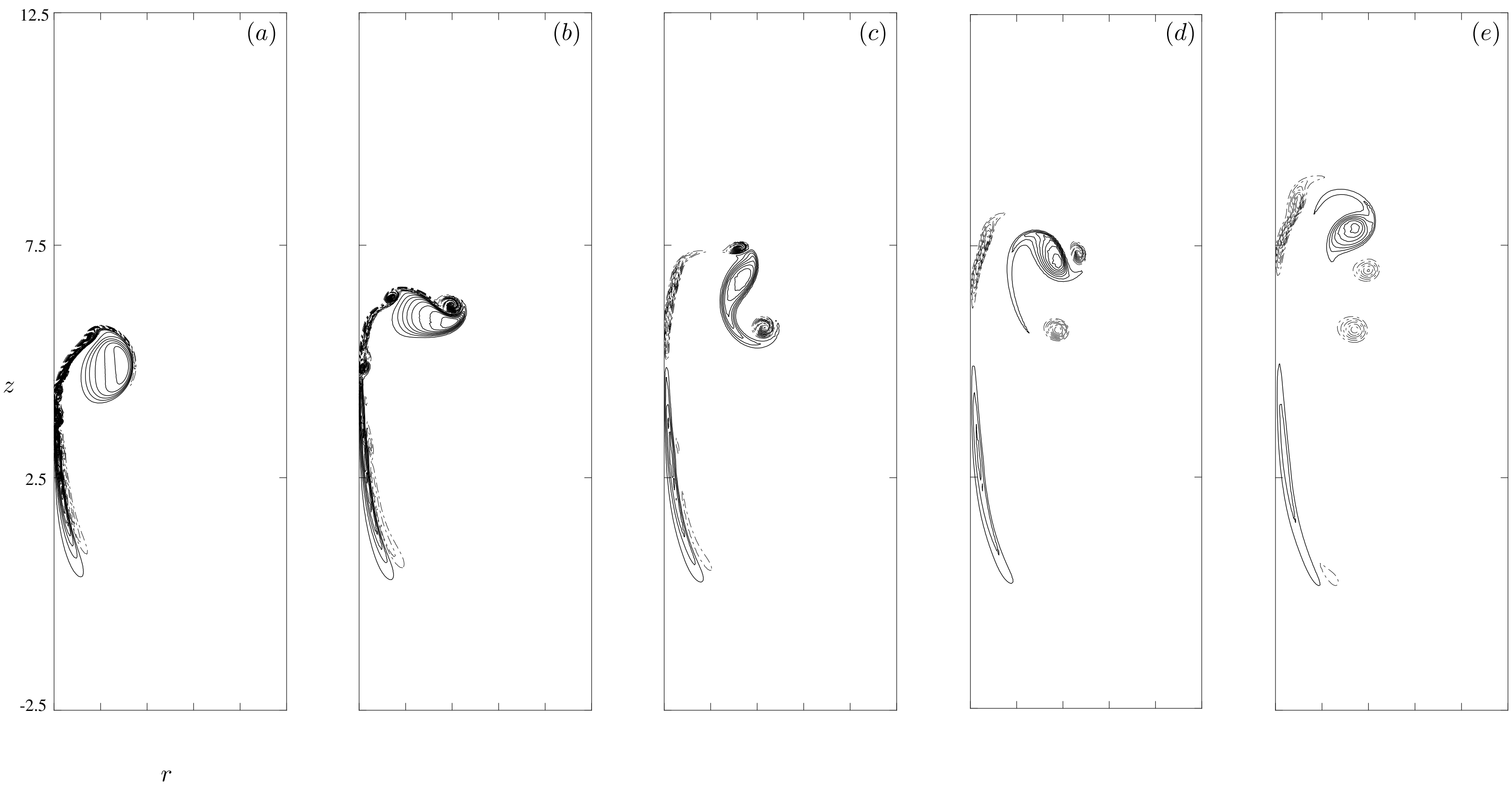

Figure 6.16: Contours of constant azimuthal vorticity at times $t = 10$ (a), $t = 13$ (b), $t = 16$ (c), $t = 19$ (d) *and* $t = 22$ (e), *for a flow with Reynolds number* $\mathrm{Re} = 2000$ *and Rossby number* $\mathrm{Ro} = 10$. *Solid lines give positive contours and dashed lines give negative contours with spacing* $\Delta\omega_\theta^+ = 0.52$ *and* $\Delta\omega_\theta^- = -0.28$.

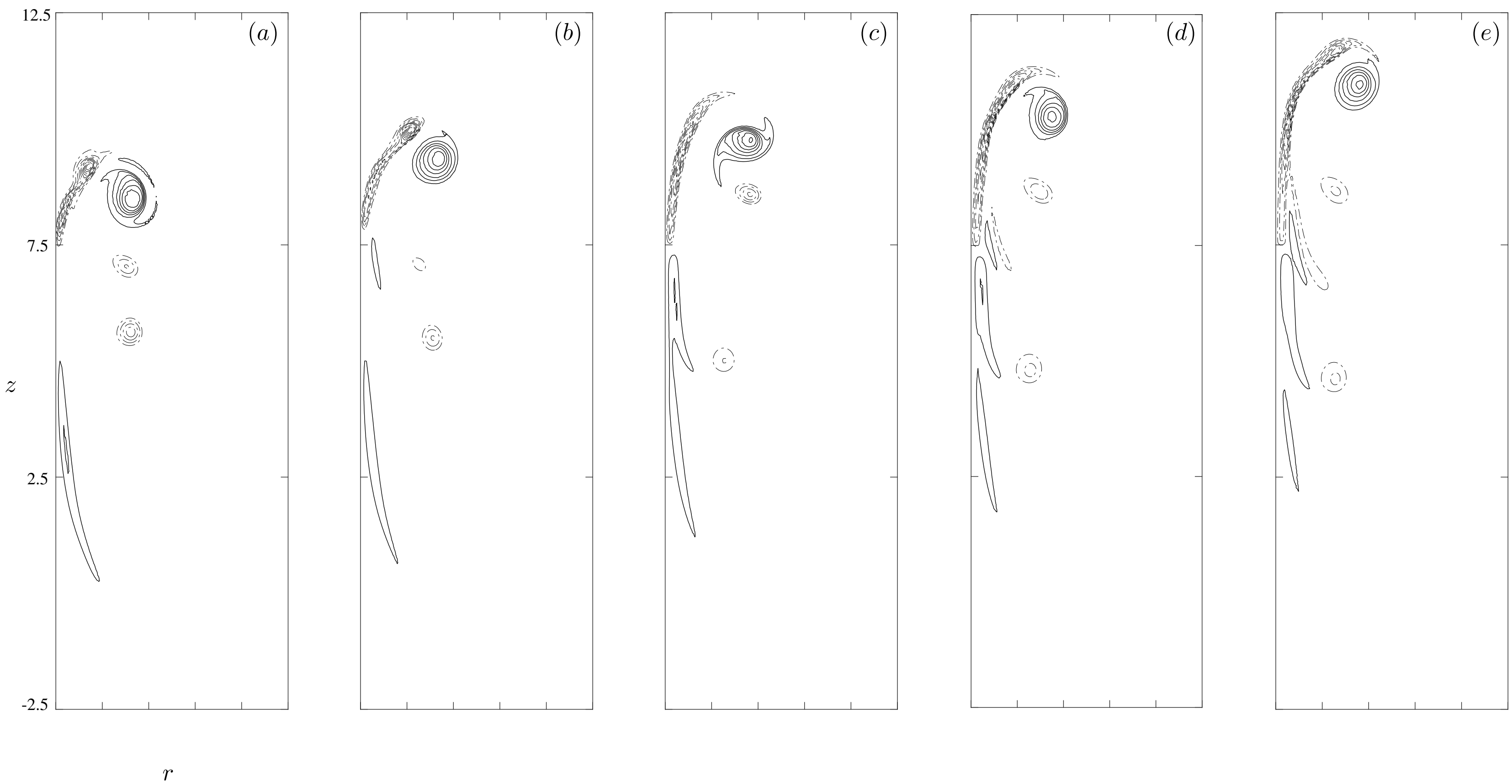

Figure 6.17: Contours of constant azimuthal vorticity at times $t = 25$ (a), $t = 28$ (b), $t = 31$ (c), $t = 34$ (d) *and* $t = 37$ (e), *for a flow with Reynolds number* $\mathrm{Re} = 2000$ *and Rossby number* $\mathrm{Ro} = 10$. *Solid lines give positive contours and dashed lines give negative contours with spacing* $\Delta\omega_\theta^+ = 0.52$ *and* $\Delta\omega_\theta^- = -0.28$.

6.3.3 Changing the mean-core radius

Table 6.1 compares the normalised circulation at time $t = 50$ of vortex rings in flows with Rossby number $\mathrm{Ro} = \infty$ and $\mathrm{Ro} = 10$. The circulation of a vortex ring at time $t = 50$ in flow with Rossby number $\mathrm{Ro} = \infty$ is given by Γ_∞ whilst Γ_{10} is the circulation of a vortex ring at time $t = 50$ in flow with Rossby number $\mathrm{Ro} = 10$. The proportion of circulation maintained by the vortex ring in the rotating to non-rotating case is given by $\Gamma_{10}/\Gamma_\infty$. Vortex rings with smaller mean-core radii have larger values of $\Gamma_{10}/\Gamma_\infty$ and therefore maintain a greater proportion of their circulation in fluid rotating with Rossby number $\mathrm{Ro} = 10$. The theory of Saffman (1970) suggests that in non-rotating fluids vortex rings with narrower vortex cores maintain their circulation better than vortex rings with fatter cores. These results show further that vortex rings with narrower vortex cores retain a greater proportion of their circulation in rotating flows.

α	Γ_∞	Γ_{10}	$\Gamma_{10}/\Gamma_\infty$
0.2	0.8365	0.6028	0.7206
0.4	0.8117	0.4661	0.5742
0.6	0.7814	0.4090	0.5234
0.8	0.7803	0.3867	0.4956
1.0	0.7692	0.3004	0.3905
$\sqrt{2}$	0.7473	0.2223	0.2975

Table 6.1: Table giving the normalised circulation at time $t = 50$ of vortex rings in rotating and non-rotating fluids. Γ_∞ is the circulation of a vortex ring at time $t = 50$ in a non-rotating fluid. Γ_{10} is the circulation of a vortex ring at time $t = 50$ in flow with Rossby number $\mathrm{Ro} = 10$. The last column gives $\Gamma_{10}/\Gamma_\infty$, the proportion of circulation maintained by the vortex ring in the rotating to non-rotating case.

The time $t = 50$ has been used to make the comparisons in table 6.1 as this is the maximum time reached during the Fraenkel-Norbury simulations. However, Hill's spherical vortex at $t = 50$ has not fully undergone vortex shedding (see figure 6.18). For a more rigorous investigation the simulations should be continued for longer to see if the same relationship is still observed at larger times. Furthermore, it should be noted that the calculation of Γ_{10} for Hill's spherical vortex using the logging method was found to be unusually high at $\Gamma_{10} = 0.3328$ for the trend set by the rest of the vortex family. On closer inspection it was found that at $t = 50$ azimuthal vorticity forming part of the vortex tail contributed towards the circulation whilst for the other vortices it did not. This can be seen in figure 6.18 where the logging region is highlighted with the red lines. The shaded red region indicates a strong patch of azimuthal vorticity that distorted the results. The contribution to the circulation of this patch was calculated to be 0.1105 which was subsequently subtracted to leave the value $\Gamma_{10} = 0.2223$ given in the table. This highlights the importance but also one of the limitations of the logging procedure.

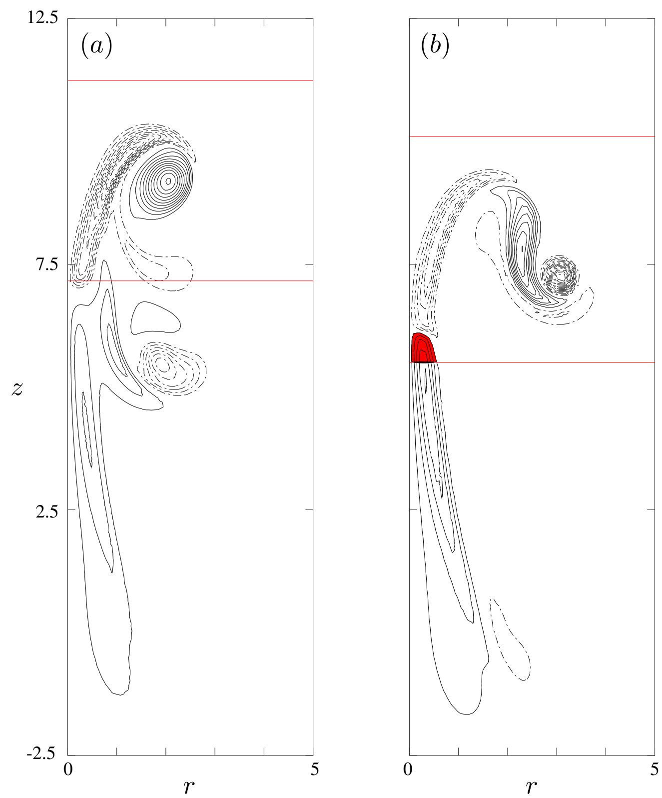

Figure 6.18: Contours of constant azimuthal vorticity at time $t = 50$ for (a) : $\alpha = 1.0$ (b) : $\alpha = \sqrt{2}$, for a flow with Reynolds number $\mathrm{Re} = 1000$ and Rossby number $\mathrm{Ro} = 10$. Solid lines give positive contours and dashed lines give negative contours with spacing $\Delta\omega_\theta^+ = 0.104$ and $\Delta\omega_\theta^- = -0.056$. The red lines indicate the boundary of the logging region.

Table 6.2 compares the average velocity of the whole motion for each vortex ring at $\mathrm{Ro} = \infty$ and $\mathrm{Ro} = 10$. In the non-rotating case we saw that fatter vortex cores maintained their propagation velocity for longer. This can be seen again in the fourth column of table 6.2. However, at $\mathrm{Ro} = 10$ all the vortex cores see a reduction in propagation velocity by approximately half (column 6, $V_{av,10}/V_{av,\infty}$). The final column of the table gives the proportion of the average velocity maintained in the rotating to non-rotating case. The results suggest that narrow vortex cores could maintain a greater proportion of their propagation velocity. However, the proportion for Hill's spherical vortex is unusually high. This can be explained by looking at Hill's vortex at $t = 50$ in figure 6.18(b). The vortex is undergoing a shedding event with the primary vortex core temporarily advected forward by the effect of a secondary vortex ring shedding from its rear. This has distorted the average velocity of the vortex ring by increasing its velocity just before $t = 50$.

		$\mathrm{Ro} = \infty$		$\mathrm{Ro} = 10$		
α	V_I	V_{av}	V_{av}/V_I	V_{av}	V_{av}/V_I	$V_{av,10}/V_{av,\infty}$
0.2	0.8488	0.6100	0.7186	0.4747	0.5593	0.7781
0.4	0.6586	0.5238	0.7953	0.3414	0.5184	0.6518
0.6	0.5357	0.4372	0.8161	0.2621	0.4893	0.5995
0.8	0.4428	0.3722	0.8406	0.2280	0.5149	0.6126
1.0	0.3703	0.3219	0.8693	0.1888	0.5097	0.5865
$\sqrt{2}$	0.2667	0.2505	0.9393	0.1585	0.5942	0.6327

Table 6.2: Table giving the average velocity of vortex rings with mean core radii $\alpha = 0.2, 0.4, 0.6, 0.8, 1.0$ and $\sqrt{2}$. V_{av} is the average velocity of a vortex ring. V_I is the initial velocity of a vortex ring. The last column $V_{av,10}/V_{av,\infty}$, gives the proportion of the velocity maintained by the vortex ring in the rotating case to the non-rotating case.

Table 6.3 similarly compares the final velocities at $t = 50$ for each vortex ring at $\mathrm{Ro} = \infty$ and $\mathrm{Ro} = 10$. Again there is evidence to suggest that vortex cores with narrower cross section maintain their propagation velocity best. The results for Hill's vortex are again distorted by its shedding of a secondary vortex towards the end of the period $t = 0 - 50$.

It was necessary to choose the final time as $t = 50$ as the narrowest Fraenkel-Norbury vortex ring with $\alpha = 0.2$ - and largest initial velocity - has almost reached the edge of the domain by this point. Although all simulations were run to $t = 70$, past $t = 50$ no reliable values for circulation and propagation distance can be obtained for the narrowest vortex cores. This is unfortunate as Hill's vortex has not fully undergone vortex shedding by this point and this has influenced the results. The experiment therefore needs to be repeated on a larger domain.

		$\mathrm{Ro} = \infty$		$\mathrm{Ro} = 10$		
α	V_I	V_{end}	V_{end}/V_I	V_{end}	V_{end}/V_I	$V_{end,10}/V_{end,\infty}$
0.2	0.8488	0.4569	0.5383	0.2722	0.3207	0.5958
0.4	0.6586	0.4004	0.6079	0.1900	0.2885	0.4745
0.6	0.5357	0.3538	0.6604	0.1578	0.2945	0.4460
0.8	0.4428	0.3049	0.6885	0.1021	0.2305	0.3348
1.0	0.3703	0.2713	0.7327	0.1052	0.2841	0.3877
$\sqrt{2}$	0.2667	0.2108	0.7906	0.1455	0.5454	0.6902

Table 6.3: Table giving the final velocity of vortex rings with mean core radii $\alpha = 0.2, 0.4, 0.6, 0.8, 1.0$ and $\sqrt{2}$. V_{end} is the final velocity of a vortex ring. V_I is the initial velocity of a vortex ring. The last column $V_{end,10}/V_{end,\infty}$, gives the proportion of the velocity maintained by the vortex ring in the rotating case to the non-rotating case.

6.4 Summary

This chapter has investigated the behaviour of Fraenkel-Norbury vortex rings in rotating and non-rotating fluids. Section 6.2 began by comparing the behaviour of different Fraenkel-Norbury vortex rings in a non-rotating fluid. Fatter-cored vortex rings see a smaller reduction in propagation velocity. Having the "fattest" vortex core Hill's spherical vortex saw the smallest reduction propagation velocity. The results were unable to conclude whether Fraenkel-Norbury vortex rings with thinner or fatter cores retained their circulation for longer.

In section 6.3 Fraenkel-Norbury vortex rings in rotating fluids are seen to shed oppositely signed vortex rings similarly to Hill's spherical vortex. Depending upon the Reynolds number and rotation rate of the flow it is possible for multiple shedding events to occur. Flows with higher Reynolds numbers and faster rotation rates see more shedding events. At Reynolds number $\mathrm{Re} \approx 2000$ multiple oppositely signed vortices were found to roll up on the original vortex ring at once.

In section 6.3.3 vortices in rotating fluids with narrow vortex cores saw a smaller reduction in propagation velocity than vortices with fatter cores. Furthermore, the proportion of circulation maintained in rotating flows to non-rotating flows was greater in narrower vortex rings.

Chapter 7

Conclusions

This thesis has provided a comprehensive investigation into the behaviour of axisymmetric vortex rings in rotating fluids using analytical and numerical methods. It has provided exact steady solutions for Hill's spherical vortex and Moffatt vortices in a rotating ideal fluid and shown how these solutions may suggest vortex motion in rotating viscous fluids may be more stable that previously thought. The work has considered how critical azimuthal swirl is to vortex motion and touched upon the effects of vortex core size on vortex ring behaviour.

7.1 Spherical vortices in ideal fluids

This thesis has provided original solutions to the rotating Euler equations. Chapter 3 derived explicit solutions of the rotating Euler equations that support steadily propagating spherical vortices. These are believed to be the only known exact vortex solutions to the rotating Euler equations. The "inner" vortex solutions take the form of members of a doubly-infinite family of vortices which swirl in such a way as to exactly cancel out the background rotation of the fluid. This inner solution matches onto an outer free-stream solution which exhibits nonlinear inertial waves which increase in amplitude as the rotation rate is increased. It was noted that due to the radiation condition this wavefield may only occur if the energy to set up the flow does not come from the vortices themselves nor be radiated into the field from infinity. It was also not clear to Taylor (1922) how such a wavefield may be set up. However, use of this inviscid solution as an initial condition in a viscous solver has demonstrated that if such a rotating vortex is generated in a fluid it is robust and is not dependent on the far-field wavefield for this robustness.

Past a critical rotation rate wave overturning was observed with closed streamlines forming in the outer fluid representing vortex rings that are concentric to the spherical vortex on the axis and which propagate with the spherical vortex. If the rotation rate is further increased beyond subsequent critical Rossby numbers additional "sibling" vortex rings are added to the vortex ring group propagating along the axis of rotation.

The stream function, ψ, of these rotating solutions is even in the Rossby number. Motion in the axial and radial directions depends only on the magnitude of the rotation of the system and not its direction, as might be expected on physical grounds. Similarly, the azimuthal swirl field is odd in the Rossby number and so the azimuthal flow is reversed if the direction of rotation of the system is reversed. Finally, the rotating solutions have the property that the non-rotating solutions are recovered in the limit $\mathrm{Ro} \to \infty$.

As an exact solution to the Euler equations and because there is evidence that it is found in nature (Turner, 1964), Hill's spherical vortex is often used as a model vortex ring (Synge and Lin, 1943). This new solution to the rotating equations now provides an analogous model vortex ring for rotating fluids.

7.2 Spherical vortices in viscous fluids

Chapter 4 began by introducing the numerical procedure used throughout this thesis presenting the derivation of the weak formulation for the rotating Navier-Stokes equations and the numerical method used to solve the nonlinear problem at each time step. It was explained how the axisymmetry of the problem would be exploited to simplify the problem to two dimensions on a meridional plane but lead to a loss of any azimuthal instabilities that would occur in a real fluid. This section also considered convergence and accuracy of the numerical scheme.

The chapter then proceeded with a numerical investigation of Hill's spherical vortex in a viscous fluid. It was unknown how closely the inviscid theory of Pozrikidis (1986) and Moffatt and Moore (1978) related to real viscous fluids. The present work has shown that the propagation of Hill's spherical vortex in a non-rotating fluid is similar to the prolate perturbation results of Pozrikidis (1986) with Hill's spherical vortex shown to detrain a wide tail of weakly rotational fluid.

This thesis has been able to confirm the results of previous published works. Chapter 4 corroborated the general findings of Verzicco et al. (1996), Brend and Thomas (2009), Watchapon (2015) and Uchiyama et al. (2015) on vortex rings in rotating fluids. In a rotating fluid Hill's spherical vortex saw a greater loss of circulation and propagation velocity due to the generation of a region of negative azimuthal vorticity ahead of the vortex ring. This region of negative azimuthal vorticity is generated by axial gradients of azimuthal swirl which is itself generated to ensure conservation of angular momentum. At moderate Reynolds numbers $(\mathrm{Re} = 1000)$ and Rossby numbers $(5 \leqslant \mathrm{Ro} \leqslant 20)$ this region of negative azimuthal vorticity was advected around the outside of the vortex ring rolling up into its own negatively signed vortex before being shed behind the primary vortex ring. The arguments of Verzicco et al. (1996) for this behaviour were reiterated and the importance of generated azimuthal swirl to this phenomenon highlighted.

Again corroborating the findings of Verzicco et al. (1996), at low Rossby number $(\mathrm{Ro} \approx 1)$ Coriolis effects dominated the flow with inertial waves emitted from the collapsing vortex ring.

This thesis then extended upon the above works - as suggested by Verzicco et al. (1996) - by considering the evolution of swirling Moffatt vortices in rotating flows. When assigned with positive (cyclonic) azimuthal swirl these initially swirling vortex rings were found to decelerate faster than Hill's spherical vortex and undergo vortex shedding more readily. However, the opposite effect was observed if assigned with negative (anticyclonic) azimuthal swirl. The reversed axial gradients of azimuthal velocity inhibited the growth of a negatively-signed region of azimuthal vorticity ahead of the vortex ring delaying vortex shedding. This is a new finding.

Chapter 5 considered the relevance of the inviscid solutions of chapter 5 to real viscous flow by using the rotating spherical vortex solutions of chapter 3 as the initial flow fields in the finite element solver. The rotating vortex rings saw a much smaller reduction in propagation velocity and circulation compared to the non-rotating vortices with vortex shedding also no longer observed. In fact, for moderate to large Rossby numbers $(\mathrm{Ro} \geq 5)$ the circulation and propagation distance of the rotating vortices is virtually indistinguishable from Hill's vortex in a non-rotating fluid. This suggests that if such rotating vortices - with swirl component cancelling out the background rotation - are found in real viscous rotating flows then the subsequent motion of that vortex ring is not as unstable as previously anticipated. This is the key finding of this work: it is possible for spherical vortex rings to propagate in rotating fluids in much the same way as they may in non-rotating fluids.

7.3 Fraenkel-Norbury vortex rings

Until now it had not been considered whether vortex rings with narrower or larger cores were able to persist for longer in a rotating fluid. As a benchmark chapter 6 began by simulating the propagation of a variety of Fraenkel-Norbury vortex rings in a non-rotating fluid. Vortex rings with narrower cores saw the greatest reduction in propagation velocity. As the vortex ring with largest vortex core in the family, Hill's spherical vortex was seen to decelerate the least.

Like Hill's spherical vortex, Fraenkel-Norbury vortex rings were observed to undergo vortex shedding. At $\mathrm{Re} = 1000$ a Fraenkel-Norbury vortex ring with mean-core radius $\alpha = 0.6$ was seen to shed two oppositely signed vortex rings. At $\mathrm{Re} = 2000$ multiple oppositely signed vortex rings were seen rolling up on the primary vortex ring simultaneously - strongly but temporarily distorting its shape - before being shed behind the primary vortex ring. Distortion of this magnitude has not been observed in previous works and it is interesting to observe how the primary vortex ring regains a coherent shape after the shedding.

Finally, the chapter considered Fraenkel-Norbury vortex rings in rotating fluids with different mean-core radii. When compared to their loss of circulation and propagation velocity in a non-rotating fluid, vortex rings with narrower vortex cores were found to maintain a disproportionally larger amount of circulation and propagation velocity in a rotating fluid. As the fattest vortex ring of the family, Hill's spherical vortex saw the greatest reduction in circulation when compared to its propagation in a non-rotating fluid.

7.4 General conclusions

Past works on vortex rings in rotating fluids (Verzicco et al., 1996; Brend and Thomas, 2009; Watchapon, 2015; Uchiyama et al., 2015) have shown how rotation promotes the premature destruction of vortex rings through the generation of negative azimuthal vorticity ahead of the vortex ring. This may then be advected around the outside of the vortex ring resulting in vortex shedding. This behaviour has been observed in the present work following the evolution of a Hill's spherical vortex. The importance of azimuthal velocity to this phenomenon has been considered and we have explored the behaviour of cyclonic and anticyclonic swirling Moffatt vortices.

The discovery of an exact vortex solution to the rotating Euler equations and observation of its robustness when used as an initial flow field in a viscous fluid suggests that it is possible for spherical vortices to propagate in rotating fluids without becoming immediately distorted. It is interesting that these solutions swirl in such a way as to cancel out the background rotation of the fluid noting that Moffatt vortices with anticyclonic swirl were more stable than their cyclonic counterparts.

Vortex shedding behaviour was also seen by Fraenkel-Norbury vortex rings which were in fact observed to undergo multiple shedding events. This research has shown that Fraenkel-Norbury vortex rings of narrower cross-section are better at retaining their circulation and propagation velocity in a rotating fluid when compared to the circulation and propagation velocity maintained in a non-rotating fluid.

It was noted in appendix B that the runtimes of the simulations in this thesis ranged from approximately 1 day to 5 days. There would be significant room for improvement on these times if FreeFem++'s adaptive mesh refinement tool *adaptmesh* was exploited. Furthermore, FreeFem++ also now supports parallel processing using MPI with an extended interface with MPI added to FreeFem++ version 3.5 in September 2017. This could be further used to improve computational speed. A full three-dimensional model was also produced in an attempt to capture behaviour due to azimuthal asymmetry which would be found in real turbulent flows. However, these simulations were computationally expensive and too slow to run at a sufficiently high resolution. An alternative choice of software could be considered for large three-dimensional computations.

7.5 Future work

Although chapter 6 has provided an initial investigation into the effect of rotation on vortices varying in vortex core size this is an area which requires further research. The results could be corroborated if the experiment was repeated for vortex rings with circular cross-section and Gaussian distributions of vorticity like in the works of Watchapon (2015) and Uchiyama et al. (2015). This type of vortex ring in a viscous fluid has substantially more supporting theory (Saffman, 1970; Tinaikar et al., 2018) allowing the non-rotating results to be verified before contrasting with the rotating results.

One of the most interesting results from this work was the behaviour of Moffatt's vortex with anticyclonic swirl in a rotating fluid and how this had a stabilising effect on the vortex motion. It does not seem a coincidence that the exact rotating vortex solutions found in chapter 3 swirl in such a way as to cancel out the background rotation of the fluid. Therefore further investigation into vortex rings with anticyclonic swirl could be conducted to better understand the stabilising effect the anticyclonic swirl has.

It has been noted that full three-dimensional simulations are computationally expensive and slow in FreeFem++ without use of adaptive mesh refinement and parallel processing. An obvious extension to this work is to run such simulations to capture the behaviour of any azimuthal asymmetry that may occur in real three-dimensional flow. Alternative software packages and mesh optimisation should be considered for achieve simulations with faster runtimes.

This work and past works on vortex rings propagating parallel to the axis of propagation have considered problems where the axis of propagation coincides with the axis of rotation. This has enabled axisymmetry to be exploited and complex three-dimensional problems simplified to two dimensions. However, in real applications it is likely that the axis of propagation of a vortex ring will not coincide with the axis of rotation and an extension to this work could consider vortex rings propagating parallel to but not along the axis of rotation. This would necessarily produce a three-dimensional non-axisymmetric problem to be investigated with three-dimensional simulations.

Appendix A

Stream function-vorticity weak formulation

This appendix outlines the derivation of the weak formulation of the stream function-vorticity and stream function-velocity problems solved in chapters 2, 4 and 6. In each of these chapters either the velocity field or vorticity field is known and the finite element method is used to calculate the corresponding stream function. This outline explicitly features the velocity field $\mathbf{u}$, however, at any point $\nabla \times \mathbf{u}$ may be replaced by $\boldsymbol{\omega}$ to give the equivalent form for vorticity.

A.1 Weak formulation of the stream function problem

For three-dimensional axisymmetric flow the stream function can be found by solving the stream function-velocity problem

$$-\nabla^2 \boldsymbol{\psi} = \nabla \times \mathbf{u}. \tag{1.1}$$

To derive an appropriate weak formulation for this problem we require for a set of vector-valued test functions $\mathbf{v} \in \mathbf{H}^1_{E_0}$ that

$$\int_{\mathcal{D}} -\nabla^2 \boldsymbol{\psi} \cdot \mathbf{v} \, \mathrm{d}\mathcal{D} = \int_{\mathcal{D}} (\nabla \times \mathbf{u}) \cdot \mathbf{v} \, \mathrm{d}\mathcal{D} \tag{1.2}$$

which exists so long as the integrals involved are well defined. This is true if

$$\boldsymbol{\psi} \in \mathbf{H}^1_E := \{\boldsymbol{\psi} \in \mathcal{H}^1 (\mathcal{D})^3 \mid \boldsymbol{\psi} = \boldsymbol{\Psi} \text{ on } \partial\mathcal{D}\}, \tag{1.3a}$$

$$\mathbf{v} \in \mathbf{H}^1_{E_0} := \{\mathbf{v} \in \mathcal{H}^1 (\mathcal{D})^3 \mid \mathbf{v} = \mathbf{0} \text{ on } \partial\mathcal{D}\}, \tag{1.3b}$$

where $\boldsymbol{\Psi}$ is the value of the stream function on the boundary and $\mathcal{H}^1(\mathcal{D})^3$ is the *Sobolev space* given by

$$\mathcal{H}^1(\mathcal{D})^3 := \left\{ \boldsymbol{\psi} : \mathcal{D} \to \mathbb{R}^3 \;\middle|\; \boldsymbol{\psi}, \frac{\partial \boldsymbol{\psi}}{\partial r}, \frac{\partial \boldsymbol{\psi}}{\partial z} \in L_2(\mathcal{D}) \right\}, \tag{1.4}$$

which ensures that $\boldsymbol{\psi}$ and its first derivatives all have finite L_2 measure

$$L_2(\mathcal{D}) := \left\{ \boldsymbol{\psi} : \mathcal{D} \to \mathbb{R}^3 \;\middle|\; \int_{\mathcal{D}} |\boldsymbol{\psi}|^2 \,\mathrm{d}\mathcal{D} < \infty \right\} \tag{1.5}$$

(see Elman et al., 2014).

Note that

$$\int_{\mathcal{D}} \nabla^2 \boldsymbol{\psi} \cdot \mathbf{v} \,\mathrm{d}\mathcal{D} = -\int_{\mathcal{D}} \nabla \boldsymbol{\psi} : \nabla \mathbf{v} \,\mathrm{d}\mathcal{D} - \int_{\mathcal{D}} \left(\frac{\psi_r v_r}{r^2} + \frac{\psi_\theta v_\theta}{r^2} \right) \mathrm{d}\mathcal{D} + \int_{\mathcal{D}} \nabla \cdot (\nabla \boldsymbol{\psi} \cdot \mathbf{v}) \;\mathrm{d}\mathcal{D} \tag{1.6a}$$

$$= -\int_{\mathcal{D}} \nabla \boldsymbol{\psi} : \nabla \mathbf{v} \,\mathrm{d}D - \int_{\mathcal{D}} \left(\frac{\psi_r v_r}{r^2} + \frac{\psi_\theta v_\theta}{r^2} \right) \mathrm{d}\mathcal{D} + \int_{\partial\mathcal{D}} (\mathbf{n} \cdot \nabla \boldsymbol{\psi}) \cdot \mathbf{v} \,\mathrm{dS} \tag{1.6b}$$

where $\nabla \boldsymbol{\psi} : \nabla \mathbf{v} = \nabla \psi_r \cdot \nabla v_r + \nabla \psi_\theta \cdot \nabla v_\theta + \nabla \psi_z \cdot \nabla v_z$.

The continuity requirements on the weak solution $\boldsymbol{\psi}$ are relaxed by integrating term $\mathbf{v} \cdot \nabla^2 \boldsymbol{\psi}$ by parts by applying identity (1.6b) to equation (1.2) to yield

$$\int_{\mathcal{D}} \nabla \boldsymbol{\psi} : \nabla \mathbf{v} \,\mathrm{d}\mathcal{D} - \int_{\partial\mathcal{D}} (\mathbf{n} \cdot \nabla \boldsymbol{\psi}) \cdot \mathbf{v} \,\mathrm{dS} + \int_{\mathcal{D}} \left(\frac{\psi_r v_r}{r^2} + \frac{\psi_\theta v_\theta}{r^2} \right) \mathrm{d}\mathcal{D} = \int_{\mathcal{D}} \nabla \times \mathbf{u} \cdot \mathbf{v} \,\mathrm{d}\mathcal{D}. \tag{1.7}$$

To avoid a singularity as $r \to 0$ introduce the scalings $\psi_r = \tilde{\psi}_r r$ and $\psi_\theta = \tilde{\psi}_\theta r$ and let $\mathrm{d}\mathcal{D} = r\mathrm{d}r\mathrm{d}z$. The weak formulation is to find $\boldsymbol{\psi} \in \mathbf{H}^1_E$ such that

$$\int_{\mathcal{D}} \nabla \boldsymbol{\psi} : \nabla \mathbf{v} \, r \,\mathrm{d}r\mathrm{d}z - \int_{\partial\mathcal{D}} (\mathbf{n} \cdot \nabla \boldsymbol{\psi}) \cdot \mathbf{v} \,\mathrm{dS} + \int_{\mathcal{D}} \left(\tilde{\psi}_r v_r + \tilde{\psi}_\theta v_\theta \right) \mathrm{d}r\mathrm{d}z = \int_{\mathcal{D}} \nabla \times \mathbf{u} \cdot \mathbf{v} \, r \,\mathrm{d}r\mathrm{d}z \tag{1.8}$$

for all $\mathbf{v} \in \mathbf{H}^1_{E_0}$ and where $\boldsymbol{\psi} = \left(r\tilde{\psi}_r, r\tilde{\psi}_\theta, \psi_z \right)$.

The boundary conditions supplied may be a combination of the Dirichlet and Neumann conditions

$$\boldsymbol{\psi} = \boldsymbol{\psi_D} \text{ on } \partial\mathcal{D}_d, \qquad \frac{\partial \boldsymbol{\psi}}{\partial n} = \boldsymbol{\psi_N} \text{ on } \partial\mathcal{D}_n. \tag{1.9}$$

Appendix B

FreeFem++ and computational resource

B.1 Introduction to FreeFem++

FreeFem++ is a free and open source language and finite element solver for partial differential equations written in C++. The software is capable of generating the mesh for complex domains using Delaunay-Voronoi triangulation. This is a triangulation of the set of points **P** in which no point in the set **P** lies inside the circumference of any of the triangles. This is demonstrated in figure B.1. Delaunay-Voronoi triangulation maximises the minimum angle in each triangle which has the result of avoiding long, narrow triangles. FreeFem++ then requires the input of an appropriate weak formulation as well as suitable boundary conditions to solve the finite element problem. The results from FreeFem++ were exported via a text file and post-processing was completed in MatLab.

B.2 Computational resource

All finite element computations in this thesis were run on The University of Nottingham's High Performance Compute Cluster Minerva comprising 166 compute nodes each with two 8-core processors. This was to done to run multiple simulations over many Reynolds and Rossby numbers simultaneously which would have been too computationally expensive for a desktop computer. For each simulation a shell script requested 6GB of RAM on one compute core. The simulations from chapters 4 and 6 had a typical runtime of 5 days

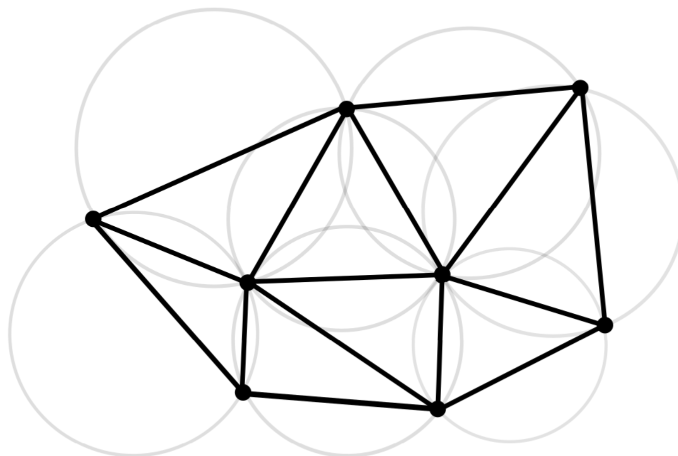

*Figure B.1: Triangulation of a group of points **P** using Delaunay-Voronoi triangulation. Points in **P** lie only on the circumference of the enclosing grey circles to the triangles.*

whilst the simulations of chapter 5 had a runtime of approximately 24 hours.

Bibliography

Acton, E. (1980). A modelling of large eddies in an axisymmetric jet, *J. Fluid Mech.* **98**(1): 1–31.

Balakrishnan, S. K. (2013). *A numerical study of some vortex ring phenomena using direct numerical simulation*, PhD thesis, University of Southampton.

Banerji, S. K. and Barave, R. V. (1931). On Oberbeck's vortices, *Phil. Mag. Fluids* **11**: 1057–1081.

Batchelor, G. K. (1967). *An Introduction to Fluid Dynamics*, Cambridge University Press.

Brend, M. A. and Thomas, P. J. (2009). Decay of vortex rings in a rotating fluid, *Physics of Fluids* **21**(4): 044105.

Cheng, M., Lou, J. and Lim, T. T. (2010). Vortex rings with swirl: a numerical study, *Physics of Fluids* **22**(9): 097101.

Davies, P. O. A. L. and Yule, A. J. (1975). Coherent structures in turbulence, *J. Fluid Mech.* **69**(3): 513–537.

Eisenga, A. H. M. (1997). *Dynamics of a vortex ring in a rotating fluid*, PhD thesis, Eindhoven University of Technology.

Eisenga, A. H. M., Verzicco, R. and van Heijst, G. J. F. (1998). Dynamics of a vortex ring moving perpendicularly to the axis of a rotating fluid, *J. Fluid Mech.* **354**: 69–100.

Elman, H. C., Silvester, D. J. and Wathen, A. J. (2014). *Finite Elements and Fast Iterative Solvers*, Oxford University Press.

Eydeland, A. and Turkington, B. (1988). A computational method of solving free-boundary problems in vortex dynamics, *J. Comp. Phys.* **78**(1): 194–214.

Fraenkel, L. E. (1970). On steady vortex rings of small cross-section in an ideal fluid, *Proc. Roy. Soc. Lond. A* **316**: 29–62.

Fraenkel, L. E. (1972). Examples of steady vortex rings of small cross-section in an ideal fluid, *J. Fluid Mech.* **51**(1): 119–135.

Gargan-Shingles, C., Rudman, M. and Ryan, K. (2015). The evolution of swirling axisymmetric vortex rings, *Physics of Fluids* **27**: 087101.

Greenspan, H. P. (1968). *The theory of rotating fluids*, Cambridge University Press.

Harper, J. F. and Moore, D. W. (1968). The motion of a spherical liquid drop at high Reynolds number, *J. Fluid Mech.* **32**(2): 367–391.

Hicks, W. M. (1899). Researches in vortex motion - part III. on spiral or gyrostatic vortex aggregates, *Phil. Trans. Roy. Soc. A* **192**: 33–99.

Hill, M. J. M. (1894). On a spherical vortex, *Phil. Trans. Roy. Soc. A* **185**: 213–245.

Keedy, H. F. (1967). *Vortex rings formed by free surface interaction*, PhD thesis, University of Michigan.

Krutzsch, C. (1939). Über eine experimentell beobachtete Erscheinung an Wirbelringen bei ihrer translatorischen Bewegung in wirklichen Flüssigkeiten, *Annalen der Physik* **427**(6): 497–523.

Lau, J. C. and Fisher, M. J. (1975). The vortex-street structure of 'turbulent' jets. Part 1, *J. Fluid Mech.* **67**(2): 299–337.

Lifschitz, A., Suters, W. H. and Beale, J. T. (1996). The onset of instability in exact vortex rings with swirl, *J. Comp. Phys.* **129**: 8–29.

Lighthill, M. J. (1967). On waves generated in dispersive systems by travelling forcing effects, with applications to the dynamics of rotating fluids, *J. Fluid Mech.* **27**(4): 725–752.

Lim, T. T. and Nickels, T. B. (1995). Vortex rings, *in* S. I. Green (ed.), *Fluid Vortices*, Kluwer.

Lugt, H. J. (1983). *Vortex Flow in Nature and Technology*, Wiley, New York.

Manton, M. J. (1976). Propagation of spherical vortices, *Aust. J. Phys.* **29**: 61–65.

Maxworthy, T. (1972). The structure and stability of vortex rings, *J. Fluid Mech.* **51**(1): 15–32.

Moffatt, H. K. (1969). The degree of knottedness of tangled vortex lines, *J. Fluid Mech.* **35**(1): 117–129.

Moffatt, H. K. and Moore, D. W. (1978). The response of Hill's spherical vortex to a small axisymmetric disturbance, *J. Fluid Mech.* **87**(4): 749–760.

Moore, D. W. (1963). The boundary layer on a spherical gas bubble, *J. Fluid Mech.* **16**(2): 161–176.

Moore, D. W., Saffman, P. G. and Whitham, G. B. (1972). The motion of a vortex filament with axial flow, *Philos. Trans. R. Soc. Lond. A* **272**: 403–427.

Naitoh, T., Okura, N., Gotoh, T. and Kato, Y. (2014). On the evolution of vortex rings with swirl, *Physics of Fluids* **26**: 067101.

Norbury, J. (1973). A family of steady vortex rings, *J. Fluid Mech.* **57**(3): 417–431.

Ooi, A., Soria, J., Lim, T. T., Kollmann, W. and Chong, M. S. (2001). A numerical study of swirling vortex rings, *In Fourteenth Australasian Fluid Mechanics Conference* pp. 375–378.

Pedlosky, J. (1987). *Geophysical Fluid Dynamics*, Springer-Verlag.

Pozrikidis, C. (1986). The nonlinear instability of Hill's vortex, *J. Fluid Mech.* **168**: 337–367.

Press, W. H., Flannery, B. P., Teukolsky, S. A. and Vetterling, W. T. (1992). *Numerical recipes in Fortran 77: The Art of Scientific Computing, 2nd ed.*, Cambridge University Press.

Protas, B. and Elcrat, A. (2016). Linear stability of Hill's vortex to axisymmetric perturbations, *J. Fluid Mech.* **799**: 579–602.

Proudman, J. and Lamb, H. (1916). On the motions of solids in a liquid possessing vorticity, *Proc. Roy. Soc. A* **92**(642): 408–424.

Richardson, L. F. (1922). *Weather Prediction by Numerical Process*, Cambridge University Press.

Saffman, P. G. (1970). The velocity of viscous vortex rings, *Stud. Appl. Math.* **49**(4): 371–380.

Saffman, P. G. (1981). Dynamics of vorticity, *J. Fluid. Mech.* **106**: 49–58.

Saffman, P. G. (1992). *Vortex Dynamics*, Cambridge University Press.

Saffman, P. G. (1997). Vortex models of isotropic turbulence, *Phil. Trans. R. Soc. Lond. A* **355**: 1949–1956.

Scase, M. and Terry, H. (2018). Spherical vortices in rotating fluids, *J. Fluid Mech.* **846**: R4.

Shariff, K. and Leonard, A. (1992). Vortex rings, *Ann. Rev. Fluid Mech.* **24**: 235–279.

Stewartson, K. (1958). On the motion of a sphere along the axis of a rotating fluid, *Q. J. Mech. Appl. Math.* **11**(1): 39–51.

Synge, J. L. and Lin, C. C. (1943). On a statistical model of isotropic turbulence, *Trans. R. Soc. Canada* **37**: 45–79.

Taylor, G. I. (1922). The motion of a sphere in a rotating liquid, *Proc. Roy. Soc. Lond. A* **102**(715): 180–189.

Tinaikar, A., Advaith, S. and Basu, S. (2018). Understanding evolution of vortex rings in viscous fluids, *J. Fluid Mech.* **836**: 873–909.

Turner, J. S. (1964). The flow into an expanding spherical vortex, *J. Fluid Mech.* **18**(2): 195–208.

Uchiyama, T., Nakano, M. and Degawa, T. (2015). Numerical simulation of the behaviour for a vortex ring convecting along the axis of a rotating field, *J. Vortex. Sci. Technol. Comp. Meth. Eng.* **2**(1).

Verzicco, R., Orlandi, P., Eisenga, A. H. M., van Heijst, G. J. F. and Carnevale, G. F. (1996). Dynamics of a vortex ring in a rotating fluid, *J. Fluid Mech.* **317**: 215–239.

Virk, D., Melander, M. V. and Hussain, F. (1994). Dynamics of a polarized vortex ring, *J. Fluid Mech.* **260**: 23–55.

Watchapon, R. (2015). Numerical investigation of a vortex ring in a rotating fluid, *Int. Conf. App. Math. Comp. Meth. Eng.* **2**: 93–97.

Widnall, S. E., Bliss, D. B. and Zalay, A. (1971). *Theoretical and experimental study of the stability of a vortex pair. In: Aircraft Wake Turbulence and Its Detection, edited by J. Olsen, A. Goldburg, and N. Rogers*, Springer, Boston, MA.

Wu, J. Z., Ma, H. Y. and Zhou, M. D. (2006). *Vorticity and Vortex Dynamics*, Springer-Verlag Berlin.